EXPANDED GRAPHITE-NOVOLAC PHENOLIC RESIN BASED ELECTROMAGNETIC INTERFERENCE (EMI) SHIELDING MATERIAL OVER THE X-BAND: SYNTHESIS, CHARACTERIZATION, ANALYSIS AND DESIGN OPTIMIZATION

A thesis submitted in partial fulfillment of the

requirements for the degree of

Doctor of Philosophy

by

Jyoti Prasad Gogoi
Registration No. 005 of 2008

Department of Physics
School of Science
Tezpur University
Napaam, Tezpur - 784028
Assam, India

December, 2012

Dedicated To

My

Beloved Parents & GrandMaa

Abstract

Wireless technology stride towards gigahertz frequency applications in modern communication system has increased the electromagnetic interference (EMI), hindering the normal operation of the electronics system. To control this ever increasing EMI pollution, the demand on efficient EMI shielding is increasing. The EMI can be minimized by using radar absorbing material (RAM) which will reduce electromagnetic waves reflections and absorb them. The issues related to RAM are: to get an enhanced broadband absorption, to make the material light weight and environmentally inert. The absorber should have an easy processing technique, easily available raw material and to reduce the overall development cost. An electromagnetic wave absorption characteristic of material in a particular frequency range, can be enhanced by tailoring its dielectric properties (complex permittivity, $\varepsilon_r = \varepsilon_r' - j\varepsilon_r''$) and magnetic properties (complex permeability, $\mu_r = \mu_r' - j\mu_r''$) along with the thickness of RAM. Generally, RAMs are dielectric or magnetic materials which can absorb and dissipate incident microwave by converting it into thermal energy. The present research work focuses on development of a dielectric EMI absorbing shielding material for use over the X-band.

Expanded graphite (EG) flakes consisting of small stacks of graphene sheets are selected as dielectric inclusions with low density and moderate electric conductivity is used as inclusions in novolac phenolic resin polymer which has good interactive property.

The EG-NPR composite developed is thermally stable up to 250-300 °C and has density <1 making it light weight.

Broadband complex permittivity of EG-NPR composites show high dielectric loss ~ (0.6-1.2) over the X-band and can be used as broadband microwave absorbing materials. Using transmission line model, the reflection loss is calculated for conductor backed single and multilayer dielectric microwave absorber over the X-band.

Absorption studies carried out using free space technique on the absorber shows minimum value of reflection loss in the X-band. The optimized multilayer system shows enhancement in absorption bandwidth almost covering the X-band.

A perforated microwave absorber is designed to improve the absorption bandwidth and reduces the weight. Perforated single layered structure shows 2GHz enhancement of bandwidth in X-band range.

Thus, a desired level of absorption in the required frequency range in X-band can be achieved by using different structural designs of EG-NPR composites.

DECLARATION BY THE CANDIDATE

I hereby declare that the thesis "**Expanded graphite-novolac phenolic resin based electromagnetic interference (EMI) shielding material over the X band: synthesis, characterization, analysis and design optimization**", being submitted to Department of Physics, Tezpur University, Tezpur, Assam in partial fulfillment for the award of the degree of Doctor of Philosophy in Physics, has previously not formed the basis for the award of any degree, diploma, associateship, fellowship or any other similar title or recognition.

Jyoti Prasad Gogoi

Date: December 29, 2012

Place: Tezpur

(Jyoti Prasad Gogoi)
Department of Physics
School of Science
Tezpur University

TEZPUR UNIVERSITY

(A Central University by an Act of Parliament)

Napaam, Tezpur-784028

DISTRICT: SONITPUR::ASSAM::INDIA

Ph. 03712-267008(O) 5551,5555 (EPABX) 9435084076 (M)

Fax: 03712-267006

Email: *nidhi@tezu.ernet.in*

CERTIFICATE OF THE PRINCIPAL SUPERVISOR

This is to certify that the thesis entitled "**Expanded graphite-novolac phenolic resin based electromagnetic interference (EMI) shielding material over the X band: synthesis, characterization, analysis and design optimization"**, Tezpur University in partial fulfillment for the award of the degree of Doctor of Philosophy in Physics is a record of research work carried out by Mr. Jyoti Prasad Gogoi under my supervision and guidance.

All helps received from various sources have been duly acknowledged.

No part of this thesis has been submitted elsewhere for award of any degree.

Date: Dec 24, 2012

Place: Tezpur

Nidhi S. Bhattacharyya
Professor
Department of Physics
Tezpur University

TEZPUR UNIVERSITY

(A Central University by an Act of Parliament)
Napaam, Tezpur-784028
DISTRICT: SONITPUR::ASSAM::INDIA

Ph. 03712-267004 (O) 9957198489 (M) **Fax: 03712-267006** **Email:** *adm@tezu.ernet.in*

Certificate of the External Examiner and ODEC

This is to certify that the thesis entitled "**Expanded graphite-novolac phenolic resin based electromagnetic interference (EMI) shielding material over the X band: synthesis, characterization, analysis and design optimization**" submitted by Mr. Jyoti Prasad Gogoi to Tezpur University in the **Department of Physics** under the **School of Science** in partial fulfillment for the award of the degree of Doctor of Philosophy in **Physics** has been examined by us on_____ and found to be satisfactory.

The committee recommends for the award of the degree of Doctor of Philosophy.

Supervisor
(N. S. Bhattacharyya)

Date: _____

External Examiner
(**)**

Date: _____

Acknowledgements

"I can no other answer make, but, thanks, and thanks."

William Shakespeare

I would like to express my deep gratitude to Prof. Nidhi S. Bhattacharyya, my research supervisor, for her patient guidance, enthusiastic encouragement and useful critiques of this research work.

I would like to thank Prof. Satyajib Bhattacharyya and Dr. Pritam Deb for their useful and constructive recommendations on this project.

I would like to thank Hon'ble Vice Chancellor of Tezpur University, Prof. Mihir Kanti Chaudhuri for giving inspiration and encouraging advice throughout my research work.

I am highly grateful to Prof. A. Choudhury, Prof. J. K. Sarma, Prof. A. Kumar, Prof. N. Das, Dr. G.A. Ahmed, Dr. D. Mahanta, Dr. P. Deb, Dr. K. Barua, Dr. P.K. Karmakar, Dr. M.K. Das, Dr. P. Nath, Mr. R. Biswas and Dr. R. Gogoi of Department of Physics and Prof. S.K. Duloi of Department of Chemical Sciences for their personal involvement, timely help, stimulating discussion to carry out research. I acknowledge the help received from the technical staff of Department of Physics.

I am thankful to Prof. K.C.James Raju, University of Hyderabad, for his valuable suggestions.

I would like to thank SAIF, Shillong, IIT Guwahati, Department of Chemical Sciences, Tezpur University for allowing me to avail the analytical facilities required in my research work.

I am extremely indebted to Department of Information Technology, Govt. of India, for their financial assistance through the project to carry out the research work

My grateful thanks are also extended to Mr. Durlav Sonowal, Dept of ECE, TU, Mr. Prakash Barman and Mr. Amar Jyoti Kalita for their help during my research work.

I would like to thank the office staff of Dept. of Physics, Mr. U. Patir and Mr. N. Sarma, technical staff of Central Workshop, Tezpur University, Mr. M. Handique, Mr. K. Rangpi, Mr. D. Gogoi, Mr. P. Rabha, Mr. S.K. Nath and Mr. M. Mali for their help and support. Thanks to the Library staff and administrative staff of Tezpur University for their help.

A special thanks to all the research scholars of Department of Physics, Tezpur University for their company and wonderful time I enjoyed with them during my research work. Anup,

Sayan, Manjit, Nibedita, Angshuman, Swatiba, Mansiba, Sovanda, Jagat, Parag, Janendra, Deepak, Madhulekha, Bondita, Biswajit, thank you all for your support and encouragement.

Thank you Madhuryya, Ankurda and Sanjib Sahooda for your kind support and care.

I thank my friends, Jamir, Prabhakar, Amrit, Champak, Amit and Dhananjay, for their encouragement.

No one walks alone on the journey of life. And I do not know where to start to thank all those people who walked with me and helped me along the way continuously urging me in my work and shared my insights. My lab-mates Subasit da, Debashis da, Kunal, Sikha, Pragyan, Tanuj, Arunav and Pulin, a big thank you for all the wonderful times, academic and otherwise, that we shared together.

No words can repay for the continuous encouragement, moral support, blessings and everything else that I received from my parents, Khagen Gogoi and Rupahi Gogoi. I am thankful to my brother Bishnu for his care and support. I am grateful to my Bordeuta, Mr. J. C. Gogoi for his untiring cooperation and suggestions throughout my research work. Thanks to Lily, Babatu, Buttu, Joon, Bhoni and all my dear cousins for your love.

Last but not the least, thank you Munu, for your help and support and for always being there.

CONTENTS

List of Tables

List of Figures

CHAPTER 7

List of symbols and abbreviations

EMI	Electromagnetic interference
MAM	microwave absorbing material
RAM	Radar absorbing material
EG	Expanded Graphite
NPR	Novolac Phenolic Resin
CNT	Carbon Nano Tube
XRD	X-ray Difraction
SEM	Scanning Electron Microscopy
TEM	Transmission Electron Microscope
TLM	*Transmission line model*
FTIR	Fourier Transform Infrared Spectroscopy
TGA	Thermo Gravimetric Analysis
CTE	Coefficient of Thermal Expansion
TRL	Through-Reflect-Line
VNA	Vector Network Analyzer
RF	Radio Frequency
RL	Reflection loss
ω	Angular frequency
γ	Propagation constant
ε_{eff}	Effective permittivity
ε_r	Relative permittivity
ε_r''	Imaginary part of the complex permittivity

ε_r'	Real part of complex permittivity
μ_{eff}	Effective permeability
μ_r	Relative permeability
μ_r''	Imaginary part of complex permeability
μ_r'	Real part of complex permeability
$\tan\delta_\varepsilon$	Dielectric loss tangent
$\tan\delta_\mu$	Magnetic loss tangent
A	Ampere
dB	decibel
E	Electric field vector
EM	Electromagnetic
f_r	Resonant frequency
GHz	Giga Hertz
σ_s	Static conductivity
σ_e	Effective conductivity
σ_a	Conductivity due to alternating field
κ	Filling factor
K	Co- efficient of thermal conductivity
Q	Quality Factor
Z_0	Characteristic impedance
λ_0	Free space wavelength
λ_g	Guide wavelength
F	Farad

CHAPTER I

INTRODUCTION TO THE RESEARCH PROBLEM

1.1 INTRODUCTION

Wireless technology usages have led the need to support simultaneous operation of different wireless system in the same environment without effecting the normal functioning of each individual system. The electromagnetic radiations emitted from various systems hinder the operation of electronic devices and communication systems causing electromagnetic interference (EMI) [1]. The electromagnetic interference (EMI) is basically electrical in nature and is due to unwanted electromagnetic emission being either radiated or conducted. The issues of tackling electromagnetic compatibility are challenging and proper EMI shielding mechanism has to be ascertained.

The EMI shielding can be achieved either by reflection or absorption of the interfering electromagnetic wave [2]. Metal is considered to be the best material for reflection electromagnetic shielding but the reflected wave may interfere with the electronic component inside the enclosure or in its vicinity. Modern warfare where radar system of weapons detection and guiding missiles are needed; hiding radar signatures and camouflaging war equipments are also important issues to be considered [3].

EMI shielding through absorption mechanism, works on the principle of absorption of the interfering electromagnetic wave by converting the wave energy into thermal energy, thereby reducing the interference to a sufficiently low value [4]. However, shielding by absorption requires certain design conditions while developing the absorber and this shielding mechanism is frequency dependent. Absorbers used for shielding in microwave or radio frequency range are termed as microwave absorbing material (MAM) or radar absorbing material (RAM). The RAM also finds applications as coating on the surface of the military aircraft to avoid detection, in radio frequency anechoic chamber, in food processing technology etc.[5-8].

In general, RAMs are fabricated in the form of sheets that consist of insulating polymer, like rubber, and magnetic or dielectric loss materials such

as ferrite, permalloy, carbon black, and short carbon fiber [5, 9]. An electromagnetic wave absorption characteristic of material depends on its dielectric properties (complex permittivity, $\varepsilon_r = \varepsilon_r' - j\varepsilon_r''$), magnetic properties (complex permeability, $\mu_r = \mu_r' - j\mu_r''$), thickness and frequency range [10]. Dielectric composite absorption at microwave frequencies depends on the ohmic loss of energy, generally achieved by adding conductive fillers like carbon black, graphite or metal particles. On the other hand, magnetic composite absorption depends on magnetic hysteresis effect of the magnetic materials, like ferrite, incorporated into the matrix [11-13]. Of the two techniques, the magnetic composite absorber has two main shortcomings; firstly, density of the magnetic materials is too high to use them in large quantity as filler of absorbers. Secondly, the resonance frequency range showing effective characteristics exist in the MHz range and hence the efficiency of absorbers decreases rapidly in the GHz and beyond this range. Thus, the technical requirement for the absorber limits the number of ferromagnetic materials that can be used in the microwave range [14]. On the other hand, dielectric RAMs using carbon based materials such as carbon black, single and multiwalled carbon nanotubes (SWCNTs and MWCNTs), short carbon fibers etc. got widest attention as RAMs due to lightweight and corrosion resistant [15-17]. Infact, the research into the development of carbon based RAMs dates back in 1936 when a quarter-wave resonant absorber based on carbon black (CB) and titanium dioxide and was patented in Netherlands [18]. During World War II, America developed "Halpern Anti Radiation Paint (HARP)", an absorbing material based on rubber filled with CB, disc shaped aluminum flakes and barium titanate and used in airborne and seaborne vehicles for radar detection avoidance with 15–20 dB absorption at the X-band [19, 20]. During that time Germans developed "Wesch" material and also produced Jaumann absorbers which is multilayer layer device of alternating resistive sheets and rigid plastics[21] . Salisbury screen was another narrow

band resonant absorber consisting of resistive sheet placed at odd multiple of ¼ wavelength from the metal plate and was patented in 1952.

With progressive development of wireless technology during the post world war period, the need of broadband absorbers became major challenge with the requirement of quality anechoic chamber for accurate indoor measurement. Carbon loaded plaster of Paris and graphite was studied for microwave absorbing materials [22].

In the 1950s, the sponge product company developed a broadband microwave absorber called Spongex composed of C-coated animal hair of thickness 50.8 mm and showed 20 dB attenuation of normal incidence in the frequency range 2.4-10 GHz [21].

During 1960s and 1970s, the particulate as well as fibrous C was used to fabricate netlike, knitted or honeycomb structures [23]. Till the discovery of carbon nanotubes (CNTs) in the 1990s, CB and graphite remained the most studied microwave absorbing materials. The CNTs including single walled and multi walled have been exploited widely in developing EMI shielding materials [15, 24-31] and showed a strong microwave absorption in the frequency range 8.2-12.4 GHz [32]. High aspect ratios (= $length/diameter$) of CNTs help in attaining percolation threshold at very low concentration [33], consequently microwave absorption properties can be achieved at low wt. % of CNTs. Although CNT/composites showed low percolation threshold, there are other issues for commercially available microwave absorbers such as cost effectiveness, ease of production etc. CNT has difficulties in mixing with polymer matrix due to poor compatibility with polymers, also breakage of CNT during processing with acids resulting in decrease of aspect ratio and moreover, making cost of CNT is about 500 times than that of graphite [34].

Another promising composite reinforcement can be expanded graphite (EG) flakes, with the characteristics of very low density ~ 0.005-0.01 g/cc, high electrical conductivity ~10^4 S/cm, good thermal and mechanical properties with resistant to environmental corrosion [35-39]. EG flakes are

bi-dimensional carbon nanostructures consisting of small stacks of graphene sheets having thickness in the range from one to few tens of nanometers and the lateral linear dimensions varying from a few micrometers up to hundreds of micrometers [40]. The percolation threshold of EG/polymer composites are found to be low in comparison to that of graphite/polymer composites. Krupa and Chodak [41] reported a percolation threshold of ~12-13 vol% for graphite/polymer composites whereas the percolation threshold was achieved at 2.5 vol% for EG/polystyrene composite as reported by RK Goyal and group [42]. A low percolation threshold of 3 wt% was reported by Zheng *et al.* [43] for high density polyethylene (HPDE)/EG nanocomposites. The low percolation threshold of EG is due to its high aspect ratio and large surface area [34]. Considering these facts EG can be used for microwave absorbing or EMI shielding materials as an alternative to CNTs. Moreover, due to its low density, EG composites will be reasonably light weight. Lee Sang-Eui and group [39] studied the microwave absorption properties of graphite nanoplatelet/epoxy composites in the frequency range 12-18 GHz and found a reflection loss ~-22dB at 15 GHz.

Another aspect to be considered while fabricating microwave absorbing material is the influence of base matrix. Reference [44] reports, that the use of phenolic resin matrix in carbon black composite instead of epoxy resin matrix enhances the electrical properties of the composite. NPR being good heat resistance has dimensional stability, flame and chemical resistance as well as low cost [45, 46] can be used as base matrix while developing microwave absorbing materials.

The flexibility of designing microwave absorber using lossy reinforcers and base matrix, is the tuning of microwave absorption for a desired frequency ranges by varying the properties of material composition [47]. Considering these tunable properties of dielectric-polymer composites, interesting application possibilities of EG-NPR composites as microwave absorbing materials for application over the X-band has been studied.

1.2 THE RESEARCH DIRECTION

The research is essentially directed towards:

- Synthesis and development of light weight dielectric composite materials as broadband EMI shielding/microwave absorber having the desirable microwave permittivity and dielectric loss properties for application over the X-band frequency.
- Investigating other necessary factor requirements of microwave absorber applications like homogeneity of filler in the base matrix, light weight, thermal, electrical and environmental inertness.
- Design and fabrication of single layer microwave absorber based on developed dielectric composites.
- Design optimization of multilayer microwave structure to enhance the absorption bandwidth.
- Geometrical modification of developed microwave absorber to improve the absorption bandwidth.

1.3 THESIS STRUCTURE AND OUTLINE

The thesis structurally consists of nine chapters and one appendix. A thorough understanding of electromagnetic wave propagation through the absorber and its equivalent Transmission line model is discussed in *chapter II*. The synthesis of expanded graphite as reinforcers in novolac phenolic resin filler as possible dielectric absorber is dealt in *chapter III*. The chapter also includes microstructural studies conducted for structural, size and ascertaining the homogeneous distribution.

Other essential property required for absorbers like thermal stability, density, water absorbance and thermal dissipation are included in *chapter IV*. *In-plane* and *through-plane* dc conductivity measurements on the developed composite system is also conducted and included in the chapter.

Chapter V includes studies on complex permittivity at microwave frequencies for different weight percentage compositions. Nicolson-Ross technique is used and a detail treatment to the approach is presented.

Single layer Dallenbach absorber using EG-NPR composite with conductor backing is designed and fabricated and the thickness is optimized to achieve minimum reflection loss and discussed in *chapter VI.*

Chapter VII describes enhancement of bandwidth of using multilayer structure where the thickness of individual layer and permittivity of the composition is optimized to achieve a broad absorption bandwidth.

A perforated absorber structure is designed on the single and double layer structure to reduce the weight and enhance bandwidth and is discussed in *chapter VIII.*

Chapter IX summarizes the suitability of the developed EG-NPR dielectric material as broadband X-band absorber. The limitations and future direction of work that can be incorporated are also highlighted.

Appendix - A gives the detail of mathematical formulation for theoretical thickness limitation for broadband microwave absorption. MATLAB programs developed for computing complex permittivity, optimizing single and multilayer layer microwave absorber parameters is also discussed in this Appendix.

References

1. Tong, X. C. *Advance Materials and Design for Electromagnetic Interference Shielding*, Taylor and Francis, London, 2009.
2. Hong, S. K., Kim, K. Y., Kim, T. Y., Kim, J. H., Park, S. W., Kim, J. H., and Cho, B. J. Electromagnetic interference shielding effectiveness of monolayer graphene, *Nanotechnology* **23**, 455704 (1-5), 2012.
3. Bahret, W. F. The beginning of stealth technology, *IEEE transaction on aerospace and electronic systems* **29**, 1377-1385, 1993.
4. Han, M., and Deng, L. Doping effect of multiwall carbon nanotubes on the microwave electromagnetic properties of NiCoZn spinel ferrites, *Applied Physics Letters* **90**, 011108(1-3), 2007.
5. Chung, D.D.L. Electromagnetic interference shielding effectiveness of carbon materials, *Carbon* **39**, 279-285, 2001.
6. W. H. Emerson, Electromagnetic wave absorbers and anechoic chambers through the years, *IEEE Trans.Antennas Propag.* 21, 484-490, 1973
7. Holloway, C. L., Delyser, R. R., German, R. F., Mckenna, P., and Kanda, M. Comparison of electromagnetic absorber used in anechoic and semi-anechoic chambers for emissions and immunity testing of digital devices, *IEEE Trans. Electromagn. Compat.* **39**, 33-47, 1997.
8. Lassen, A., and Ovesen, L. Nutritional effects of microwave cooking, *Nutrition & Food Science* **95** (4), 8 - 10, 1995.
9. Elimat, Z. M. AC electrical conductivity of poly (methyl methacrylate) /carbon black composite, *J Phys D* **39**, 2824-28, 2006.
10. Michielssen, E., Sajer, J., Ranjithan, S., and Mittra, R. Design of lightweight, broad-band microwave absorbers using genetic algorithms, *IEEE. T. Microw. Theory* **41**, 1024-1030, 1993
11. Du, J. H., Sun, C., Bai, S., Su, G., Ying, Z., and Cheng, H. M. Microwave electromagnetic characteristics of a microcoiled carbon fibers/paraffin wax composite in Ku band, *J Mater Res Soc* **17**, 1232-36, 2002.

12. Luo, X., and Chung, D. D. L. Electromagnetic interference shielding using continous carbon-fiber carbon-matrix and polymer-matrix composite, *Composites: Part B* **30**, 227-31, 1999.
13. Das, N. C., Khastgir, D., Chaki, T. K., and Chakraborty, A. Electromagnetic interference shielding effectiveness of carbon black and carbon fibre filled EVA and NR based composite, *Composites: Part A* **31**, 1069-81, 2000.
14. Wallace, J. L. Broadband magnetic microwave absorbers: fundamental limitations, *IEEE Trans Magn* **29**, 4209-14, 1993.
15. Yang, Y., Gupta, M.C., Dudley, K.L., and Lawrence, R.W. Novel carbon nanotube - polystyrene foam composites for electromagnetic interference shielding, *Nano Letters* **5**, 2131-2134, 2005.
16. Liu, Z., Bai, G., Huang, Y., Ma, Y., Du, F., Li, F., Guo, T., and Chen, Y. Reflection and absorption contributions to the electromagnetic interference shielding of single-walled carbon nanotube/polyurethane composites, *Carbon*, **45**, 821–827, 2007.
17. Rosa, I. M. D., Dinescu, A., Sarasini, F., Sarto, M. S., and Tamburrano, A. Effect of short carbon fibers and MWCNTs on microwave absorbing properties of polyester composites containing nickel-coated carbon fibers, *Comp. Sci. Technol.* **70**, 102–109, 2010
18. Machinerieen, N. V. *Dispositif et procÃ©dÃ© pour l'amÃ©lioration de dispositifs de production et de rÃ©ception d'ondes Ã©lectriques ultra-courtes*, **French Patent 802 728**, 1936.
19. *Stonier, R. A.* Stealth aircraft & technology from world war II to the gulf [J], *SAMPE Journal* **27**, 9-18, 1991.
20. Halpern, O. *Method and means for minimizing reflection of high frequency radio waves*, **U.S. Pat. No. 2923934**, February 2, 1960.
21. Saville, P. *Review of Radar Absorbing Materials*, Technical Memorandum DRDC Atlantic TM 2005-003, http://www.dtic.mil/dtic/tr/fulltext/u2/a436262.pdf, 2005.

22. Pratt, B. C. *Nondirectional, metal- backed, electromagnetic radiation- absorptive films,* **US Patent 2992425,** July 11, 1961.
23. Stubbs, H. V. G., Wickenden, B. V. A., Howell, W. G., Perry, E. D. *Review of Radar Absorbing Materials,* **UK Patent GB 2058469A,** 1981.
24. Li, N., Huang, Y., Du, F., He, X., Lin, X., Gao, H., Ma, Y., Li, F., Chen, Y., and Eklund, P. C. Electromagnetic interference (EMI) shielding of single-walled carbon nanotube epoxy composites, *Nano Lett.* **6**, 1141-1145, 2006.
25. Che, R. C., Peng, L. M., Duan, X. F., Chen, Q., and Liang, X. L. Microwave absorption enhancement and complex permittivity and permeability of Fe encapsulated within carbon nanotubes, *Adv. Mater.* **16**, 401-405, 2004.
26. Fan, Z., Luo, G., Zhang, Z., Zhou, L., and Wei, F. Electromagnetic and microwave absorbing properties of multi-walled carbon nanotubes/polymer composites, *Mater. Sci. Eng. B* **132**, 85-89, 2006.
27. Kim, H. M., Kim, K., Lee, C. Y., Joo, J., Cho, S. J.,Yoon, H. S., Pejakovic, D. A., Yoo, J. W., and Epstein, A. J. Electrical conductivity and electromagnetic interference shielding of multiwalled carbon nanotube composites containing Fe catalyst, J. *Applied Physics Letters* **84**, 589-591, 2004.
28. Watts, P. C. P., Ponnampalam, D. R., Hsu, W. K., Barnes, A., and Chambers, B. The complex permittivity of multi-walled carbon nanotube-polystyrene composite films in X-band, *Chemical Physics Letters* **378**, 609-614, 2003.
29. Xiang, C., Pan, Y., Liu, X., Sun, X., Shi, X., and Guo, J. Microwave attenuation of multiwalled carbon nanotube-fused silica composites, *Appl. Phys. Lett.* **87**, 123103-1-3, 2005.
30. Gui, X., Ye, W., Wei, J., Wang, K., Lv, R., Zhu, H., Kang, F., Gu, J., and Wu, D. Optimization of electromagnetic matching of Fe-filled carbon nanotubes/ferrite composites for microwave absorption, *J. Phys. D: Appl. Phys.* **42**, 1-5, 2009.

31. Bi, C., Zhu, M., Zhang, Q., Li, Y., and Wang, H., Synthesis and electromagnetic wave absorption properties of multi-walled carbon nanotubes decorated by $BaTiO_3$ nanoparticles, *J. Nanosci.Nanotechnol.* **11**, 1030-1036, 2011.
32. Park, K. Y., Lee, S. E., Kim, C. G., and Han, J. H. Fabrication and electromagnetic characteristics of electromagnetic wave absorbing sandwich structures, *Compos. Sci. Technol.***66**, 576-584, 2006.
33. Ramasubramaniam, R., Chen, J., and Liu, H. Homogeneous carbon nanotube /polymer composites for electrical applications, *J. Appl. Phys. Lett.* **83**, 2928-2930, 2003.
34. Goyal, R. K., Samant, S. D., Thakar, A. K., and Kadam, A. Electrical properties of polymer/expanded graphite nanocomposites with low percolation, *J. Phys. D: Appl. Phys.* **43**, 365404-1-7, 2010.
35. Celzard A., Marechˆe, J. F., Furdin, G., and Puricelli, S. Electrical conductivity of anisotropic expanded graphite-based monoliths, *J. Phys. D: Appl. Phys* **33**, 3094-3101, 2000.
36. Chen, G., Wu, D., Weng, W., He, B., and Yan, W. Preparation of polystyrene-graphite conducting nanocomposites via intercalation polymerization, *J. Polym Int* **50**, 980-85, 2001.
37. Chen, G., Wu, C., Weng, W., Wu, D., and Yan, W. Preparation of polystyrene/graphite nanosheet composite, *J. Polym Commun.* **44**, 1781-84, 2003.
38. **Debelak, B., and Lafdi, K.** Use of expanded graphite filler to enhance polymer Physical properties, *Carbon* **45**, 1727-34, 2007.
39. Lee, S. E., Choi, O., and Hahn, H.T. Microwave properties of graphite nanoplatelet/epoxy composites, *J. Appl. Phys.* **104**, 033705-1- 7, 2008.
40. Du, X., Skachko, I., Barker, A., and Andrei, E. Y. Approaching ballistic transport in suspended graphene, *Nature Nanotechnol.* **3**, 491–495, 2008.
41. Krupa, I., and Chodak, I. Physical properties of thermoplastic/ graphite composite, *Eur Polym J* **37**, 2159–2168, 2001.

42. Goyal, R.K., Jagadale, P.A., and Mulik, U.P. Thermal, mechanical, and dielectric properties of polystyrene/expanded graphite nanocomposites, *J. Appl. Polym. Sci.* **111,** 2071-2077, 2009
43. Zheng, W., Lu, X., and Wong, S.C. Electrical and mechanical properties of expanded graphite-reinforced high-density polyethylene, *J. Appl. Polym. Sci.* **91,** 2781-2788, 2004.
44. Kakati, B. K., and Deka, D. Effect of resin matrix precursor on the properties of graphite composite bipolar plate for PEM fuel cell, *Energ Fuel.* **21,** 1681-87, 2007.
45. Bishop, G. R., and Sheard, P. A. Fire-resistant composites for structural sections, *Compos Struct* **21,** 85-89, 1992.
46. Knop, A., and Pilato, L. A. *Phenolic Resins/Chemistry, Applications and Performance. Future Directions,* Springer Verlag, Berlin, 1985.
47. Liu, Z., Bai, G., Huang, Y., Li, F., Ma, Y., Guo, T., He, X., Lin, X., Gao, H., and Chen, Y. Microwave absorption of single-walled carbon nanotubes/soluble cross-linked polyurethane composites, *J. Phys. Chem. C* **111,** 13696-13700, 2007.

CHAPTER II

THEORY OF ELECTROMAGNETIC INTERFERENCE SHIELDING: ELECTROMAGNETIC WAVE ABSORPTION

2.1 INTRODUCTION

The electromagnetic spectra especially from 0.3 GHz to 300 GHz frequency has been highly exploited in defense as well as by commercial industries. This has led to the need for either avoiding detection through camouflaging, as in military applications, or reducing the electromagnetic pollution to avoid interference. Knowledge of physical optics and its interaction with materials is essential to minimize reflections, emissions and hence suppression of the electromagnetic waves. Interaction of the microwave with different materials is explicated in figure 2.1.

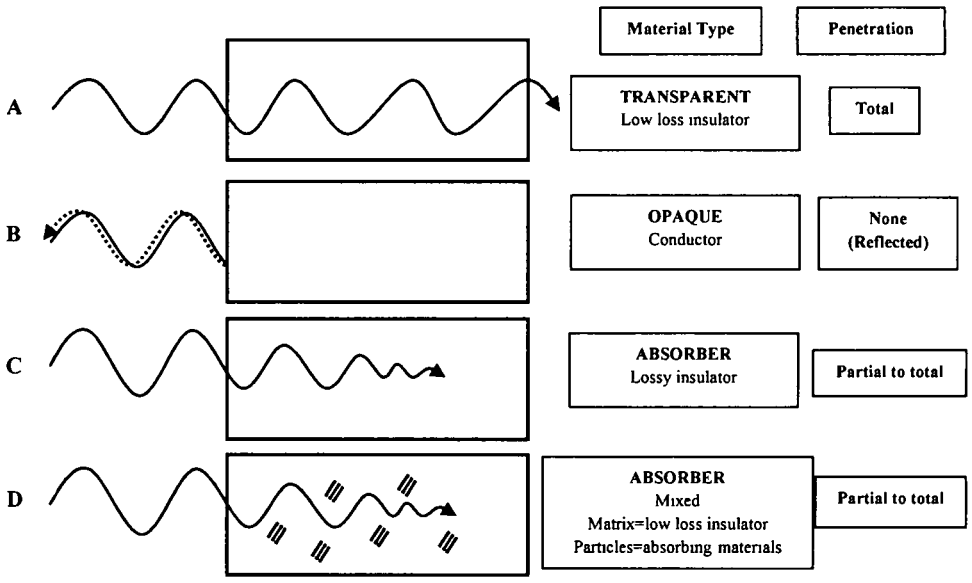

Figure 2.1 Interaction of microwaves with different materials (Sutton, 1989, [1])

As seen in case D of figure 2.1, the electromagnetic waves can be suppressed by using composites with fillers reinforced in a matrix. Electromagnetic wave comes across different interactions with variety of microscopic boundary conditions due to the inclusions in the hetero-structure. The localized field variations have a strong effect on absorption of energy at such boundaries and the electric field intensity falls of fast. The dissipation of

energy is mostly in form of heat etc [2, 3]. The interaction can be quantified mainly by the two complex parameters of the absorber material viz. the complex permittivity, $\varepsilon_r = \varepsilon_r' - j\varepsilon_r''$ and the complex permeability, $\mu_r = \mu_r' - j\mu_r''$. The electric component of electromagnetic wave gets attenuated by dielectric polarization and conduction loss [4] and magnetic component by hysteresis and resonance (domain wall and electron spin (FMR)) of the absorbing system [5, 6]. The absorbing material considered in present investigation is dielectric in nature. Understanding the interaction of electromagnetic waves with dielectric material parameters is essential and is initially discussed in this chapter. Propagation of electromagnetic wave in a homogenous media has been treated as an equivalent transmission line model (TLM) in many books and research papers [7-9]. Design and realization of single and multilayer planar absorbing structure in X-band is carried out using TLM and is discussed in the later part of the chapter.

2.2. ELECTROMAGNETIC THEORY FOR DIELECTRIC ABSORBER.

The absorption of microwaves in dielectric medium depends on the material's complex permittivity. The mathematical formulation of this loss mechanism can be obtained using Maxwell's wave equations [10].

The modified Ampere law equation in phasor form is

$$\nabla \times \bar{H} = \bar{J} + j\omega\bar{D} \tag{2.1}$$

where $\bar{D} = \varepsilon\bar{E}$ (2.2)

$$\bar{J} = \bar{J}_i + \bar{J}_c \tag{2.3}$$

$$\bar{J}_c = \sigma_s\bar{E} \tag{2.4}$$

$\bar{D}$ is the electric flux density and ε is the permittivity

$\bar{J}_i$ is the impressed electric current density, i.e. an excitation to the system by an outside source.

$\bar{J}_c$ is the conduction current density, caused by application of an external field.

σ_s is the conductivity.

From equations (2.1), (2.3) and (2.4), we have

$$\nabla \times \bar{H} = \bar{J}_i + \sigma_s \bar{E} + j\omega \bar{D} \quad (2.5)$$

When the microwaves penetrate and propagate through a dielectric material having electric dipoles, the dipoles align with the applied external field [11, 12]. This action causes a term to be added to the electric flux density that has the same vector direction as the applied field. The equation (2.2) can be described as

$$\bar{D} = \varepsilon_0 \bar{E} + \varepsilon_0 \chi_e \bar{E} \quad (2.6)$$

The term χ_e is the electric susceptibility and gives a relationship between the electric field and the electric flux density caused by the presence of the dielectric. Rewriting equation (2.6) as

$$\bar{D} = \varepsilon_0 (1 + \chi_e) \bar{E} \quad (2.7)$$

or

$$\bar{D} = \varepsilon_0 \varepsilon_r \bar{E} \quad (2.8)$$

ε_r , the relative permittivity of the medium is a complex quantity expressed as

$$\varepsilon_0 \varepsilon_r = \varepsilon' - j\varepsilon'' \quad (2.9)$$

where, ε_0 , is the permittivity of free space (ε_0= 8.86 x 10^{-12} F/m), $\varepsilon'$is the real part of complex permittivity and ε'' is the effective relative dielectric loss factor [13].

When an oscillating electric field interacts with the dipole, the dipole rotates to align itself according to the polarity. During the alignment the energy is lost through the generation of heat (friction) and the acceleration and deceleration of the rotational motion. The degree to which the dipole is out of phase with the incident electric field is a characteristic to the material and depends on frequency of the oscillating electric field, which determines the magnitude of the imaginary part of the permittivity. The larger the imaginary part, more the energy is being dissipated through the alignment motion and

hence, less energy is available to propagate past the dipole. Thus, the imaginary part of the relative permittivity directly relates to loss in the system.

The equation (2.5) by using equations (2.8) and (2.9), is given as

$$\nabla \times \bar{H} = \bar{J}_i + \sigma_s \bar{E} + j\omega(\varepsilon' - j\varepsilon'')\bar{E} \quad (2.10)$$

$$\nabla \times \bar{H} = \bar{J}_i + (\sigma_s + \omega\varepsilon'')\bar{E} + j\omega\varepsilon'\bar{E} \quad (2.11)$$

$$\nabla \times \bar{H} = \bar{J}_i + \sigma_e \bar{E} + j\omega\varepsilon'\bar{E} \quad (2.12)$$

where, σ_e, is the effective conductivity, consists of static conductivity, σ_s and conductivity due to the alternating field, σ_a such that

$$\sigma_e = \sigma_s + \omega\varepsilon'' \quad (2.13)$$

or

$$\sigma_e = \sigma_s + \sigma_a \quad (2.14)$$

Equation (2.12) can be written as

$$\nabla \times \bar{H} = \bar{J}_i + j\omega\varepsilon'\left(1 - j\frac{\sigma_e}{\omega\varepsilon'}\right)\bar{E} \quad (2.15)$$

$$\nabla \times \bar{H} = \bar{J}_i + j\omega\varepsilon'(1 - jtan\delta_e)\bar{E} \quad (2.16)$$

Loss tangent, $tan\delta_e$ is expressed as

$$tan\delta_e = \frac{\sigma_e}{\omega\varepsilon'} \quad (2.17)$$

Equation (2.15) can be further expanded as

$$\nabla \times \bar{H} = \bar{J}_i + j\omega\varepsilon'\left(1 - j\frac{\sigma_s}{\omega\varepsilon'} - j\frac{\varepsilon''}{\varepsilon'}\right)\bar{E} \quad (2.18)$$

In equation (2.18), the first term $\frac{\sigma_s}{\omega\varepsilon'}$ describes the loss due to collisions of electrons with other electrons and atoms. As $\sigma_s \to \infty$, the electric field, $\bar{E} \to 0$, for a finite current density as illustrated by the equation given below

$$\bar{E} = \frac{J_c}{\sigma_s} \quad (2.19)$$

In conductors, the term $\frac{\sigma_s}{\omega\varepsilon'}$ dominates the other term $\frac{\varepsilon''}{\varepsilon'}$. The effective conductivity is almost entirely due to the collisions of electrons, and the polarization dependent term is dropped. Maxwell's equation (2.18) reduces to

$$\nabla \times \bar{H} \approx \bar{J}_i + (j\omega\varepsilon_0 + \sigma_s)\bar{E} \quad (2.20)$$

The second term $\varepsilon'' / \varepsilon'$ describes the amount of energy supplied by an external electric field that gets dissipated in alignment motion of dipole and heat which is more evident in dielectrics. The effective conductivity is almost entirely due to polarization loss (dipole motion), and hence the first term is neglected in the formulation and the Maxwell's equation (2.18) reduces to

$$\nabla \times \bar{H} \approx \bar{J}_i + j\omega\varepsilon'(1 - j\frac{\varepsilon''}{\varepsilon'})\bar{E} \tag{2.21}$$

Absorber can be considered as a dielectric block with finite non-zero static conductivity and polarization loss through which a plane electromagnetic wave propagates. As the wave originates from outside the block, the impressed sources, $\bar{J}_i$, are zero.

The instantaneous time domain vector wave equations (Helmholtz equations), can be derived after some mathematical manipulations of Maxwell's equations and are given as

$$\nabla^2\bar{E} = \mu\sigma_s\frac{\partial\bar{E}}{\partial t} + \mu\varepsilon\frac{\partial^2\bar{E}}{\partial t^2} \tag{2.22}$$

$$\nabla^2\bar{H} = \mu\sigma_s\frac{\partial\bar{H}}{\partial t} + \mu\varepsilon\frac{\partial^2\bar{H}}{\partial t^2} \tag{2.23}$$

The phasor form (frequency domain) of wave equations (2.22) and (2.23) are

$$\begin{aligned}\nabla^2\bar{E} &= \mu\sigma_s(j\omega)\bar{E} + \mu\varepsilon(j\omega)^2\bar{E} \\ &= j\omega\mu(\sigma_s + j\omega\varepsilon)\bar{E}\end{aligned} \tag{2.24}$$

$$\begin{aligned}\nabla^2\bar{H} &= \mu\sigma_s(j\omega)\bar{H} + \mu\varepsilon(j\omega)^2\bar{H} \\ &= j\omega\mu(\sigma_s + j\omega\varepsilon)\bar{H}\end{aligned} \tag{2.25}$$

Let $j\omega\mu(\sigma_s + j\omega\varepsilon) = \gamma^2$ (2.26)

The equations (2.24) and (2.25) reduce to

$$\nabla^2\bar{E} - \gamma^2\bar{E} = 0 \tag{2.27}$$

$$\nabla^2\bar{H} - \gamma^2\bar{H} = 0 \tag{2.28}$$

Where $\gamma = \sqrt{j\omega\mu(\sigma_s + j\omega\varepsilon)} = \alpha + j\beta$ (2.29)

α, is the attenuation constant which defines the rate at which the fields of the electromagnetic wave attenuates as the wave propagates and **β** is the phase constant defining the rate at which the phase changes as the wave propagates. Separating the real and imaginary parts of equation (2.29) we have

$$\alpha = \omega\sqrt{\frac{\mu\varepsilon}{2}\left[\sqrt{1+\left(\frac{\sigma_s}{\omega\varepsilon}\right)^2}-1\right]} \tag{2.30}$$

$$\beta = \omega\sqrt{\frac{\mu\varepsilon}{2}\left[\sqrt{1+\left(\frac{\sigma_s}{\omega\varepsilon}\right)^2}+1\right]} \tag{2.31}$$

In equations (2.27) and (2.28), the operator (∇^2) is the vector Laplacian operator and in rectangular coordinates this vector Laplacian operator is related to scalar Laplacian operator [14] as

$$\bar{F} = F_x\hat{a}_x + F_y\hat{a}_y + F_z\hat{a}_z \tag{2.32}$$

$$\nabla^2\bar{F} = (\nabla^2F_x)\hat{a}_x + (\nabla^2F_y)\hat{a}_y + (\nabla^2F_z)\hat{a}_z \tag{2.33}$$

The scalar Laplacian is expressed as

$$\nabla^2 f = \frac{\partial^2 f}{\partial x^2} + \frac{\partial^2 f}{\partial y^2} + \frac{\partial^2 f}{\partial z^2} \tag{2.34}$$

The phasor equations (2.27) and (2.28) can be written as

$$(\nabla^2\bar{E}_x)\hat{a}_x + (\nabla^2\bar{E}_y)\hat{a}_y + (\nabla^2\bar{E}_z)\hat{a}_z = \gamma^2(\bar{E}_x\hat{a}_x + \bar{E}_y\hat{a}_y + \bar{E}_z\hat{a}_z) \tag{2.35}$$

$$(\nabla^2\bar{H}_x)\hat{a}_x + (\nabla^2\bar{H}_y)\hat{a}_y + (\nabla^2\bar{H}_z)\hat{a}_z = \gamma^2(\bar{H}_x\hat{a}_x + \bar{H}_y\hat{a}_y + \bar{H}_z\hat{a}_z) \tag{2.36}$$

Equating the vector components on both sides of each phasor wave equation, one can obtain the phasor field components [(E_x, E_y, E_z) and (H_x, H_y, H_z)] as follows

$$\frac{\partial^2\bar{E}_x}{\partial x^2} + \frac{\partial^2\bar{E}_x}{\partial y^2} + \frac{\partial^2\bar{E}_x}{\partial z^2} = \gamma^2\bar{E}_x \tag{2.37}$$

$$\frac{\partial^2\bar{E}_y}{\partial x^2} + \frac{\partial^2\bar{E}_y}{\partial y^2} + \frac{\partial^2\bar{E}_y}{\partial z^2} = \gamma^2\bar{E}_y \tag{2.38}$$

$$\frac{\partial^2\bar{E}_z}{\partial x^2} + \frac{\partial^2\bar{E}_z}{\partial y^2} + \frac{\partial^2\bar{E}_z}{\partial z^2} = \gamma^2\bar{E}_z \tag{2.39}$$

$$\frac{\partial^2\bar{H}_x}{\partial x^2} + \frac{\partial^2\bar{H}_x}{\partial y^2} + \frac{\partial^2\bar{H}_x}{\partial z^2} = \gamma^2\bar{H}_x \tag{2.40}$$

$$\frac{\partial^2 \bar{H}_y}{\partial x^2} + \frac{\partial^2 \bar{H}_y}{\partial y^2} + \frac{\partial^2 \bar{H}_y}{\partial z^2} = \gamma^2 \bar{H}_y \tag{2.41}$$

$$\frac{\partial^2 \bar{H}_z}{\partial x^2} + \frac{\partial^2 \bar{H}_z}{\partial y^2} + \frac{\partial^2 \bar{H}_z}{\partial z^2} = \gamma^2 \bar{H}_z \tag{2.42}$$

The field components of time-harmonic electromagnetic wave must individually satisfy the above six partial differential equations. For uniform plane wave, $\bar{E}$ and $\bar{H}$ lie in a plane perpendicular to the direction of propagation and also they are perpendicular to each other. Moreover, $\bar{E}$ and $\bar{H}$ are uniform in the plane $\perp$ to the direction of propagation and vary along the direction of propagation. If the electromagnetic wave propagates through the absorber in y-direction (figure 2.2), the uniform plane has only z-component of the electric field and x-component of the magnetic field which are both functions of y only.

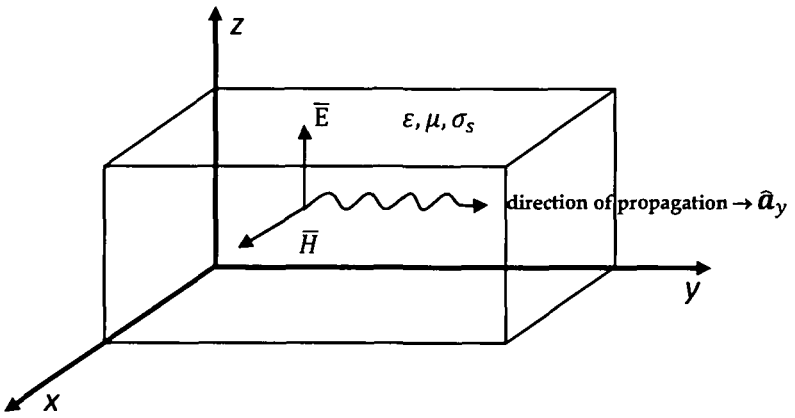

Figure 2.2. Uniform plane wave propagate in y-direction within a dielectric block

The wave equations for the two field components ($\bar{E}_z$,$\bar{H}_x$) are

$$\frac{d^2 \bar{E}_z}{dy^2} - \gamma^2 \bar{E}_z = 0 \tag{2.43}$$

$$\frac{d^2 \bar{H}_x}{dy^2} - \gamma^2 \bar{H}_x = 0 \tag{2.44}$$

The general solution to the wave equations (2.43) and (2.44) are

$$\bar{E}_z(y) = E_1 e^{\gamma y} + E_2 e^{-\gamma y}$$
$$= E_1 e^{(\alpha + j\beta)y} + E_2 e^{-(\alpha + j\beta)y}$$

$$= E_1 e^{\alpha y} e^{j\beta y} + E_2 e^{-\alpha y} e^{-j\beta y} \quad (2.45)$$

and $\bar{H}_x(y) = H_1 e^{\gamma y} + H_2 e^{-\gamma y}$

$$= H_1 e^{(\alpha + j\beta)y} + H_2 e^{-(\alpha + j\beta)y}$$

$$= H_1 e^{\alpha y} e^{j\beta y} + H_2 e^{-\alpha y} e^{-j\beta y} \quad (2.46)$$

Assuming the uniform plane wave as travelling in $+y$ direction, the electric field

$$\bar{\mathrm{E}} = \bar{E}_z \hat{\boldsymbol{a}}_z = E_0 e^{-\gamma y} \hat{\boldsymbol{a}}_z \quad (2.47)$$

The corresponding magnetic field, found from the source free Maxwell's equations

$$\nabla \times \bar{E} = -j\omega\mu\bar{H} \quad (2.48)$$

$$\bar{H} = -\frac{1}{j\omega\mu}\nabla \times \bar{E} = -\frac{1}{j\omega\mu}\left[\frac{\partial \bar{E}_z}{\partial y}\hat{\mathbf{a}}_x - \frac{\partial \bar{E}_z}{\partial x}\hat{\mathbf{a}}_y\right]$$

$$= -\frac{1}{j\omega\mu}\left[\frac{\partial}{\partial y}(E_0 e^{-\gamma y})\hat{\boldsymbol{a}}_x\right]$$

$$= -\frac{1}{j\omega\mu}(-\gamma E_0 e^{-\gamma y})\hat{\boldsymbol{a}}_x$$

$$= \frac{\gamma}{j\omega\mu} E_0 e^{-\gamma y}\hat{\boldsymbol{a}}_x = \bar{H}_x \hat{\boldsymbol{a}}_x \quad (2.49)$$

The intrinsic impedance (η) of the wave is defined as the ratio of the electric field and magnetic field phasors (complex amplitudes)

$$\eta = \frac{\bar{\mathrm{E}}_z}{\bar{\mathrm{H}}_x} = \frac{\mathrm{E}_0 e^{-\gamma y}}{\frac{\gamma}{j\omega\mu}\mathrm{E}_0 e^{-\gamma y}} = \frac{j\omega\mu}{\gamma} = \frac{j\omega\mu}{\sqrt{j\omega\mu(\sigma_s + j\omega\varepsilon)}} = \sqrt{\frac{j\omega\mu}{\sigma_s + j\omega\varepsilon}} \quad (2.50)$$

$$\eta = |\eta| e^{j\theta_\eta} = \sqrt{\frac{j\omega\mu}{\sigma_s + j\omega\varepsilon}} \quad (2.51)$$

The magnitude of the complex intrinsic wave impedance is

$$|\eta| = \frac{\sqrt{\frac{\mu}{\varepsilon}}}{\left[1 + \left(\frac{\sigma_s}{\omega\varepsilon}\right)^2\right]^{\frac{1}{4}}} \quad (2.52)$$

Intrinsic impedance of the medium determines the amount of electromagnetic wave which will get reflected at the air-absorber interface and the amount which will propagate through the medium. Once the incident wave enters the absorbing material, the wave should exponentially decay with distance, y, by the factor, $e^{-\alpha y}$ where α is the attenuation constant as shown in figure 2.3. Considering, $\sigma_s = 0$ and expanding equation (2.29), α can be expressed [15] as

$$\alpha = \frac{\sqrt{2}\pi f}{c} \times \sqrt{(\mu_r''\varepsilon_r'' - \mu_r'\varepsilon_r') + \sqrt{(\mu_r''\varepsilon_r'' - \mu_r'\varepsilon_r')^2 + (\varepsilon_r'\mu_r'' + \varepsilon_r''\mu_r')^2}} \qquad (2.53)$$

It is seen from the above equation that larger the values of complex permittivity and permeability, larger will be the attenuation of the microwave energy. However, larger value of complex permittivity and permeability results in more reflection due to impedance mismatch at the absorber interface

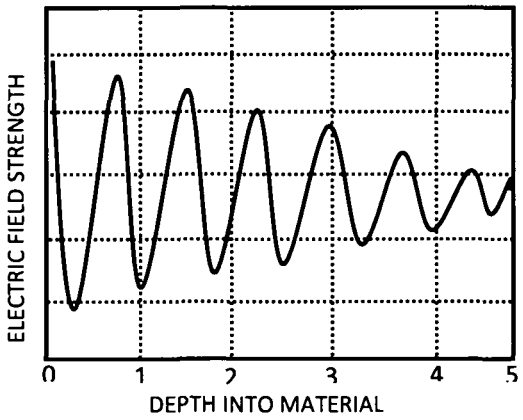

Figure 2.3 Progressive attenuation of electric field strength into the depth of material.

thus restricting the electromagnetic wave from entering the media [16]. Thus a compromise has to be worked out while choosing the material for the absorber.

2.3. TRANSMISSION LINE ANALOGY FOR MICROWAVE ABSORBER

Plane electromagnetic waves propagating in bulk slabs can be modeled by transmission line equations [8]. TLM is a numerical technique based on temporal and spatial sampling of electromagnetic fields. The transmission lines are simulated as propagation domain, where the electric and magnetic vectors of propagating electromagnetic wave are made equivalent to voltages and currents on the network, respectively.

2.3.1. Transmission line modeling for single layer absorber

A transmission line carrying TEM wave is represented as distributed elements in a network having series impedance $Z = R + j\omega L$ and shunt admittance $Y = G + j\omega C$ per unit length [7] as shown in figure 2.4.

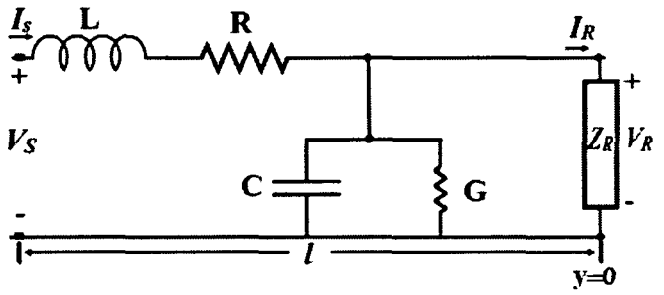

Figure 2.4 A circuit representation of a transmission line

The voltage and current distribution along the transmission line are functions of both time and position and are mainly determined from the shape, dimension and the properties of the conductors and dielectrics [17]. For a uniform transmission line having the constants *R, L, C* and *G* per unit length, the voltage and current equations can be written in the differential form as

$$\frac{\partial \tilde{V}}{\partial y} + L\frac{\partial \tilde{I}}{\partial t} + R\tilde{I} = 0 \qquad (2.54)$$

$$\frac{\partial \tilde{I}}{\partial y} + C\frac{\partial \tilde{V}}{\partial t} + G\tilde{V} = 0 \qquad (2.55)$$

If the voltages and currents vary sinusoidally with time, the phasor notation of equations (2.54) and (2.55) become

$$\frac{\partial V}{\partial y} + (R + j\omega L)I = 0 \quad (2.56)$$

$$\frac{\partial I}{\partial y} + (G + j\omega C)V = 0 \quad (2.57)$$

The analogous relation between electric and magnetic field components of plane wave to the transmission line parameters are given as $\frac{\partial E_z}{\partial y} + j\omega\mu H_x = 0$ and $\frac{\partial H_x}{\partial y} + (\sigma_s + j\omega\varepsilon)E_z = 0$.

Differentiating equations (2.56) and (2.57) with respect to x and combining gives

$$\frac{\partial^2 V}{\partial y^2} - (R + j\omega L)(G + j\omega C)V = 0 \quad (2.58)$$

$$\frac{\partial^2 I}{\partial y^2} - (R + j\omega L)(G + j\omega C)I = 0 \quad (2.59)$$

A possible solution for these equations would be of the form

$$V \text{ or } I = Ae^{-\gamma y} + Be^{\gamma y} \quad (2.60)$$

$$\text{where } \gamma^2 = (R + j\omega L)(G + j\omega C) \quad (2.61)$$

When the variation with time is expressed explicitly, the first term of the expression (2.60) represents a wave travelling in forward direction and the second term represents a wave travelling in reverse direction.

In hyperbolic function form, the solutions to equations (2.58) and (2.59) are

$$V = A_1 \cosh \gamma y + B_1 \sinh \gamma y \quad (2.62)$$

$$I = A_2 \cosh \gamma y + B_2 \sinh \gamma y \quad (2.63)$$

The constants A_1, A_2, B_1 and B_2 are evaluated by applying boundary conditions

$$V = V_R, I = I_R \quad at\ y = 0$$

$$V = V_s, I = I_s \quad at\ y = y_1$$

Substituting these boundary conditions in (2.62) and (2.63), the coefficients are found as

$$A_1 = V_R \tag{2.64}$$

$$B_1 = -\sqrt{\frac{R+j\omega L}{G+j\omega C}}\, I_R \tag{2.65}$$

and

$$A_2 = I_R \tag{2.66}$$

$$B_2 = -\sqrt{\frac{G+j\omega C}{R+j\omega L}}\, V_R \tag{2.67}$$

The characteristic impedance (Z_0) of the transmission line is related to the primary constants R, L, G and C as

$$Z_0 = \sqrt{\frac{Z}{Y}} = \sqrt{\frac{R+j\omega L}{G+j\omega C}} \tag{2.68}$$

The characteristic impedance (Z_0) is analogous to the intrinsic impedance of the wave given by equation (2.50) i.e. $\eta = \sqrt{\frac{j\omega\mu}{\sigma_s + j\omega\varepsilon}}$

Considering the location of the terminating impedance Z_R the reference point (y = 0), the other end is left of this reference point, i.e. in the -y direction as shown in fig. 2.4. Using the expressions from (2.64) to (2.68) and writing $l = -y_1$, equations (2.62) and (2.63) becomes

$$V_S = V_R \cosh \gamma l + Z_0 I_R \sinh \gamma l \tag{2.69}$$

$$I_S = I_R \cosh \gamma l + \frac{V_R}{Z_0} \sinh \gamma l \tag{2.70}$$

The general expression for the input impedance of the transmission line is obtained by dividing equation (2.69) by equation (2.70) i.e.

$$Z_{in} = \frac{V_s}{I_s} = \frac{V_R \cosh \gamma l + Z_0 I_R \sinh \gamma l}{I_R \cosh \gamma l + \frac{V_R}{Z_0} \sinh \gamma l} \quad (2.71)$$

or

$$Z_{in} = Z_0 \frac{Z_R + Z_0 \tanh \gamma l}{Z_0 + Z_R \tanh \gamma l} \quad (2.72)$$

The expression (2.72) gives the input impedance of the transmission line terminated by a load Z_R. The reflection coefficient is expressed as

$$\Gamma = \frac{Z_{in} - Z_0}{Z_{in} + Z_0} \quad (2.73)$$

2.3.2. Transmission line modeling for Multilayer Absorber

The transmission line section in figure 2.4 is extended to multi section as shown in figure 2.5 then the input impedance at the i^{th} layer is given as

$$Z_{in} = Z_{oi} \frac{Z_{i-1} + Z_{oi} \tanh \gamma_i l_i}{Z_{oi} + Z_{i-1} \tanh \gamma_i l_i} \quad (2.74)$$

Where Z_{oi} is the characteristic impedance of the i^{th} layer.

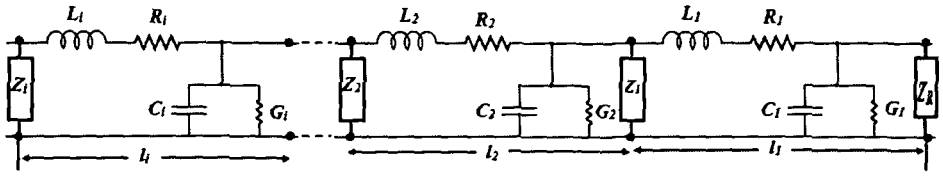

Figure 2.5 *A circuit representation of a multi section transmission line*

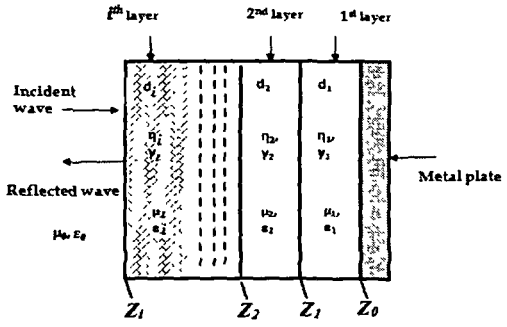

Figure 2.6 Distributed parameters of a multilayer absorber structure [18]

Similar to equation (2.74), the input impedance of a plane wave incident normal to the surface of a absorber or composite substrate backed by a metal as shown in figure 2.6, can be expressed as

$$Z_{in} = \eta_i \frac{Z_{i-1} + \eta_i \tanh \gamma_i d_i}{\eta_i + Z_{i-1} \tanh \gamma_i d_i} \quad . \qquad (2.75)$$

Where η_i is the intrinsic impedance of the i^{th} layer and is calculated from $\eta = \sqrt{\frac{j\omega\mu}{\sigma_s + j\omega\varepsilon}}$. (Equation (2.51)). For free space medium, $\sigma_s = 0$ and $\mu = \mu_0 = 4\pi \times 10^{-7}(N/A^2)$ and $\varepsilon = \varepsilon_0 = 8.8541 \times 10^{-12} F/m$, so the value of $\eta = \eta_0 \approx 377\ \Omega$.

The reflection coefficient of the normal incidence plane wave is expressed [16, 27] as

$$\Gamma = \frac{Z_{in} - 377}{Z_{in} + 377} \qquad (2.76)$$

2.4 DESIGN OF MICROWAVE ABSORBERS

The two essential requirements for absorption type EMI shielding material, for uniform plane electromagnetic wave from external far field source are (i) low reflection at the air-absorber interface and (ii) high attenuation of plane wave within the bulk of the absorber [19]. Zero reflection at the air-absorber interface can be achieved by impedance matching condition, $\eta_0 \approx 377\ \Omega$ (equation 2.50 and 2.51). Practical design relations of an absorber should evaluate the reflection loss value determining the effectiveness of microwave energy absorbed and from TLM simulation [20]. The reflection loss, RL_c, of a metal backed absorber is expressed as

$$RL_c = 20\log|\Gamma| \qquad (2.77)$$

The reflection loss of the absorber depends upon the intrinsic material parameter complex permittivity, ε_r complex permeability, μ_r and conductivity (σ_s). Thickness (d) is another important parameter influencing the reflection loss behavior of the absorber [21].

2.4.1 Thickness considerations

A maximal microwave absorption of a dielectric absorber occurs at a matching thickness, d_m, when d_m **equals to an odd multiple of** λ_g / 4, [22], where,

$$\lambda_g = \lambda_0 / (|\varepsilon_r||\mu_r|)^{1/2} \quad (2.78)$$

$|\varepsilon_r|$ and $|\mu_r|$ are the moduli of complex permittivity (ε_r) and complex permeability (μ_r) respectively. A part of the incident wave is reflected from the front surface of the material while the other part is transmitted. The transmitted wave propagates through the absorber and undergoes total reflection from the absorber-metal surface and propagates back through the front face of the absorber. If the two reflected wave one from the front face and other from the absorber-metal surface is equal in magnitude and 180° out of phase, they cancel each other and there will be no total reflection. Since the transmitted wave travel twice, the thickness of the absorber should be quarter wavelength [16, 23]. The schematic diagram of single layer and multilayer quarter wavelength absorber is shown in figure 2.7 and figure 2.8 respectively.

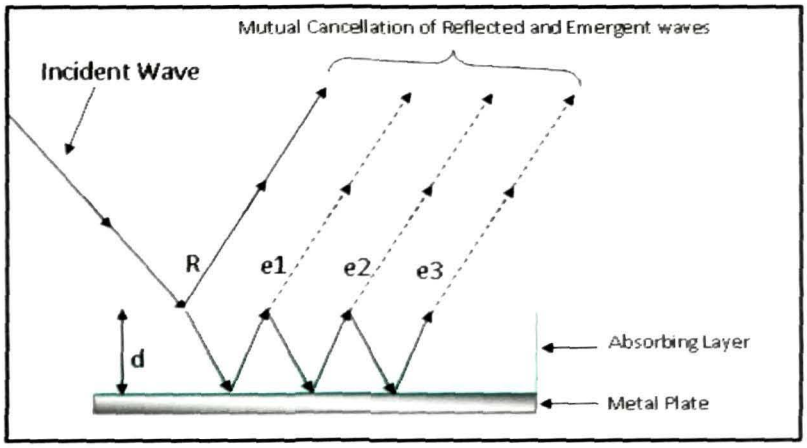

Figure 2.7 A schematic diagram of single layer quarter wavelength absorber

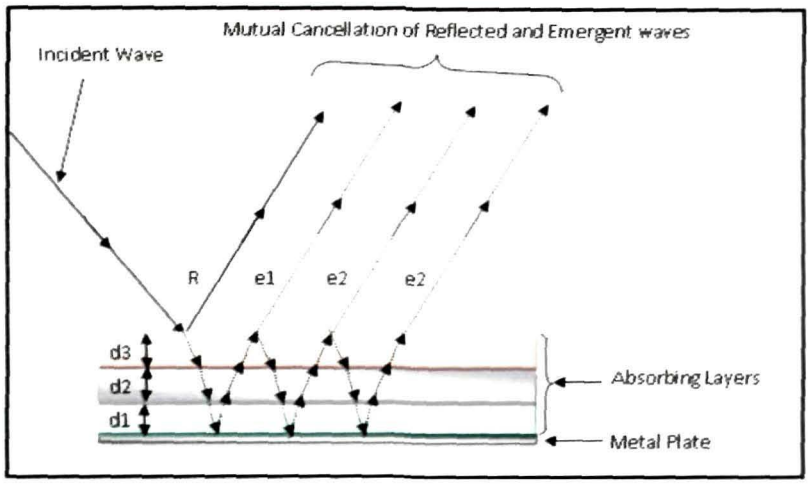

Figure 2.8 A schematic diagram multilayer layer quarter wavelength absorber

The theoretical limit of total thickness for a broadband response for multilayer absorber structure [24] is given by inequality

$$\left|\int_0^\infty \ln|R(\lambda)|d\lambda\right| \leq 2\pi^2 \sum_i \mu_{si} d_i \qquad (2.79)$$

where R is the reflection coefficient, λ is the wavelength and the μ_{si} is the static permeability and d_i is the thickness of the i^{th} layer. For nonmagnetic broadband microwave absorber, $(\mu_{si} = 1)$, and using decibel scale of the reflection , RL_c=20log(R), the above equation can be reduce to

$$\int 2.303\, RL_c(\lambda)\, d\lambda \,/\, 40\pi^2 \leq \sum_i d_i \qquad (2.80)$$

The theoretical thickness limits for a frequency bandwidth (8.2-12.4) GHz corresponding to wavelength $\Delta\lambda = \lambda_{upper} - \lambda_{lower} = 12.39mm$ to achieve 30dB absorption level over the X-band, of a multilayer nonmagnetic microwave absorber should not be less than2.1mm. The detail derivation is given in Appendix-A.

2.4.2 Single-layer design consideration

The schematic diagram of a single layer absorber consist of a flat metallic surface coated with a thin layer of dielectric material often called a

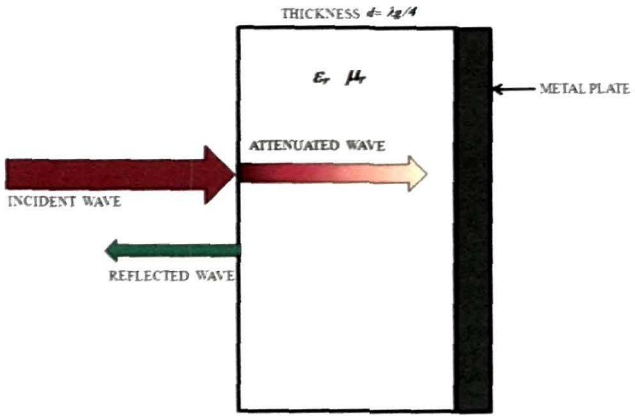

Figure 2.9 A schematic diagram of single layer absorber (Dallenbach absorber)

Dallenbach layer, is shown in figure 2.9. A Dallenbach layer is composed of homogenously distributed lossy reinforcers like carbon black, metal particles, graphite, CNTs etc.[25] in a base matrix and is placed on a conducting plane. It is classified as a resonance absorber in that it is designed to be a quarter wavelengths in thickness so that the electromagnetic waves reflected from the first and second interfaces of the absorber are 180^0 degrees out of phase, resulting in destructive interference. The electromagnetic wave is also absorbed as it passes through the layer and impedance matching is used to reduce the reflection from the air/absorber interface [26]. Recalling equation (2.75) $Z_{in} = \eta_i \frac{Z_{i-1}+\eta_i tanh\, \gamma_i d_i}{\eta_i + Z_{i-1} tanh\, \gamma_i d_i}$ for the conductor backed single layer dielectric absorber, impedance at the metal plate i.e. $Z_{i-1} = 0$ and considering the conductivity of the Dallenbach layer, $.\sigma_s = 0$, the input impedance at the air-absorber interface will reduce to

$$Z_1 = Z_{in} = \eta_0 \sqrt{\frac{\mu_{r1}}{\varepsilon_{r1}}}\, tanh\,(j2\pi f / c)\sqrt{\mu_{r1}\varepsilon_{r1}}\, d_1 \qquad (2.81)$$

$$\eta_1 = \eta_0 \sqrt{\mu_{r1} / \varepsilon_{r1}} \qquad (2.82)$$

$$\gamma_1 = j(2\pi f / c)\sqrt{\mu_{r1}\varepsilon_{r1}} \qquad (2.83)$$

$$\mu_{r1} = \mu'_{r1} - j\mu''_{r1} \qquad (2.84)$$

$$\varepsilon_{r1} = \varepsilon'_{r1} - j\,\varepsilon''_{r1} \qquad (2.85)$$

Equations (2.84) and (2.85) represent the relative complex permeability and permittivity of the Dallenbach layer. Using equations (2.76), (2.77) and (2.81), the reflection loss (dB) of the single layer absorber can be expressed as

$$RL_c = 20\log\left|\frac{\eta_0\sqrt{\mu_{r1}/\varepsilon_{r1}}\tanh(j2\pi f/c)\sqrt{\mu_{r1}\varepsilon_{r1}}d_1-\eta_0}{\eta_0\sqrt{\mu_{r1}/\varepsilon_{r1}}\tanh(j2\pi f/c)\sqrt{\mu_{r1}\varepsilon_{r1}}d_1+\eta_0}\right| \quad (2.86)$$

or

$$RL_c = 20\log\left|\frac{\sqrt{\mu_{r1}/\varepsilon_{r1}}\tanh(j2\pi f/c)\sqrt{\mu_{r1}\varepsilon_{r1}}d_1-1}{\sqrt{\mu_{r1}/\varepsilon_{r1}}\tanh(j2\pi f/c)\sqrt{\mu_{r1}\varepsilon_{r1}}d_1+1}\right| \quad (2.87)$$

Optimizing the material parameters and thickness, RL_c can be tuned for a particular frequency.

2.4.3 Multilayer design consideration

One of the requirements for microwave absorbing material is to have a wide range absorption bandwidth. Bandwidth of a single-layer absorber, is generally insufficient. Broader absorption band can be obtained from a multilayer approach. The multilayer dielectric absorber concept benefits from the change of effective impedance with the distance into the material, so that the reflections are minimized and a broad band matching can be achieved [3]. The impedance and thickness of the layers of the absorbers are to be optimized to achieve minimum mismatch at the air-absorber interface. Reflection loss formulation for double layer and triple layer are discussed in subsequent subsection.

Double layer

A schematic diagram of double layer conductor backed absorber is shown in figure 2.10. The expression for input impedance Z_{in} of the double-layer absorber backed by the metal for normal incidence can be obtained by

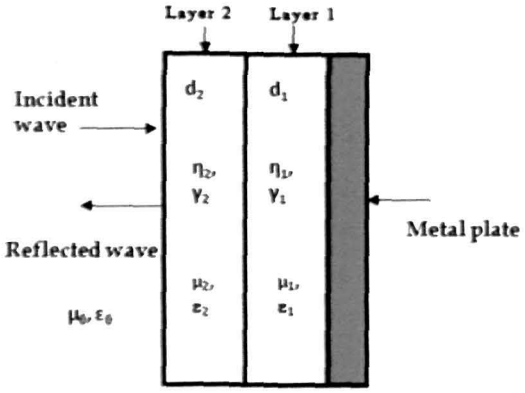

Figure 2.10 A schematic diagram of graded double layer absorber [18]

substituting the expression for input impedance Z_1 of the inner layer backed by the metal in the general expression (2.75) for input impedance of the front layer. Considering the conductivity of both the layers is zero and using equation (2.75) and (2.81), the input impedance for a double layer absorber is expressed as follows

$$Z_{in} = \eta_2 \frac{Z_1 + \eta_2 \tanh \gamma_2 d_2}{\eta_2 + Z_1 \tanh \gamma_2 d_2} \tag{2.88}$$

$$Z_1 = \eta_1 \tanh \gamma_1 d_1 \tag{2.89}$$

$$\eta_2 = \eta_0 \sqrt{\mu_{r2} / \varepsilon_{r2}} \tag{2.90}$$

$$\gamma_2 = j(2\pi f / c)\sqrt{\mu_{r2}\varepsilon_{r2}} \tag{2.91}$$

Substituting these in equation (2.87) the input impedance will be

$$Z_2 = Z_{in} = \eta_2 \frac{\eta_1 \tanh \gamma_1 d_1 + \eta_2 \tanh \gamma_2 d_2}{\eta_2 + \eta_1 \tanh (\gamma_1 d_1) \tanh (\gamma_2 d_2)}$$

or

$$Z_2 = \eta_0 \sqrt{\mu_{r2} / \varepsilon_{r2}} \left[\frac{\sqrt{\mu_{r1}/\varepsilon_{r1}} \tanh j(2\pi f/c)\sqrt{\mu_{r1}\varepsilon_{r1}} d_1 + \sqrt{\mu_{r2}/\varepsilon_{r2}} \tanh j(2\pi f/c)\sqrt{\mu_{r2}\varepsilon_{r2}} d_2}{\sqrt{\mu_{r2}/\varepsilon_{r2}} + \sqrt{\mu_{r1}/\varepsilon_{r1}} \tanh (j(2\pi f/c)\sqrt{\mu_{r1}\varepsilon_{r1}} d_1) \tanh j(2\pi f/c)\sqrt{\mu_{r2}\varepsilon_{r2}} d_2)} \right] \tag{2.92}$$

The reflection loss expression of the double layer absorber is obtained by using equations (2.75), (2.78) and (2.91) as

$$RL_c = 20\log\left|\frac{\sqrt{\mu_{r2}/\varepsilon_{r2}}\left[\frac{\sqrt{\mu_{r1}/\varepsilon_{r1}}\tanh j(2\pi f/c)\sqrt{\mu_{r1}\varepsilon_{r1}}d_1 + \sqrt{\mu_{r2}/\varepsilon_{r2}}\tanh j(2\pi f/c)\sqrt{\mu_{r2}\varepsilon_{r2}}d_2}{\sqrt{\mu_{r2}/\varepsilon_{r2}} + \sqrt{\mu_{r1}/\varepsilon_{r1}}\tanh(j(2\pi f/c)\sqrt{\mu_{r1}\varepsilon_{r1}}d_1)\tanh j(2\pi f/c)\sqrt{\mu_{r2}\varepsilon_{r2}}d_2)}\right] - 1}{\sqrt{\mu_{r2}/\varepsilon_{r2}}\left[\frac{\sqrt{\mu_{r1}/\varepsilon_{r1}}\tanh j(2\pi f/c)\sqrt{\mu_{r1}\varepsilon_{r1}}d_1 + \sqrt{\mu_{r2}/\varepsilon_{r2}}\tanh j(2\pi f/c)\sqrt{\mu_{r2}\varepsilon_{r2}}d_2}{\sqrt{\mu_{r2}/\varepsilon_{r2}} + \sqrt{\mu_{r1}/\varepsilon_{r1}}\tanh(j(2\pi f/c)\sqrt{\mu_{r1}\varepsilon_{r1}}d_1)\tanh j(2\pi f/c)\sqrt{\mu_{r2}\varepsilon_{r2}}d_2)}\right] + 1}\right| \quad (2.93)$$

Optimization of the complex permittivity, permeability and thickness of the individual layers, is to be carried out for broadband microwave absorption over the desired frequency range.

Triple layer

A three layer graded dielectric absorber backed by a conductor can be designed as shown in figure 2.11. The principle of microwave absorption of the three layer structure is similar to the double layer dielectric absorber.

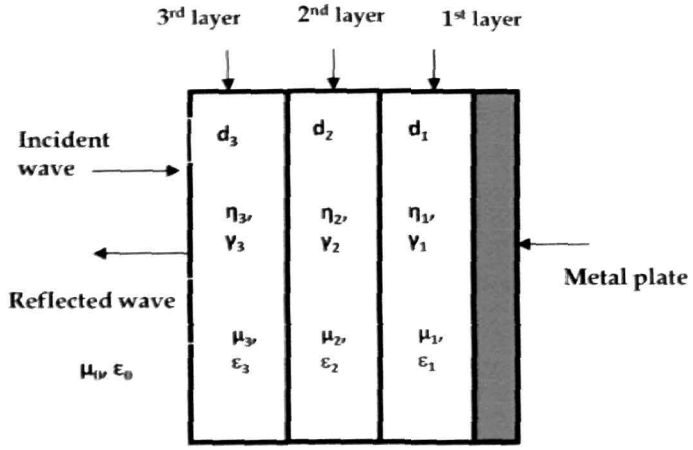

Figure 2.11 A schematic diagram of graded double layer absorber [18]

The input impedance at the front layer of the absorber is calculated by substituting the expression for input impedance Z_2 and Z_1 of the inner layers backed by the metal in the general expression (2.75). From equation (2.75) and

considering the conductivity of individual layers as zero, the input impedance is expressed as

$$Z_3 = Z_{in} = \eta_3 \frac{Z_2 + \eta_3 \tanh \gamma_3 d_3}{\eta_3 + Z_2 \tanh \gamma_3 d_3} \tag{2.94}$$

$$\eta_3 = \eta_0 \sqrt{\mu_{r3} / \varepsilon_{r3}} \tag{2.95}$$

$$\gamma_3 = j(2\pi f / c)\sqrt{\mu_{r3}\varepsilon_{r3}} \tag{2.96}$$

Substituting the value of Z_1 and Z_2 from equation (2.81) and (2.92) in equation (2.94), input impedance for the three layer absorber can be expressed as

$$Z_3 = \eta_3 \frac{\eta_2 \frac{\eta_1 \tanh \gamma_1 d_1 + \eta_2 \tanh \gamma_2 d_2}{\eta_2 + \eta_1 \tanh(\gamma_1 d_1)\tanh(\gamma_2 d_2)} + \eta_3 \tanh \gamma_3 d_3}{\eta_3 + \eta_2 \frac{\eta_1 \tanh \gamma_1 d_1 + \eta_2 \tanh \gamma_2 d_2}{\eta_2 + \eta_1 \tanh(\gamma_1 d_1)\tanh(\gamma_2 d_2)} \tanh \gamma_3 d_3} \tag{2.97}$$

The reflection loss expression of the double layer absorber is obtained by using equations (2.75), (2.78) and (2.96) as

$$RL_c = 20\log \left| \frac{\eta_3 \frac{\eta_2 \frac{\eta_1 \tanh \gamma_1 d_1 + \eta_2 \tanh \gamma_2 d_2}{\eta_2 + \eta_1 \tanh(\gamma_1 d_1)\tanh(\gamma_2 d_2)} + \eta_3 \tanh \gamma_3 d_3}{\eta_3 + \eta_2 \frac{\eta_1 \tanh \gamma_1 d_1 + \eta_2 \tanh \gamma_2 d_2}{\eta_2 + \eta_1 \tanh(\gamma_1 d_1)\tanh(\gamma_2 d_2)} \tanh \gamma_3 d_3} - \eta_0}{\eta_3 \frac{\eta_2 \frac{\eta_1 \tanh \gamma_1 d_1 + \eta_2 \tanh \gamma_2 d_2}{\eta_2 + \eta_1 \tanh(\gamma_1 d_1)\tanh(\gamma_2 d_2)} + \eta_3 \tanh \gamma_3 d_3}{\eta_3 + \eta_2 \frac{\eta_1 \tanh \gamma_1 d_1 + \eta_2 \tanh \gamma_2 d_2}{\eta_2 + \eta_1 \tanh(\gamma_1 d_1)\tanh(\gamma_2 d_2)} \tanh \gamma_3 d_3} + \eta_0} \right| \tag{2.98}$$

While designing proper selection of materials and optimization of thickness of each layer is carried out for enhanced performance of the absorber.

2.5 Conclusions

Dielectric absorber can be modeled as lossy fillers reinforced in a polymer base matrix. Electromagnetic wave propagating through the absorber can be simulated as Transmission Line where the electric and magnetic components find analogy with voltage and current propagating through the line. The intrinsic impedance and the reflection loss of the absorber can be optimized using the intrinsic material parameters viz. complex permittivity

and permeability. The absorber thickness plays an important role in the design of the absorber for phase cancellation of incident and emergent wave. Proper selection of intrinsic impedance and thickness of the individual layer is to be done for design of multilayer absorber to achieve, broadband absorption over the desired frequency range.

References

1. Sutton, H. W. Microwave Processing of Ceramic Materials, *Am. Ceram. Soc. Bull.* 68 (2),376-386, 1989.
2. Han, Mangui., and Deng, Longjiang. Doping effect of multiwall carbon nanotubes on the microwave electromagnetic properties of NiCoZn spinel ferrites, *Applied Physics Letters* 90, 011108(1-3), 2007.
3. Iqbal, N. M., et al. A Study of The EMC Performance of a Graded-Impedance, Microwave, Rice-Husk Absorber, *Progress In Electromagnetics Research*, 131, 19-44, 2012.
4. Jadhav, N. R., and Puri, V. Microwave Absorption, Conductivity and Complex Pemittivity of Fritless Ni(1- X)CuxMn2O4 ($0 \leq X \leq 1$) Ceramic Thick Film: Effect Of Copper, *Progress In Electromagnetics Research C*, 8, 149-160, 2009.
5. Fu, Shun-Li., et al. Synthesis of hexagonal Fe microflakes with excellent microwave absorption performance, *Cryst Eng Comm*, **14**, 6827-6832, 2012.
6. Gairola, P. S., et al. Modified composition of barium ferrite to act as a microwave absorber in X-band frequencies, *Solid State Communications*, 150 (3-4), 147-151, 2010.
7. Jordan, C. Edward., and Balmain, G. Keith. *Electromagnetic Waves and Radiating Systems*, 2nd ed., Prentice Hall Inc., USA, 1968.
8. Sjöberg, Daniel. Analysis of wave propagation in stratified structures using circuit analogues, with application to electromagnetic absorbers, *Eur. J. Phys.* 29, 721–734, 2008.
9. Bronwell, Arthur. Transmission-Line Analogies of Plane Electromagnetic-Wave Reflections, *Proceedings of the I.R.E.*, 32(4) 233-241, 1944.
10. [Balanis, A. C. *Advanced Engineering Electromagnetics*, John Wiley & Sons, USA, 1989.
11. [Lidstrom, Pelle., et al. Microwave assisted organic syntheisi-a review, *Tetrahedron* , 57, 9225-9283, 2001.
12. Soethe, Lilian Viviane., et al. Radar absorbing materials based on titanium thin film obtained by sputtering technique, *J. Aerosp.Technol. Manag.*, 3(3), 279-286, 2011.

13. Michielssen, E., et al. Design of Lightweight, Broad-Band Microwave Absorbers Using Genetic Algorithms, *IEEE. T. Microw. Theory* 41, 1024-1030, 1993.

14. Griffiths, J. David. *Introduction to Electrodynamics*, 2nd ed., Prentice Hall International, Inc., Englewood Cliffs, 1989.

15. Zhang, B., et al. Microwave absorbing properties of de-aggregated flake shaped carbonyl iron particle composites at 2-18 GHz, *IEEE. T. Magn.* 42, 1778-1781, 2006.

16. Saville, Paul. Review of Radar Absorbing Materials, *Technical Memorandum DRDC Atlantic TM 2005-003*, 2005.

17. Chen, F. L., et al. *Microwave Electronics Measurement and Materials Characterization*, John Wiley & Sons, Ltd., England, 2004.

18. Qin, F., and Brosseau, C. A review and analysis of microwave absorption in polymer composites filled with carbonaceous particles, *Journal of Applied Physics* 111(6), 061301(1-24) 2012.

19. Oikonomou, A., Giannakopoulou, T., and Litsardakis, G. Design, fabrication and characterization of hexagonal ferrite multi-layer microwave absorber, *Journal of Magnetism and Magnetic Materials* 316(2), e827–e830, 2007.

20. Liu, Zunfeng., et al. Microwave Absorption of Single-Walled Carbon Nanotubes/Soluble Cross-Linked Polyurethane Composites, *J. Phys. Chem. C* 111, 13696-13700, 2007.

21. Micheli, D., et al. X-Band microwave characterization of carbon-based nanocomposite material, absorption capability comparison and RAS design simulation, *Compos. Sci. Technol.* 70, 400-409, 2010.

22. Zhang, L., et al. The electromagnetic characteristics and absorbing properties of multi-walled carbon nanotubes filled with Er2O3 nanoparticles as microwave absorbers, *Mater. Sci. Eng. B.* 153, 78–82, 2008.

23. Theory and application of RF/Microwavr absorbers, Tech notes, Emerson and Cuming Microwave Products, *www.eccosorb.com/resource-white-papers.htm*

24. Rozanov, N. K. Ultimate Thickness to Bandwidth Ratio of Radar Absorbers, *IEEE Transaction on Antennas and Propagation* 48(8), 1230-1234, 2000.

25. Timmerman, A. T., CA *Patent 2026535*. 2000.

26. Saville, Paul. Optimisation of Dallenbach Layers using Real Materials, *Technical Memorandum, DRDC Atlantic TM 2007-012*, 2007.

27. Cho Shin Han., and Kim , Soo Sung. Two layered microwave absorber of ferrite and carbon fiber composite substrate, *Journal of Magnetics*, 3 (2), 64-67, 1998.

CHAPTER III

COMPOSITE – PREPARATION AND MICROSTRUCTURAL STUDIES

3.1 INTRODUCTION

Expansion of electronic and telecommunication systems for civil and military applications have increased electromagnetic interference (EMI) putting new issues on studies involving the microwave absorbing material technology [1,2]. The challenge is in development of thin, flexible and light absorbing material with broad band absorption. Cost of processing technique and raw materials are other criteria to be considered, especially for a large scale production. Adequate combination of constituent materials and mechanism of synthesis may produce materials with specific requirements.

Composite type dielectric microwave absorber is composed of absorbing dielectric fillers in the polymer base matrix, where the design flexibility lies in tuning the dielectric characteristics like, the dielectric constant and the dissipation factor of energy, of the absorbing centre i.e. fillers. Distribution of fillers in the polymer matrix alters the extent of microwave interaction and for the homogeneous absorption of electromagnetic wave in all the directions and through the thickness within the absorbing material, uniform distribution of fillers in the matrix is desirable [2,3]. There are different processing routes, such as the impregnation of synthetic foams, fabrics and nonwoven substrates and manufacturing of paints and rubbers [4]. In present investigation absorbing material is made by mechanical mixing of filler and polymer in powder form and subsequent thermal treatment of the mixture.

Material choice and synthesis technique are discussed in the starting of the chapter. This is followed by microstructural studies viz. XRD, TEM, SEM and FTIR; to find the size and shape of the reinforcers and determine its distribution in the base matrix.

3.2 MATERIAL SELECTION AND SYNTHESIS

3.2.1 Material selection

Expanded graphite (EG) flakes have been selected as fillers and dispersed homogenously in insulating polymer matrix to develop dielectric absorber type EMI shielding material.

Selection of inclusions

EG flakes have electrical conductivity ~ 10^4 S/cm with very low density ~ 0.03 to 0.15 g/cc and are light weight [5-9]. The presence of functional groups such as -OH, -COOH [5] in the EG gives a good physical interaction with the polymer matrix and is chosen as the 'lossy filler'. EG flakes are consist of small stacks of graphene sheets of thickness ranges from 1 upto a few tens of nanometers and lateral linear dimensions varying from a few micrometers up to hundreds of micrometers. The EG flakes are synthesized from natural graphite flakes using chemical oxidation and thermal treatment method. The synthesis processes is much cheaper than that of carbon nanotubes, that is one more reason for choosing EG over CNT in this investigation [10].

Selection of host matrix

Novolac phenolic resins (NPR) are condensed polymerization product of phenol and formaldehyde with water as byproduct. The polymerization takes place when the molar ratio of formaldehyde to phenol is less than one and it is brought to completion using acid-catalysis such as oxalic acid, hydrochloric acid or sulfonate acids. In the initial stage (A-stage), the polymer is of low molecular mass, soluble and fusible. As the condensation continues more molecules are involved and resin becomes rubbery, thermoplastic phase, which is only partially soluble (B-stage). The resin is then cured to fully cross-linked intractable material(C- Stage) (figure.3.1). NPRs are amorphous (not

crystalline) thermoplastics and they are solid at room temperature and will soften and flow at temperatures 150-220°F (65 °C - 105 °C). They are cheaper than epoxies and easily available, have good heat resistance, electrical insulation, dimensional stability, flame and chemical resistance [11, 12]. The hydroxyl and methylene linkages present in NPR chemical structure facilitates bonding for composite formation [13], and is selected as the base matrix.

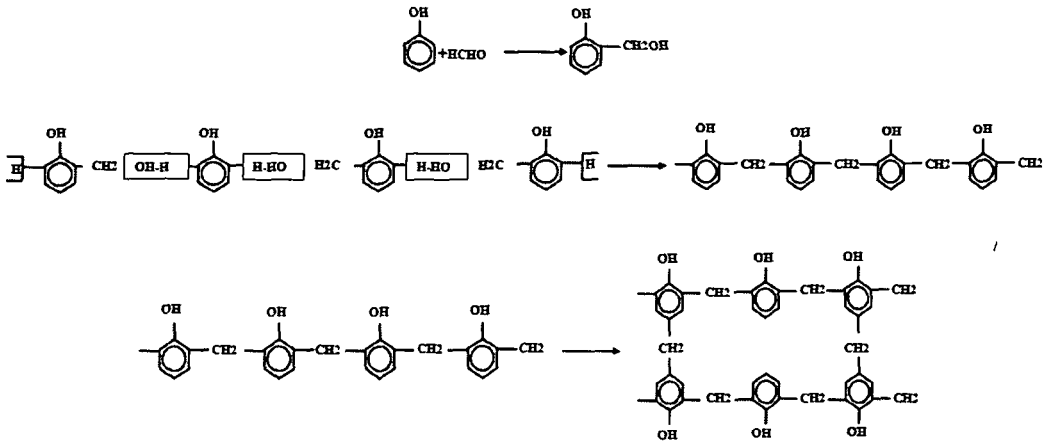

Figure.3.1. Polymerization of Novolac Phenolic Resin

3.2.2 Synthesis of Expanded graphite (EG)

EG flakes are synthesized from natural graphite (NG) flakes using chemical oxidation and thermal treatment method. Graphite is made up of layer planes of hexagonal arrays or networks of carbon atoms separated from each other by weak Van der Waals' forces (figure 3.2). Each layer of carbon atom is bonded to three other carbon atoms by covalent single bond of length 1.42 Å. The fourth valence electron is delocalized over the whole layer like the π-electrons of large aromatic molecule, accounting for the high anisotropic quasimetallic properties of the graphite. In the ideal graphite structure the carbon layers are arranged in alternating sheets in such a way, that carbon atoms in any layer lie over the midpoint of the carbon hexagonal layer. The

distance between the layers in the direction of the c-axis is 3.35 Å. This distance is too great for formation of strong chemical bond, because of the large gap between the basal planes of graphite. Various chemical groups can be intercalated inside them under certain chemical or electrochemical conditions. The graphite compound formed is known as graphite intercalated compound. On thermal treatment the intercalated molecule causes large expansion of the graphite basal planes and the degree of such expansion can be as high as 300 times. In this study, natural graphite flakes of size less than 2μm (supplier Mass Graphite & Carbon products, Mehsana, India) are dried at 75 °C in vacuum oven for 8 hrs to remove the moisture content and then mixed with saturated acid consisting of sulfuric acid and concentrated nitric acid in a volume ratio 3:1 for 12 h to form graphite intercalated compound (GIC). Nitric acid serves as an oxidizer and sulfuric acid as an intercalant. The mixture is stirred from time to time to obtain uniform intercalation of each flake. The chemically treated flakes are then thoroughly rinsed with water until the pH level of the solution reaches 7 and dried at 60 °C in vacuum oven for 5 hours. Treated GIC is then suddenly exposed to high temperature in a **muffle furnace maintained at temperatures 800-900** °C to get EG flakes

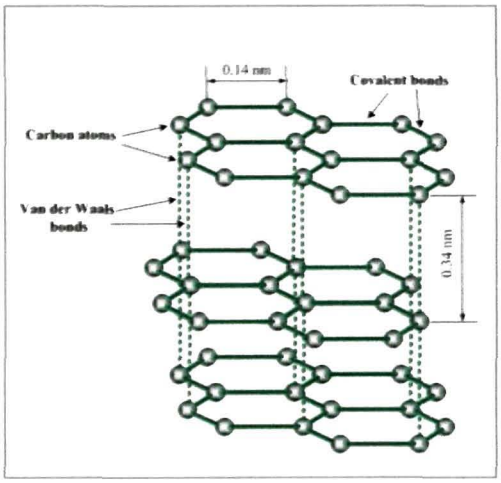

Figure.3.2 Schematic **diagrams of graphite structure**

3.2.3 Fabrication of dielectric composite material

Novolac type phenolic resin is mixed with 10% hexamethylene tetramine as harderner (supplier Pheno Organic Limited, New Delhi). The EG flakes and NPR powder are mechanically blended at ~ 15000 rpm for different weight percentages of EG in the base matrix. Mathematically, if total weight of the composite is Z′ grams and X′ and Y′ are the weights of EG and NPR respectively i.e. Z′ = X′ + Y′, then, for *N* wt. % of EG/NPR composite, amount of EG present in the composite is given by

$$EG = X' = (N/100) \times Z' \text{ grams} \quad (3.1)$$

and amount of NPR present in the composite is given by

$$NPR = Y' = (Z'-X') \text{ grams} \quad (3.2)$$

Using the relation (3.1) and (3.2), a uniform mixture of EG flakes and NPR powder is obtained with 5, 7, 8, 10, 20, 30, 40 and 50 wt. % of EG. The mixture is placed in a specially designed three-piece die-mould consisting of a cavity, upper and lower plunger with spacer) and initially heated up to 95–100 °C. A pressure up to 1.5-2 tons is slowly applied and the fixture with the sample is isothermally heated at 150 °C for 2 hours and then allowed to cool at room temperature. The processing chart is given in figure 3.3.

Pellets of different dimensions are molded for different characterization. A three piece die mould with spacer, with the provision of varying the thickness, d, of the sample is designed and fabricated as: (a) for microwave characterization in the X-band with the sample dimension of 10.16 mm × 22.86 mm × *d* mm (figure 3.4) and (b) for free space microwave absorption testing sample dimension of 152 mm× 152 mm × d mm (figure 3.5).

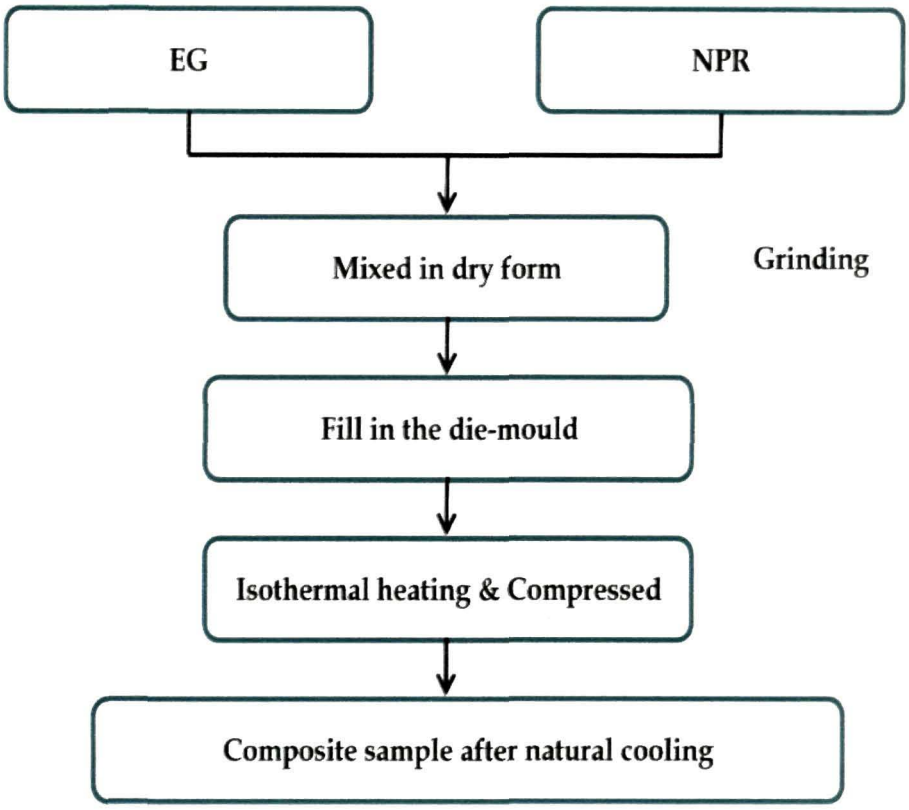

Figure 3.3 Block diagram of composite preparation

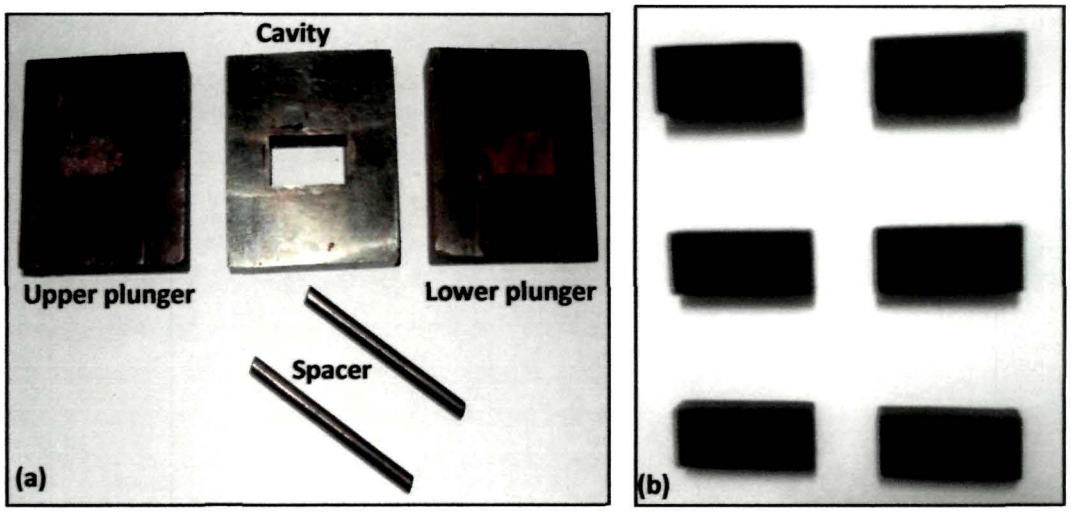

Figure.3.4 (a) Three piece die mold and (b) Prepared EG-NPR composites for X band characterization

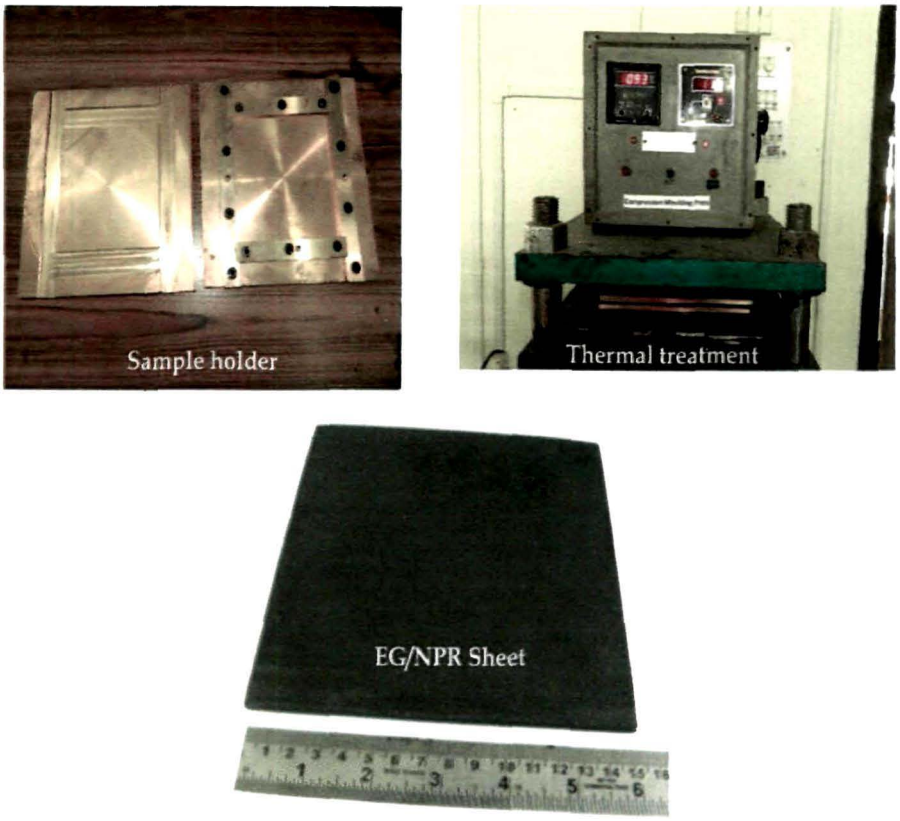

Figure.3.5 EG/NPR composite sheet preparation for free space absorption testing

3.3 MICROSTRUCTURAL STUDIES

Propagation of electromagnetic wave, passing through the composite material depends not only on the intrinsic properties of the constituents, but also on the distribution, the size of the inclusions and the change in structural configuration of the inclusion particles in the composite matrix. Microstructural analysis gives complete through analysis of the composite deciding its utility as substrate in the microwave technology. Micro-structural studies conducted are described in following sub sections.

3.3.1 X-ray diffraction

X-ray diffraction studies are an important tool for structural analysis and gives information of various phases present in the specimen. X-ray diffractometer (Rigaku Miniflex 200) with monochromatic CuKα radiation (λ=1.54178 Å) is used over a 2θ angle from 10° to 70° to obtain the inter-planar spacing and microstrain of EG. The d-spacing of the graphite flakes is calculated using the Bragg's Equation [14]. Single line approximation method [15] is used to calculate the microstrain (χ) of both NG and EG flakes. Room temperature X-ray patterns of NPR, NG, EG and EG/NPR composite are shown in Fig. 3.6. A broad peak is observed at 2θ angles of about 20° for NPR indicating an amorphous behavior as shown in fig.3.6 (a). From fig 3.6 (b) a high crystalline nature of NG is confirmed from the characteristic peak observed at 2θ = 26.86° due to (*002*) plane corresponding to inter-layer spacing (*d002*) 0.332nm. Fig.3.6 (c) shows that the characteristic peak of EG is observed at slightly lower angle, 2θ = 26.62°, corresponding to inter-layer spacing (*d002*) 0.335nm. Expansion in inter-layer spacing clearly confirms the formation of EG from NG. As the graphite platelets expand, a compressive microstrain is expected in the graphite platelets. The calculated microstrain increases from 0.7% for NG to 1.36% for EG. The increased microstrain corroborates the increased *d* spacing confirming the formation of EG. Further, in fig. 3.7 (a) the value of intensity (in a.u) along y-axis in the XRD plot shows a very large variation (70,000 for natural graphite and 2,500 for expanded graphite) showing that for same volume sample the graphite crystallite is less in expanded graphite. EG formed by expansion in graphite platelets of NG is shown in

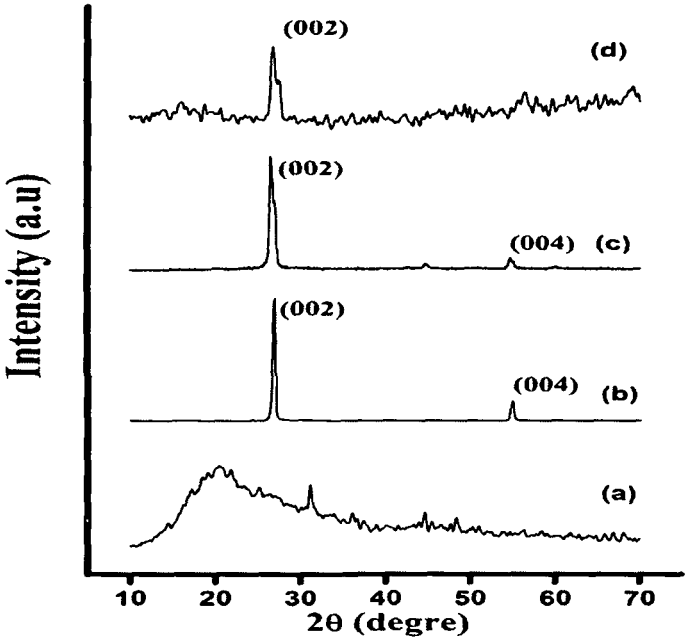

Figure.3.5 XRD patters of (a) NPR, (b) NG, (c) EG and (d) EG/NPR

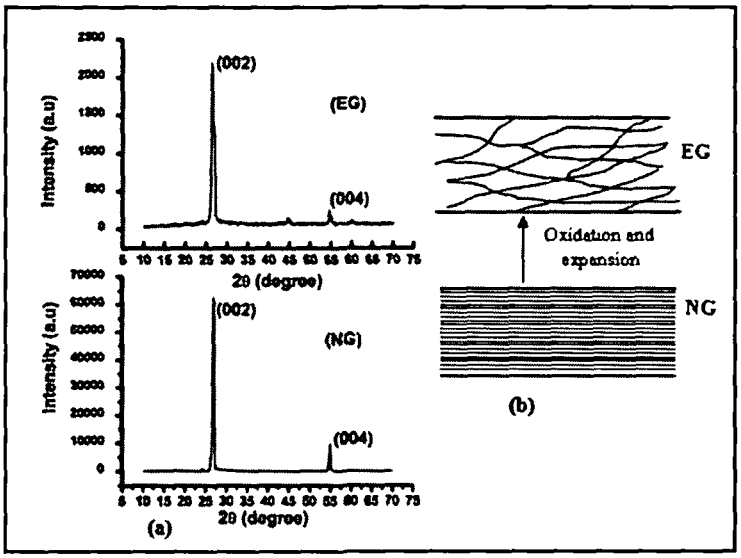

Figure3.7 (a) XRD patters of NG & EG, (b) schematic orientation of graphite platelets in NG & EG

schematically in fig. 3.7 (b) representing the orientation of graphite platelets before and after the expansion. The sharp reflection at $2\theta = 26.62°$ is observed in fig.3.6 (d) implying that in EG/NPR composite the single graphite nanosheets consist of multilayer graphite sheets with a *d*-spacing of 0.335 nm. Intrusion of NPR polymer molecules does not change the nanostructure of graphite, and hence its crystal structure is retained.

3.3.2 Transmission Electron Micrographs

Transmission electron microscopy (TEM) is the premier tool for understanding the internal microstructure of materials at the nanometer level. Electrons have an important advantage over X-rays in that they can be focused using electromagnetic lenses. One can obtain real-space images of materials with resolutions of the order of a few tenths to a few nanometers, depending on the imaging conditions, and simultaneously obtain diffraction information from specific regions in the images (e.g. small precipitates) as small as 1 nm [16]. The TEM study of EG flakes is carried out using JEOL JEM-2100 transmission electron microscope installed at the Sophisticated Analytical Instrumentation Facility (SAIF), North-Eastern Hill University (NEHU), Shillong, India. The micrographs is taken at 200 kV accelerating voltage at different magnifications. TEM (fig. 3.8 (a-d)) image of EG flakes reveal its morphological structure. Fig. 3.8(a) shows the lateral linear dimension of ~20μm with induced disorderness in graphite structure due to acid intercalation followed by exfoliation. The TEM images also suggest the destacking of the ordered graphitic structure. From fig. 3.8 (b) and (c) it is observed that EG sheets have thickness of 10–40 nm and length of about 400 nm, indicating a large aspect ratio (width-to-thickness), which facilitates to yield the conductive network. High resolution images in fig.3.8 (d), shows that

the graphite nanosheets consists of thinner graphite nano lamellae of thickness 5 nm and with inter-layer spacing of ~ 0.335 nm.

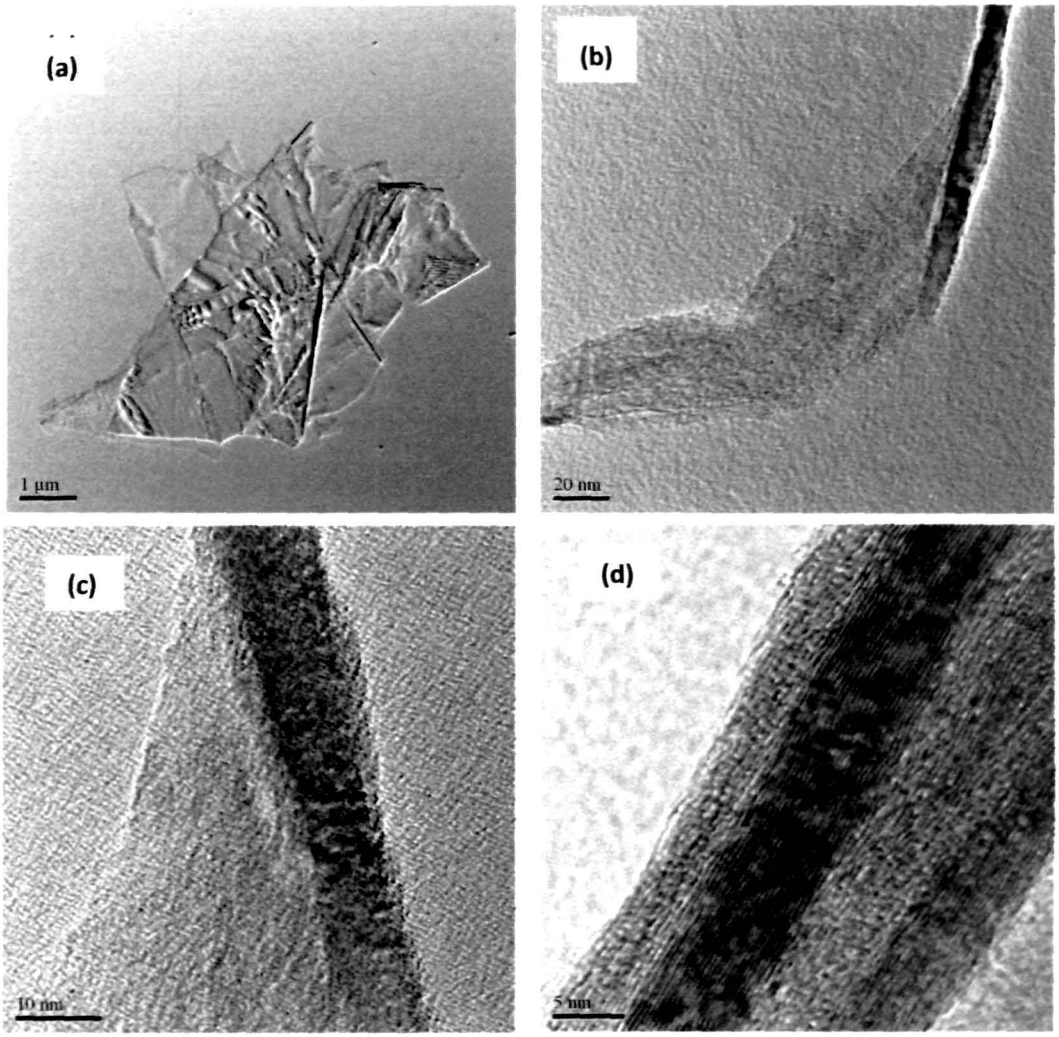

Figure3.8 (a-d) TEM images of EG flakes

3.3.2 Scanning Electron Micrographs

Scanning electron microscopy (SEM) is a very sensitive technique for studying the size and distribution pattern of the inclusions in the polymer matrix. The SEM study is carried out using a JEOL JSM 6390 LV model scanning electron microscopy installed at Central Instrumentation Facility (CIF), Tezpur University, India. It is based on the principle of irradiating the

specimen with finally focused electron beam. The electron beam on striking the surface releases secondary electrons back scattered electrons, Auger electrons, characteristic X-rays and several other types of radiation from small part of the specimen. The surface SEM secondary electrons are generally collected to form the image. The surface of each samples are platinum coated using a sputtering unit before taking the micrographs. The micrographs are taken at 10-11 A probe current

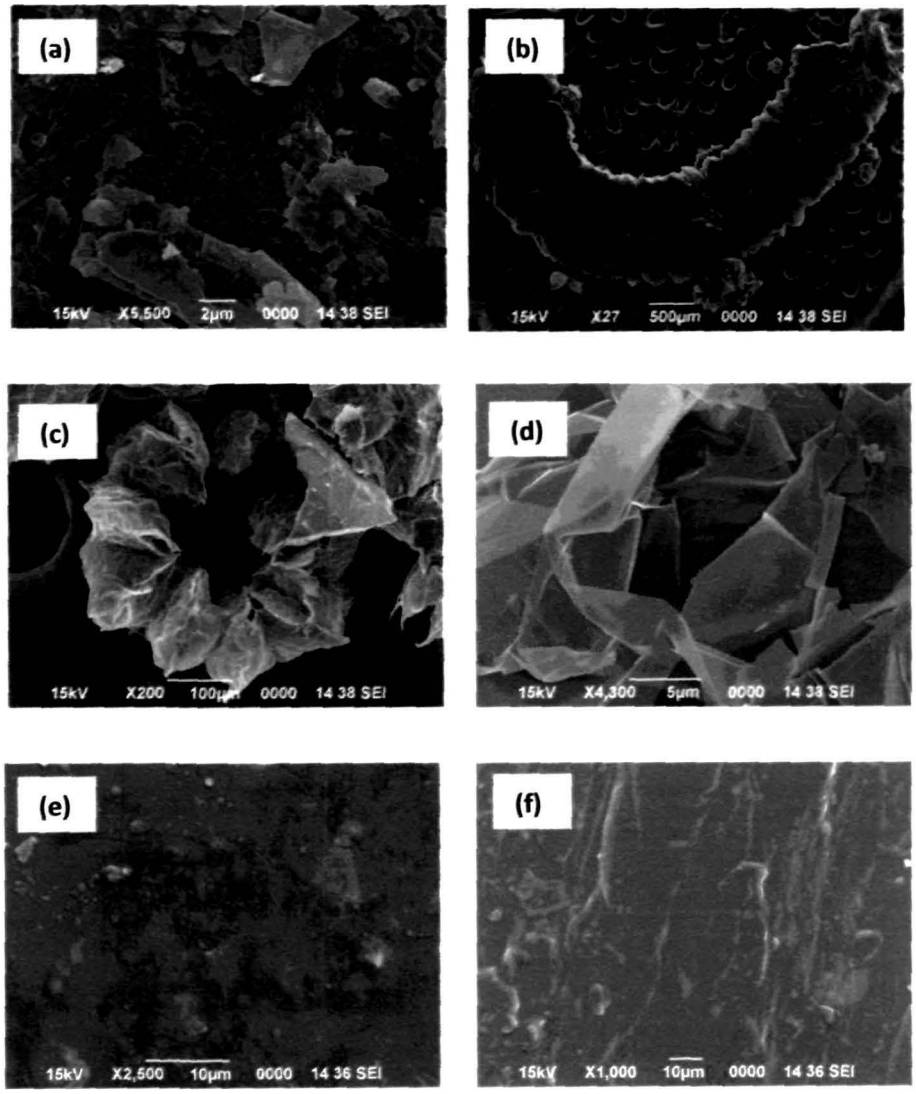

Figure3.9 (a) SEM micrograph of (a) NG, (b), (c) & (d) EG, (e) EG/NPR composite surface and (f) fractured EG/NPR composite

and 20 KV accelerating voltage at different resolutions. Figure 3.9 (a)-(f) shows the SEM micrographs of NG, EG and EG/NPR composites. Figure 3.9 (a) shows the SEM micrograph of natural graphite (NG) flakes of irregular shape and sizes ranging from 2 μm to 20 μm (approximately). Figure 3.9 (b and c) is of expanded graphite flake with magnification of x 27 and x 200 respectively, having vermicular or worm shaped with loose and porous structure that is due to opening of planar carbon networks wedged at the edge surface of the crystallite by surface groups. Figure 3.9 (d) shows EG at higher magnification (x 4300), where it can be seen that the structure of EG basically consists of numerous graphite sheets of nanometers thickness and micrometer diameter. This structure endows EG with high surface area. In fig. 3.9 (e) the surface morphology shows almost a uniform distribution of crushed EG in the NPR polymer composite. Figure 3.9 (f) shows the distribution of EG inside the bulk of novolac phenolic resin composite.

3.3.4 Fourier Transform Infrared spectra Spectroscopy (FTIR)

The FTIR spectroscopy study of NG, EG, NPR and EG/NPR composites have been conducted for understanding the bond structure and different interactions taking place among the various constituents in the composites. The FTIR spectra have been recorded using a Perkin Elmer spectrum 100 spectrophotometer and Nicolet Impact 410 spectroscopy installed at Tezpur University, India. FTIR spectra of NG, EG, Novolac Phenolic Resin and EG/Novolac phenolic resin composite are shown in figure 3.10. In figure 3.10 (a) the absorption band at 3484 cm^{-1} is assigned to hydrogen bonded -OH group. The peak due to $-CH_2-$ stretching vibration is observed at 2925.10 cm^{-1}. The peaks in between the 1441 - 1599 cm^{-1} are of C-C stretching vibration. The peak at 1232.63 cm^{-1} is of Ar-O- stretching vibration and peak at 1097 cm^{-1} is of CH_2-OH stretching vibration [17]. This suggested that novolac phenolic resin having hydroxyl and methylene group's

linkages are responsible for bonding with EG. FTIR spectra of NG gave absorption peaks at 1037.73, 1628.76 and 3598.72 cm^{-1} as shown in figure 3.10 (b). Here, the peaks at 1037.73 cm^{-1} is due to C-O stretching vibration of ether. The peak at 1628.76 cm^{-1} is C-O stretching of ketone group. The broad absorption peak at 3598.72 cm^{-1} is of hydrogen bonded O-H stretching vibration.

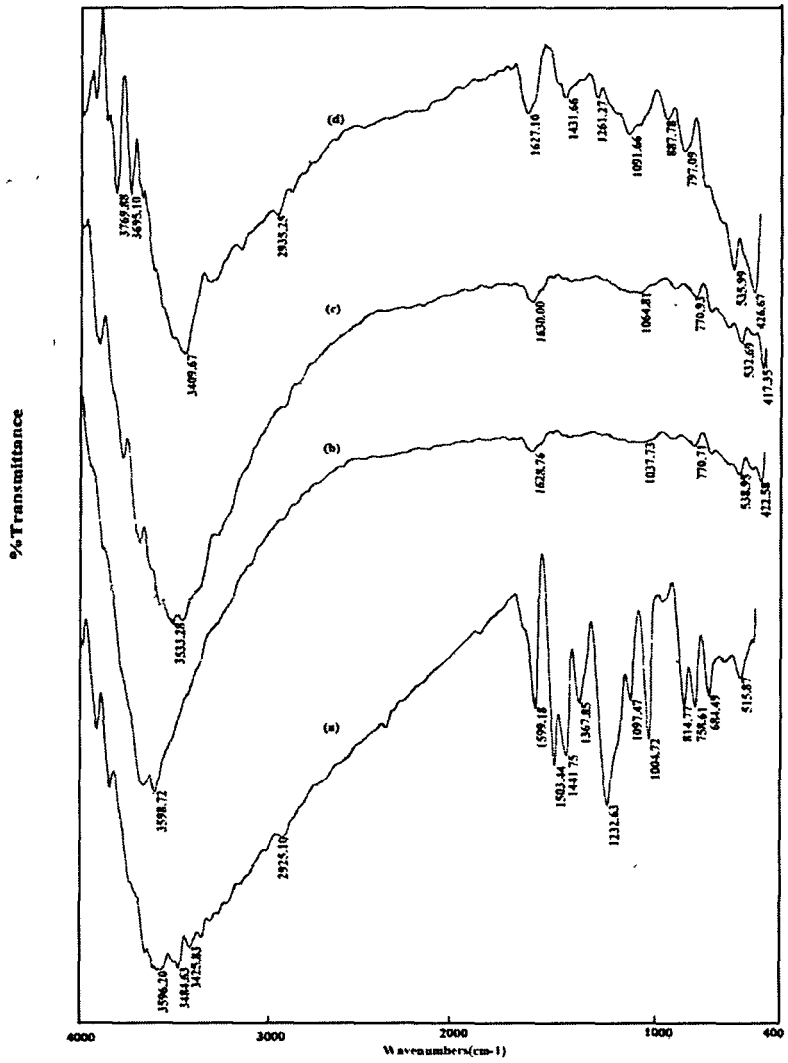

Figure3.10. FTIR spectra of (a) Novolac Phenolic resin(NPR), (b)Natural graphite, (c)Exfoliated graphite (EG) & (d) EG/NPR composite

Figure 3.10 (c) shows the spectra of expanded graphite in which the wave number of some of the peaks are shifted to higher wave number and some towards the lower wave number. It is observed that a strong band is appearing at 353.28 cm^{-1}, which can be assigned to O-H stretching vibration of phenolic or alcoholic functional groups present in the EG. The presence of carboxyl functional groups can also be detected at around 1630 cm^{-1}. During the treatment of natural graphite with acids some of the carbon double bonds are oxidized, leading to the presence of oxygen-containing functional groups on expanded graphite which will facilitate physical and chemical interactions between EG and polymer. Figure 3.10 (d) shows the FTIR spectra of EG/NPR composite. The peaks in between 3695.10 to 3769.88 cm^{-1} is due to free hydroxyl group of the phenols. The absorption band at 3409.67 cm^{-1} is of hydrogen bonded -OH group. The peaks at 2935.25 cm^{-1} is due to $-CH_2-$ stretching vibration. The peaks at 1627.10 cm^{-1} is of C-O stretching of ketone group. C-C stretching vibration is responsible for the peak at 1431.66 cm^{-1}. The peak at 1261.27 cm^{-1} is of Ar-O- stretching vibration and peak at 1091.66 cm^{-1} is of CH_2-OH stretching vibration. The FTIR spectrum of the composite shows the presence of both phases of fillers and the matrix and no new peaks has been observed showing that the interaction between EG and NPR is physical in nature.

3.4 CONCLUSIONS

Expanded graphite flakes are synthesized from natural graphite flakes by chemical oxidation and thermal treatment method. Formation of EG is confirmed from XRD pattern showing the expansion of the graphite basal planes along c-axis and decrease in diffraction intensity. For EG (2500 a.u) in comparison to NG (70,000 a.u). XRD studies of EG/NPR composites exhibit that intrusion of NPR polymer molecules does not change the nanostructure of graphite sheets, thus EG retain its crystal structure. TEM analysis EG flakes

shows graphite sheet thickness is in nanometer ranges and a high aspect ratio which yield a good conductive network. SEM studies showed that EG flakes are vermicular or worm shaped with loose and porous structure. SEM images of composites material shows the material have homogenous distribution of EG in the base matrix. FTIR spectra analysis reveals that acid treatment of NG during synthesis oxidizes some of the carbon double bonds leading to the presence of oxygen-containing functional groups on expanded graphite which *will facilitate physical and chemical interactions between EG and polymer.* Also, FTIR shows presence of hydroxyl and methylene group's in NPR which is responsible for bonding with EG and the interaction is physical in nature.

References

1. Yusoff, A.N., Abdullah, M. H., Ahmad, S.H., Jusoh, S. F., Mansor, A. A. and Hamid, S. A. A. Electromagnetic and absorption properties of some microwave absorbers, *Journal of Applied Physics* 92, 876-880, 2002.
2. Lee, S. M. *International Encyclopedia of Composites*. VHC Publishers, New York, 1991.
3. Hourquebie, P., Blondel, B., Dhume, S. Microwave and optical properties of soluble conducting polymers, *Synthetic Metals*. 85, 1437-1438, 1997.
4. Oh, J. H., Oh, K. S., Kim, C. G., Hong, C. S. Design radar absorbing structures using glass/epoxy composite containing carbon black in the X frequency ranges, Composites Part B: Engineering 35, 49-56, 2004.
5. Celzard A., Marechˆe, J. F., Furdin, G. and Puricelli, S. Electrical conductivity of anisotropic expanded graphite-based monoliths, *J. Phys. D: Appl. Phys* 33, 3094-3101, 2000.
6. Chen, G., Wu, D., Weng, W., He, B. and Yan, W. Preparation of polystyrene–graphite conducting nanocomposites via intercalation polymerization, *J. Polym Int* **50**, 980-85, 2001.
7. Chen, G., Wu, C., Weng, W., Wu, D. and Yan, W. Preparation of polystyrene/graphite nanosheet composite, *J. Polym Commun.* 44, 1781-84, 2003.
8. Debelak, B. and Lafdi, K. Use of expanded graphite filler to enhance polymer physical properties, *Carbon* 45, 1727-34, 2007.
9. Yasmin, A., Luo, J. J. and Daniel, I. M. Processing of expanded graphite reinforced polymer nanocomposites, *Compos Sci Tech* **66**, 1179–86, 2006..
10. Goyal, R. K., Samant, S. D., Thakar, A. K. and Kadam, A. Electrical properties of polymer/expanded graphite nanocomposites with low percolation, *J. Phys. D: Appl. Phys.* **43**, 365404-1-7, 2010.
11. Bishop, G. R. and Sheard, P. A. Fire-resistant composites for structural sections, *Composite Structures* **21**, 85–89, 1992.

12. Knop, A. and Pilato, L.A. *Phenolic Resins:Chemistry, Applications and Performance: Future Directions*, Springer, Berlin, 1985.

13. Kumar, H., Tripathi, S.K., Mistry, S. and Bajpai, G. Synthesis, Synthesis, characterization and application of coatings based on epoxy novolac and liquid rubber blend, *E-Journal of Chemistry* **6**, 1253–1259, 2009.

14. Cullity, B. D. *Elements of X-ray diffraction*, Addison Wesley, Massachusetts, 1978.

15. Delhez, R., Keijser, T. H. D., Langford, J. I., Louer, D., Mittemeijer, E. J., Sonneveld, E. J., Young, R.A. (Ed.), *The Reitveld Method*, Oxford University press, Oxford,1956.

16. Ruska, E., The Development of Electron Microscopy, Nobel Lecture, December 8, 1986, http://nobelprize.org/nobel_prize/physics/laureates/1986/ruska-lecture.pdf.

17. Dhakate, S. R., Sharma, S., Borah, M., Mathur, R. B. and Dhami, T. L. Development and Characterization of Expanded Graphite-Based Nanocomposite as Bipolar Plate for Polymer Electrolyte Membrane Fuel Cells (PEMFCs), *J. Energy & Fuels* **22**, 3329–3334, 2008.

CHAPTER IV

CHARACTERIZATION OF THE DIELECTRIC COMPOSITE MATERIAL: PHYSICAL, THERMAL AND ELECTRICAL

4.1 INTRODUCTION

In Radar targets and communication devices, the factors such as weight, dimensional stability and environmental properties plays important role and impose restrictions in the absorber material selection and design. Moreover, absorbing materials are characterized by converting the energy of electromagnetic wave into thermal energy; hence thermal stability and thermal conductivity of the material are to be studied [1-5].

In this chapter density, water absorbance, thermal stability and thermal conductivity of EG/NPR composite is studied to show its utility as absorber material. Electrical conductivity increases the microwave losses and hence the absorption. Both in-plane and through-plane dc electrical conductivity studies is carried out on EG/NPR composite system [6].

Some of the measurement setups were indigenously built in the laboratory with essential calibration. A comprehensive description of the set-up wherever necessary with results are described in the following sections.

4.2 PHYSICAL PROPERTIES

4.2.1 Density and Water Absorbance

Light weight microwave absorbers are easy to install and this in turn makes them suitable for free space applications. Density of a composite gives an idea of the compactness of the material and its weight. Measurement of density of the EG/NPR composites are carried out by using Archimedes's principle [7]. The samples of dimension 10.16 mm × 22.86 mm × 4.7 mm are prepared and weight measured in air, W_{air}. The composite is suspended in water and apparent immersed weight of the sample is measured, referred as W_{app}. Then the experimental bulk density (d_s) of the composite is measured by the Archimedes principle and is given by

$$d_s = \frac{W_{air}}{W_{air} - W_{app}} \times D_{water} \tag{4.1}$$

or $d_s = \frac{W_{air}}{W} \times D_{water}$ (4.2)

Where

W_{air} = Weight of the sample in air (gm)

W_{app} = Weight of the sample in air - weight of the displaced water (gm)

D_{water} = Density of water at room temperature (=0.997 g/cc at 25 °C)

Water absorbance studies of the material help in determining the porosity of the material and humid and wet environmental conditions in which the system can work without affecting its microwave performance. The percentages of water absorption of the composites are determined according to the expression

$$Water\ absorbance\ (\%) = \frac{W_t - W_0}{W_0} \times 100 \quad (4.3)$$

where W_t and W_0 are the weights of the wet and dry composites respectively.

Table 4.1 Density and percentage of water absorbance of EG/NPR composites

Sample composition	Density (g/cc)	(%)Water absorbance
5 wt. % EG/NPR	0.83	0.08
7 wt. % EG/NPR	0.84	0.08
8 wt. % EG/NPR	0.85	0.08
10 wt. % EG/NPR	0.87	0.08
20 wt. % EG/NPR	0.90	0.09
30 wt. % EG/NPR	0.91	0.10
40 wt. % EG/NPR	0.93	0.10
50 wt. % EG/NPR	0.96	0.10

Table 4.1 shows that the bulk density increases with increase in EG content. Composites with higher wt. % of EG contain less amount of NPR than

composites with low wt. % of EG. Decrease of density for composites with higher NPR content is due to the increase in ultimate weight loss during curing process. Percentages of water absorbance of the composites for 48 hours are tabulated in table 4.1. It is found that there is a slight increase of weight gain with increasing EG concentration in the composites due to presence of porosity in the samples. The maximum weight gain is only ~0.1 %.

4.3 THERMAL PROPERTIES

4.4.1 Thermal gravimetric Analysis (TGA)

The thermal gravimetric analysis (TGA) is performed to predict the thermal stability of a material at temperatures up to 1000°C. The TGA for pure NPR, EG and (5, 7, 8, 10, 20, 30, 40 and 50 wt. %) EG/NPR composites are carried out on Thermal Analyzer, Model STA 6000, Perkin Elmer. Figure.4.1 shows the thermal stability of NPR, EG and EG/ NPR composite measured by TGA in air atmosphere. TGA curve of NPR shows that there is a small weight loss up to 150 °C. The major weight loss occurs due to evolution of volatiles in between the temperature 350- 450 °C. Overall there is 75-80% weight loss up to 800 °C in air atmosphere. From the figure it is seen that TGA curve of EG shows thermal stability up to 600 °C. From 600 °C to 800 °C moderate weight losses and above 800 °C continuous weight loss up to 850 °C is observed, this is due to surface complexes formed during oxidation. The total weight loss up to 850 °C is 10-15%. The EG/NPR composites with 5 to 50 wt. % show a very small weight loss up to 300 °C. From 300 to 400 °C, a moderate weight loss and above 400 °C continuous weight loss is observed up to 900 °C. It is seen that addition of EG flakes in the matrix enhances the thermal stability in comparison to pure matrix. Although, all the composites show almost same stability upto 300 °C, but with increasing EG content overall weight loss decreases. EG flakes form a heat conductive network in the matrix and with

increasing EG content the conductive path is easily achieved [8].A maximum weight loss is observed for 5 wt. % weight loss of 55-60 % and minimum for 50 wt. % weight loss of 25-30% EG/NPR composites upto 850 °C.

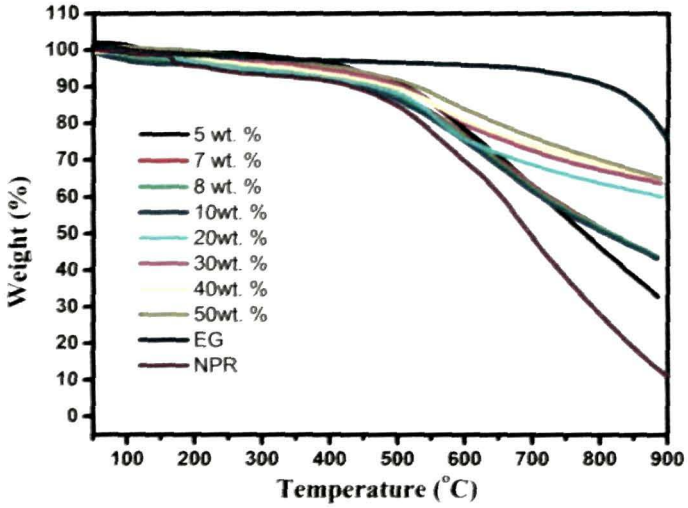

Figure 4.1 Thermal gravimetric analysis (TGA) curves of EG, NPR and (5-50) wt. % EG/NPR composite.

4.4.2 Thermal conductivity

Primary mechanism of microwave absorption in dielectric RAM is dielectric loss in which microwave energy is irreversibly transformed to Joule thermal energies. It is important to dissipate away the heat developed in the composites due to microwave absorption. Thermal conductivity ascertains the extent heat can be dissipated by the material, and hence the dimensional stability. A set-up is developed in the laboratory to measure the thermal conductivity of the samples and described below.

Set up fabrication and measurement

There are different techniques for thermal conductivity measurements in insulators. Lee's method is the most popular one [9], but it suffers from the need of bulky steam system for heating and high possibility of radial heat flow. There are other advanced methods (e. g NPL's (UK) Guarded Hot Plate Method) which are very accurate but expensive. The set up is indigenously

designed and fabricated in the laboratory by using more robust components: guarded hot plate, solid state transducer and amplifier [10]. The theory of the ***instrument is based on Lee's method.***

Design of modified Lee's method

The instrument consists of two brass slabs where one acts as heat source and other as sink. The sample to be tested is placed between the source and sink. The exposed portion of the source and sink is covered with heat insulating-seal to ensure no radial heat flow. A thermostatic electric heater is used to heat the source and sink is kept at room temperature. A spring system is attached to the other end of sink to ensure good contact between source, sample and sink with the advantage of easy placement of the sample. A non-conducting casing is used for mounting the system. The schematic diagram of the instrument is shown in figure 4.2.

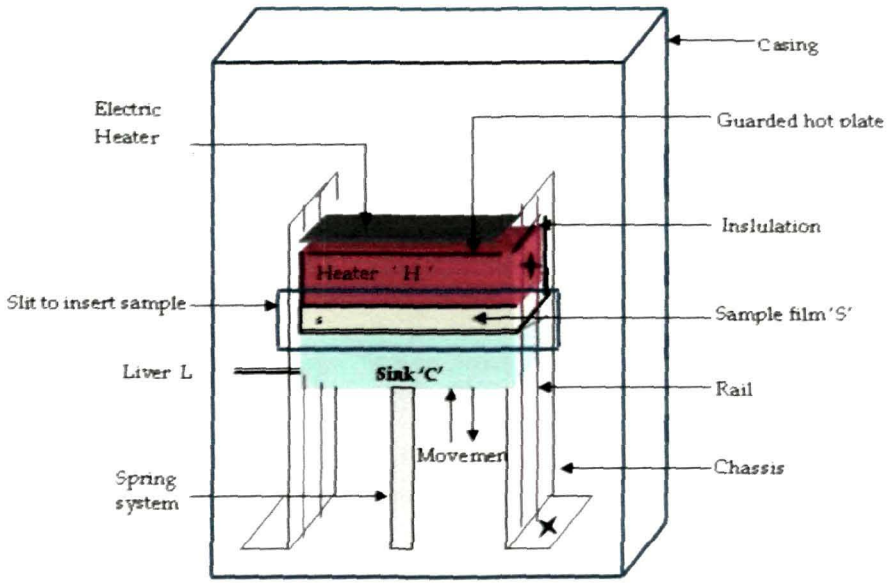

Figure 4.2 Schematic diagram of thermal conductivity measurement set-up

Transducer element

Temperature of the slabs is measured by a transducer element, transistor. It works on the principle of Peltier effect. The schematic of the

transducer system is shown in figure 4.3. The system can measure both absolute and relative temperatures of the slabs using a switch.

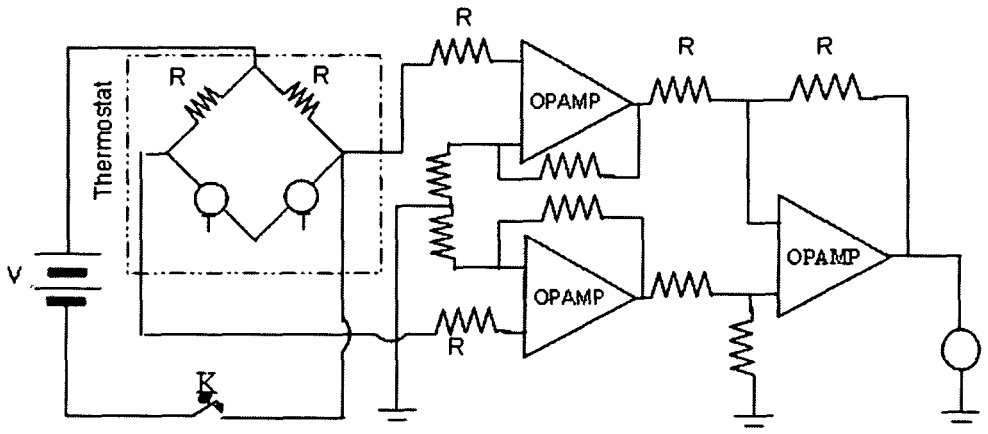

Figure 4.3 Circuit diagram of the transducer system
OPAMP = Operational Amplifier, R = Resistance=1KΩ, T = Transistor

Working principle

The experimental sample S is trapped between the source and sink. The area of sample is kept same as the area of the slab. The source is heated and heat conducts through the sample to the sink. The rate at which heat (Q) conducts through the specimen is equal to the rate at which the sink losses heat

$$Q = \frac{KA(\theta_1 - \theta_2)}{d} \tag{4.4}$$

where

K is the coefficient of thermal conductivity of the specimen

A is the area of the sample

d is thickness of the sample

θ_1 and θ_2 are temperatures of the source and sink at steady state

If M is the mass of the slab, s, the specific heat of the slab material, the rate of cooling of the sink at θ_2 is

$$Q = MS\left(\frac{d\theta}{dt}\right)_{\theta=\theta_2} \tag{4.5}$$

where

$d\theta/dt$ is the rate of fall of temperature at θ_2

From equation 4.3 and 4.4

$$\frac{KA(\theta_1-\theta_2)}{d} = MS\left(\frac{d\theta}{dt}\right)_{\theta=\theta_2} \tag{4.6}$$

$$K = \frac{dMS\left(\frac{d\theta}{dt}\right)_{\theta=\theta_2}}{A(\theta_1-\theta_2)} \tag{4.7}$$

The rate of cooling is found by heating the sink to a temperature above θ_2. The sample is then placed between the source and sink and source is heated. The temperature of the source is allowed to reach an equilibrium temperature with the sink. t, the time of fall of temperature of the sink is noted at regular intervals. The slope of the tangent drawn to this plot gives the value of rate of fall of temperature.

Thermal conductivity measurement results

The thermal conductivity of the prepared samples measured with the above techniques is tabulated in table 4.2. Table 4.2 shows the variation of thermal conductivity for EG/NPR composites. It can be seen that thermal conductivity increases with increase in filler content. The effective thermal properties of composite depend on the intrinsic, microstructural properties of the filler, homogeneity of its distribution and compactness of the filler [11, 12]. Heat transfer in this composite takes place via NPR-EG interface. The increasing EG

flakes effectively form better conductive network in the NPR and improve thermal conductivity significantly.

Table 4.2 Thermal conductivity of EG/NPR composites

Sample composition	K (W/m ^{0}K)
Pure NPR	0.027
5 wt. % EG/NPR	0.210
7 wt. % EG/NPR	0.262
8 wt. % EG/NPR	0.275
10 wt. % EG/NPR	0.312
20 wt. % EG/NPR	0.418
30 wt. % EG/NPR	0.521
40 wt. % EG/NPR	0.598
50 wt. % EG/NPR	0.642

4.4.4. Coefficient of Thermal Expansion - Setup Development and Measurement

Thermal expansion coefficients of the prepared samples are measured with comparator method. The experimental setup, developed in the laboratory [10] is shown in figure 4.4. The setup consists of a glass cavity containing inlet and outlet for steam. A glass rod is used as holder to place the sample inside the cavity. A thermometer is placed near the sample to measure its temperature. A travelling microscope of least count 0.01 mm monitors the change in the dimension of the sample. The length of the sample is made manifolds than the cross sectional dimensions so as the change can be taken linearly. Prior to placing the sample the change in length of the glass for the same increase in temperature is observed which is found to be negligible as compared to the change in the sample length.

The initial length of the sample is l_1 (say) at room temperature, t_1°C. After passing steam at 100°C through the cavity a steady temperature is reached value (t_2°C) and the new linear dimension is l_2.

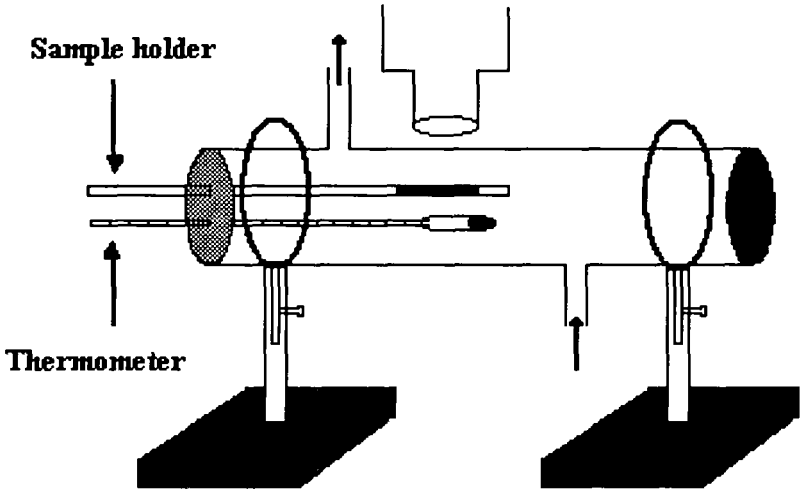

Figure 4.4 Setup for thermal expansion coefficient measurement

The thermal expansion coefficient (α_1) can be found from

$$\alpha_1 = \frac{l_2 - l_1}{l_1 \times (t_2 - t_1)} \text{ per °C} \qquad (4.8)$$

Thermal Expansion Coefficient Measurement Results

The coefficient of thermal expansion (CTE) of EG/NPR composites are tabulated in table 4.4. It is seen that CTE decreases with increasing EG percentages in the composites. It is because the heat conductive network of EG drain away the heat created or supplied in the composite and there is little accumulation of thermal energy in the composite, consequently linear thermal expansion is very less. Increasing wt. % of EG consolidated the conductive network and hence decreases the CTE. Thus, the developed composites show dimensional stability.

Table 4.3 Coefficient of thermal expansion (CTE) of EG/NPR composites

Sample composition	$\alpha_1 \times 10^{-6} (K^{-1})$
Pure NPR	80
5 wt. % EG/NPR	25.2
7 wt. % EG/NPR	24.6
8 wt. % EG/NPR	24.1
10 wt. % EG/NPR	22.7
20 wt. % EG/NPR	19.23
30 wt. % EG/NPR	17.75
40 wt. % EG/NPR	16.18
50 wt. % EG/NPR	14.29

4.4 ELECTRICAL CONDUCTIVITY

In-plane and through-plane dc electrical conductivity of the EG/NPR composite is measured by two probe method using Keithley 2400-C source meter interfaced with PC using GPIB port. Initially, resistance of the samples is calculated from current-voltages (I-V) characteristics at room temperature. The resistivity of a bulk samples is based on accurate measurement of resistance and the sample dimensions. For a homogenous bar of length, L and uniform cross section *A*, the resistance, *R*, is related to the resistivity, ρ, by

$$R = \rho L/A \tag{4.9}$$

The reciprocal of ρ gives the conductivity (σ) of the samples given as

$$\sigma = 1/\rho \tag{4.10}$$

The schematic diagram of in-plane and through plane dc conductivity measurement is shown in figure 4.5.

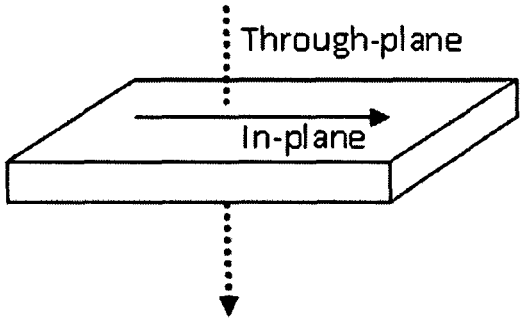

Figure 4.5 Schematic diagram of plane of dc conductivity measurement

The *in-plane* and *through-plane* I-V characteristics of EG-NPR composites with different wt. % are shown in figure 4.6 and figure 4.7 respectively. The slope of the curve gives the reciprocal of resistance, R. From equation (4.9) and (4.10), both the in-plane and through plane conductivity of the composites is calculated and tabulated in table 4.4. It is seen that the electrical conductivity increases with increasing EG loadings. EG/NPR composites consist of insulating phenolic resin phase (~10^{-11} S/cm) and conducting EG flakes (~10^{4}S/cm) [13]. Pure NPR shows insulating behavior, however, inclusion of EG loadings (~5wt. %) transform the insulating composites to semiconducting state. In this investigation, EG is synthesized from NG using 3:1 volume ratio of concentrated sulfuric acid and nitric acid, this assists in increasing the surface area [14], removing contaminants from EG surface, reducing the pores and unbonded interfaces between EG and phenolic resin, thus establishing a conductive network of EG in the composite system and hence the enhanced conductivity.

4.4.1 In-plane dc electrical conductivity

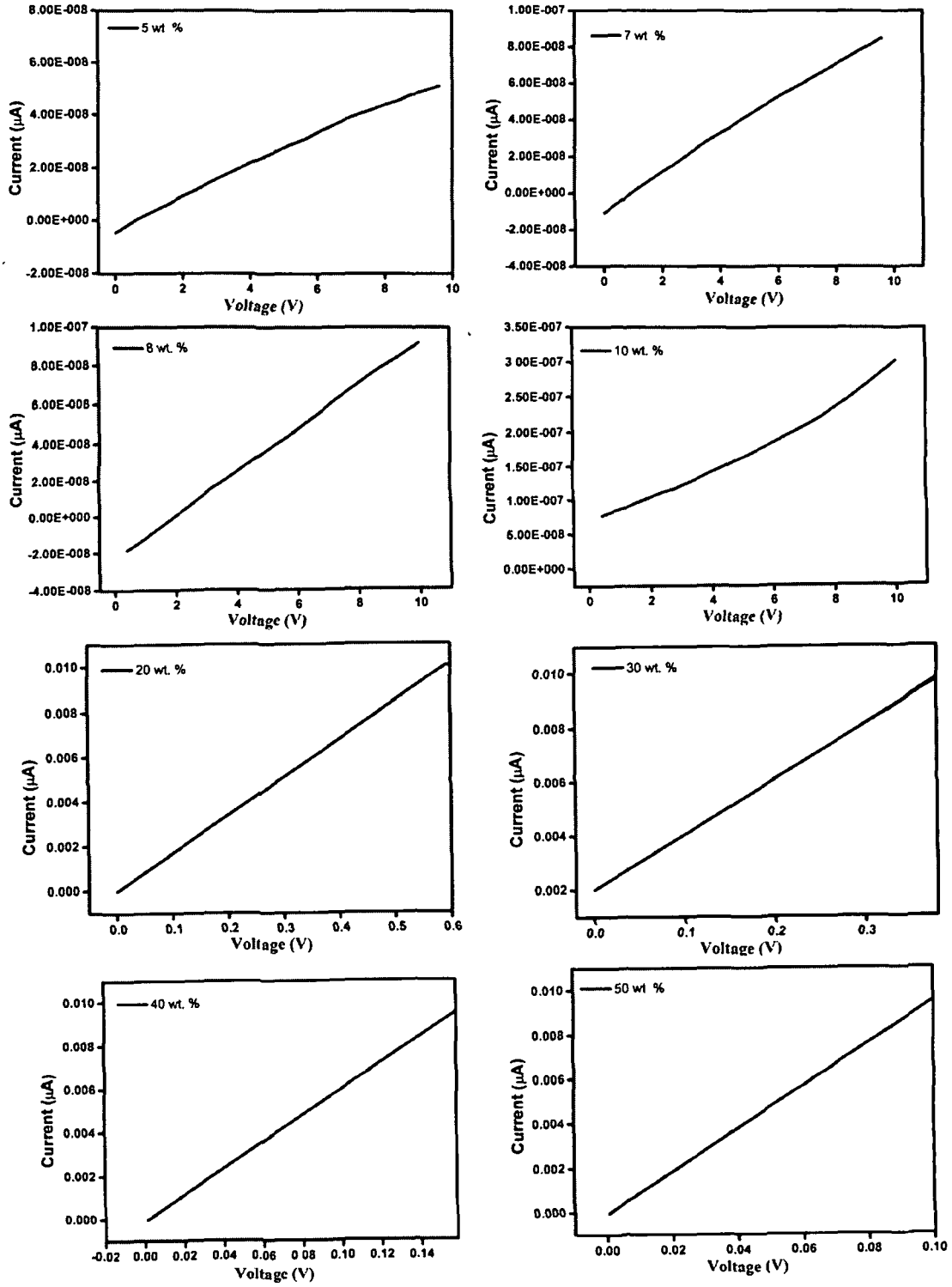

Figure 4.6 In plane *I-V* characteristics of EG-NPR composites

4.4.2. Through-plane dc electrical conductivity

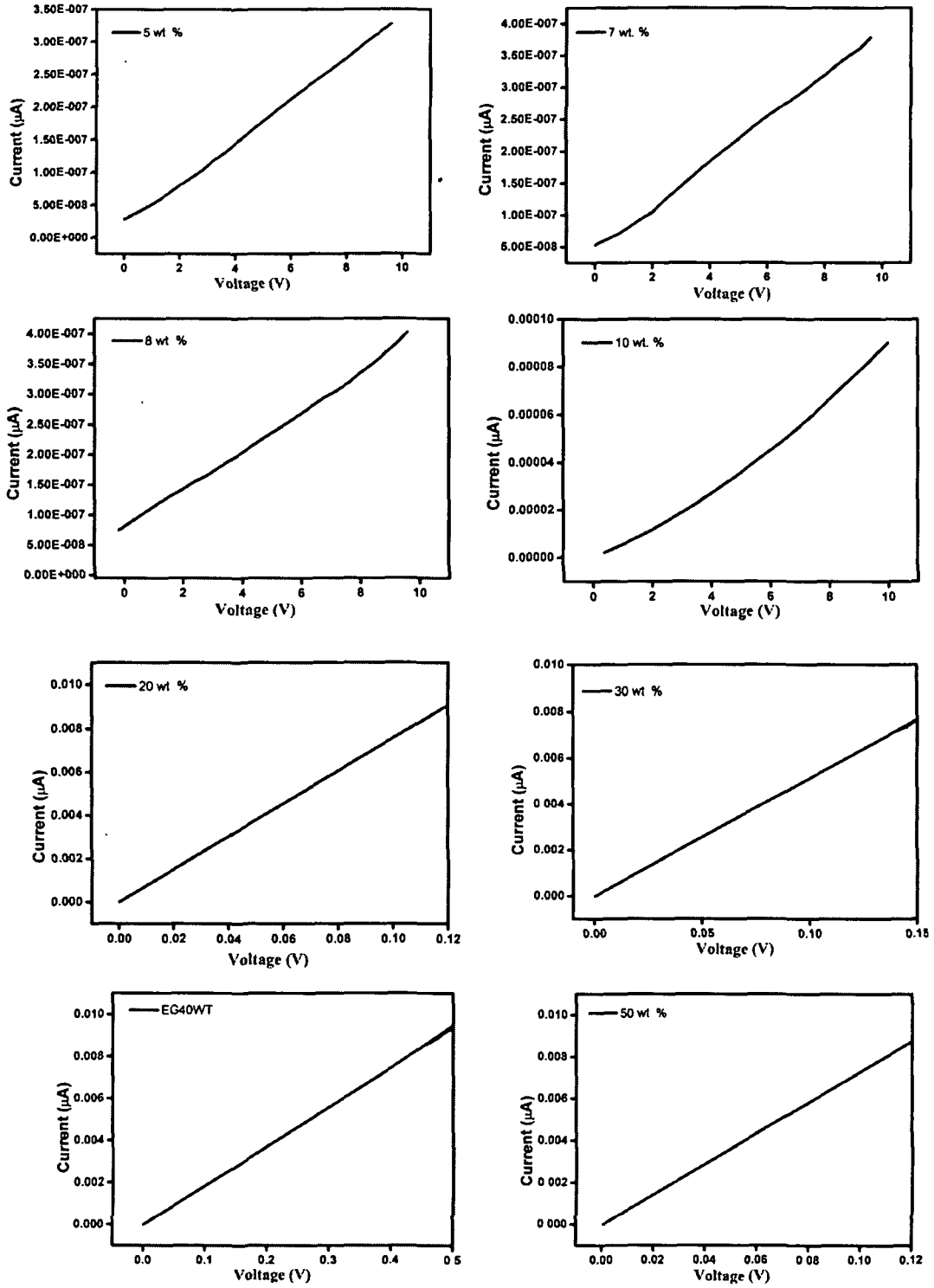

Figure 4.7. Through plane I-V characteristics of EG/NPR composites

Table 4.4: In plane and through plane dc electrical conductivity of EG/NPR composites

Sample composition	In plane conductivity σ_{in} (S/cm)	Through plane conductivity σ_{thru} (S/cm)
Pure NPR	2.4E-11	4.8E-13
5 wt. % EG/NPR	6.05E -07	5.526 E-10
7 wt. % EG/NPR	4.96E-06	5.98 E-10
8 wt. % EG/NPR	9.88E-06	7.12 E-10
10 wt. % EG/NPR	4.78E-05	1.58 E-10
20 wt. % EG/NPR	0.0135	1.296 E-03
30 wt. % EG/NPR	10.00	0.108
40 wt. % EG/NPR	108.00	0.1257
50 wt. % EG/NPR	147.00	0.3267

4.5. CONCLUSIONS

EG-NPR composite system shows low density <1 and has negligible water absorption. The TGA curve shows that the developed composite is thermally stable up to 300 °C. Thermal conductivity and thermal dimensional stability shows significant improvement with increase in weight % of EG flakes in the matrix. The increasing EG flakes improve the conductive network in the NPR enhancing the electrical conductivity. EG-NPR composite system shows promises to be useful for free space microwave shielding applications.

References

[1] Gong, C., Zhang, J., Yan, C., Cheng, X., Zhang, J., Yu, L., Jin, Z. and Zhang, Z. Synthesis and microwave electromagnetic properties of nanosized titanium nitride, *J. Mater. Chem.* **22**, 3370-3376, 2012.

[2] Folgueras, L. C., Rezende, M. C. Hybrid multilayer structures for use as microwave absorbing material, in SBMO/IEEE MTT-S International Microwave & Optoelectronics Conference (IMOC 2007), Salvador, Brazil, 483 - 487.

[3] Zivkovic, I. and Murk, A. Boron nitride loading for thermal conductivity improvement of composite microwave absorbers, *Electronics Letters* **48**, 1130 - 1131, 2012.

[4] Martin, R. H. *Composite materials: fatigue and fracture,* ASTM, Philadelphia, USA, 1995.

[5] Zou, C., Fothergill, J. C. and Rowe, S. W. The effect of water absorption on the dielectric properties of epoxy nanocomposites, *IEEE Transactions on Dielectrics and Electrical Insulation* **15**, 106-117, 2008.

[6] Feng, X., Liao, G., Du, J., Dong, L., Jin, K., Jian, X. Electrical conductivity and microwave absorbing properties of nickel-coated multiwalled carbon nanotubes/poly(phthalazinone ether sulfone ketone)s composites, *Polymer Engineering and Science* **48**, 1007-1014, 2008.

[7] Pratten, N.A. The precise measurement of the density of small samples, *Journal of Material Science* **16**, 1737-1747, 1981.

[8] Cao, P., Qi, S. H. and Li, S. S. Preparation and thermal properties of novolac resin/ graphite nanosheet composites, *Advanced Materials Research* **391-392**, *209-213, 2012.*

[9] Alam, M., Rahman, S., Halder, P.K., Raquib, A. and Hasan, M. Lee's and Charlton's method for investigation of thermal conductivity of insulating materials, *IOSR Journal of Mechanical and Civil Engineering* **3**, 53-60, 2012.

[10] Juti Rani Deka, Study of Polystyrene-Alumina and Polystyrene-Titania Composites as Substrate for Microstrip Line and Resonator in C- and X- Bands, Ph. D. Thesis, Tezpur University, India, 2005.

[11] Todd, M. G. and Shi, F. G., Characterizing the interphase dielectric constant of polymer composite materials: effect of chemical coupling agents, *J. Appl. Phys.* **94**, 4551-4557, 2003.

[12] Kulijanin, J., Vučković, M., Čomor, M.I., Bibić, N., Djoković V. and Nedeljković, J. M., Influence of CdS-filler on the Thermal Properties of Polystyrene, *European Polymer Journal*, **38**, 1659-1662, 2002.

[13] Celzard A., Marechˆe, J. F., Furdin, G. and Puricelli, S. Electrical conductivity of anisotropic expanded graphite-based monoliths, *J. Phys. D: Appl. Phys* **33**, 3094-3101, 2000.

[14] Lucas, C.H., Peinado, A. J. L., González, J. D. L., Cervantes, M. L. R., Aranda, R. M. M. Study of oxygen-containing groups in a series of graphite oxides: physical and chemical characterization. *Carbon* **33**, 1585–1592, 1995.

CHAPTER V

MICROWAVE CHARACTERIZATION OF EXPANDED GRAPHITE - NOVOLAC PHENOLIC RESIN COMPOSITES OVER THE X-BAND

5.1 INTRODUCTION

In dielectric materials, the main properties that enable them to be applicable as microwave absorber are the dielectric constant and the loss at the operational frequency. Referring equation (2.77), chapter II, the reflection loss estimation of a conductor backed absorber design depends on the values of ε_r. Accurate measurement of complex permittivity ($\varepsilon_r=\varepsilon_r'-j\varepsilon_r''$) determines the performance and geometry of the absorber over a range of frequency band. Several methods have been reported on material property characterizations at microwave frequencies based on transmission lines and resonant structures developed from transmission lines [1-7]. Most accurate resonant method is the cavity perturbation method but has the limitation of single frequency operation [8, 9]. Broadband characterization of the dielectric properties of material is possible using nonresonant methods [10]. Nicolson and Ross [11] developed a transmission/reflection technique for obtaining the complex permittivity of linear materials over a broad range of microwave frequencies.

The chapter discusses determination of complex permittivity of the expanded graphite-novolac phenolic resin (EG-NPR) composites over the X-band frequency. A MATLAB program is developed to compute the complex permittivity of the composites from the measured value of S_{11} and S_{21}. Dielectric loss tangent, attenuation constant and microwave conductivity are calculated from the measured values of complex permittivity. Further, to substantiate the microwave characterization of the test materials at microwave frequencies, complex permittivity measurement is carried out using cavity perturbation technique [2, 8, 9].

5.2 WORKING PRINCIPLE OF NICOLSON-ROSS METHOD

The working principle of Nicholson-Ross method which is a transmission/reflection method and systematically analyzed in literature

[11]. Figure 5.1 shows a typical measurement configuration for a transmission/reflection method. The details of the waveguide method are described in reference [25]. A sample of rectangular shape with permittivity $\varepsilon = \varepsilon_0\varepsilon_r$ and permeability $\mu = \mu_0\mu_r$ is inserted into a segment of transmission line with characteristic impedance Z_0. Let d and Z be the thickness and the new characteristic impedance of the segment in which the material is installed.

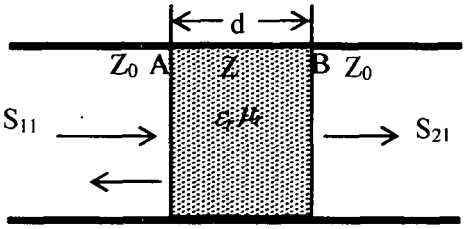

Figure 5.1 A schematic diagram of transmission/reflection method with rectangular shape material inserted

The characteristic impedance $Z=\sqrt{\mu_r/\varepsilon_r}\,Z_0$ where μ_r and ε_r are complex quantities if the material is lossy in nature. For an infinite thickness d the reflection coefficient of the microwave at the air-sample interface (A) is given as

$$\Gamma = \frac{Z-Z_0}{Z+Z_0} = \frac{\sqrt{\frac{\mu_r}{\varepsilon_r}}-1}{\sqrt{\frac{\mu_r}{\varepsilon_r}}+1} \tag{5.1}$$

If the thickness d is finite, the transmission coefficient through the segment AB is given as

$$T = exp\left[-j\left(\frac{\omega}{c}\right)\sqrt{\mu_r\varepsilon_r}d\right] \tag{5.2}$$

The scattering coefficient S_{21} and S_{11} of the slabs are given as

$$S_{21}(\omega) = \frac{(1-\Gamma^2)T}{1-\Gamma^2T^2} \tag{5.3}$$

$$S_{11}(\omega) = \frac{(1-T^2)\Gamma}{1-\Gamma^2T^2} \tag{5.4}$$

Let

$$V_1 = S_{21} + S_{11} \tag{5.5}$$

$$V_2 = S_{21} - S_{11} \tag{5.6}$$

If $X = \frac{1-V_1V_2}{V_1-V_2}$ (5.7)

Then using equations (5.3)-(5.7), the reflection coefficient can be found as

$$\Gamma = X \pm \sqrt{X^2 - 1} \quad (5.8)$$

For equation (5.8), the appropriate sign is chosen such that $|\Gamma| \leq 1$.

Similarly, using equations (5.3)-(5.7), the transmission coefficient T can be found as

$$T = \frac{V_1-\Gamma}{1-V_1\Gamma} \quad (5.9)$$

Rearranging equation (5.1), let us define

$$\frac{\mu_r}{\varepsilon_r} = \left(\frac{1+\Gamma}{1-\Gamma}\right)^2 = c_1 \quad (5.10)$$

Rearranging equation (5.2), let us define

$$\mu_r\varepsilon_r = -\left[\frac{c}{\omega d}\ln\left(\frac{1}{T}\right)\right]^2 = c_2 \quad (5.11)$$

From equations (5.10) and (5.11),

$$\varepsilon_r = \sqrt{\frac{c_2}{c_1}} \quad (5.12)$$

$$\mu_r = \sqrt{c_1c_2} \quad (5.13)$$

Right-hand side of equation (5.12) and (5.13) is a complex term. Separating real and imaginary parts, the complex permittivity and permeability values can be obtained.

5.3 MICROWAVE PARAMETERS OF EG-NPR COMPOSITES

5.3.1 Measurement of complex permittivity

The measurement set up for X-band permittivity characterization is

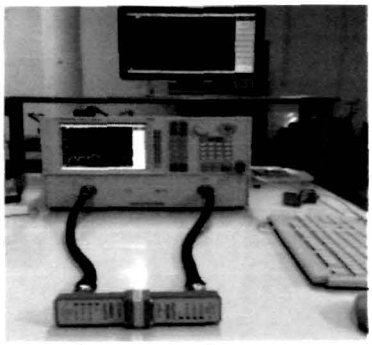

Figure 5.2 X-band microwave characterization set up using transmission/reflection technique

shown in figure 5.2. The setup broadly consists of an Agilent E8362C vector network analyzer, Agilent WR-90 X11644A rectangular waveguide line and an interfacing computer to collect the data. Prior to measurements, the system is calibrated using Thru-Reflect-Line (TRL) method [12, 13]. In thru calibration,

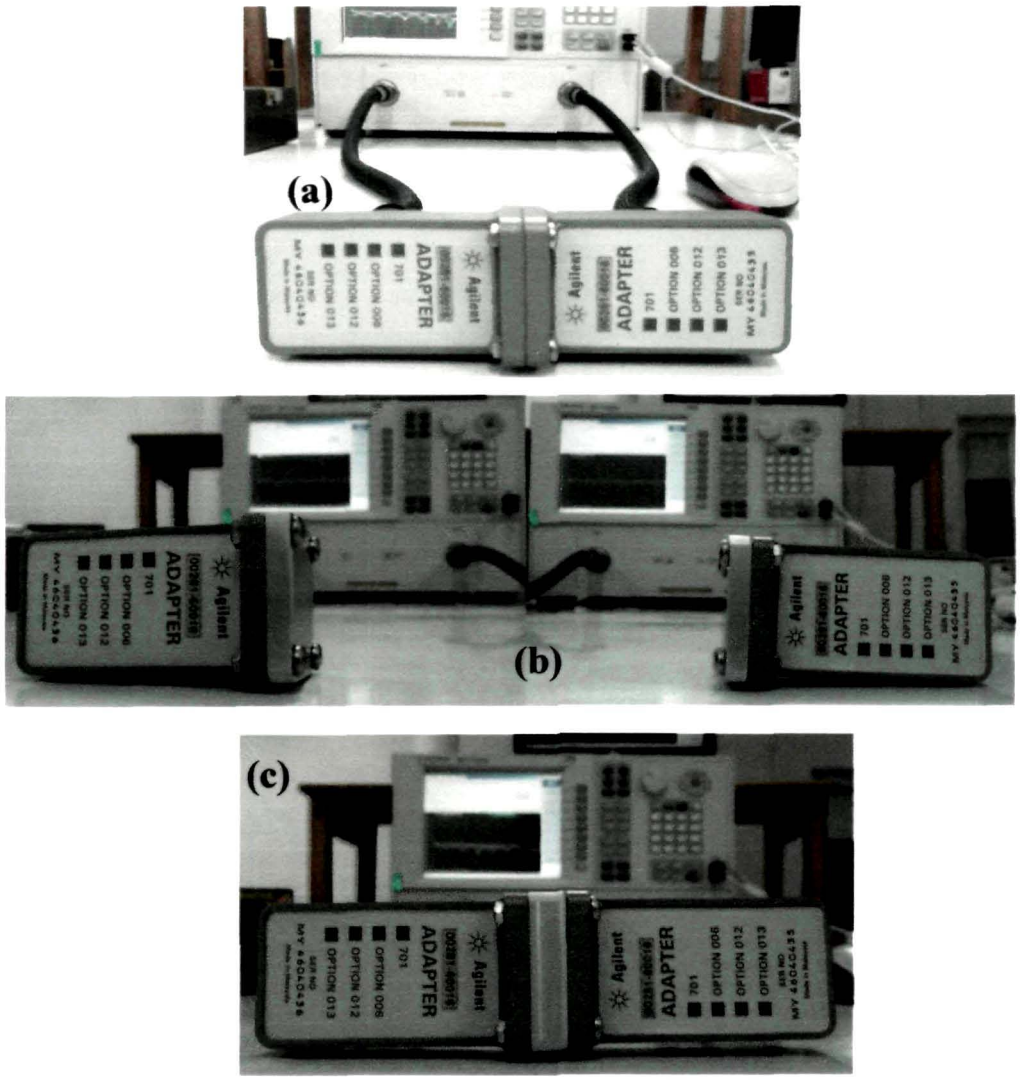

Figure 5.3 TRL calibration using Agilent WR90-X11644A calibration kit (a) Thru-calibration, (b) reflect-calibration and (c) Line-calibration

the two ports are connected directly at the desired reference plane as shown in figure 5.3(a), whereas for reflect calibration, the ports are terminated with a load such that high reflection occurs (fig.5.3 (b)). The two ports are connected by a quarter wavelength segment in line calibration (fig.5.3 (c)). After TRL calibration, the EG-NPR composites of dimension 10.38 mm x 22.94 mm x 3.7 mm (chapter 3, Section 3.2.3) are inserted in the sample holder of length 9.78 mm (shown in fig.5.4) and mounted on the zero reference plane i.e at the adapter of port 1 (fig 5.2). The scattering parameters (S_{11} and S_{21}) measured are transformed to the sample edges as described in reference [25].

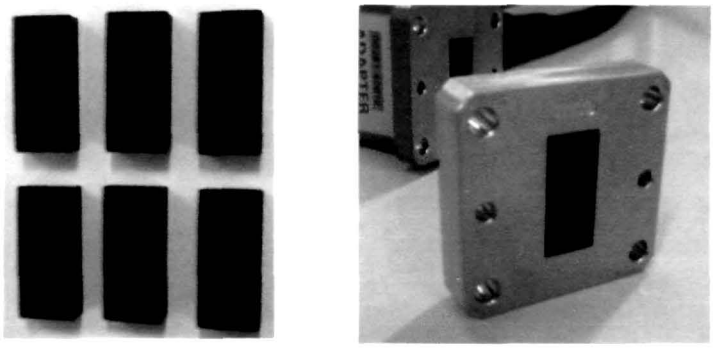

Figure 5.4 (a) Developed EG-NPR composites samples and (b) X-band flange filled with sample of EG-NPR composite for X-band characterization

The transformed S11 and S21 parameter are substituted in the equations (5.5 to 5.13) to determine the complex permittivity and permeability of the composites. The computation is carried out by a developed MATLAB program based on Nicolson Ross method discussed in the above section. The details of the program is discussed in Appendix-A. The algorithm of the developed program is as follows:

Step 1: Read data (S_{21} and S_{11}) from files.

Step 2: Calculate V_1, V_2, X and find Γ.

Step 3: Choosing the value of Γ such that $|\Gamma| \leq 1$.

Step 4: Calculate T using V_1 and Γ.

Step 5: Calculate ε_r and μ_r using T and Γ.

The computed values of ε_r and μ_r thus obtained are compared with the values obtained from Agilent 85071E material measurement software employing Nicolson Ross method.

5.3.2 Analysis of measured complex permittivity and complex permeability

Microwave characterizations of EG-NPR composites are carried out using developed MATLAB program mentioned above and the results are validated by Agilent 85071E material measurement software. Both the computations show similar results. The measured values of complex permittivity of (5, 7, 8, 10, 20, 30, 40 and 50) wt. % EG-NPR composites are plotted as a function of frequency over the ranges 8.2 GHz to 12.4 GHz. The

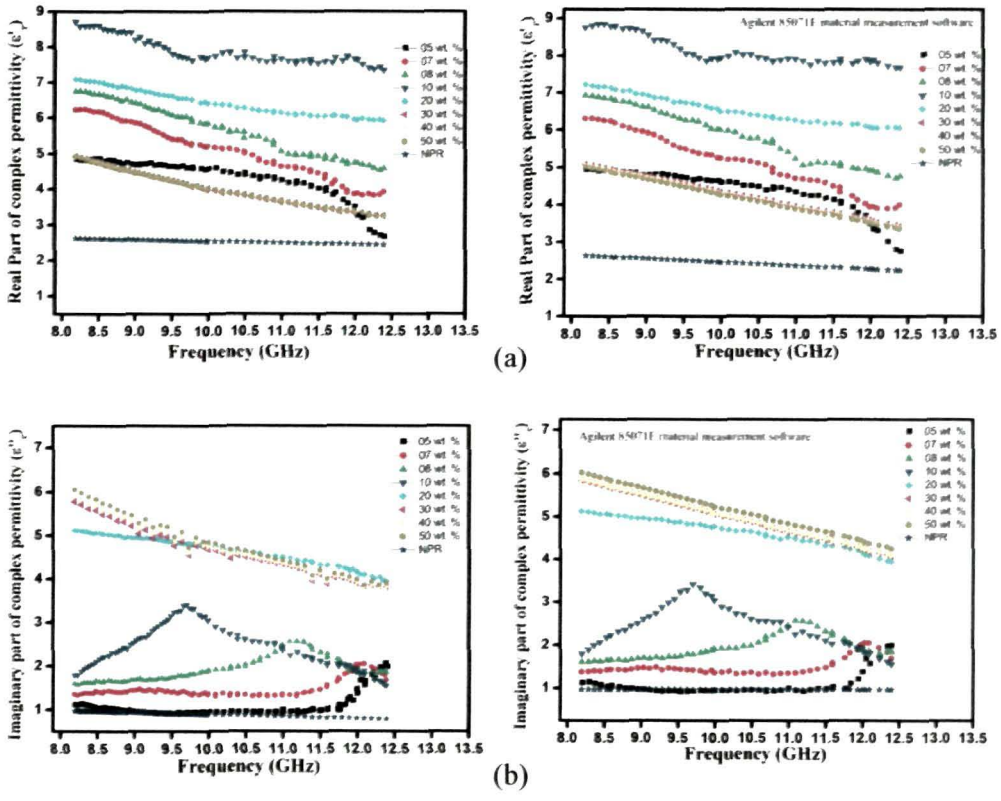

Figure 5.4 Complex permittivity spectra for 5 to 50 wt. % EG-NPR composites with developed program and Agilent software (a) Real parts and (b) Imaginary parts

real parts (ε_r') and imaginary parts (ε_r'') of complex permittivity of the composites are shown in figure 5.5(a) and figure 5.5(b) with increase of EG wt. %. ε_r' decreases linearly with increasing frequency for all the compositions. The ε_r' values increases from 5 wt. % to 10 wt. % and for further increase in EG weight % the values starts decreasing from 20 wt. % to 50 wt. % EG wt. % in the composites. The real part of permittivity spectra is tabulated in table 5.1.

Table 5.1 Variation of ε_r' values of EG-NPR composites

wt. % of EG-NPR composites	Real permittivity (ε_r')	
	at 8.2 GHz	at 12.4 GHz
5 wt. %	4.7	2
7 wt. %	6.2	4
8 wt. %	6.8	4.8
10 wt. %	8.6	7.7
20 wt. %	7.1	6.6
30 wt. %	4.9	3.5
40 wt. %	4.9	3.5
50 wt. %	4.9	3.5

With increase in EG wt. % in the composite the ε_r'' values increases over the test frequency range. As seen in plot figure 5.5(b). The ε_r'' spectra for 5 wt. % shows almost a constant value of ~1.0 till 11.5 GHz and at 12.4 GHz a resonance peak is observed with ε_r''~ 1.9. With increase in the EG wt. % the values of ε_r'' increases and the resonance peak values of 1.9, 2.07, 2.5 and 3.42 are observed at 12.4 GHz, 12.0 GHz, 11.16 GHz and 9.7 GHz for 5, 7, 8 and 10 wt. % composites, respectively. The ε_r'' spectra for 20 wt. % to 50 wt. % show a

decreasing trend with increase in frequency with maximum values of ~6.2 at 8.2 GHz to minimum value of ~4 at 12.4 GHz for 50 wt. % composite.

The EG/NPR composite is a heterogeneous system consisting of NPR as insulating section and EG as conducting section, with EG encapsulated within the polymer. The insulating sections acts like a high resistive path for flow of free electrons, however some electrons may still conduct by tunneling effect [14]. Within the composite system, there could be two paths of electromagnetic propagation as shown in figure 5.6. In one path, line of electric flux can pass from EG flakes-polymer-EG flakes and in the other path through direct contact between the EG flakes. This is in analogy to reference [15] where M. Matsumoto and Y. Miyata have discussed a model for metal-polymer composite, with filler conductivity of ~10^4S/cm.

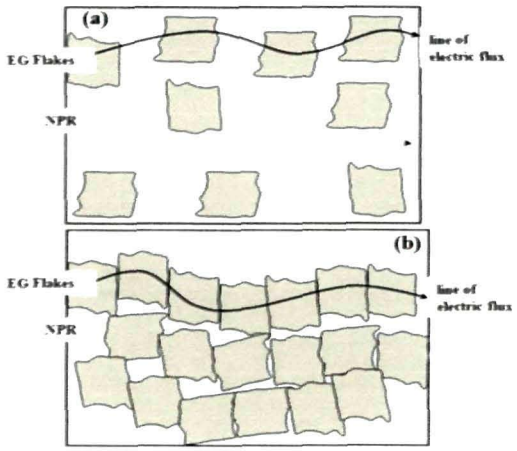

Figure 5.6 Schematic diagram of electromagnetic propagation within the composite system

The first path of conduction is effective for composites with lower EG percentages, forming interfacial polarization and probably leads to the loss mechanism due to the associated relaxation phenomenon. EG flakes have π–electrons that can travel freely within the flakes and accumulate at the EG-NPR interface, forming a structure similar to a boundary-layer capacitor which generates the interfacial electric dipolar polarization [16], which may increase the loss. The second path of conduction, however, will be more

effective for higher filler concentration which increases the interaction between the fillers. As EG conductivity is quite high as compared to polymer, increasing EG content increases the effective conductivity which in turn increases the loss factor ε_r''. In the same reference [15], the modeling done for higher concentration metal particles embedded in polymer matrix showed a decreasing trend for real and imaginary part of permittivity with frequency, as is observed in EG-NPR composite system.

The computation of complex permeability of EG-NPR composites is found to be of a constant value of real part ($\mu_r' \approx 1$), and imaginary part ($\mu_r'' \approx 0$) over the entire X band frequency confirming that the composites are non-magnetic in nature.

5.3.3 Analysis of calculated dielectric loss tangent

The dielectric loss tangent $\left(tan\delta_e = \varepsilon_r'' / \varepsilon_r'\right)$ of the developed composites is calculated using the measured value of ε_r' and ε_r'' over the X band. Figure 5.7 shows the frequency dependent $tan\delta_e$ variation for different (5, 7, 8, 10, 20, 30, 40 and 50) wt. % EG-NPR composites. The $tan\delta_e$ spectra for 5 wt. % composites shows a constant value ~ 0.22 from 8.2 GHz to ~11.6 GHz and then abruptly increase to a maximum value ~0.89 at 12.4 GHz correspondence to the resonance peak of ε_r'' spectra for 5 wt. % composite. The $tan\delta_e$ spectra for 7, 8 and 10 wt. % composites show that the maximum $tan\delta_e$ peak decreases and shifts to lower frequencies of 12.0 GHz, 11.16 GHz and 9.7 GHz, respectively. The composites from 20 wt. % to 50 wt. % EG show a linear increasing trend with EG wt. %, however, the compositions show constant value $tan\delta_e$ over the X-band. A $tan\delta_e$>1 is observed for the 30, 40 and 50 wt. % compositions with maximum value of ~1.20 for 50 wt. %. Dielectric loss greater than unity suggest that the material has high dissipation factor rather than storage capacity. From the dielectric loss spectra for the composites it is seen that the developed EG-NPR composites have the potential characteristics for microwave absorption.

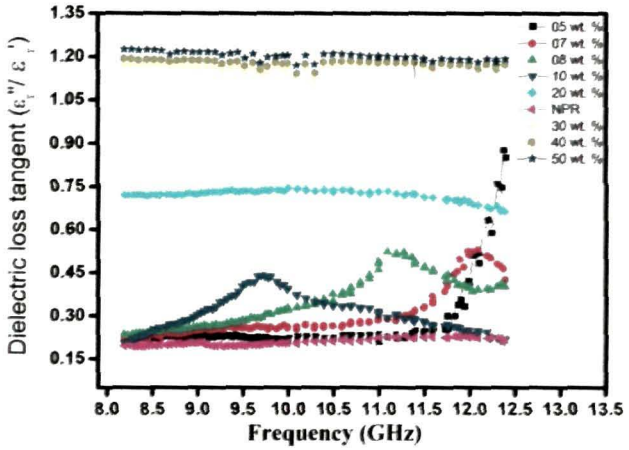

Figure 5.7 Dielectric loss tangent spectra of EG-NPR composites over the X-band

5.3.4 Analysis of calculated attenuation constant

The attenuation constant (α) of the developed EG-NPR composites is calculated from the measured value of ε_r' and ε_r'' over the X band using the equation (2.53)

$$\alpha = \frac{\sqrt{2}\pi f}{c}\sqrt{(\mu_r''\varepsilon_r'' - \mu_r'\varepsilon_r') + \sqrt{(\mu_r''\varepsilon_r'' - \mu_r'\varepsilon_r')^2 + (\varepsilon_r'\mu_r'' + \varepsilon_r''\mu_r')^2}} \quad (5.14)$$

Figure 5.8 shows the values of α for 5, 7, 8, 10, 20, 30, 40 and 50 wt. %EG as a function of frequency. The plot indicates increase α for higher EG loadings. Increase in attenuation can be attributed to conduction loss, dielectric relaxation and interfacial polarization [17, 18]. Conduction loss is due to directional motion of charge carriers and is dependent on composites conductivity. Dielectric relaxation occurs because of the orientation polarization of intrinsic dipoles. Presence of conducting EG in insulating NPR produce interfacial polarization. Higher percentages of EG increase these properties and consequently attenuation increases. It is also observed that a maximum value of attenuation is achieved for 5 wt. %, 7 wt. %, 8 wt. % and 10 wt. % EG/NPR composites at 12.4, 12, 11 and 9.5 GHz, respectively. The composite with 20, 30, 40 and 50 wt. % shows a value of high attenuation constant over the entire X band, which may be due to high conduction loss.

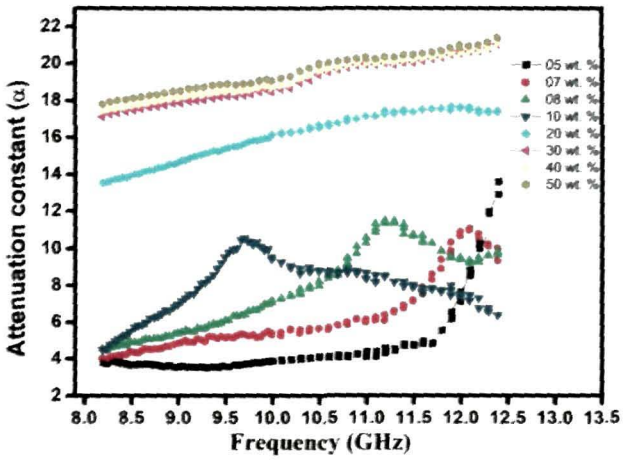

Figure 5.8 Attenuation constant spectra of EG-NPR composites over the X-band

5.3.5 Analysis of microwave conductivity

The electrical conductivity (σ) of the EG-NPR composites in microwave frequencies is calculated by using the equation, $\sigma = 2\pi f \varepsilon_0 \varepsilon_r''$, where f is the microwave frequency, ε_0 is the permittivity of free space ($\varepsilon_0 = 8.854 \times 10^{-12}$ F m^{-1}) and ε_r'' is the measured imaginary permittivity[19]. Microwave conductivity of 5, 7, 8, 10, 20, 30, 40 and 50 wt. % EG-NPR composites plotted against frequency is shown in figure 5.9. It is observed that σ increases with increases of EG wt. % in the composites. The 5 wt. % composite shows almost a constant value ~0.5 S/m from 8.2 GHz till 11 GHz and then gradually increases to a maximum ~1.4 S/m at 12.4 GHz, however for 7, 8 and 10 wt. % EG-NPR composites the maximum peak value of σ is shifted towards lower frequency with increase in wt. %. The maximum peak for 7 wt. %(σ~1.4 S/m), 8 wt. %(σ~16 S/m) and 10 wt. %(σ~1.8 S/m) is observed at 12 GHz, 11.2 GHz and 9.6 GHz respectively. For higher compositions 20, 30, 40 and 50 wt. %, the σ graph is almost constant over the X-band, though it increases with EG wt. %. The EG-NPR composites system have conducting EG flakes and insulating NPR and can be described by a parallel resistor-capacitor circuit model [19]. For lower EG wt. % compositions

the ease of electrical conduction is hindered by insulating phase but with increase in wt. %, EG flakes form a continuous conductive network and ease of electrical conduction is enhanced, as shown in figure 5.6, Also, a capacitive behavior occurs between faces of EG flakes and NPR. The capacitance, C, of a single capacitor is directly proportional to the surface area and inversely proportional to the distance between EG faces. With increases of EG wt. % the distance between the faces decrease and the surface area increases, thus the capacitance for higher wt. % composites enhances [20]. The capacitance impedance ($Z_c = 1 / j2\pi fC$) reduces as the value of C increases [21] and hence facilitates microwave conduction easily for higher wt. % EG-NPR composites.

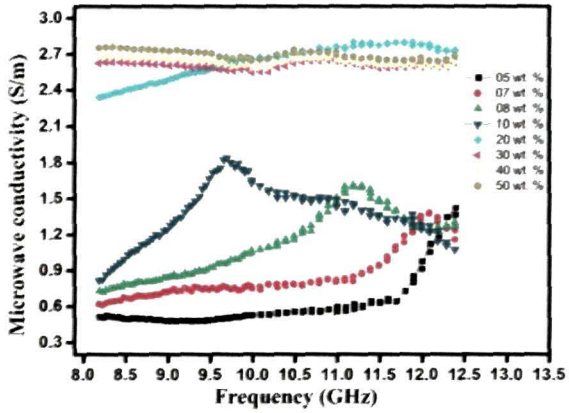

Figure 5.9 Microwave conductivity of EG-NPR composites over the X-band

5.4 SUBSTANTIATION OF PERMITTIVITY VALUE- BY CAVITY RESONATOR TECHNIQUE

The complex permittivity of the EG-NPR composites measured so far is substantiated by cavity perturbation technique [8, 22, 23]. A TE_{103} cavity is designed at 9.9 GHz to measure the complex permittivity of the composites. An iris is used to couple the oscillations excited within the cavity with outside microwave measurement system as shown in figure 5.10(a). The diameter of iris hole for critical coupling in the cavity is found to be 8.42 mm. The quality factor (Q) of the cavity is obtained by sweeping the cavity in the frequency

range 8.2 GHz to 12.4 GHz using Agilent E8362C VNA as shown in figure 5.10(b).

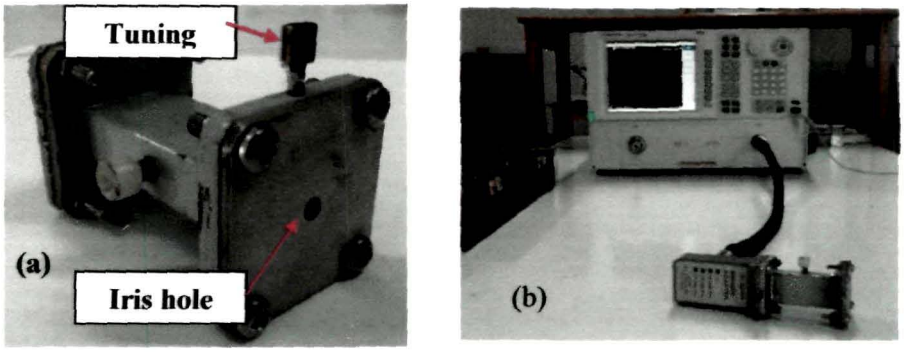

Figure.5.10 (a) A TE103 rectangular resonant cavities with tuning screw and iris hole

(b) Cavity perturbation measurement of complex permittivity

During microwave excitation of the cavity, a frequency shift (both +ve and -ve) takes place from the design frequency due to mismatch. A tuning screw is incorporated into the cavity to remove this mismatch,(figure 5.10). The Q of the cavity is calculated using the formula given as

$$Q = \frac{\text{Re}\,sonant\ frequency}{3dB\ band\ width} = \frac{f_r}{(f_2 - f_1)} \tag{5.14}$$

f_2 and f_1 are the frequencies corresponding to 3 dB point, such that $f_2 > f_1$ and f_r is the resonant frequency. The Q for the TE_{103} reflection cavity is experimentally found to be 1833.52.

The EG-NPR composite sample of dimension $1mm^3$ sizes is inserted into the TE_{103} cavity at the maximum electric field position using a Teflon sample holder. On insertion of the samples, the resonant frequency of empty cavity and Q factor alters due to change in the overall capacitance and conductance of the cavity without perturbing the inductance [23]. If f_1 and f_0 are the resonant frequencies with and without the samples, the **real** (ε_r') and **imaginary part of permittivity** (ε_r'') are given by [24]

$$\epsilon_r' = 1 + \frac{f_0^2 - f_1^2}{f_1^2}\frac{V_c}{4V_s} \quad (5.15)$$

$$\epsilon_r'' = \frac{V_c}{4V_s}\left[\frac{f_0^2}{f_1^2}\left(\frac{1}{Q_1} - \frac{1}{Q_0}\right)\right] \quad (5.16)$$

where, V_S is the volume of the sample, V_C is the volume of the cavity, Q_1, Q_0 are the respective quality factors (Q) of the cavity with and without the sample. Through this technique microwave characterization can be done for only one frequency corresponding to resonant frequency of the cavity.

The measured values of ε_r' and ε_r'' of different EG-NPR composites are tabulated in table 5.1 and compared with the values obtained from Nicolson Ross Method at 9.9 GHz. The real and imaginary part of the complex permittivity the composite samples from both the techniques are comparable.

Table 5.2 Complex permittivity of developed EG-NPR composite at 9.9 GHz

Sample	At 9.9 GHz			
	Cavity perturbation technique		Nicolson Ross technique	
	ε_r'	ε_r''	ε_r'	ε_r''
NPR	2.47	0.76	2.53	0.8
5 wt. % EG-NPR	4.48	0.89	4.5	0.92
7wt. % EG-NPR	5.21	1.36	5.2	1.4
8 wt. % EG-NPR	5.76	1.74	5.8	1.85
10 wt. % EG-NPR	7.66	3.08	7.71	3.17
20 wt. % EG-NPR	6.33	4.23	6.41	4.68
30wt. % EG-NPR	3.89	4.54	4.03	4.7
40wt. % EG-NPR	3.86	4.63	4.02	4.83
50 wt. % EG-NPR	3.75	4.78	4.01	4.91

5.5 CONCLUSIONS

Microwave characterization of EG-NPR composites are performed over the X-band. The complex permittivity and permeability are computed from measured values of S_{21} and S_{11} using Nicolson Ross method. The results obtained from this method are substantiated by cavity resonator method and found to be in close proximity. The real permittivity ε_r' increases linearly from 5 to 10 wt. % but further increase in EG wt. % decreases its value. Enhancement of ε_r'', is observed with increase in EG percentage in NPR. Both real and imaginary part of complex permittivity shows a decreasing trend with frequency. The complex permeability measurement shows the real part is closed to unity and imaginary part equals to zero confirming the composite to be purely dielectric. Dielectric loss tangent ($tan\delta_e$), attenuation constant (α) and microwave conductivity (σ) are calculated using the measured values of ε_r' and ε_r''. Composite with higher EG concentration in matrix shows higher loss. α and σ values shows an increase with EG wt. % in the composites.

The complex permittivity studies conducted on developed EG-NPR composite shows its potential to be used as microwave absorbing material for applications over the X-band.

References

[1] Hajian, M., Mathew, K. T., and Ligthart, L. P., Measurement of complex permittivity with waveguide resonator using perturbation technique, *Microwave and Optical Technology Letters.* **21**, 269-272, 1999.

[2] Murthy, V. R. K., Sunderam, S., and Viswanathan, B. *Microwave Materials*, Narosa Publishing House, New Delhi, 1990.

[3] Chen, L. F., Ong, C. K., Neo, C. P., Varadan, V. V., and Varadan, V. K. *Microwave Electronics Measurement and Material Characterization*, John Willey and Sons, West Sussex, England, 2004.

[4] Yamashita, E., Atsuki, K., and Hirahata, T. Microstrip dispersion in a wide frequency range, *IEEE Trans. Microw. Theory Tech.* **29**, 610-611, 1981.

[5] Yamashita, E., Atsuki K., and Ueda, T., An approximate dispersion formula of microstrip lines for computer aided design of microwave integrated circuits, *IEEE Trans. Microw. Theory Tech.* **27**, 1036-1038, 1979.

[6] Al-Moayed, N. N., Afsar, M. N., Khan, U. A., McCooey, S., and Obol, M. Nano ferrites microwave complex permeability and permittivity measurements by T/R technique in waveguide, *IEEE Transactions on Magnetics* **44**, 1768-1772, 2008.

[7] Jarvis, J. B., Vanzura, E. J., and Kissick, W. A. Improved technique for determining complex permittivity with the transmission/reflection method, *IEEE Trans. Microw. Theory Tech.* **38**, 1096-1103, 1990.

[8] Carter, R. G. Accuracy of microwave cavity perturbation measurements, *IEEE Trans. Microw. Theory Tech.* **49**, 918-923, 2001.

[9] Chao, S. H. Measurements of microwave conductivity and dielectric constant by the cavity perturbation method and their errors, *IEEE Trans. Microw. Theory Tech.***33**, 519-526, 1985.

[10] Krupka, J. Frequency domain complex permittivity measurements at microwave frequencies, *Meas. Sci. Technol.* **17**, 55-70, 2006.

[11] Nicolson, A.M., and Ross, G.F. Measurement of the intrinsic properties of materials by time-domain techniques, *IEEE. T. Instrum. Meas.* 19, 377-382, 1970.

[12] TRL/LRM Calibration, Agilent E5070B/E5071B ENA Series RF Network Analyzers,1st Edition, Agilent Technologies, No. 16000-95026, Japan, 2004

[13] Engen, G. F., and Hoer, C. A. Thru-reflect-line: An improved technique for calibrating the dual six-port automatic network analyzer, *IEEE Trans. Microw. Theory Tech.* **27**, 987-993, 1979.

[14] Zheng, W., Wong, S. C., and Sue, H. J. Transport behavior of PMMA/expanded graphite nanocomposites, *Polymer* **43**, 6767-73, 2002.

[15] Matsumoto, M., and Miyata, Y. Complex permittivity based on equivalent circuit model for polymer/metal composite frequency dependence of permittivity as function of concentration, *IEEE Trans Dielectr Electr Insul* **6**, 27-34, 1999.

[16] Zhang, X.F., Guan, P.F., and Dong, X.L., Multidielectric polarizations in the core/shell Co/graphite nanoparticles, *Appl. Phys. Lett.* **96**, 223111-223113, 2010.

[17] Paton, K.R., and Windle, A.H. Efficient microwave energy absorption by carbon nanotubes, *Carbon* **46**, 1935-1941, 2008.

[18] Duan, Y., Liu, S., Wen, B., Guan, H., and Wang, G. A discrete slab absorber: absorption efficiency and theory analysis, *J. Compos. Mater.* **40**, 1841-1851, 2006.

[19] Zhai, Y., Zhang, Y., and Ren, W. Electromagnetic characteristic and microwave absorbing performance of different carbon-based hydrogenated acrylonitrile-butadiene rubber composites, *Materials Chemistry and Physics* **133**, 176- 181, 2012.

[20] Mohanraj, G.T., Chaki, T.K., Chakraborty, A., Khastgir, D. AC impedance analysis and EMI shielding effectiveness of conductive SBR composites, *Polym. Eng. Sci.* **46**, 1342-1349, 2006.

[21] Micheli, D., Apollo, C., Pastore, R., and Marchetti, M. X-Band microwave characterization of carbon-based nanocomposite material, absorption capability comparison and RAS design simulation, *Compos. Sci. Technol.* **70**, 400–409, 2010.

[22] Sunny, V., Kurian, P., Mohanan, P., Joy, P.A., and Anantharaman, M.R. A flexible microwave absorber based on nickel ferrite nanocomposite, *Journal of Alloys and Compounds* **489**, 297-303, 2010.

[23] Borah S. *Study of microstrip transmission line and adaptable radial stub resonator on nickel substituted cobalt ferrite/ LDPE nanocomposite as magneto – dielectric substrate at X- band,* Ph. D. Thesis, Tezpur University, India, 2011.

[24] Ku, H. S., Ball, J. A. R., Siores, E., and Horsfield, B. Microwave processing and permittivity measurement of thermoplastic composites at elevated temperature, *Journal of Materials Processing Technology.* **89-90**, 419-424, 1999.

CHAPTER VI

DESIGN OF SINGLE LAYER MICROWAVE ABSORBER: THICKNESS OPTIMIZATION AND REFLECTION LOSS MEASUREMENT OVER THE X-BAND

6.1 INTRODUCTION

The main requirements of microwave absorber are low reflection at the interface layer with the air and high attenuation within the absorber of the incident microwave signal. To realize the conditions, the primary requirement is that the absorbing materials should be lossy in nature [1-3]. However as discussed in the chapter II section 2.2, a high lossy material also reflects the microwave signal incident from free space due to impedance mismatch at the air-absorber interface [4]. To obtain a low reflecting surface with attenuating characteristics, proper designing of microwave absorber is required. Microwave characterization discussed in chapter V show that the developed EG-NPR composites can be potentially used as microwave absorbing materials over the X-band.

In this chapter, theoretical calculation of reflection loss of 5, 7, 8, 10, 20, 30, 40 and 50 wt. % EG-NPR composites are studied with optimized thickness for each composition. Based on the theoretical results a practical design structure of single layer Dallenbach absorber is developed and tested for free space microwave absorption over the entire X-band.

6.2 MICROWAVE ABSORPTION REQUISITES

Minimization of reflection

The reflection phenomenon mainly occurs at two location; firstly at the air-absorber interface and secondly from the metal backing of the RAM. Technically, reflection at the interface can be minimized by making input impedance of RAM close to that of free space. The input impedance at the air-RAM interface is determined from the equation [1],

$$Z_{in} = Z_0\sqrt{\mu_r/\varepsilon_r}\tanh[j(2\pi fd/c)\sqrt{\varepsilon_r\mu_r}]$$

where, Z_0=377 Ω.

The expression shows the dependence of Z_{in} on RAM material properties viz. the complex permittivity, ε_r (= $\varepsilon_r' - j\varepsilon_r''$), complex permeability μ_r (=$\mu_r' - j\mu_r''$), and external parameters like the thickness, d, of the RAM and incident microwave frequency, f.

Realization of impedance matching condition between the RAM and the free space interface, the ratio of μ_r'/ε_r' should approach to unity [1]. For a EG-NPR dielectric composite μ_r =1- j.0, the intrinsic tunable parameter to achieve impedance matching, is by making ε_r' close to unity.

Enhancing attenuation

Within the composite, microwave energy decays exponentially with distance y by factor $e^{-\alpha y}$ where the attenuation constant (α) as described in Chapter II section 2.2 is reduced to

$$\alpha = \frac{\sqrt{2}\pi f}{c} \times \sqrt{(-\varepsilon_r^{'}) + \sqrt{(-\varepsilon_r^{'})^2 + (\varepsilon_r^{''})^2}}$$

The expression indicates that attenuation of microwave power increases with ε_r and since the real part (ε_r') is the constrained by the condition for low reflection at the interface, for increasing attenuation the imaginary part (ε_r'') can only be enhanced.

Thickness Considerations

Effective reflected wave can be minimized by reducing the reflected wave from the front-face interface and from the back face (absorber-metal) interface which can be achieved by phase cancellation following the principle of destructive interference. [5-9] One type of microwave absorber design is a Dallenbach absorber[6] in which a quarter wavelength thickness of absorbing layer, composed of homogenously distributed lossy reinforcers, is placed on a

metal plate. The thickness which depends on the operating frequency is an important parameter for the design of the absorber (Chapter II, Section 2.4).

6.3 REFLECTION LOSS FROM COMPLEX PERMITTIVITY VALUES WITH THICKNESS OPTIMIZATION

From the transmission line model (TLM), referred in chapter II, the input impedance at the air-absorber interface of a single layer absorber backed by a perfect electric conductor (PEC) as shown in figure 6.1, is given[10-13] as

$$Z_{in} = \eta_0\sqrt{\mu_r / \varepsilon_r}\, tanh\,(j2\pi f/c)\sqrt{\mu_r\varepsilon_r}d \tag{6.1}$$

Where $\eta = \eta_0\sqrt{\mu_r / \varepsilon_r}$ (6.2)

$$\gamma = j(2\pi f / c)\sqrt{\mu_r\varepsilon_r} \tag{6.3}$$

$$\mu_r = \mu'_r - j\mu''_r \tag{6.4}$$

$$\varepsilon_r = \varepsilon'_r - j\,\varepsilon''_r \tag{6.5}$$

The reflection loss (dB) of the single layer absorber can be expressed as

$$RL_c = 20\log\left|\frac{Z_{in}-\eta_0}{Z_{in}+\eta_0}\right| \tag{6.6}$$

or

$$RL_c = 20\log\left|\frac{\eta_0\sqrt{\mu_r/\varepsilon_r}\, tanh\,(j2\pi f/c)\sqrt{\mu_r\varepsilon_r}d-\eta_0}{\eta_0\sqrt{\mu_r/\varepsilon_r}\, tanh\,(j2\pi f/c)\sqrt{\mu_r\varepsilon_r}d+\eta_0}\right| \tag{6.7}$$

or

$$RL_c = 20\log\left|\frac{\sqrt{\mu_r/\varepsilon_r}\, tanh\,(j2\pi f/c)\sqrt{\mu_r\varepsilon_r}d-1}{\sqrt{\mu_r/\varepsilon_r}\, tanh\,(j2\pi f/\,)\sqrt{\mu_r\varepsilon_r}d+1}\right| \tag{6.8}$$

In the present study, the values of complex permeability for all the developed composites are found to be, $\mu'_r = 1\ and\ \mu''_r = 0$, and the equation (6.8) is reduced to

$$RL_c = 20\log\left|\frac{\sqrt{1/\varepsilon_r}\, tanh\,(j2\pi f/c)\sqrt{\varepsilon_r}d-1}{\sqrt{1/\varepsilon_r}\, tanh\,(j2\pi f/c)\sqrt{\varepsilon_r}d+1}\right| \tag{6.9}$$

Equation (6.9) shows that RL_c value depends on the complex permittivity and thickness of the composite material. For a fixed composition of EG-NPR composite and a single absorbing layer, the absorption can be further enhanced by optimizing the thickness (d).

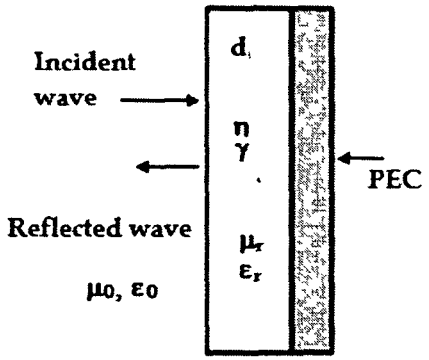

Figure 6.1 Design structure of conductor backed single layer absorber

A MATLAB program is developed based on equation (6.9) to estimate the minimum RL_c value for different EG-NPR composites by varying thickness, d, over the X-band.

The algorithm of the program is as follows:

Step 1: Read data from file.

Step 2: For each frequency from 8.2 GHz to 12.4 GHz at the step size of 0.02 GHz, calculate RL_c for each frequency for a fixed thickness. Store data and calculate RL_c for the other frequencies of the same thickness.

Step 3: Repeat step 2 for other thickness and store the data.

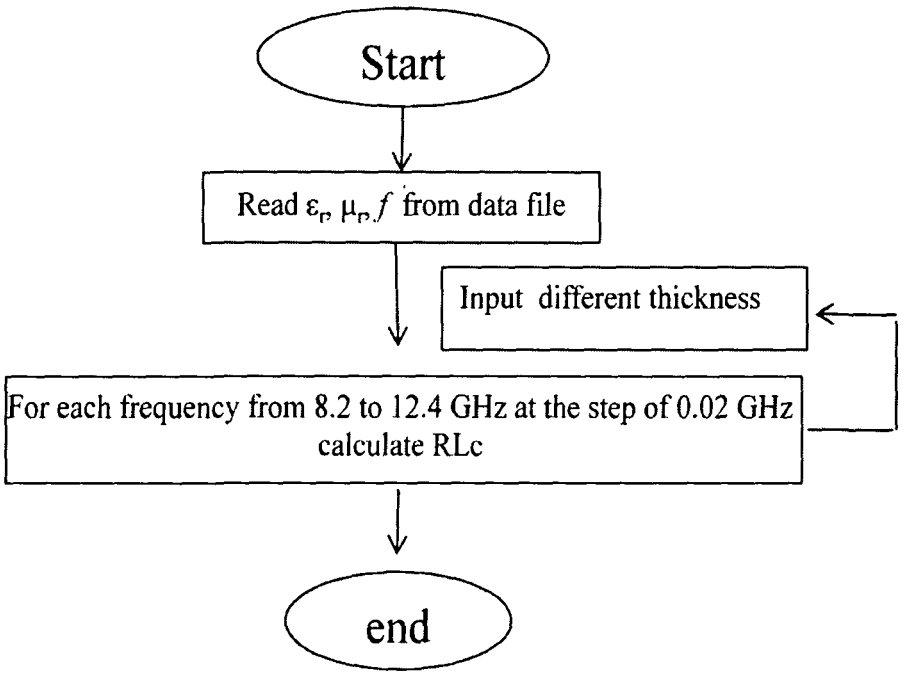

Figure 6.2 Flow chart for single layer absorber program

6.3.1 COMPUTED REFLECTION LOSS

The reflection loss, RL_c values of conductor backed (5, 7, 8, 10, 20, 30, 40 and 50) wt. % EG-NPR composites with different thickness (d=2, 4, 6 mm) are calculated as a function of frequency over the X-band. Most applications of microwave absorber, especially for strategic defense, the optimum thickness required are about 4mm [14], hence the thickness is varied within 2 to 6mm limit. Figure 6.3 shows the frequency dependent calculated RL_c, real and imaginary impedance values of the developed composites of 2 mm thickness in the frequency range 8.2 GHz to 12.4 GHz. It is seen from figure 6.3(a) that RL_c >-10dB for all the composites except 20 wt. % EG is observed, which is due to impedance mismatch at the air-substrate interface and makes the surface more reflecting. According to equation (6.1), minimum reflection takes place when the real input impedance, Z_{in}' approaches 377Ω and the

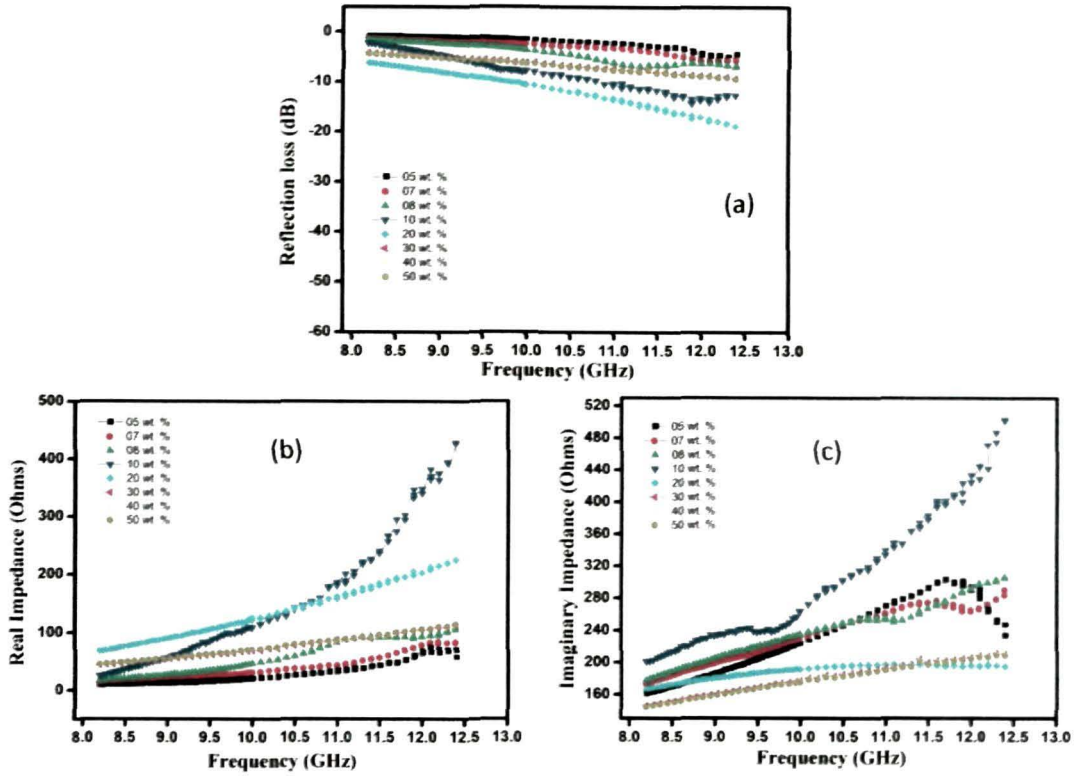

Figure 6.3 Calculated (a) reflection loss, (b) real impedance and (c) imaginary impedance of 2mm thickness single layer EG-NPR composites absorber design

corresponding imaginary input impedance; Z_{in}'', approaches zero Ω [15]. Figure 6.3 (a) and (b), indicates that the real and imaginary impedance of the composites are not approaching to the matching criteria simultaneously over the entire X-band. Hence the values of RL_c for 2 mm thickness EG-NPR composites are very low for all the compositions. The RL_c values of 4 mm thickness absorber design is shown in the figure 6.4(a), where RL_c~-53 dB is observed for 5 wt. % composition at 12.4 GHz. The RL_c peaks show a shift towards the lower frequency with decrease in the value as EG concentration in the composite increases. 7 wt. %, 8 wt. % and 10 wt. % EG-NPR composite show a maximum RL_c~–27 dB, -20dB and -10 dB with peaks at 12 GHz, 11 GHz and 9.5 GHz, respectively. However 20 wt. % composites show a

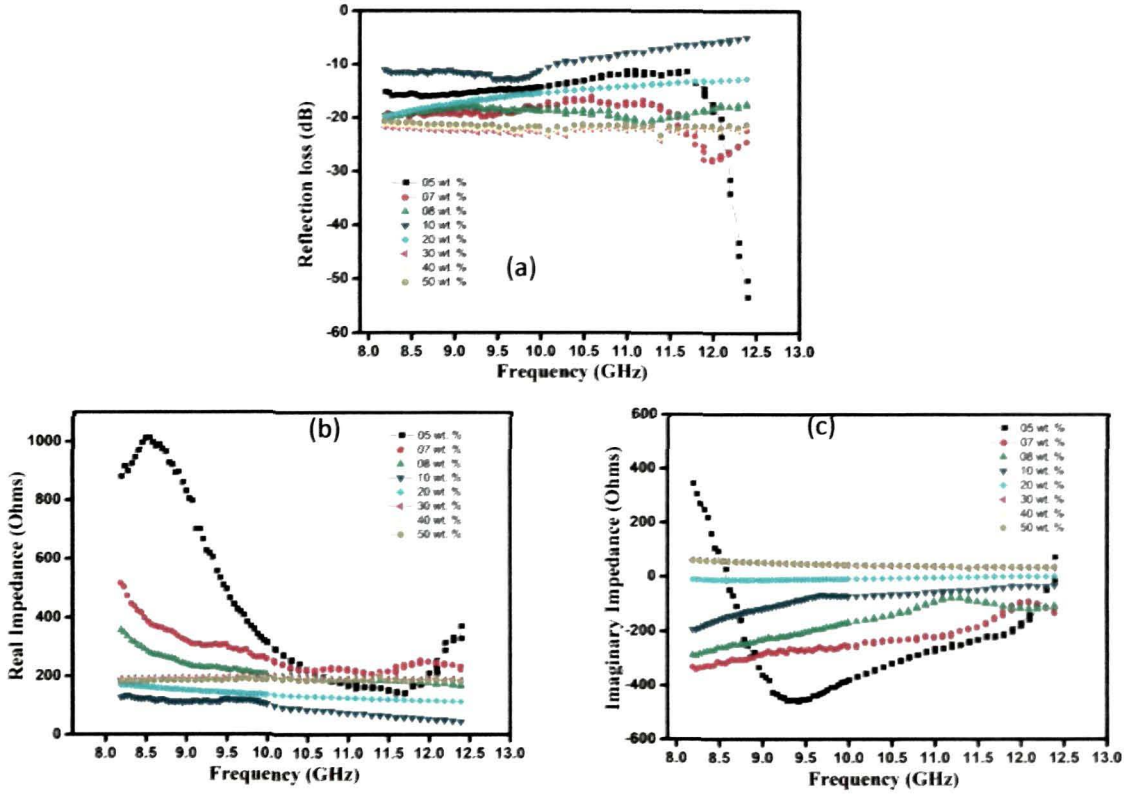

Figure 6.4 Calculated (a) reflection loss, (b) real impedance and (c) imaginary impedance of 4mm thickness single layer EG-NPR composites absorber design

constant RL_c ~ 13dB and 30 wt. %, 40 wt. % and 50 wt. % composites show RL_c~-20dB over the entire X-band. Analyzing the impedance matching condition for these compositions of 4 mm thickness, it is seen from figure 6.4(b) and (c) that at 12.4 GHz, Z_{in}' and Z_{in}'' for 5 wt. % composite are found to be 375 Ω and 75 Ω respectively which is the closest to the required values of 377 Ω and 0 Ω. Hence the best impedance matching is observed at 12.4 GHz with RL_c~ -53dB for this composition. For other compositions of 7 wt. %, 8 wt. % and 10 wt. %, the maximum impedance matching condition occurs at 12 GHz, 11 GHz and 9.5 GHz, respectively, although the values of Z_{in}' and Z_{in}'' are not too close to that of free space impedance. The reflection loss graphs of the composites with 6 mm thickness absorber design are shown in figure

6.5(a). A RL_C >-10 dB is observed for composites from 5 to 20 wt. % EG over the X-band, except for 5 wt. % composites at 12.4 GHz, RL_C is found to be ~22dB.

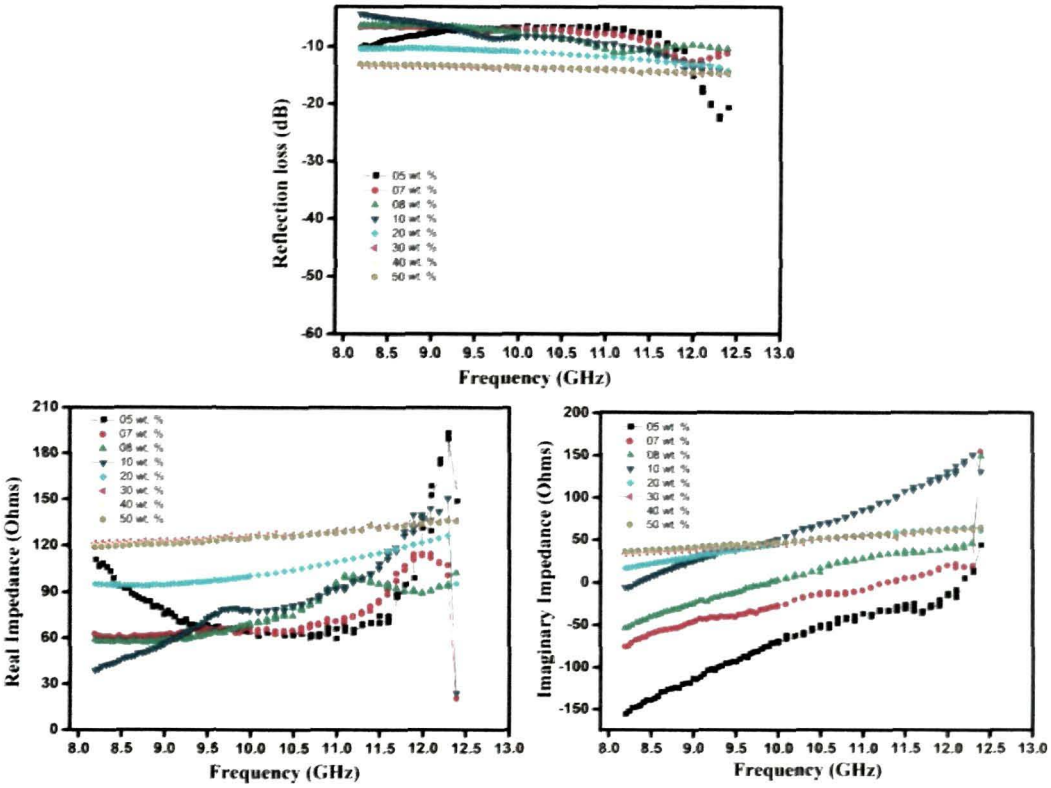

Figure 6.5 Calculated (a) reflection loss, (b) real impedance and (c) imaginary impedance of 6mm thickness single layer EG-NPR composites absorber design

Composites from 30 to 50 wt. % EG show almost a constant RL_C~-12dB over the X-band. Real and imaginary impedance graphs elucidated in figure 6.5 (b) and (c) respectively, shows that none of the composites approached the impedance matching condition of real part →377Ω and imaginary part →zero simultaneously over the entire frequency range. Hence, the composites with 6 mm thickness single layer absorber gives a low value of RL_C in the frequency range of 8.2 GHz to 12.4 GHz.

The above discussion corroborated that the effect of thickness parameters in designing a single layer absorber is very crucial. As compared

to 2mm and 6mm thickness, 4mm sample shows good RL_c over the test frequency range. The absorber thickness relates to the frequency of operation in a single layer absorber which is basically resonant in nature [16]. Maximal microwave absorption occurs at matching thickness, d_m, when d_m equals to an odd multiple of $\lambda_m / 4$ where $\lambda_m / 4 = \lambda_0 / (|\varepsilon_r||\mu_r|)^{1/2}$, the condition for phase cancellation [17]. Referring to 4 mm thickness absorber design, reflection loss graph (figure 6.4(a)), a maximal microwave absorption or reflection loss occurs at 12.4 GHz for 5 wt. % composition. Calculating the value of d_m for this composite at 12.4 GHz, it is found to be 3.6 mm which is closed to 4 mm, and hence RL_c~-53dB is obtained. Other composites of 7, 8 and 10 wt. % EG showing RL_c~-27 dB, -20 dB and -10 dB at 12 GHz, 11 GHz and 9.5 GHz have the calculated d_m values of 3.2mm, 3mm and 2.8 mm respectively.

Based on the theoretical results, a practical conductor backed single layer microwave absorber is designed using the developed EG-NPR composites and a thickness of 4mm is maintained for all the composites to justify the measured reflection loss value with the calculated RL_c

6.4 FREE SPACE REFLECTION LOSS MEASUREMENT

6.4.1 Measurement Technique

A schematic representation of free space reflection loss measurement is shown in figure 6.6. The microwave power is incident on the sample with dimension of 152 mm x 152 mm x 4 mm. The incident wave is partly reflected from the interface surface and partly absorbed [18, 19]. If P_{in} is the incident power density on the sample, P_R is the reflected power density and P_A is the absorbed power by the test sample, then

$$P_{in} = P_R + P_A \qquad (6.10)$$

If RL_m and A, are the measured reflection loss and the absorption loss in decibels (dB), respectively, then

$$RL_m = 10 \log P_R/P_{in} \quad (6.11)$$

$$A = 10 \log P_A/P_{in} \quad (6.12)$$

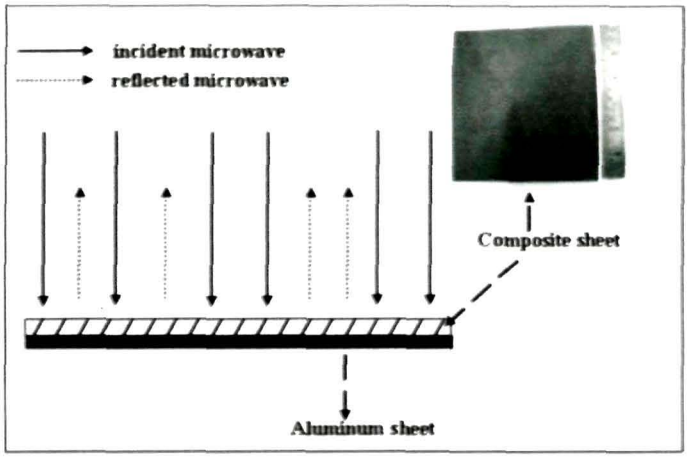

Figure.6.6 Schematic representation of microwave absorption measurement

Here, RL_m is a measure of the microwave-absorbing efficiency. More the absolute value of RL_m, higher the microwave absorption ability will be.

6.4.2 Measurement Setup

Free space microwave absorption test measurement system requires the sample of large dimension. Fabrication of a large size sample requires a fair amount of inclusions and matrix material. In laboratory scale, it is inconvenient to synthesize a large sample with uniformity. An effort is made to reduce the dimension of the test samples without compromising on the measurement standard. A pair of spot focusing horn lens antenna will focus the microwave radiation to a single spot at the focal point of the lens, so a small sample size situated at the focal point of the spot focusing lens will be sufficient to carry out the microwave absorption testing. The use of lens also

reduces the edge effect from the samples during the measurement. The schematic diagram of free space absorption measurement using spot focusing horn lens is shown in figure 6.7.

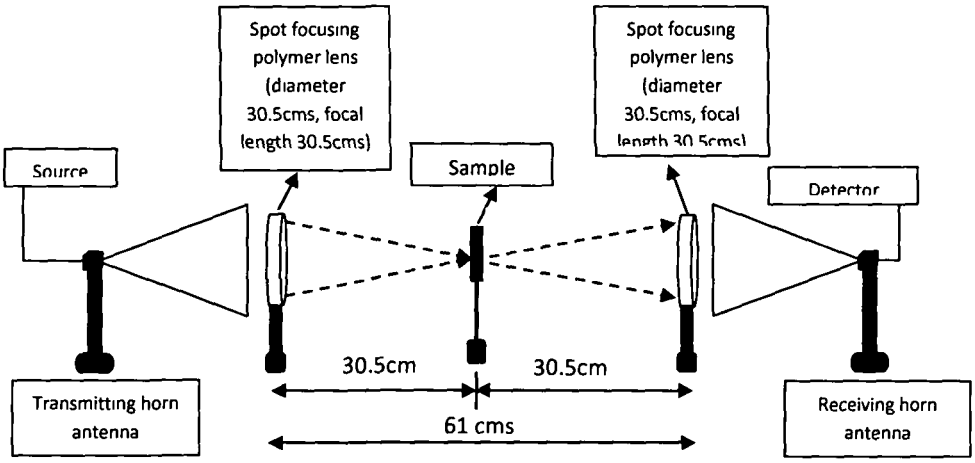

Figure.6.7 Schematic diagram of free space microwave absorption measurement using spot focusing horn lens antenna

Development of Spot Focusing Horn Lens Antenna

A plano-convex lens is designed based on the application of phase equivalence to a generally curved aperture connected to a planar surface as shown in figure 6.8. An expression which dictates the aperture profile can be derived in terms of the lens focal length f_L by applying the phase equivalence condition to figure 5.8 such that

$$\frac{\sqrt{(f_L+x)^2+y^2}}{v_0} = \frac{f_L}{v_0} + \frac{x}{v} \qquad (6.13)$$

Where v is the velocity of microwave in the material and is related to dielectric constant of the material as

$$v = \frac{v_0}{n} = \frac{v_0}{\sqrt{\varepsilon^r}} \qquad (6.14)$$

Using equation (6.13) and (6.14), the expression for lens profile is

$$x^2(n^2-1)+2f_L x(n-1)-y^2=0 \qquad (6.15)$$

An expression for the maximal axial thickness (d') can be found by assigning a value to the diameter of the lens and replacing the point (x, y) with (d, r), where, r, is the radius of the planar aperture.

$$d' = -\frac{f_L}{n+1}+\sqrt{\left(\frac{f_L}{n+1}\right)^2+\frac{r^2}{n-1}} \qquad (6.16)$$

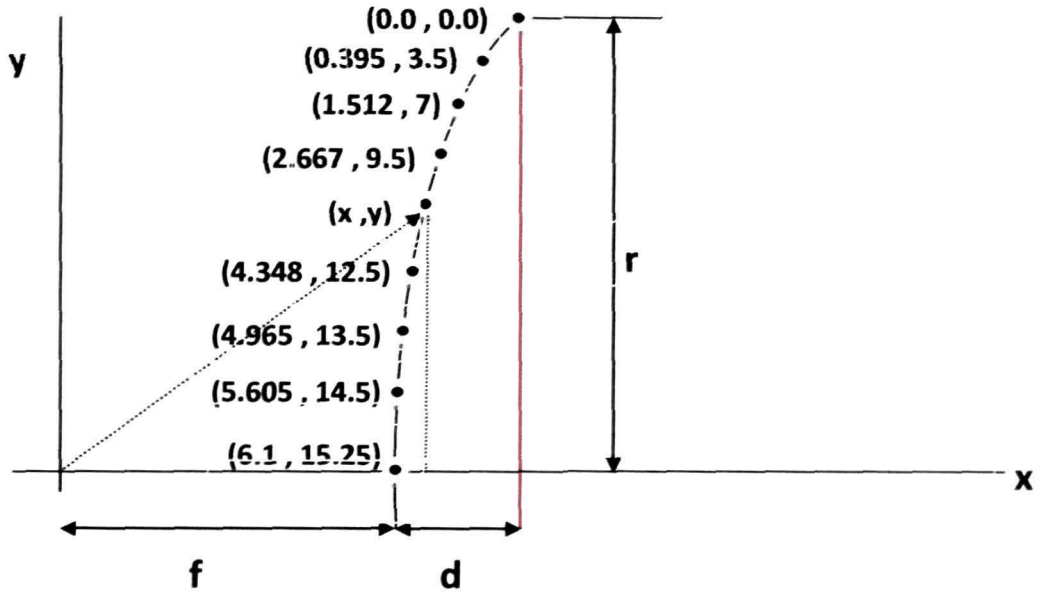

Figure.6.8 Upper half section of a general plano-convex lens system

Polyethylene with refractive index (n = 1.5 or $\varepsilon' = 2.25$) is used to make the lens. The focal length and diameter of the plano-convex lens (f_L) is kept at 30.5 cm. The tip of the lens is taken as r = 0 the axial thickness is also zero and at the centre, r = 15.25 cm the lens structure has maximal axial thickness. Axial lens thickness (d) corresponding to different (r) values is shown in the fig.6.8. Reference for the thickness is taken from the planar side (red line in the fig.6.8). The figure shows only the upper half section of the plano-convex lens system, the same design is to be repeated lower half section. Complete

dimension plano-convex lens is shown in figure 6.9. The fabricated spot focusing lens are mounted back to back to an X-band horn antennas such that the receiver, the sample and the transmitter lies in the same plane as shown in figure 6.7. The lens system is calibrated for maximum power along the x and y-axis. Figure 6.10 (a) and (b) shows the calibration graph of power variation along the pole axis and along the normal to the pole axis. A maximum power is observed at the focal point at a distance 30.5 cm from the lens along the pole axis.

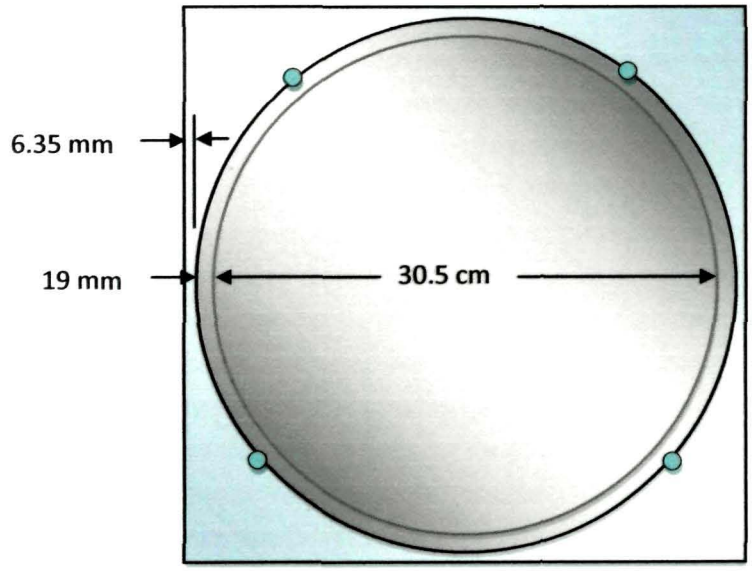

Figure.6.9 Frequency independent Plano convex lens and mounting scheme

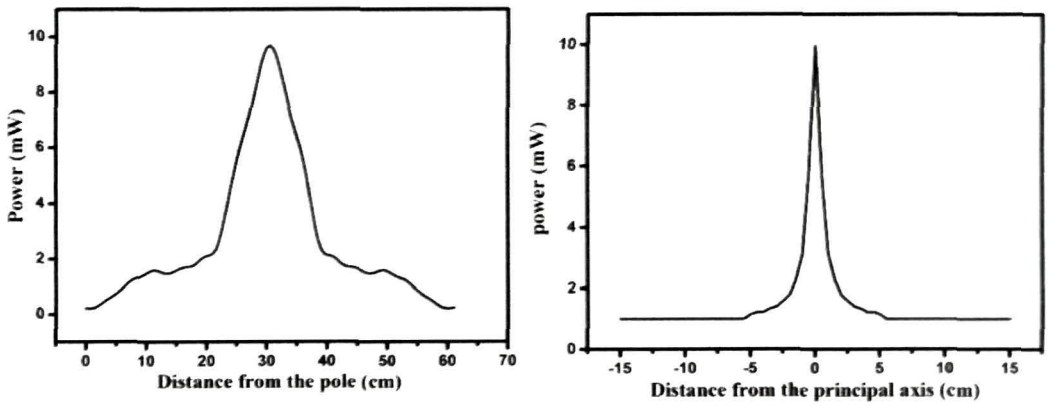

Figure.6.10 Calibration of the spot focusing lens (a) variation along the pole axis and (b) along the normal to the pole axis

6.4.3. Results and analysis of measured re lection loss value for single layer absorber

The photograph of free space microwave measurement set up is shown in figure 6.11. The set up consist of two spot focusing horn lens antennas connected to Agilent E8362C vector network analyzer using extendable cables and a sample holder between the lens to hold the absorber. The conductor backed EG-NPR sample is placed at the focal point of the lens system at a height of 15.25 cm from the base. Prior to RL_m measurements, the system is calibrated using Thru-Reflect-Line (TRL) method [20, 21]. The reflection loss of the designed absorbers is measured using the expression (6.11). Figure.6.12 shows the experimental results of RL_m for the EG/NPR composites in 8.4-12.4 GHz range. The composite with 5 wt. % EG shows maximum RL_m~-43 dB while the calculated RL_c~-53dB both being at 12.4 GHz which is in general agreement in terms of order of magnitude even though the values are not in close agreement. With increasing EG wt. % in the composite, the absorption peak shifts towards the lower end of X-band with reduced wave absorption ability. The RL_m values of -20dB, -16dB and -12 dB are observed for 7 wt.%, 8wt.% and 10wt.% EG with absorption peak at 12 GHz, 10.42 GHz and 9.75 GHz respectively, a trend found to be is as predicted by theory. It may be mentioned that a wide bandwidth absorption of at least -10dB is obtained (fig. 6.12) for 7 wt. %, 8 wt. % and 10 wt. % in the frequency ranges of 11.0 - 12.4 GHz, 9.8 - 11.2 GHz and 9.3 - 10.1 GHz respectively. Hence, for a small thickness of 4 mm, a wide absorption bandwidth can be obtained over different frequency ranges. However, unlike the computed values shown in figure 6.4, RL_m for 20 to 50 wt. % composite shows nominal values of ~-2 dB. It may be due to high in-plane electrical conductivity of the composites, as discussed in chapter IV, sub-section 4.4 which renders the surface reflecting. However, the S_{21} (dB) parameters tested for these composites of 20 to 50 wt. % EG are found to be high as shown in figure 6.13.

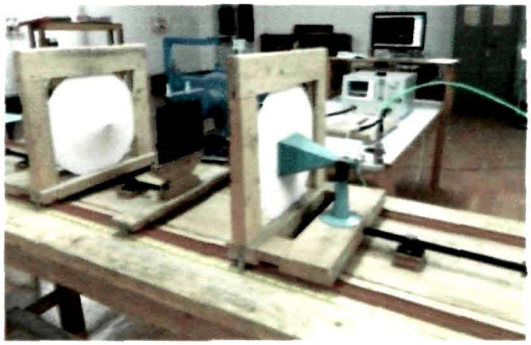

Figure.6.11 Free space microwave absorption testing of single layer (5 to 50 wt. %) EG-NPR composites over the X-band

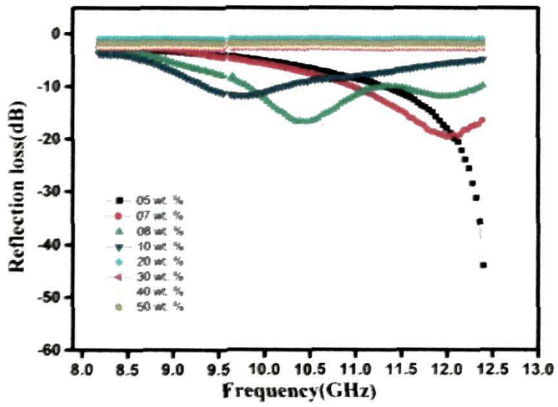

Figure.6.12 Measured Reflection loss of 4 mm thickness single layer EG-NPR composites over the X-band

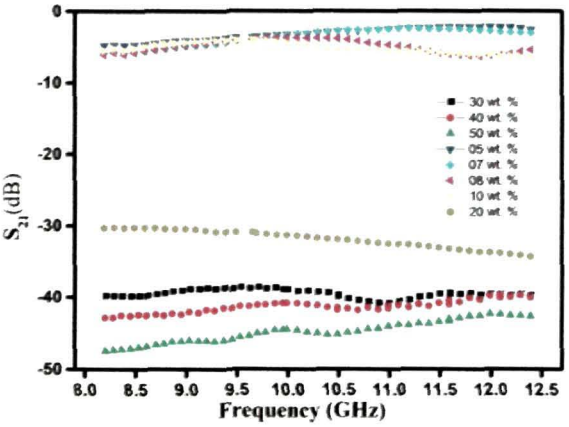

Figure.6.13 Measured S_{21} parameters of 4 mm thickness single layer EG-NPR composites over the X-band

The free space S_{21} (dB) parameters is measured as 20log (P_t/P_{in}) where P_t is the transmitted power received by the receiving antenna and P_{in} is the incident power from the transmitting antenna. The sample is placed at the focus of the lens but in this arrangement the metal plate is removed from the back of EG-NPR samples, unlike the reflection loss measurement set up. An average value of S_{21}~-45dB, -42 dB, -40dB and -31dB is observed for 50 wt. %, 40 wt. %, 30 wt. %, and 20 wt. % composites respectively.

Thus, the measured reflection loss value of 5 to 50 wt. % composites show that the 5 wt. %, 7 wt. %, 8 wt. % and 10 wt. % EG-NPR composites has the potential to be used as dielectric substrate for conductor back single layer design over the X-band. The composites from 30 to 50 wt. % EG shows very low microwave absorption ability over the X-band when backed by a metal plate, but due to high value of S_{21}(dB) parameters, the composites could be used as shielding material in certain applications where components are to be protected from external microwave radiation only.

6.5 CONCLUSIONS

EG-NPR composite is developed as a conductor backed single layer absorber, using transmission line model, where the thickness of the dielectric absorber substrate is optimized for maximum reflection loss over the X-band. The 4 mm layer thickness shows better results than 2 mm and 6 mm for the same compositions. Free space technique is used to measure the reflection loss. 5 wt. % EG-NPR composite shows a maximum reflection loss of -43dB at 12.4GHz. The reflection loss decreases with increase in EG wt. % and the reflection loss peak shifts to the lower frequency. A -10dB absorption of ~1GHz is observed for 7 to 10 wt. % composites, showing a promise of a broadband microwave absorber over the X-band. Moreover, the absorption frequency ranges can be shifted by nearly changing the wt. % of EG while keeping the thickness constant at 4 mm as desired in many applications.

References

1. Zhang, B., Feng, Y., Xiong, J., Yang, Y. and Lu, H. Microwave-absorbing properties of de-aggregated flake-shaped carbonyl-iron particle composites at 2- 18 GHz, *IEEE Transactions on Magnetics* **42**, 1178-1781, 2006.
2. Xiao, H. M., Liu, X. M. and Fu, S. Y. Synthesis, magnetic and microwave absorbing properties of core-shell structured $MnFe_2O_4/TiO_2$ nanocomposites, *Composites Science and Technology* **66**, 2003-2008, 2006.
3. Verma, A., Saxena, A.K., Dube, D.C. Microwave permittivity and permeability of ferrite-polymer thick films, *Journal of Magnetism and Magnetic Material* **263**, 228-234, 2003.
4. Ma, Z., Zhang, Y., Cao, C, T., Yuan, J., Liu Q, F., and Wang, J, B., Attractive microwave absorption and the impedance match effect in zinc oxide and carbonyl iron composite, *Physica B* **406**, 4620-624,2011.
5. Salisbury, W. W. *Absorbent body for electromagnetic waves*, U.S. Patent 2 599 944, June 10, 1952.
6. Dallenbach, W., Kleinsteuber, W. Reflection and absorption of decimeter-waves by plane dielectric layers, *Hochfreq. u Elektroak* **51**, 152-156,1938.
7. Engheta, N. Thin absorbing screens using metamaterial surfaces, in IEEE International Symposium on Antennas and Propagation 2, San Antonio, Texas, 392-395, 2002.
8. Knott, E.F., Shaeffer, J.F., Tuley, M.T. *Radar cross section*, Artech House, New York, 1993.
9. Reinert, J., Psilopoulos, J., Grubert, J. and Jacob, A. F. On the potential of graded-chiral dallenbach absorbers, *Microwave and Optical TechnologyLetters* **30**, 254-257, 2001.

10. Srivastava, R.K., Narayanan, T.N., Mary, R.A.P., Anantharaman,M.R., Srivastava , A., Vajtai, R., Ajayan, P.M. Ni filled flexible multi-walled carbon nanotube-polystyrene composite films as efficient microwave absorbers, *Appl. Phys. Lett.* **99**, 113116-1-3, 2011.
11. Shen, G., Xu, Z., Li, Y. Absorbing properties and structural design of microwave absorbers based on W-type La-doped ferrite and carbon fiber composites, *Journal of Magnetism and Magnetic Materials* **301**, 325-330, 2006.
12. Park, K. Y., Lee, S. E., Kim, C. G., Han, J. H. Fabrication and electromagnetic characteristics of electromagnetic wave absorbing sandwich structures, *Compos. Sci. Technol.***66**, 576-584, 2006.
13. Meshram, M.R., Agrawal, N.K. and Sinha, B. Characterization of M-type barium hexagonal ferrite-based wide band microwave absorber, *J. Magn. Magn. Mater.* **271**, 207-214, 2004.
14. Feng, Y.B., Qiu, T. and Shen, C.Y. Absorbing properties and structural design of microwave absorbers based on carbonyl iron and barium ferrite, *J. Magn. Magn. Mater.* **318**, 8-13, 2007.
15. Micheli, D., Apollo, C., Pastore, R., Marchetti, M. X-Band microwave characterization of carbon-based nanocomposite material, absorption capability comparison and RAS design simulation, *Compos. Sci. Technol.* **70**, 400-409, 2010.
16. Rashid, A. K., Shen, Z. and Mittra, R. On the optimum design of a single-layer thin wideband radar absorber, in IEEE International Symposium on Antennas and Propagation (AP-S/URSI 2011), Spokane, Washington, 2916 - 2919, 2011.
17. Zhang, L., Zhu, H., Song, Y., Zhang, Y., Huang, Y. The electromagnetic characteristics and absorbing properties of multi-walled carbon

nanotubes filled with Er_2O_3 nanoparticles as microwave absorbers, *Mater. Sci. Eng. B.* **153,** 78–82, 2008.

18. Fan, Z., Luo, G., Zhang, Z., Zhou, L., Wei, F. Electromagnetic and microwave absorbing properties of multi-walled carbon nanotubes/polymer composites, *Mater. Sci. Eng. B* **132,** 85–89, 2006.
19. He, Y., Gong, R., Nie, Y., He, H. and Zhao, Z. Optimization of two-layer electromagnetic wave absorbers composed of magnetic and dielectric materials in gigahertz frequency band. Journal of Applied Physics 98, 084903-1-5, 2005.
20. Ghodgaonkar, D.K., Varadan, V.V., Varadan, V.K. A free-space method for measurement of dielectric constants and loss tangents at microwave frequencies, *IEEE T. Instrum. Meas.* **37,** 789-793, 1989.
21. Varadan, V. V., Hollinger, R. D., Ghodgaonkar, D. K., Varadan V. K. Free-space, broadband measurements of high-temperature, complex dielectric properties at microwave frequencies, *IEEE Transactions on Instrumentation and Measurement* **40,** 842-846, 1991.

CHAPTER VII

MULTI-LAYER MICROWAVE ABSORBER: DESIGN OPTIMIZATION AND REFLECTION LOSS MEASUREMENT OVER THE X-BAND

7.1 INTRODUCTION

X-band frequency region finds wide use in wireless communication purposes like military communication satellites (7.9 to 8.4 GHz for uplink & 7.25 to 7.75 GHz for downlink), precision approach radar (PAR) (9.0-9.2 GHz), terrestrial communication and networking (10.15 to 10.7 GHz), motion detectors (10.525 GHz), traffic light crossing detectors (10.4 GHz), weather radars (9.3-9.5 GHz) and also in medical sciences [1-7] etc. The prolific usage of X-band frequency spectrum creates interference among themselves as well as for devices working in other operating frequency bands [8, 9]. To reduce the X-band interference, efficient microwave absorber is required. A good absorber must combine antagonistic properties: a significant conductivity to increase the loss and a low dielectric constant to reduce the reflection over a broad frequency band. The single layer design which depends on intrinsic properties of the material, though efficient for particular frequency, does not give broadband absorption due to impedance mismatch at the air-substrate interface. Single layer absorber developed so far using EG-NPR composites exhibit microwave absorption of RL_m~ -20dB to -43dB but over a limited frequency band. A maximum bandwidth of ~1GHz is observed for -10dB absorption within the X-band.

The primary issue in using composite material is how to effectively modify the permittivity of a composite medium as a function of the intrinsic permittivity of the phases, their weight fraction, thickness and their geometrical arrangement associated with the material mixture. Literature [10-12] reports that a multilayer absorber reduces the reflection by gradual tapering of impedance from that of free space to a highly lossy state. Practical design of a multilayer absorber using EG-NPR composite system requires optimization of layer arrangement and their individual thicknesses to achieve

the design factors such as broadband microwave absorption within limited thickness and weight.

The chapter focuses on achieving a broad bandwidth in the frequency range 8.2 to 12.4 GHz using multilayer arrangements of different composition of EG-NPR composites and keeping the thickness as optimum. Using the optimized design, conductor backed double and triple layered microwave absorbers are designed using transmission line model for multilayer structure [13, 14] and tested for free space microwave absorption over the X-band.

The 20dB absorption bandwidth means that the frequency bandwidth can achieve 99% of reflection loss and obtaining a bandwidth wider than 2 GHz will be adequate for a small thickness <6mm dielectric multilayer absorber[14].

7.2 DESIGN AND THICKNESS OPTIMIZATION OF DOUBLE LAYERED ABSORBER

The schematic diagram of a conductor backed double layered absorber consists of EG-NPR composite layers having intrinsic properties

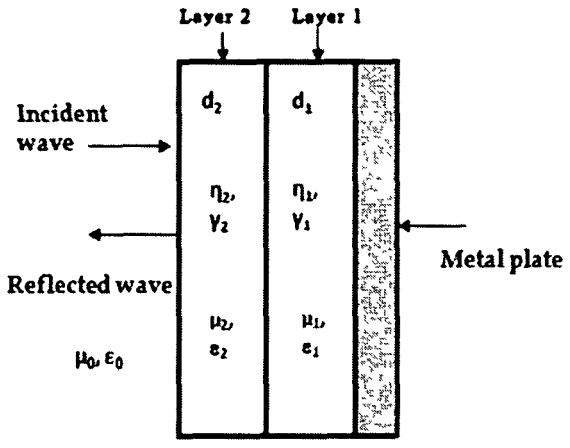

Figure 7.1 A schematic diagram of EG-NPR graded double layer absorber

$\varepsilon_{r1}, \mu_{r1}, \eta_1, \gamma_1, d_1$ for the layer-1 close to the metal plate and $\varepsilon_{r2}, \mu_{r2}, \eta_2, \gamma_2, d_2$ for the layer-2 as front-facing to the free space and is shown in figure 7.1. EG-NPR composites are nonmagnetic and $\mu_{r1} = \mu_{r2} = 1 - j0$.

The input impedance (Z_{in}) and reflection loss (RL_c) calculation of a conductor backed double layer absorber as discussed in chapter II, subsections 2.3.2, can be reduced to

$$Z_{in} = \eta_0\sqrt{1/\varepsilon_{r2}}\left[\frac{\sqrt{1/\varepsilon_{r1}}\tanh j(2\pi f/c)\sqrt{\varepsilon_{r1}}d_1+\sqrt{1/\varepsilon_{r2}}\tanh j(2\pi f/c)\sqrt{\varepsilon_{r2}}d_2}{\sqrt{1/\varepsilon_{r2}}+\sqrt{1/\varepsilon_{r1}}\tanh (j(2\pi f/c)\sqrt{\varepsilon_{r1}}d_1)\tanh j(2\pi f/c)\sqrt{\varepsilon_{r2}}d_2)}\right] \quad (7.1)$$

and

$$RL_c = 20\log\left|\frac{\sqrt{1/\varepsilon_{r2}}\left[\frac{\sqrt{1/\varepsilon_{r1}}\tanh j(2\pi f/c)\sqrt{\varepsilon_{r1}}d_1+\sqrt{1/\varepsilon_{r2}}\tanh j(2\pi f/c)\sqrt{\varepsilon_{r2}}d_2}{\sqrt{1/\varepsilon_{r2}}+\sqrt{1/\varepsilon_{r1}}\tanh (j(2\pi f/c)\sqrt{\varepsilon_{r1}}d_1)\tanh j(2\pi f/c)\sqrt{\varepsilon_{r2}}d_2)}\right]-1}{\sqrt{1/\varepsilon_{r2}}\left[\frac{\sqrt{1/\varepsilon_{r1}}\tanh j(2\pi f/c)\sqrt{\varepsilon_{r1}}d_1+\sqrt{1/\varepsilon_{r2}}\tanh j(2\pi f/c)\sqrt{\varepsilon_{r2}}d_2}{\sqrt{1/\varepsilon_{r2}}+\sqrt{1/\varepsilon_{r1}}\tanh (j(2\pi f/c)\sqrt{\varepsilon_{r1}}d_1)\tanh j(2\pi f/c)\sqrt{\varepsilon_{r2}}d_2)}\right]+1}\right| \quad (7.2)$$

From the above equations, it is seen that RL_c value of the absorber depends on frequency dependent complex permittivity, $\varepsilon_{r1}, \varepsilon_{r2}$ and the thickness d_1, d_2 of the individual layers. Optimization of both the parameters viz. complex permittivity of individual layers $\varepsilon_{r1}, \varepsilon_{r2}$ and the thickness d_1, d_2 is important to achieve strong absorption over a broadband frequency. Single layer absorption studies carried out in Chapter VI shows that the compositions with higher weight % of EG (>20 wt.%) shows high reflections, hence compositions of 5 wt. %, 7 wt. %, 8 wt. % and 10 wt. % EG-NPR composites are chosen to develop the two layer combination and are designated as **a**, **b**, **c** and **d**, respectively. Say, if the two layer combination selected are 5 wt. % for layer 1 and 7 wt. % for layer 2, the combination will be, **ab**, and the individual thickness, d_1, for 5 wt. % and d_2 for 7 wt. % layers are varied within the total thickness of absorber, $d = d_1 + d_2$ to obtain the minimum value of RL_c over the X-band frequency. To optimize the layer

thickness for this design absorber, a MATLAB program is developed based on the equations (7.1) and (7.2) and that finds the minimum RL_c for the following combinations of two EG-NPR composites layers systems, is tabulated in table 7.1.

Table 7.1 EG-NPR composites double layer design combinations

Air-absorber Interface layer	Sample code I-II-layer*	Sample wt. % combination (I-II-layer)
a-interface	ba	7-8 wt.%
	ca	8-5 wt.%
	da	10-5 wt.%
b-interface	ab	5-7 wt.%
	cb	8-7 wt.%
	db	10-7 wt.%
c-interface	ac	5-8 wt.%
	bc	7-8 wt.%
	dc	10-8 wt.%
d-interface	ad	5-10 wt.%
	bd	7-10 wt.%
	cd	8-10 wt.%

*refer figure 7.1 for layer number

The scheme of thickness variation is shown in figure 7.3. In this program the total thickness of the absorber is varied from 3mm to 5.4mm at a step size of 0.5mm in order to find the required bandwidth of absorption. The program is run for the whole thickness range in one slot, and updates the pointer with minimum value of RL_c. The program is executed for a thickness range say, 3mm to 3.4mm and then the next iteration is for the combination of individual thickness d_1 and d_2 within the total thickness, d to get the minimum

RL_c value as well as wide absorption bandwidth. The value is stored and the program is executed for the next thickness until it covers the complete thickness range. The minimum thickness of the individual layer is kept as 0.5 mm considering the limits of practical fabrication of the absorber layer.

The algorithm of the program for double layer absorber design is given as follows

Step 1: Read data (ε_{r1}, ε_{r2}, μ_{r1}, μ_{r2}, c) from files.

Step 2: For each of total thickness from 3 mm to 5.4 mm at the step size of 0.5 mm such as (3-3.4, 3.5-3.9,....5-5.4).

Step 3: Within a given thickness, d we choose 1000 combinations of randomly chosen two layer thicknesses (>= 0.5 mm) such that $d1+ d2=d$ (d is the thickness in step 2).

Step 4: We find the particular combination of layer thicknesses for which RL_c is minimum using equation (7.2). We store the thickness combination (d_1 and d_2), frequency band, $RL_c(min)$, Z_{real}, Z_{imag}.

Step 5: We continue step 2 for other thicknesses.

The flow chart of double layer design is given below

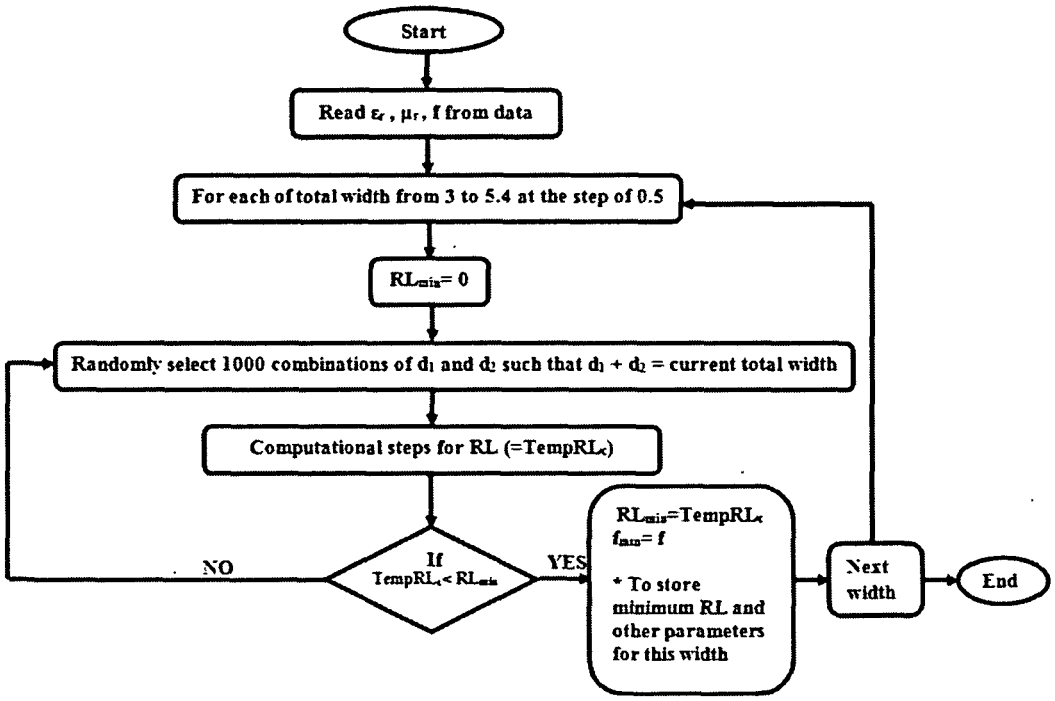

Figure 7.2 Flow chart for reflection loss calculation of double layer absorber design

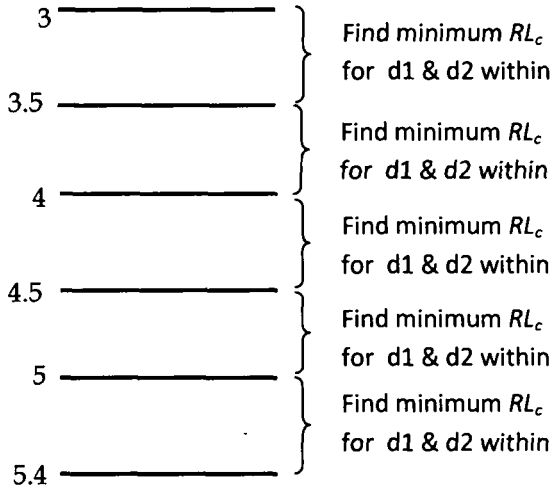

Figure 7. 3 The scheme of thickness variation to find minimum RL_c and required absorption bandwidth

7.2.1. RESULTS OF CALCULATED REFLECTION LOSS WITH OPTIMIZED THICKNESS OF DOUBLE LAYER MICROWAVE ABSORBER

The frequency dependent RL_C, real impedance Z_{in}' and imaginary impedance Z_{in}'' results of the double layer design **ba** with optimized thickness of individual layer is plotted in figure 7.4 (a), (b) and (c) respectively. The maximum absorption peak with -25dB and -30dB absorption bandwidth and optimized individual layer thickness is tabulated in table 7.2.

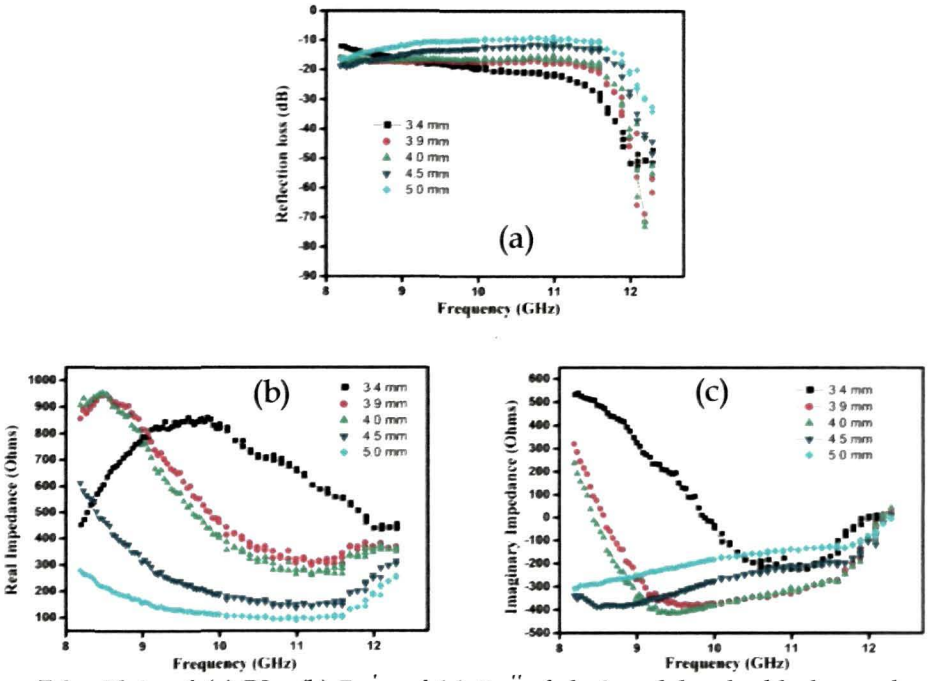

Figure 7.4 Plots of (a) RL_C, (b) Z_{in}' *and* (*c*) Z_{in}'' of designed **ba** double layer absorber with optimized thickness over the X-band

Table 7.2 Performance parameters of the designed **ba** double layer absorber with optimized thickness of the layers

Total thickness (mm)	Thickness of individual layers (mm)		Maximum absorption and associated frequency		Bandwidth (GHz)	
	d1	d2	RL_{cmin}(dB)	f_0 (GHz)	-25dB	-30dB
3.4	2.9	0.5	-54.1	12.1	1.01	0.71
3.9	2.0	1.9	-73.4	12.2	0.6	0.41
4	1.6	2.4	-83.4	12.2	0.51	0.42
4.5	0.5	4.0	-48.3	12.3	0.35	0.26
5	0.5	4.5	-34.0	12.3	0.21	0.12

Figures 7.5(a), (b) and (c) shows the frequency dependent RL_c, real impedance, $Z_{in}{}'$ and imaginary impedance $Z_{in}{}''$ results, respectively, of the double layer design as **ca** with optimized individual layer thickness. The maximum absorption peak with -25dB and -30dB absorption bandwidth and optimized individual layer thickness is tabulated in table 7.3.

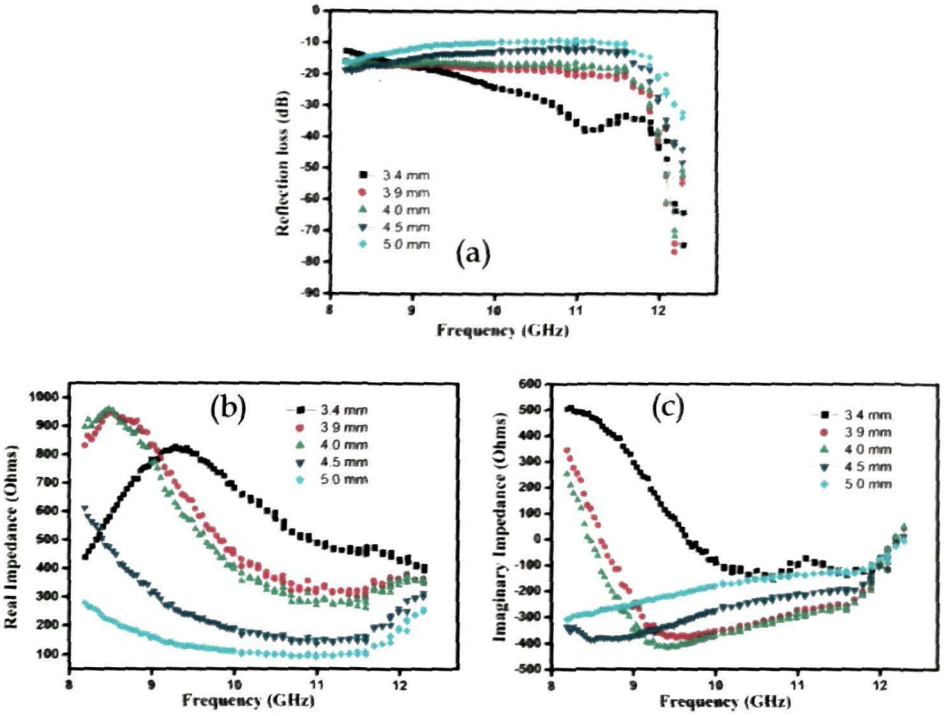

Figure 7.5 Plots of (a) RL_c, (b) $Z_{in}{}'$ *and* (c) $Z_{in}{}''$ of designed **ca** double layer absorber with optimize thickness over the X-band

Table 7.3 Performance parameters of the designed **ca** double layer absorber with optimize thickness of the layers

Total thickness (mm)	**Thickness of individual layers (mm)**		Maximum absorption and associated frequency		**Bandwidth (GHz)**	
	d1	**d2**	**RL_{cmin}(dB)**	**f_0 (GHz)**	**-25dB**	**-30dB**
3.4	2.5	0.9	-79.80	12.3	2.2	1.5
3.9	1.7	2.2	-82.45	12.2	0.56	0.40
4	1.4	2.6	-75.20	12.2	0.4	0.43
4.5	0.5	4.0	-48.18	12.3	0.32	0.27
5	0.5	4.5	-33.94	12.3	0.23	0.12

Figure 7.6(a), (b) and (c) shows the frequency dependent RL_c, real impedance Z_{in}' and imaginary impedance Z_{in}'' results respectively, of the double layer design with **da** combination and optimized layer 1 and layer 2 thicknesses. The maximum absorption peak, -25dB and -30dB absorption bandwidth and optimized individual layer thickness is tabulated in table 7.4.

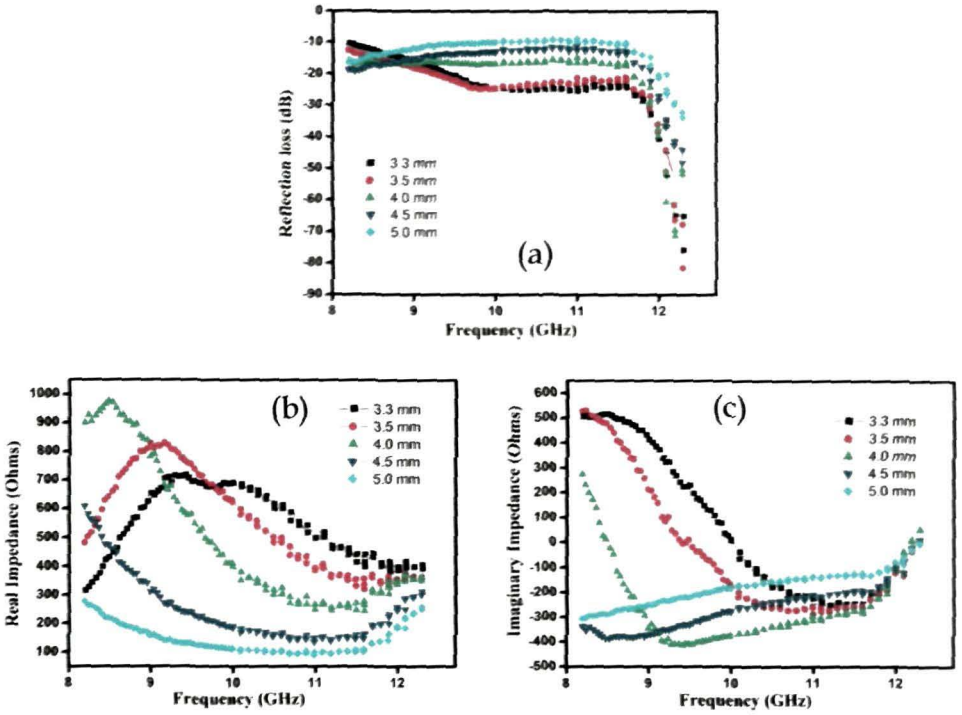

Figure 7.6 Plots of (a) RLc, (b) Z_{in}' and (c) Z_{in}'' of designed **da** double layer absorber with optimize thickness over the X-band

Table 7.4 Performance parameters of the designed **da** double layer absorber with optimize thickness of the layers

Total thickness (mm)	**Thickness of individual layers (mm)**		Maximum absorption and associated frequency		**Bandwidth (GHz)**	
	d1	**d2**	**RL_{cmin}(dB)**	**f_0 (GHz)**	**-25dB**	**-30dB**
3.3	1.8	1.5	-80.3	12.3	0.63	0.43
3.5	1.8	1.7	-82.7	12.3	0.54	0.39
4	1.0	3.0	-70.8	12.2	0.42	0.34
4.5	0.5	4.0	-47.9	12.3	0.34	0.25
5	0.5	4.5	-33.8	12.3	0.22	0.11

Figure 7.7(a), (b) and (c) shows the frequency dependent RL_C, real impedance Z_{in}' and imaginary impedance Z_{in}'' results respectively, of the double layer design **ab** with optimized thickness. The maximum absorption peak, -25dB and -30dB absorption bandwidth and optimized individual layer thickness is tabulated in table 7.5.

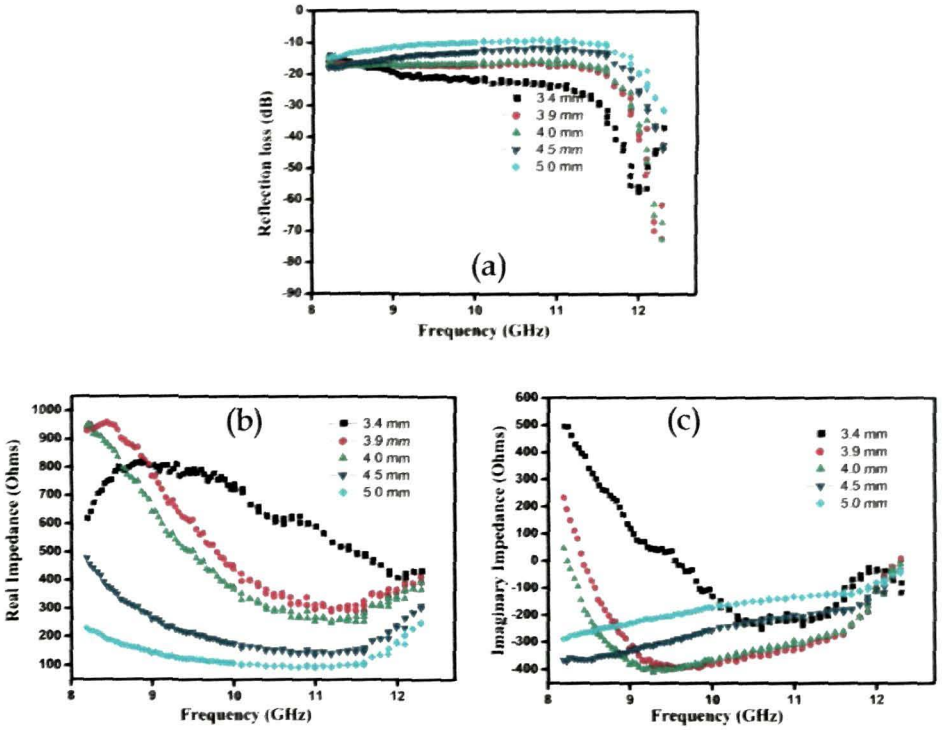

Figure 7.7 Plots of (a) RL_C, (b) Z_{in}' *and* (c) Z_{in}'' of designed **ab** double layer absorber with optimize thickness over the X-band

Table 7.5 Performance parameters of the designed **ab** double layer absorber with different thickness of the layers

Total thickness (mm)	Thickness of individual layers (mm)		Maximum absorption and associated frequency		Bandwidth (GHz)	
	d1	d2	RL_{cmin}(dB)	f_0 (GHz)	-25dB	-30dB
3.4	0.5	2.9	-58.4	12	1.04	0.74
3.9	3.3	0.6	-70.9	12.3	0.52	0.41
4	3.5	0.5	-73.1	12.3	0.5	0.41
4.5	4.0	0.5	-43.9	12.3	0.33	0.23
5	4.5	0.5	-31.6	12.3	0.19	0.07

Figure 7.8(a), (b) and (c) shows the frequency dependent RL_c, real impedance Z_{in}' and imaginary impedance Z_{in}'' results, respectively, of the double layer design for **cb** combination with optimized thickness. The maximum absorption peak, -25dB and -30dB absorption bandwidth and optimized individual layer thickness is tabulated in table 7.6.

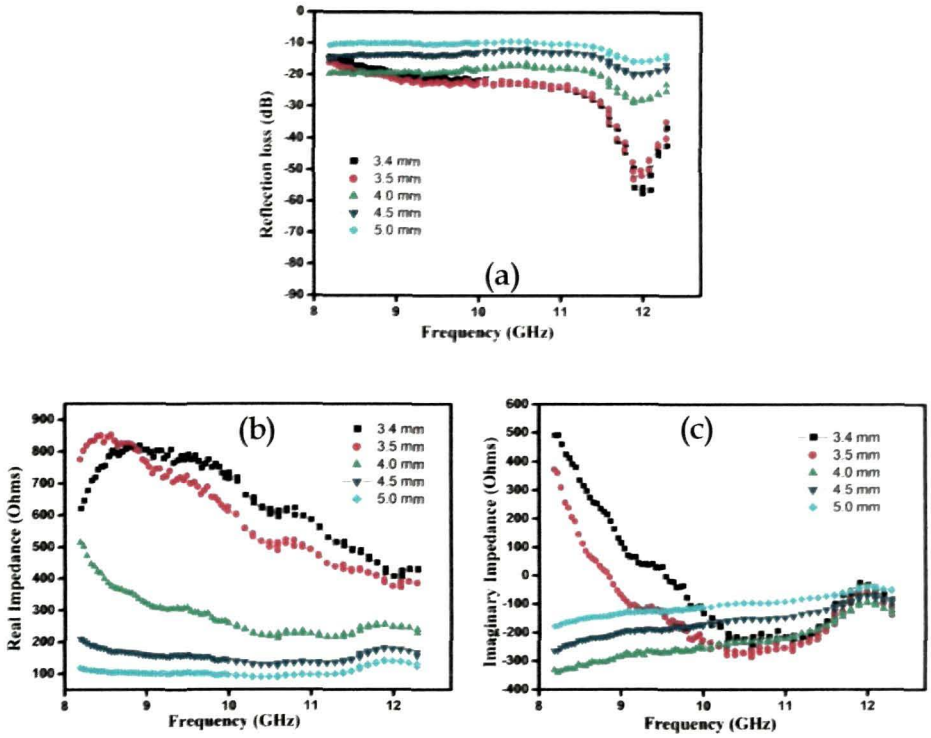

Figure 7.8 Plots of (a) RL_c, (b) Z_{in}' *and* (*c*) Z_{in}'' of designed **cb** double layer absorber with optimize thickness over the X-band

Table 7.6 Performance parameters of the designed **cb** double layer absorber with different thickness of the layers

Total thickness (mm)	Thickness of individual layers (mm)		Maximum absorption and associated frequency		Bandwidth (GHz)	
	d1	d2	RL_{cmin}(dB)	f_0 (GHz)	-25dB	-30dB
3.4	0.5	2.9	-58.6	12	1.09	.79
3.5	0.5	3.0	-53.4	12	1.02	.78
4	0.5	3.5	-28.8	11.9	0.54	--
4.5	0.5	4.0	-20.1	11.9	--	--
5	0.5	4.5	-15.8	12	--	--

Figure 7.9(a), (b) and (c) shows the frequency dependent RL_C, real impedance Z_{in}' and imaginary impedance Z_{in}'' results, respectively, for the double layer design **db** with thickness optimization. The maximum absorption peak, -25dB and -30dB absorption bandwidth and optimized individual layer thickness is tabulated in table 7.7.

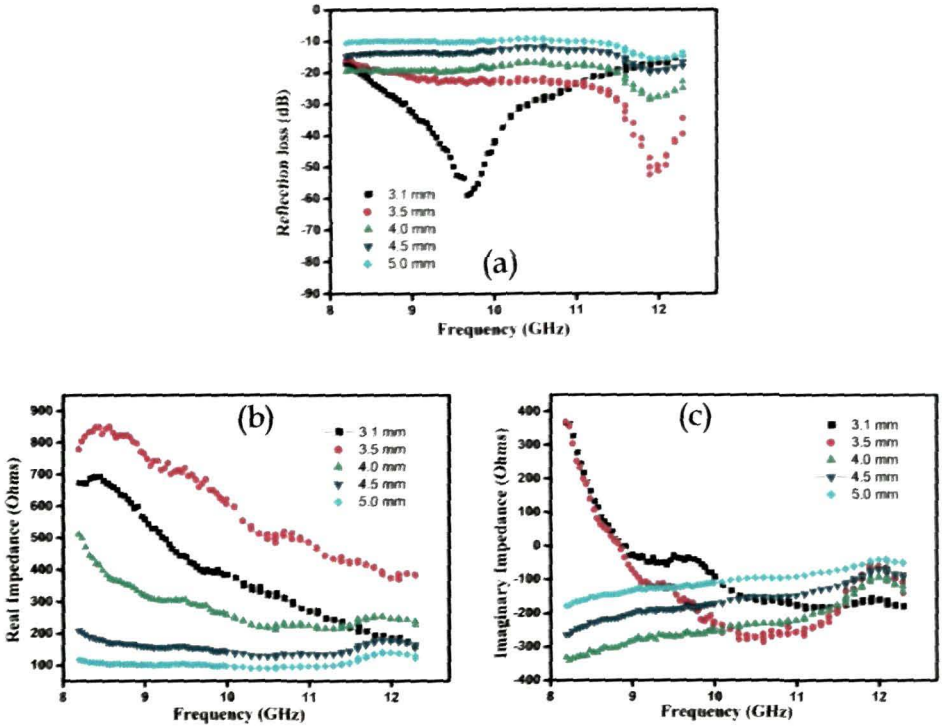

Figure 7.9 Plots of (a) RL_C, (b) Z_{in}' *and* (c) Z_{in}'' of designed **db** double layer absorber with optimize thickness over the X-band

Table 7.7 Performance parameters of the designed **db** double layer absorber with different thickness of the layers

Total thickness (mm)	Thickness of individual layers (mm)		Maximum absorption and associated frequency		Bandwidth (GHz)	
	d1	d2	RL_{cmin}(dB)	f_0 (GHz)	-25dB	-30dB
3.1	2.6	0.5	-58.9	9.67	2.27	1.46
3.5	0.5	3.0	-52.8	12	0.97	0.73
4	0.5	3.5	-28.6	11.9	0.57	--
4.5	0.5	4.0	-20.0	11.9	--	--
5	0.5	4.5	-15.8	12	--	--

Figure 7.10(a), (b) and (c) shows the frequency dependent RL_c, real impedance Z_{in}' and imaginary impedance Z_{in}'' results respectively, of the double layer design **ac** with thickness optimization of individual layers. The maximum absorption peak with -25dB and -30dB absorption bandwidth and optimized individual layer thickness is tabulated in table 7.8.

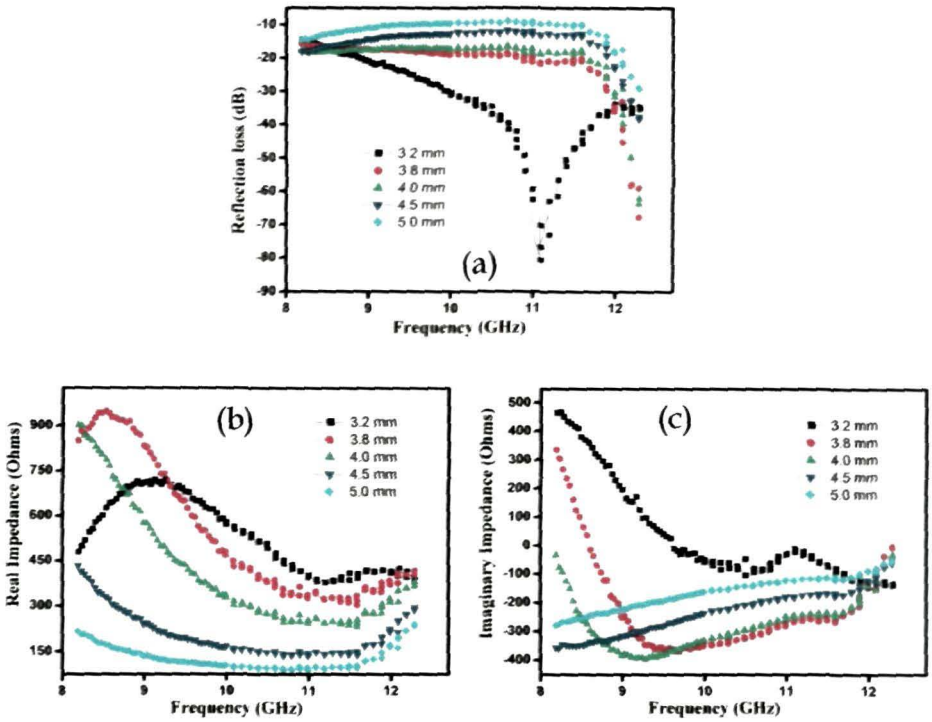

Figure 7.10 Plots of (a) RL_c, (b) Z_{in}' *and* (c) Z_{in}'' of designed **ac** double layer absorber with optimized thickness over the X-band

Table 7.8 Performance parameters of the designed **ac** double layer absorber with different thickness of the layers

Total thickness (mm)	Thickness of individual layers (mm)		Maximum absorption and associated frequency		Bandwidth (GHz)	
	d1	d2	RL_{cmin}(dB)	f_0 (GHz)	-25dB	-30dB
3.2	0.5	2.7	-80.7	11.1	2.78	2.33
3.8	3.3	0.5	-82.6	12.3	0.50	0.37
4	3.5	0.5	-63.7	12.3	0.35	0.30
4.5	4.0	0.5	-38.3	12.3	0.26	0.15
5	4.5	0.5	-29.2	12.3	0.13	0.04

Figure 7.11(a), (b) and (c) shows the frequency dependent RL_c, real impedance Z_{in}' and imaginary impedance Z_{in}'' results respectively, of the double layer design **bc** with optimized thickness. The maximum absorption peak with -25dB and -30dB absorption bandwidth and optimized individual layer thickness is tabulated in table 7.9.

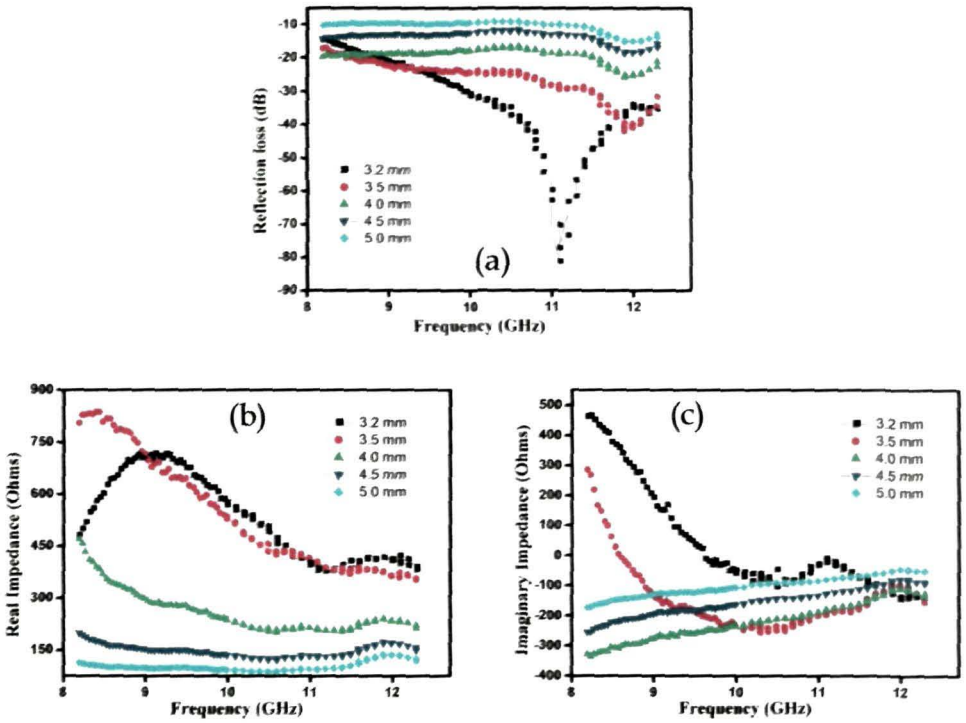

Figure 7.11 Plots of (a) RL_c, (b) Z_{in}' *and* (*c*) Z_{in}'' of designed **bc** double layer absorber combination with optimize thickness over the X-band

Table 7.9 Performance parameters of the designed **bc** double layer absorber with different thickness of the layers

Total thickness (mm)	Thickness of individual layers (mm)		Maximum absorption and associated frequency		Bandwidth (GHz)	
	d1	d2	RL_{cmin}(dB)	f_0 (GHz)	-25dB	-30dB
3.2	0.5	2.7	-81.1	11.1	2.79	2.35
3.5	3.0	0.5	-41.8	11.9	1.6	.74
4	3.5	0.5	-25.8	11.9	--	--
4.5	4.0	0.5	-18.8	12	--	--
5	4.5	0.5	-15.3	12	--	--

Figure 7.12(a), (b) and (c) shows the frequency dependent RL_c, real impedance Z_{in}' and imaginary impedance Z_{in}'' results respectively, of the double layer design **dc** with optimized layer thickness. The maximum absorption peak, -25dB and -30dB absorption bandwidth and optimized individual layer thickness is tabulated in table 7.10.

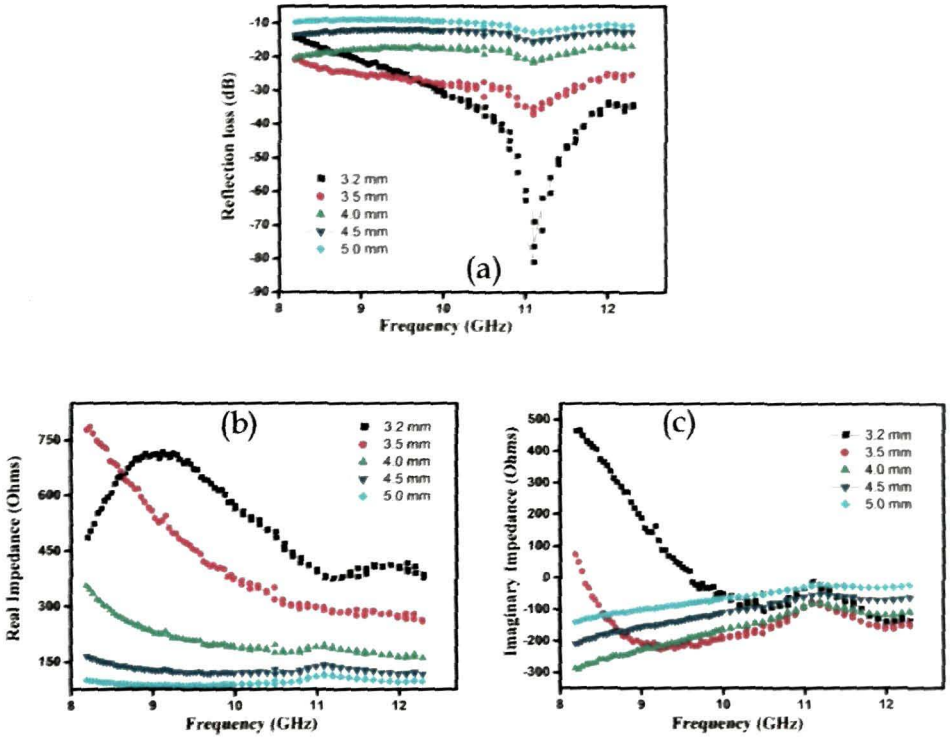

Figure 7.12 Plots of (a) RL_c, (b) Z_{in}' *and* (c) Z_{in}'' of designed **dc** double layer absorber with optimize thickness over the X-band

Table 7.10 Performance parameters of the designed **dc** double layer absorber with different thickness of the layers

Total thickness (mm)	Thickness of individual layers (mm)		Maximum absorption and associated frequency		Bandwidth (GHz)	
	d1	d2	RL_{cmin}(dB)	f_0 (GHz)	-25dB	-30dB
3.2	0.5	2.7	-81.0	11.1	2.8	2.36
3.5	0.5	3.0	-37.0	11.1	2.66	.69
4.0	0.5	3.5	-21.7	11.1	--	--
4.5	0.5	4.0	-15.7	11.1	--	--
5.0	0.5	4.5	-12.8	11.1	--	--

Figure 7.13(a), (b) and (c) shows the frequency dependent RL_c, real impedance Z_{in}' and imaginary impedance Z_{in}'' results, respectively, of the double layer design **ad** with optimized layer thickness. The maximum absorption peak, -25dB and -30dB absorption bandwidth and optimized individual layer thickness is tabulated in table 7.11.

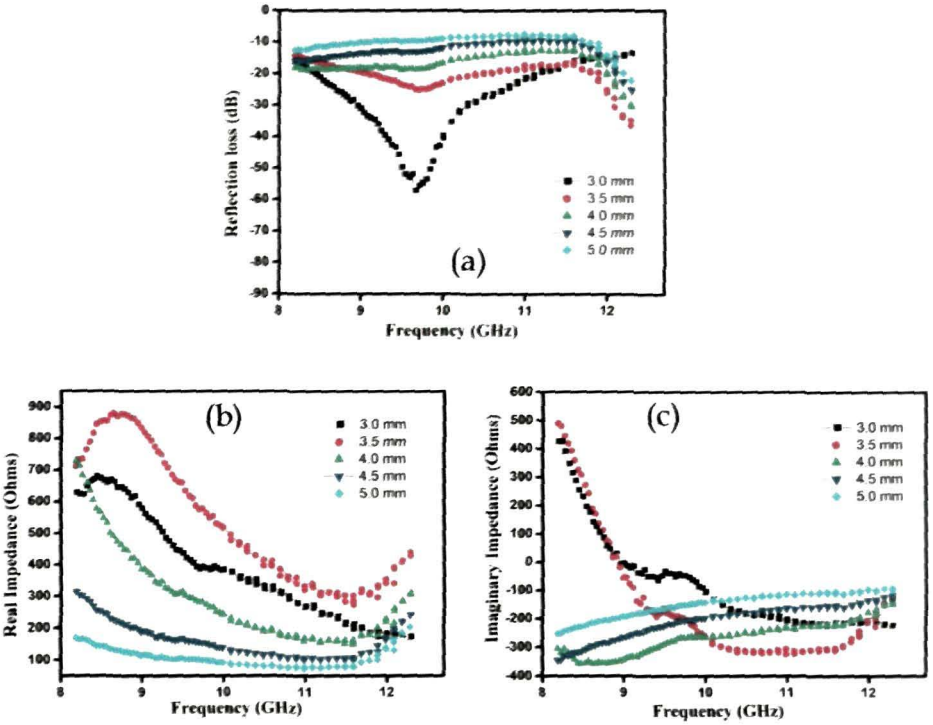

Figure 7.13 Plots of (a) RL_c, (b) Z_{in}' *and* (c) Z_{in}'' of designed **ad** double layer absorber with optimize thickness over the X-band

Table 7.11 Performance parameters of the designed **ad** double layer absorber with different thickness of the layers

Total thickness (mm)	Thickness of individual layers (mm)		Maximum absorption and associated frequency		Bandwidth (GHz)	
	d1	d2	RL_{cmin}(dB)	f_0 (GHz)	-25dB	-30dB
3	1.3	1.7	-57.1	9.67	1.96	1.35
3.5	3.0	0.5	-38.1	12.3	0.30	0.17
4	3.5	0.5	-30.5	12.3	0.21	--
4.5	4.0	0.5	-25.3	12.3	--	--
5	4.5	0.5	-22.1	12.3	--	--

Figure 7.14(a), (b) and (c) shows the frequency dependent RL_C, real impedance Z_{in}' and imaginary impedance Z_{in}'' results respectively, of the double layer design **bd** with optimized layer thickness. The maximum absorption peak, -25dB and -30dB absorption bandwidth and optimized individual layer thickness is tabulated in table 7.12.

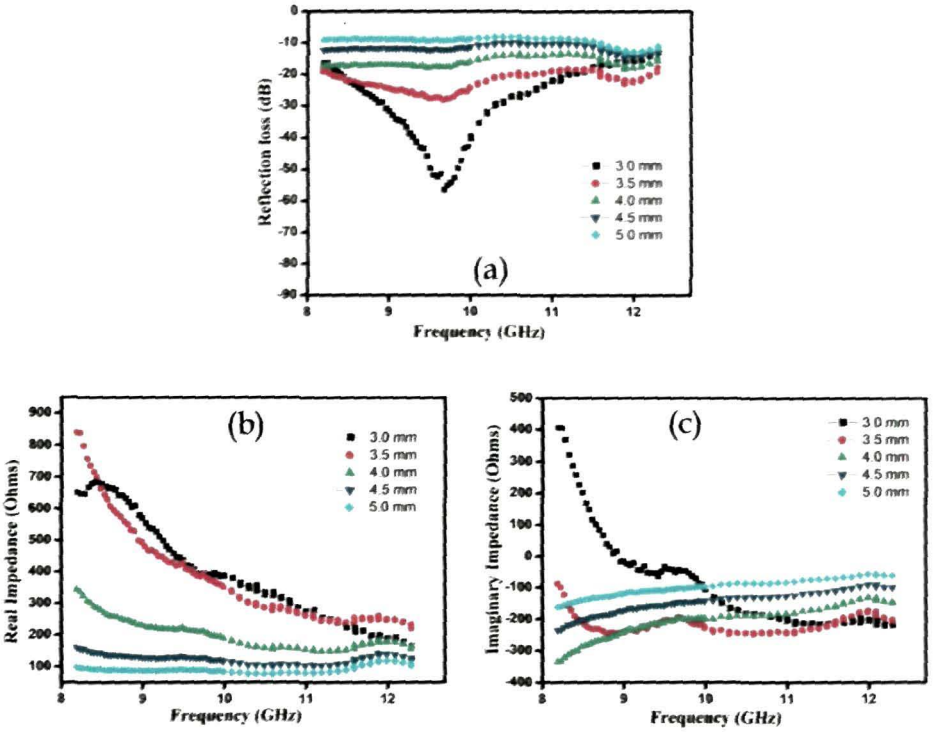

Figure 7.14 Plots of (a) RL_C, (b) Z_{in}' *and* (c) Z_{in}'' of designed **bd** double layer absorber with optimize thickness over the X-band

Table 7.12 Performance parameters of the designed **bd** double layer absorber with different thickness of the layers

Total thickness (mm)	Thickness of individual layers (mm)		Maximum absorption and associated frequency		Bandwidth (GHz)	
	d1	d2	RL_{cmin}(dB)	f_0 (GHz)	-25dB	-30dB
3	1.5	1.5	-56.5	9.67	2.01	1.37
3.5	2.9	0.6	-28.1	9.67	0.64	--
4	3.5	0.5	-18.2	12	--	--
4.5	4.0	0.5	-14.9	12	--	--
5	4.5	0.5	-13.1	12	--	--

Figure 7.15(a), (b) and (c) shows the frequency dependent RL_C, real impedance Z_{in}' and imaginary impedance Z_{in}'' results respectively, of the double layer design **cd** with optimized thickness. The maximum absorption peak with -25dB and -30dB absorption bandwidth and optimized individual layer thickness is tabulated in table 7.13.

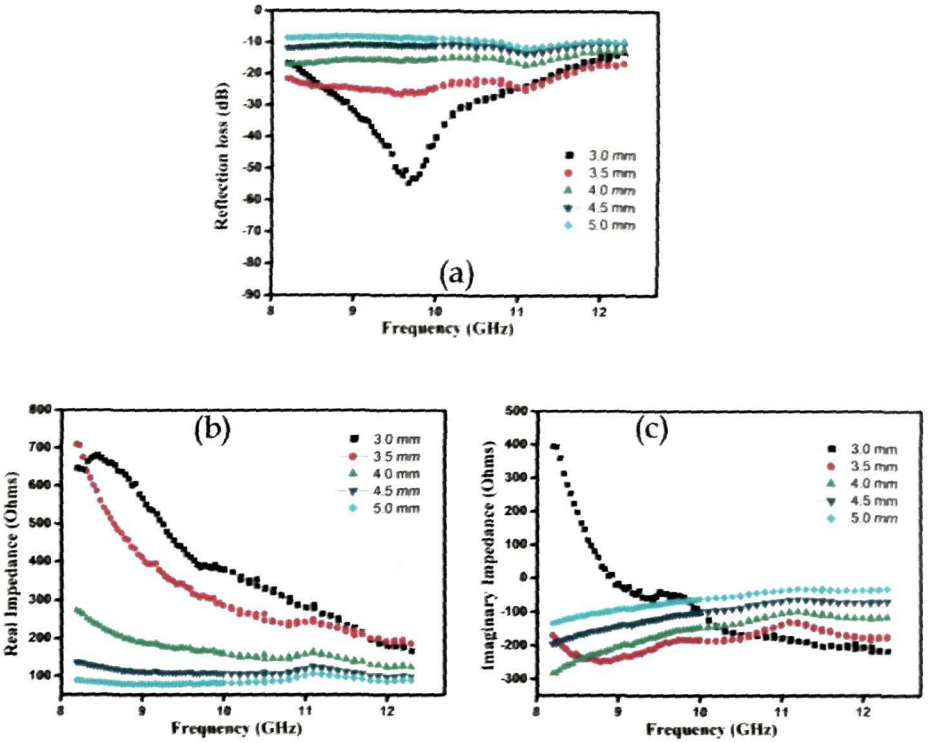

Figure 7.15 Plots of (a) RL_C (b) Z_{in}' *and* (c) Z_{in}'' of designed **cd** double layer absorber with optimized thickness over the X-band

Table 7.13 Performance parameters of the designed **cd** double layer absorber with different thickness of the layers

Total thickness (mm)	Thickness of individual layers (mm)		Maximum absorption and associated frequency		Bandwidth (GHz)	
	d1	d2	RL_{cmin}(dB)	f_0 (GHz)	-25dB	-30dB
3	1.6	1.4	-54.8	9.65	2.19	1.37
3.5	3.0	0.5	-26.6	9.59	--	--
4	3.5	0.5	-17.3	8.22	--	--
4.5	4.0	0.5	-13.6	11.1	--	--
5	4.5	0.5	-11.8	11.1	--	--

From the double layer optimization carried out, EG-NPR composites absorber design with RL_c>-50dB and -25dB bandwidth > 2 GHz and -30dB >1 GHz over the X-band frequency are selected and is tabulated in table 7.14.

Design combination with 8 wt. % composite as the interfacing layer shows better broadband absorption bandwidth > 2.5 GHz for -25dB absorption and absorption bandwidth >2 GHz for -30dB absorption. Table 7.14 shows that maximum absorption peak varies in frequency position for different design combination of the composites layer and this property can be used for tuning the required frequency bandwidth over the X-band. Based on these calculated results, practical double layer microwave absorbers are fabricated using the appropriate wt. % EG-NPR composites.

Table 7.14 Selected EG-NPR based double layer design combination with -25dB and -30dB absorption bandwidth greater than 2 GHz and 1 GHz respectively

Air-absorber interface layer	Layer combination with total thickness	Thickness of individual layer (mm)		Bandwidth in (GHz)		Maximum absorption and associated frequency (GHz)	
		d1	d2	-25 dB	-30 dB	RL_{cmin}(dB)	f_0 (GHz)
a-interface	ca_3.4	2.5	0.9	2.2	1.5	-79.8	12.3
b-interface	db_3.1	2.6	0.5	2.27	1.46	-58.9	9.67
c-interface	ac_3.2	0.5	2.7	2.78	2.33	-80.7	11.10
	bc_3.2	0.5	2.7	2.79	2.35	-81	11.1
	dc_3.2	0.5	2.7	2.80	2.36	-81	11.1
d-interface	ad_3.0	1.3	1.7	1.96	1.35	-57.1	9.67
	bd_3.0	1.5	1.5	2.01	1.37	-56.5	9.67
	cd_3.0	1.6	1.4	2.19	1.37	-54.8	9.65

7.2.2. RESULTS AND ANALYSIS OF MEASURED REFLECTION LOSS VALUE OF DOUBLE LAYER MICROWAVE ABSORBER

Using free space microwave absorption measurement technique as discussed in chapter 6, the reflection loss measurement of the selected designed double layer absorber as given in table 7.14, is carried out over the X-band. The double layer sample are fabricated in the following way: Let us consider the fabrication of the design **ca_3.4** which consist of 5 wt. % composites as the air-absorber interface layer with thickness, d_1=2.5 mm, and 8 wt. % composites is the inner layer close to metal plate with thickness, d_2=0.9 mm. Initially, both the composites with respective thickness are prepared seperately using mechanical mixing and thermal treatment method and then combined them using the thermal treatment at 150 °C. The double layer composites developed is kept of the dimension of 152mm × 152mm × d mm for free space microwave absorption testing. The measured reflection loss, RL_m, values of the fabricated **ca_3.4, db_3.1, ac_3.2, bc_3.2, dc_3.2, ad_3.0, bd_3.0, cd_3.0** samples are plotted in figure 7.15A, as a function of frequency. The RL_m value of **ca_3.4** design having total thickness 3.4 mm shows -25dB absorption bandwidth of 1.63 GHz in the frequency range 10.67 GHz to 12.3 GHz and -30dB absorption bandwidth of 1.31 GHz in the frequency range 11.0 GHz to 12.3 GHz with maximum absorption of ~ -45dB at 12.3 GHz. The RL_m graph exhibit similar trend as the calculated RL_c (fig.7.5) but the -25dB and -30dB absorption bandwidth and maximum absorption

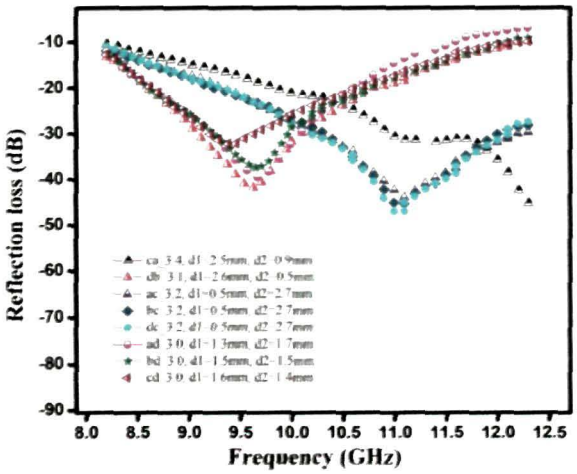

Figure 7.15 A Measured reflection loss value of designed double layer absorbers

peak is slightly less than computed values. The RL_m for other designs **db_3.1, ac_3.2, bc_3.2, dc_3.2, ad_3.0, bd_3.0** and **cd_3.0** show -25dB absorption bandwidth of 1.54 GHz, 2.47 GHz, 2.43 GHz, 2.46 GHz, 1.30 GHz, 1.27 GHz, 1.06 GHz, respectively in the frequency bands of 8.86-10.4 GHz, 9.83-12.3 GHz, 9.87-12.3 GHz, 9.84-12.3 GHz, 8.95-10.25 GHz, 8.96-10.23 GHz and 8.96-10.02 GHz respectively and -30dB absorption bandwidth of the respective designs are 0.9 GHz, 1.77 GHz, 1.60 GHz, 1.75 GHz, 0.78 GHz, 0.67 GHz and 0.35 GHz in the frequency bands 9.12-10.02 GHz, 10.31-12.08 GHz, 10.37-11.97 GHz, 10.28-12.03 GHz, 9.27-10.05 GHz, 9.28-9.95 GHz and 9.23-9.58 GHz. The maximum measured absorption peaks of **db_3.1** design combination is -40.94 dB at 9.63 GHz in comparison to RL_c ~-60dB at the same frequency. Similarly, RL_m for **ac_3.2** design is -44dB at 11.09 GHz corresponding to RL_c~ -78dB at 11.09 GHz, RL_m for **bc_3.2** design ~-45dB at 11.02 GHz corresponding to RL_c~-80dB at the same frequency, RL_m for **dc_3.2** design is -46dB at 11.05 GHz and RL_c for the same design is -81dB at 11.1 GHz, the RL_m for **ad_3.0** design is -39dB at 9.66 GHz and the calculated RL_c **ad_3.0** design ~-57dB at 9.67 GHz, the **bd_3.0** design show maximum absorption peak RL_m ~-37dB at 9.66 GHz and RL_c ~ -56dB at 9.67 GHz, the RL_m for **cd_3.0** design stucture is -32dB at 9.37 GHz and the calculated RL_c for this deisgn is -54dB at 9.65 GHz.

The frequency of minimum measured reflection loss peak and calculated minimum reflection loss peak shows close proximity, however the theoretical return loss value is higher than experimental return loss values for all the combinations.

The absorber is modeled as transmission line using some approximations like the electrical conductvity ignored during design formulation etc., which practically may have effect on microwave absorption. Some deviation in measured and calculated value may occur due to shortcomings in the fabrication process in which the layers of two composite systems at the interface may intermingle marginally changing the wt.% of EG

thus modifying the impedance matching condition. The -25dB and -30dB absorption bandwidth obtained are sufficinetly good for a dielectric absorber of overall thickness less than 4 mm and the developed aborber could be used as broadband microwave absorber over the X-band.

7.3 DESIGN AND THICKNESS OPTIMIZATION OF TRIPLE LAYERED ABSORBER

Bandwidth of the microwave absorber can be further enhanced by augmenting numbers of layers without compromising the total thickness of the absorbing structure [15]. A three layer EG-NPR composite dielectric absorber is designed in which the composition and layer thickness is optimized to get the best performance. The schematic diagram of a conductor backed triple layer absorber consists of EG-NPR composite layers having intrinsic parameters $\varepsilon_{r1}, \mu_{r1}, \eta_1, \gamma_1, d_1$ for the layer 1 in vicinity to the metal plate, layer 2 with intrinsic parameters $\varepsilon_{r2}, \mu_{r2}, \eta_2, \gamma_{2,}, d_2$ as sandwiched layer and

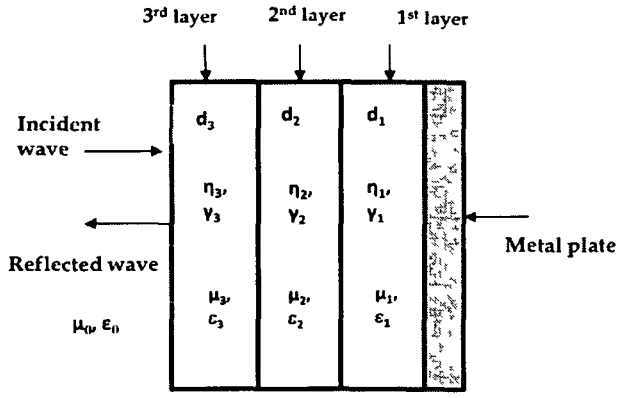

Figure 7.16 A schematic diagram of EG-NPR graded triple layer absorber

$\varepsilon_{r3}, \mu_{r3}, \eta_3, \gamma_{3,}, d_3$ parameters for the front-facing layer-3 with the free space as shown in figure 7.16. The nonmagnetic characteristics of the composites, renders the complex permeability $\mu_{r1} = \mu_{r2} = \mu_{r3} = 1 - j0$. The input

impedance, Z_{in}, and computed reflection loss, RL_c, are determined from the conductor backed triple layer absorber discussed in chapter II, subsections 2.3.2.3, and for the dielectric absorber reduces to

$$Z_3 = \eta_3 \frac{\eta_2 \frac{\eta_1 \tan h\, \gamma_1 d_1 + \eta_2 \tan h\, \gamma_2 d_2}{\eta_2 + \eta_1 \tan h\,(\gamma_1 d_1) \tan h\,(\gamma_2 d_2)} + \eta_3 \tan h\, \gamma_3 d_3}{\eta_3 + \eta_2 \frac{\eta_1 \tan h\, \gamma_1 d_1 + \eta_2 \tan h\, \gamma_2 d_2}{\eta_2 + \eta_1 \tan h\,(\gamma_1 d_1) \tan h\,(\gamma_2 d_2)} \tan h\, \gamma_3 d_3} \tag{7.3}$$

$$RL_c = 20\log \left| \frac{\eta_3 \frac{\eta_2 \frac{\eta_1 \tan h\, \gamma_1 d_1 + \eta_2 \tan h\, \gamma_2 d_2}{\eta_2 + \eta_1 \tan h\,(\gamma_1 d_1) \tan h\,(\gamma_2 d_2)} + \eta_3 \tan h\, \gamma_3 d_3}{\eta_3 + \eta_2 \frac{\eta_1 \tan h\, \gamma_1 d_1 + \eta_2 \tan h\, \gamma_2 d_2}{\eta_2 + \eta_1 \tan h\,(\gamma_1 d_1) \tan h\,(\gamma_2 d_2)} \tan h\, \gamma_3 d_3} - \eta_0}{\eta_3 \frac{\eta_2 \frac{\eta_1 \tan h\, \gamma_1 d_1 + \eta_2 \tan h\, \gamma_2 d_2}{\eta_2 + \eta_1 \tan h\,(\gamma_1 d_1) \tan h\,(\gamma_2 d_2)} + \eta_3 \tan h\, \gamma_3 d_3}{\eta_3 + \eta_2 \frac{\eta_1 \tan h\, \gamma_1 d_1 + \eta_2 \tan h\, \gamma_2 d_2}{\eta_2 + \eta_1 \tan h\,(\gamma_1 d_1) \tan h\,(\gamma_2 d_2)} \tan h\, \gamma_3 d_3} + \eta_0} \right| \tag{7.4}$$

where $\eta_1 = \eta_0 \sqrt{1 / \varepsilon_{r1}}$ (7.5)

$$\eta_2 = \eta_0 \sqrt{1 / \varepsilon_{r2}} \tag{7.6}$$

$$\eta_3 = \eta_0 \sqrt{1 / \varepsilon_{r3}} \tag{7.7}$$

$$\gamma_1 = j(2\pi f / c) \sqrt{\varepsilon_{r3}} \tag{7.8}$$

$$\gamma_2 = j(2\pi f / c) \sqrt{\varepsilon_{r3}} \tag{7.9}$$

$$\gamma_3 = j(2\pi f / c) \sqrt{\varepsilon_{r3}} \tag{7.10}$$

From the above equations, it is seen that RL_c value of the absorber depends on frequency dependent complex permittivity, $\varepsilon_{r1}, \varepsilon_{r2}, \varepsilon_{r3}$ and the thickness of the individual layers, d_1, d_2, d_3. The minimum RL_c value is achieved by optimization of effective intrinsic properties of the three layers and the thickness. For the three layer design, the four material compositions of 5 wt. %, 7 wt. %, 8 wt. % and 10 wt. % EG-NPR composites are considered and designated **A**, **B**, **C** and **D**, respectively. The three layers combination of fixed thickness, d, is considered at a time, for example if, 5 wt. % is assigned to layer 1, 7 wt. % is assigned to layer 2 and 8 wt. % assigned to layer 3, the combination is termed as **ABC** and the corresponding layer thickness as d_1, d_2 and d_3 so that $d = d_1 + d_2 + d_3$. A MATLAB program discussed in

Appendix-A, is developed based on the equations 7.3 to 7.10 to optimize the layer thickness for the triple layer absorber and finds the minimum RL_c for the following combinations tabulated in table 7.15.

Table 7.15 EG-NPR composites triple layer design combinations

Air-absorber Interface layer	Sample code I-II-III layer	Sample wt. % combination (I-II-III layer)
A-interface	BDA	7-10-5 wt. %
	BCA	7-8-5 wt. %
	CDA	8-10-5 wt. %
	CBA	8-7-5 wt. %
	DCA	10-8-5 wt. %
	DBA	10-7-5 wt. %
B-interface	ADB	5-10-7 wt. %
	ACB	5-8-7 wt. %
	CAB	8-5-7 wt. %
	CDB	8-10-7 wt. %
	DAB	10-5-7 wt. %
	DCB	10-8-7 wt. %
C-interface	ABC	5-7-8 wt. %
	ADC	5-10-8 wt. %
	BAC	7-5-8 wt. %
	BDC	7-10-8 wt. %
	DAC	10-5-8 wt. %
	DBC	10-7-8 wt. %
D-interface	ACD	5-8-10 wt. %
	ABD	5-7-10 wt. %
	BCD	7-8-10 wt. %
	BAD	7-5-10 wt. %
	CBD	8-7-10 wt. %
	CAD	8-5-10 wt. %

The scheme of thickness variation for three layer system is shown in figure 7.18. Similar to double layer optimization, the total thickness of the absorber is

varied from 3mm to 5.4mm at a step size of 0.5mm in order to find the required bandwidth of absorption. The program is executed for one particular total thickness range say 3mm to 3.4mm and then finds the combination of individual thickness d_1, d_2 and d_3 to calculate the minimum RL_c and maximum absorption bandwidth over the range. The value is stored and the program is executed for the next thickness until it covers the allotted thickness range. The minimum thickness of the individual layer is fixed at 0.5mm for ease of practical fabrication of the absorber.

The algorithm of the program for three layer absorber design is given as follows

Step 1: Read data (ε_{r1}, ε_{r2}, ε_{r3}, μ_{r1}, μ_{r2}, μ_{r3}, c) from files.

Step 2: For each of total thickness from 3 mm to 5.4 mm at the step size of 0.5 mm such as (3-3.4, 3.5-3.9,....5-5.4).

Step 3: Within a given thickness d we choose 1000 combinations of randomly chosen three layer thickness (>= 0.5 mm) such that $d_1+ d_2+d_3=d$ (d is the thickness in step 2).

Step 4: We find the particular combination of layer thicknesses for which RL_c is minimum using equation (7.4). We store the thickness combination (d_1, d_2 *and* d_3), frequency band, RL_c(min), Z_{real}, Z_{imag}.

Step 5: we continue step 2 for other thicknesses.

The flow chart of three layer design is given below

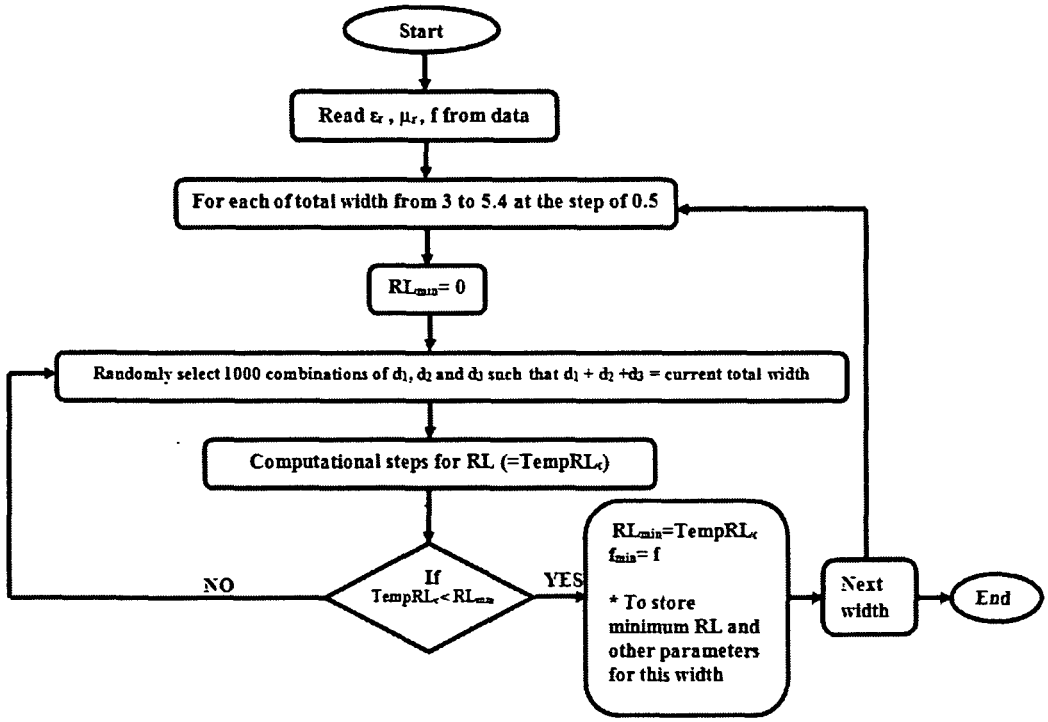

Figure 7.17 Flow chart of three layer absorber design optimization

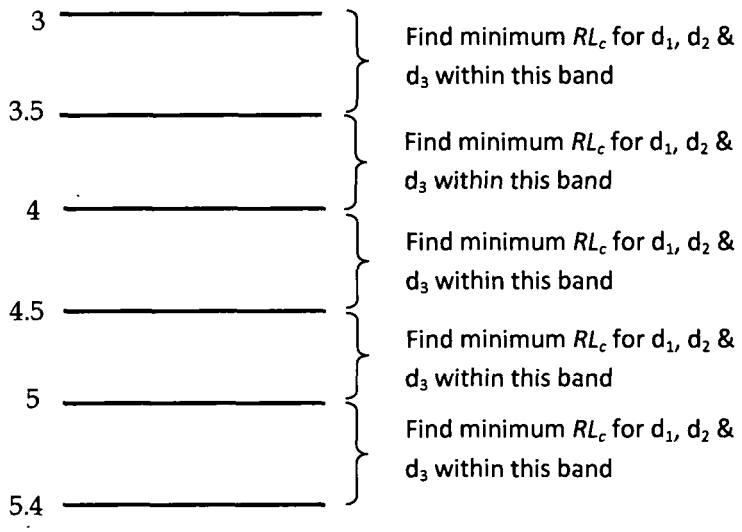

Figure 7. 18 The scheme of thickness variation to find minimum RL_c and required absorption bandwidth

7.3.1. RESULTS OF CALCULATED REFLECTION LOSS AND OPTIMIZED THICKNESS OF TRIPLE LAYER MICROWAVE ABSORBER

The frequency dependent RL_c, real impedance, Z_{in}' and imaginary impedance, Z_{in}'', and the triple layer design **BCA** with optimized layer thickness is plotted in figure 7.19 (a), (b) and (c), respectively. The maximum absorption peak, -25dB and -30dB absorption bandwidth and optimized individual layer thickness is tabulated in table 7.16.

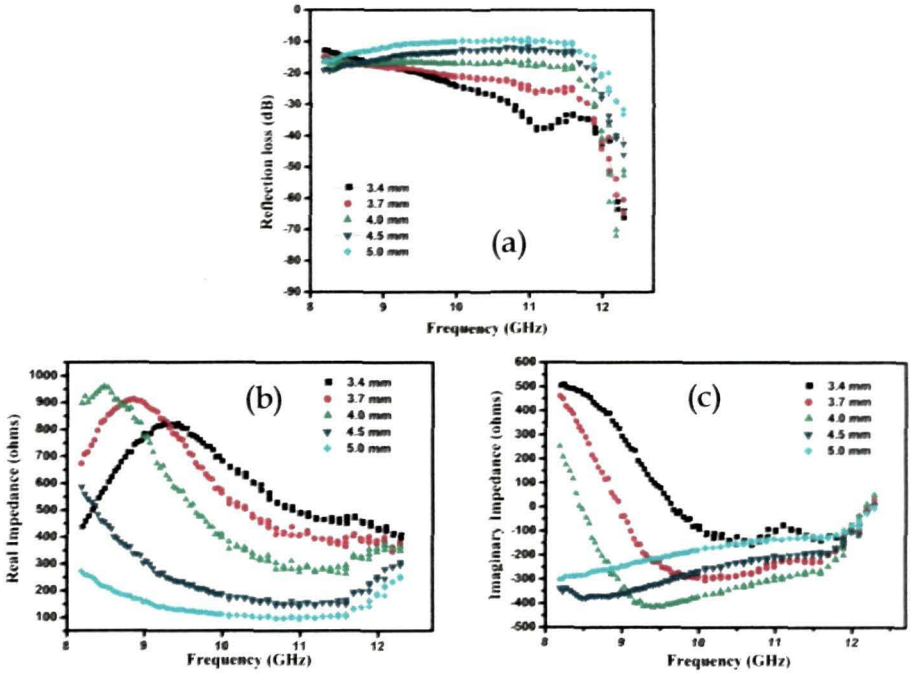

Figure 7.19 Plots of (a) RLc (b) Z_{in}' and (c) Z_{in}'' of designed **BCA** combined triple layer absorber with optimized thickness over the X-band

Table 7.16 Performance parameters of the designed **BCA** triple layer absorber with different thickness of the layers

Total thickness (mm)	Thickness of individual layers (mm)			Maximum absorption with corresponding frequency		Bandwidth in (GHz)	
d	**d1**	**d2**	**d3**	**$RL_{c\ min}$ (dB)**	**f_0 (GHz)**	**-25dB**	**-30dB**
3.4	0.5	2.0	0.9	-36.1	12.3	2.06	1.53
3.7	1.0	1.1	1.6	-31.6	12.2	0.76	0.49
4	0.8	0.6	2.6	-18.7	12.2	0.42	0.34
4.5	0.6	0.5	3.4	-15.3	12.3	0.34	0.24
5	0.5	0.5	4.0	-12.9	12.3	0.23	0.08

Figure 7.20(a), (b) and (c) shows the frequency dependent RL_c, real impedance Z_{in}' and imaginary impedance Z_{in}'' results respectively, of the triple layer design **BDA** with optimized thickness. The maximum absorption peak with -25dB and -30dB absorption bandwidth and optimized individual layer thickness is tabulated in table 7.17.

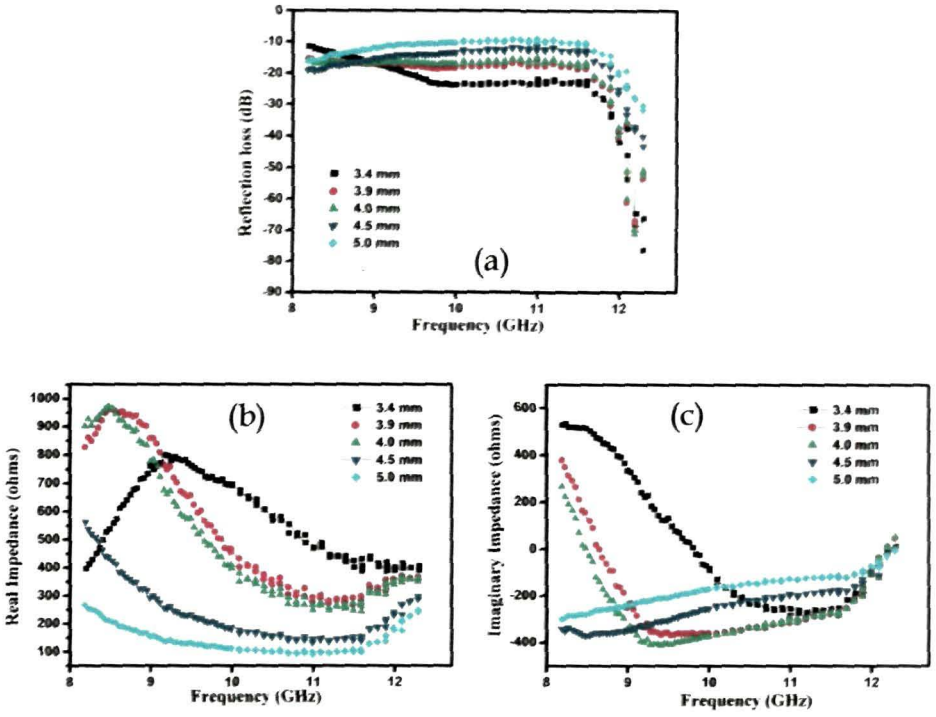

Figure 7.20 Plots of (a) RL_c, (b) Z_{in}' *and* (*c*) Z_{in}'' of designed **BDA** triple layer absorber with optimize thickness over the X-band

Table 7.17 Performance parameters of the designed **BDA** triple layer absorber with different thickness of the layers

Total thickness (mm)	**Thickness of individual layers (mm)**			**Maximum absorption with corresponding frequency**		**Bandwidth in (GHz)**	
d	**d1**	**d2**	**d3**	**$RL_{c\ min}$ (dB)**	**f_0 (GHz)**	**-25dB**	**-30dB**
3.4	1.2	0.7	1.5	-43.6	12.3	0.64	0.44
3.9	0.6	0.7	2.7	-21.8	12.2	0.44	0.42
4	0.5	0.5	3.0	-12.6	12.2	0.43	0.40
4.5	0.6	0.5	3.4	-10.2	12.3	0.32	0.21
5	0.5	0.5	4.0	-9.6	12.3	0.19	0.02

Figure 7.21(a), (b) and (c) shows the frequency dependent RL_c, real impedance Z_{in}' and imaginary impedance Z_{in}'' results respectively, of the triple layer design **CBA** with optimized thickness. The maximum absorption peak with -25dB and -30dB absorption bandwidth and optimized individual layer thickness is tabulated in table 7.18.

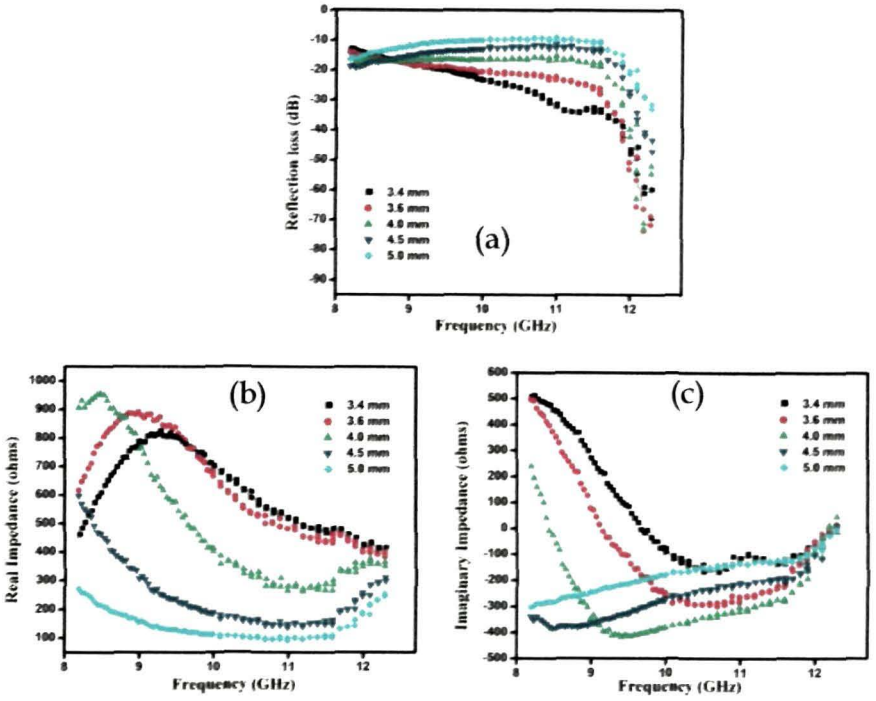

Figure 7.21 Plots of (a) RL_c, (b) Z_{in}' *and* (c) Z_{in}'' of designed **CBA** triple layer absorber with optimize thickness over the X-band

Table 7.18 Performance parameters of the designed **CBA** triple layer absorber with different thickness of the layers

Total thickness (mm)	**Thickness of individual layers (mm)**			**Maximum absorption with corresponding frequency**		**Bandwidth in (GHz)**	
d	**d1**	**d2**	**d3**	**$RL_{c\ min}$ (dB)**	**f_0 (GHz)**	**-25dB**	**-30dB**
3.4	2.2	0.5	0.7	-41.0	12.3	2.0	1.41
3.6	1.4	1.2	1.0	-40.2	12.3	0.86	0.65
4	0.5	1.0	2.4	-20.9	12.2	0.47	0.36
4.5	0.5	0.5	3.5	-17.5	12.3	0.36	0.27
5	0.7	0.5	3.8	-15.3	12.3	0.25	0.07

Figure 7.22(a), (b) and (c) shows the frequency dependent RL_c, real impedance $Z_{in}{}'$ and imaginary impedance $Z_{in}{}''$ results respectively, of the triple layer design **CDA** with optimized thickness. The maximum absorption peak with -25dB and -30dB absorption bandwidth and optimized individual layer thickness is tabulated in table 7.19.

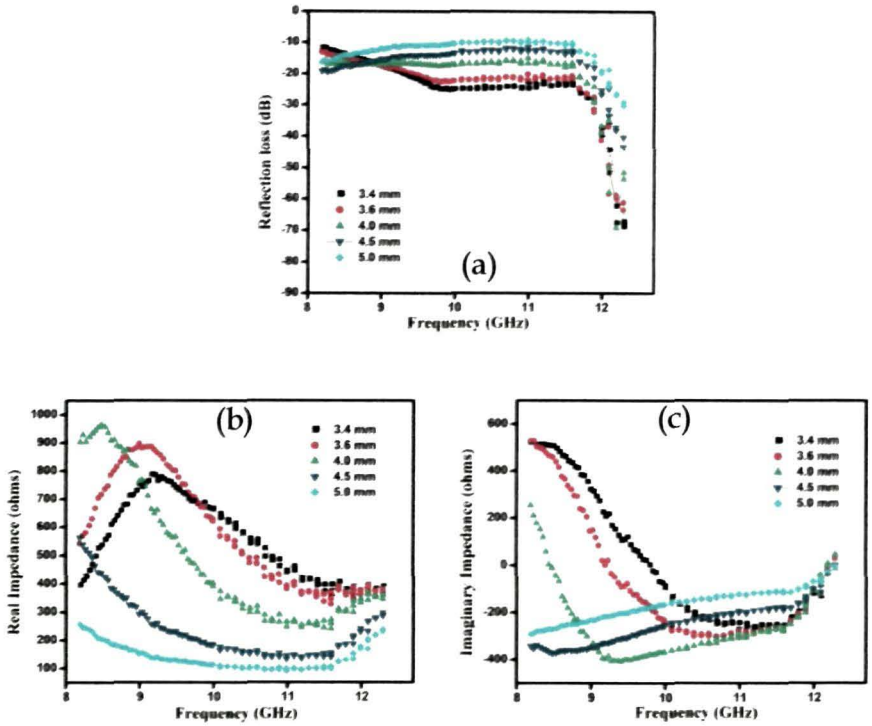

Figure 7.22 Plots of (a) RL_c, (b) $Z_{in}{}'$ *and* (*c*) $Z_{in}{}''$ of designed **CDA** triple layer absorber with optimize thickness over the X-band

Table 7.19 Performance parameters of the designed **CDA** triple layer absorber with different thickness of the layers

Total thickness (mm)	Thickness of individual layers (mm)			Maximum absorption with corresponding frequency		Bandwidth in GHz	
d	**d1**	**d2**	**d3**	**$RL_{c\ min}$ (dB)**	**f_0 (GHz)**	**-25dB**	**-30dB**
3.4	0.7	1.1	1.6	-35.0	12.3	2.38	0.45
3.6	0.8	0.8	2.0	-19.8	12.2	0.63	0.44
4	0.6	0.5	2.9	-12.9	12.2	0.39	0.37
4.5	0.5	0.6	3.4	-29.0	12.3	0.3	0.24
5	0.6	0.6	3.8	-7.8	12.3	0.21	0.04

Figure 7.23(a), (b) and (c) shows the frequency dependent RL_c, real impedance Z_{in}' and imaginary impedance Z_{in}'' results respectively, of the triple layer design **DBA** with optimized thickness. The maximum absorption peak with -25dB and -30dB absorption bandwidth and optimized individual layer thickness is tabulated in table 7.20.

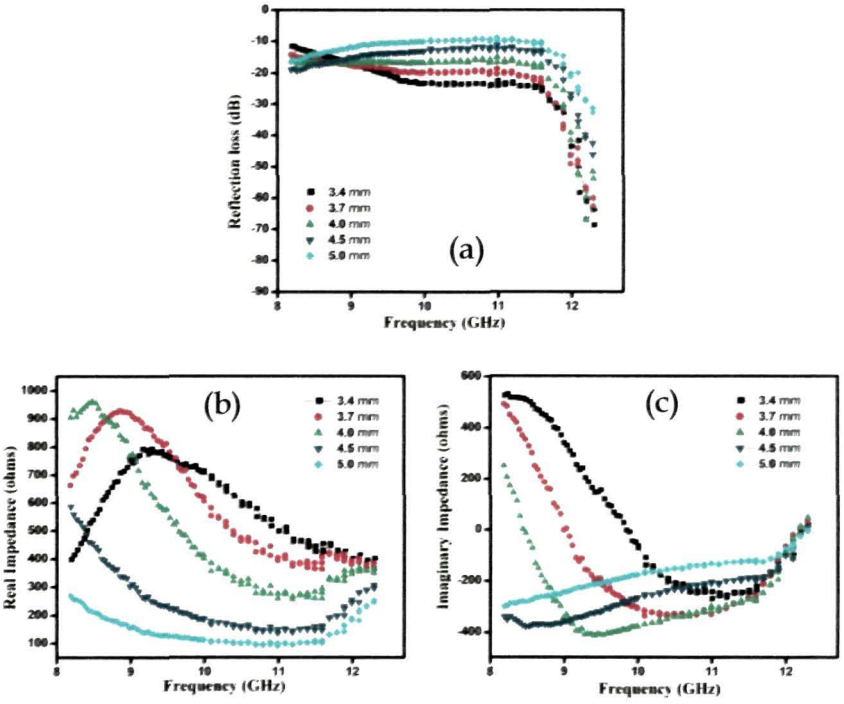

Figure 7.23 Plots of (a) RL_c, (b) Z_{in}' *and* (*c*) Z_{in}'' of designed **DBA** triple layer absorber with optimize thickness over the X-band

Table 7.20 Performance parameters of the designed **DBA** triple layer absorber with different thickness of the layers

Total thickness (mm)	**Thickness of individual layers (mm)**			**Maximum absorption with corresponding frequency**		**Bandwidth in (GHz)**	
d	**d1**	**d2**	**d3**	**$RL_{c\ min}$ (dB)**	**f_0 (GHz)**	**-25dB**	**-30dB**
3.4	1.6	0.5	1.3	-40.5	12.3	0.72	0.57
3.7	1.0	1.1	1.6	-24.3	12.3	0.65	0.49
4	0.7	0.8	2.5	-32.2	12.2	0.45	0.42
4.5	0.6	0.5	3.4	-13.8	12.3	0.34	0.27
5	0.6	0.6	3.8	-14.7	12.3	0.22	0.08

Figure 7.24(a), (b) and (c) shows the frequency dependent RL_c, real impedance Z_{in}' and imaginary impedance Z_{in}'' results respectively, of the triple layer design **DCA** with optimized thickness. The maximum absorption peak with -25dB and -30dB absorption bandwidth and optimized individual layer thickness is tabulated in table 7.21.

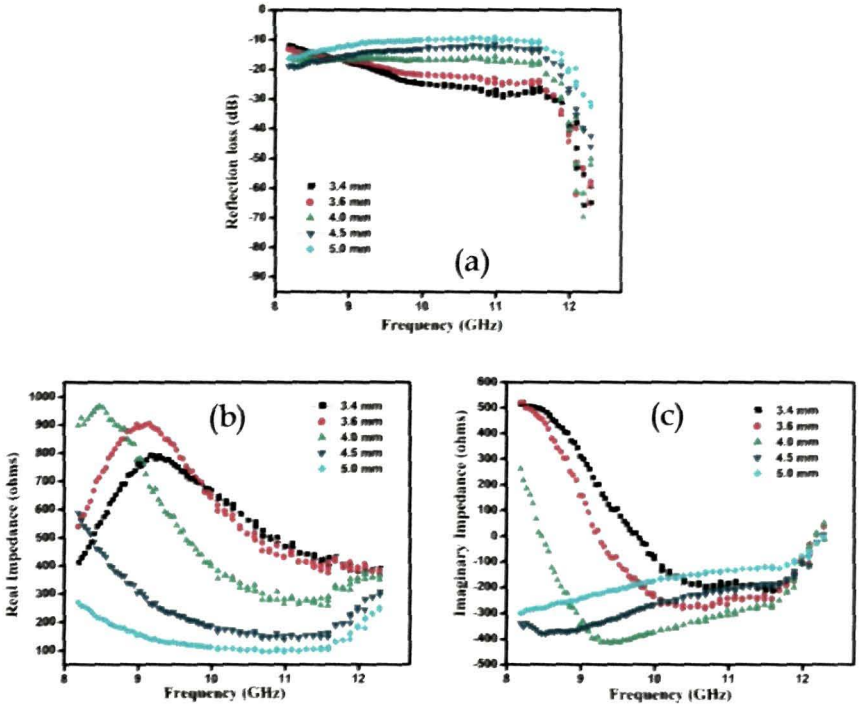

Figure 7.24 Plots of (a) RL_c, (b) Z_{in}' *and* (c) Z_{in}'' of designed **DCA** triple layer absorber with optimize thickness over the X-band

Table 7.21 Performance parameters of the designed **DCA** triple layer absorber with different thickness of the layers

Total thickness (mm)	**Thickness of individual layers (mm)**			**Maximum absorption with corresponding frequency**		**Bandwidth in (GHz)**	
d	**d1**	**d2**	**d3**	**$RL_{c\ min}$ (dB)**	**f_0 (GHz)**	**-25dB**	**-30dB**
3.4	1.5	0.6	1.3	-48.7	12.3	1.94	0.52
3.6	1.2	0.7	1.7	-69.0	12.3	0.71	0.44
4	0.7	0.6	2.8	-14.3	12.2	0.42	0.38
4.5	0.5	0.5	3.4	-12.9	12.3	0.31	0.22
5	0.5	0.6	3.9	-11.7	12.3	0.21	0.06

Figure 7.25(a), (b) and (c) shows the frequency dependent RL_c, real impedance Z_{in} and imaginary impedance Z_{in}'' results respectively, of the triple layer design **ACB** with optimized thickness. The maximum absorption peak with -25dB and -30dB absorption bandwidth and optimized individual layer thickness is tabulated in table 7.22.

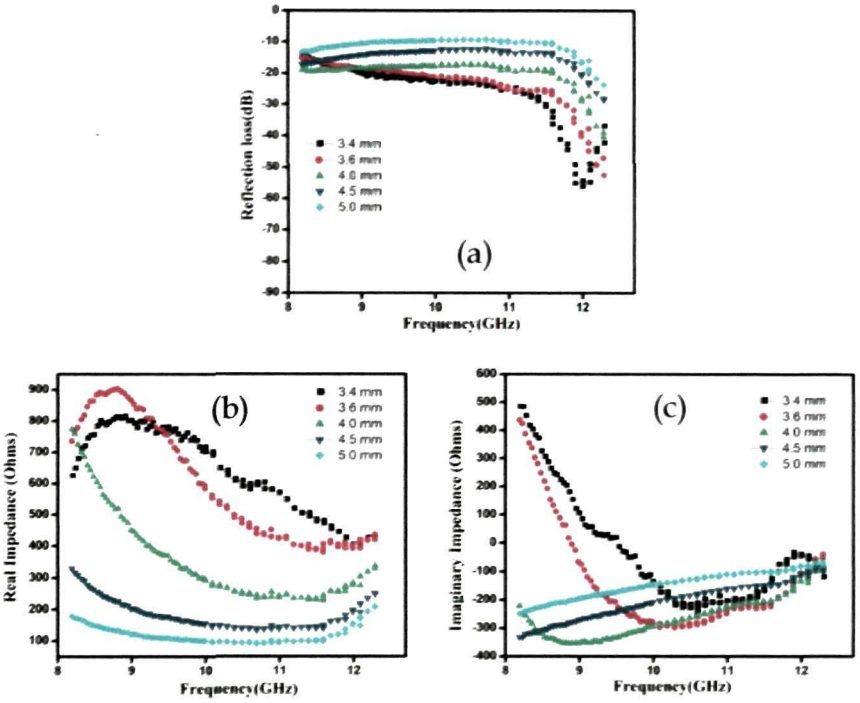

Figure 7.25 Plots of (a) RL_c, (b) Z_{in}' *and* (*c*) Z_{in}'' of designed **ACB** triple layer absorber with optimize thickness over the X-band

Table 7.22 Performance parameters of the designed **ACB** triple layer absorber with different thickness of the layers

Total thickness (mm)	**thickness of individual layers (mm)**			**Maximum absorption with corresponding frequency**		**Bandwidth in (GHz)**	
d	**d1**	**d2**	**d3**	**$RL_{c\ min}$ (dB)**	**f_0 (GHz)**	**-25dB**	**-30dB**
3.4	0.5	0.6	2.3	-42.9	12	1.23	0.84
3.6	2.6	0.5	0.5	-24.9	12.3	1.15	0.51
4	2.9	0.5	0.5	-19.2	12.3	0.4	0.25
4.5	3.4	0.5	0.6	-16.1	12.3	0.2	--
5	3.9	0.6	0.5	-11.7	12.3	--	--

Figure 7.26(a), (b) and (c) shows the frequency dependent RL_c, real impedance $Z_{in}{}'$ and imaginary impedance $Z_{in}{}''$ results respectively, of the triple layer design **ADB** with optimized thickness. The maximum absorption peak with -25dB and -30dB absorption bandwidth and optimized individual layer thickness is tabulated in table 7.23.

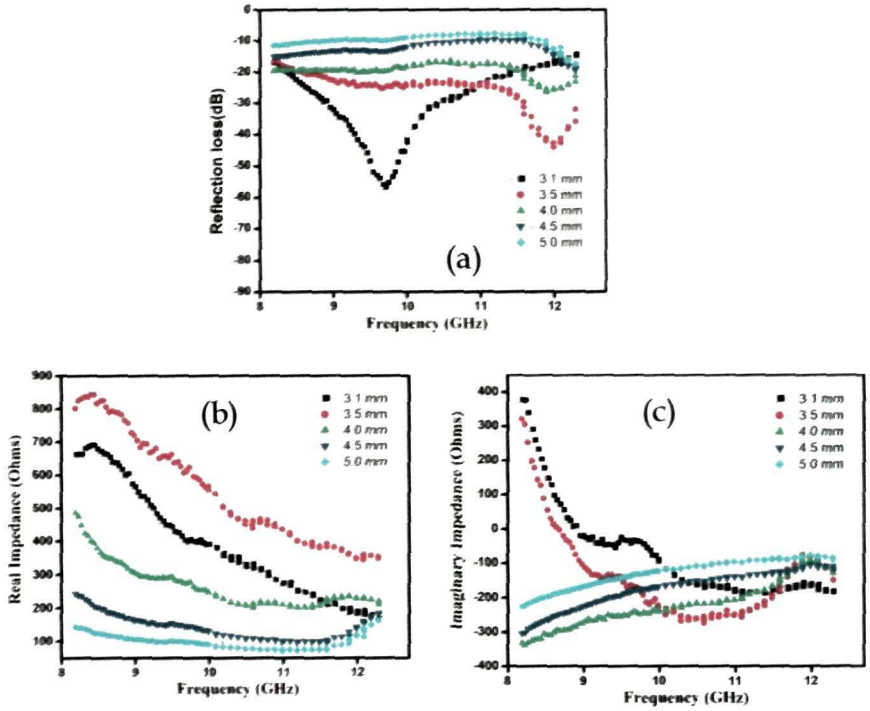

Figure 7.26 Plots of (a) RL_c, (b) $Z_{in}{}'$ *and* (c) $Z_{in}{}''$ of designed **ADB** triple layer absorber with optimize thickness over the X-band

Table 7.23 Performance parameters of the designed **ADB** triple layer absorber with different thickness of the layers

Total thickness (mm)	**Thickness of individual layers (mm)**			**Maximum absorption with corresponding frequency**		**Bandwidth in (GHz)**	
	d1	**d2**	**d3**	**$RL_{c\ min}$ (dB)**	**f_0 (GHz)**	**-25dB**	**-30dB**
3.1	0.5	2.1	0.5	-35.8	9.7	2.23	1.45
3.5	0.5	0.6	2.4	-19.4	11.9	1	0.72
4	0.6	0.5	2.8	-12.1	11.9	--	--
4.5	3.4	0.5	0.6	-12.2	12.3	--	--
5	4.0	0.5	0.5	-10.3	12.3	--	--

Figure 7.27(a), (b) and (c) shows the frequency dependent RL_c, real impedance Z_{in}' and imaginary impedance Z_{in}'' results respectively, of the triple layer design **CAB** with optimized thickness. The maximum absorption peak with -25dB and -30dB absorption bandwidth and optimized individual layer thickness is tabulated in table 7.24.

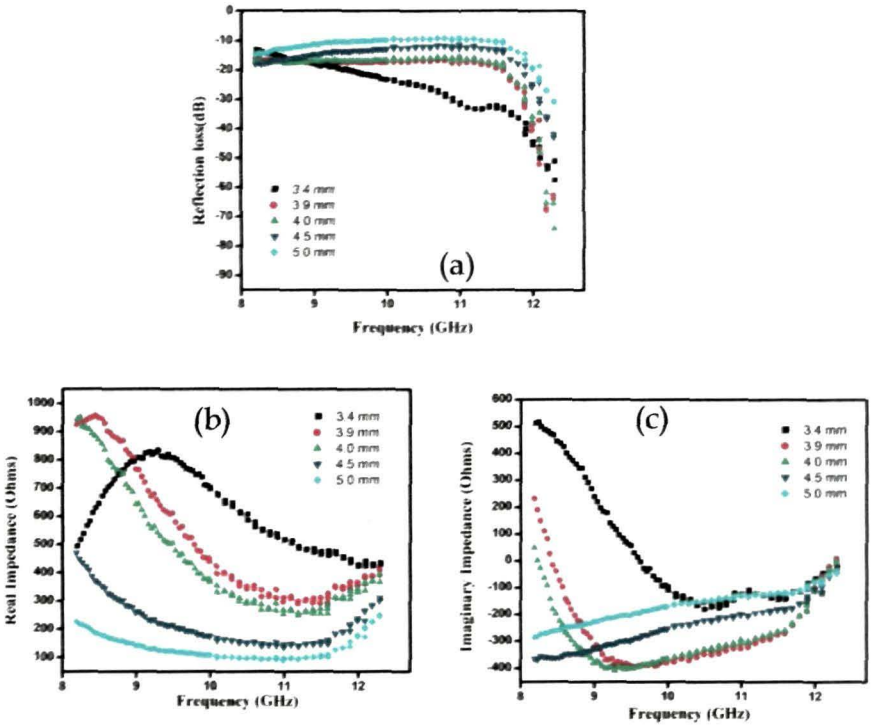

Figure 7.27 Plots of (a) RL_c, (b) Z_{in}' *and* (*c*) Z_{in}'' of designed **CAB** triple layer absorber with optimize thickness over the X-band

Table 7.24 Performance parameters of the designed **CAB** triple layer absorber with different thickness of the layers

Total thickness (mm)	**Thickness of individual layers (mm)**			**Maximum absorption with corresponding frequency**		**Bandwidth in (GHz)**	
d	**d1**	**d2**	**d3**	**$RL_{c\ min}$ (dB)**	**f_0 (GHz)**	**-25dB**	**-30dB**
3.4	2.2	0.7	0.5	-56.8	12.3	1.85	1.43
3.9	0.6	2.7	0.6	-62.7	12.3	0.54	0.45
4	0.5	2.9	0.5	-24.2	12.3	0.46	0.93
4.5	0.5	3.4	0.5	-22.3	12.3	0.31	0.22
5	0.6	3.9	0.6	-16.6	12.3	0.17	0.06

Figure 7.28(a), (b) and (c) shows the frequency dependent RL_c, real impedance Z_{in}' and imaginary impedance Z_{in}'' results respectively, of the triple layer design **CDB** with optimized thickness. The maximum absorption peak with -25dB and -30dB absorption bandwidth and optimized individual layer thickness is tabulated in table 7.25.

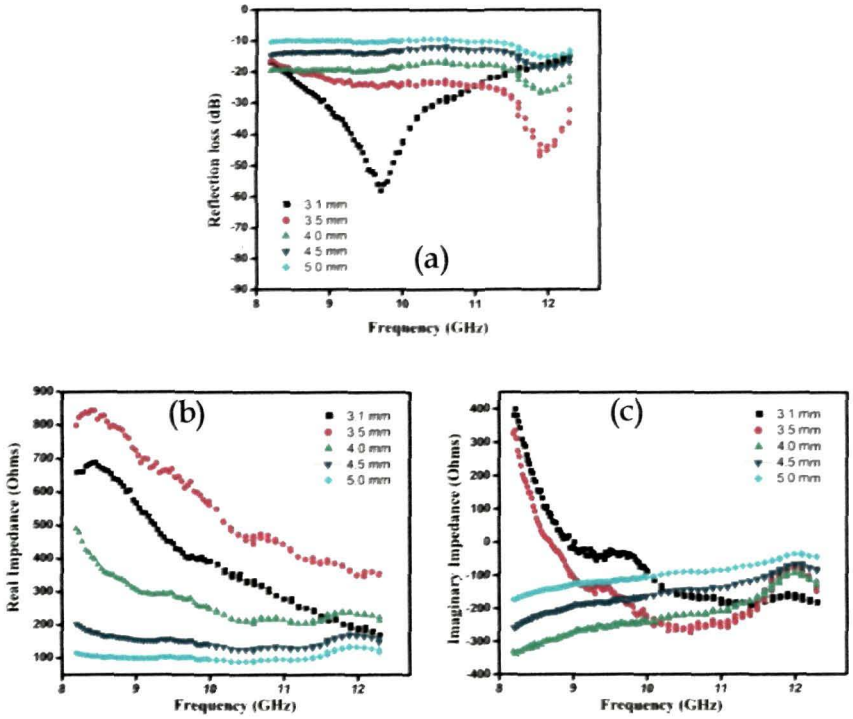

Figure 7.28 Plots of (a) RL_c, (b) Z_{in}' *and* (c) Z_{in}'' of designed **CDB** triple layer absorber with optimize thickness over the X-band

Table 7.25 Performance parameters of the designed **CDB** triple layer absorber with different thickness of the layers

Total thickness (mm)	**Thickness of individual layers (mm)**			**Maximum absorption with corresponding frequency**		**Bandwidth in (GHz)**	
	d1	**d2**	**d3**	**$RL_{c\ min}$ (dB)**	**f_0 (GHz)**	**-25dB**	**-30dB**
3.1	0.5	2.0	0.6	-37.1	9.7	2.31	1.46
3.5	0.5	0.5	2.4	-18.7	11.9	0.96	0.72
4	0.5	0.5	3.0	-17.8	11.9	0.34	--
4.5	0.6	0.5	3.4	-11.3	11.9	--	--
5	0.6	0.5	3.9	-8.0	12.0	--	--

Figure 7.29(a), (b) and (c) shows the frequency dependent RL_C, real impedance Z_{in}' and imaginary impedance Z_{in}'' results respectively, of the triple layer design **DAB** with optimized thickness. The maximum absorption peak with -25dB and -30dB absorption bandwidth and optimized individual layer thickness is tabulated in table 7.26.

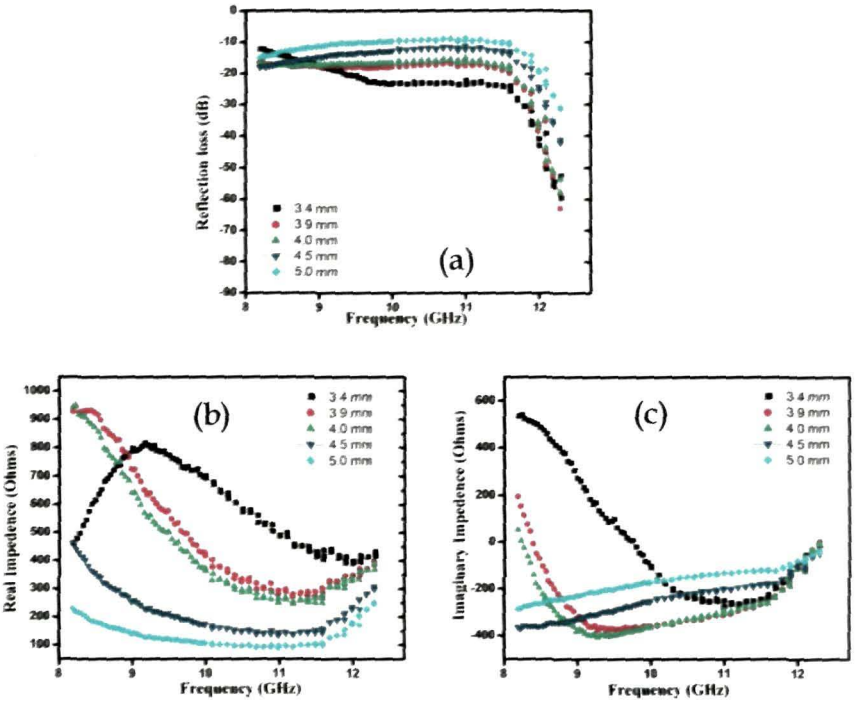

Figure 7.29 Plots of (a) RL_C, (b) Z_{in}' *and* (c) Z_{in}'' of designed **DAB** triple layer absorber with optimize thickness over the X-band

Table 7.26 Performance parameters of the designed **DAB** triple layer absorber with different thickness of the layers

Total thickness (mm)	Thickness of individual layers (mm)			Maximum absorption with corresponding frequency		Bandwidth in (GHz)	
	d1	d2	d3	$RL_{C\ min}$ (dB)	f_0 (GHz)	-25dB	-30dB
3.4	1.6	1.3	0.5	-50.3	12.3	0.73	0.58
3.9	0.9	2.4	0.5	-31.6	12.3	0.54	0.43
4	0.6	2.9	0.5	-16.3	12.3	0.5	0.4
4.5	0.5	3.4	0.6	-16.4	12.3	0.32	0.21
5	0.5	4.0	0.5	-11.4	12.3	0.19	0.04

Figure 7.30(a), (b) and (c) shows the frequency dependent RL_c, real impedance Z_{in}' and imaginary impedance Z_{in}'' results respectively, of the triple layer design **DCB** with optimized thickness. The maximum absorption peak with -25dB and -30dB absorption bandwidth and optimized individual layer thickness is tabulated in table 7.27.

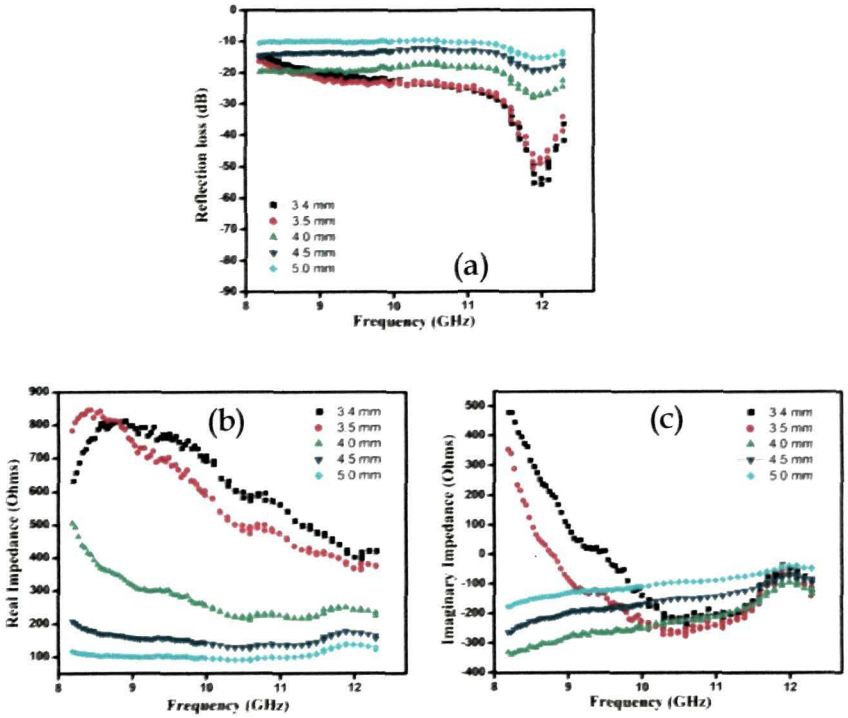

Figure 7.30 Plots of (a) RL_c, (b) Z_{in}' *and* (*c*) Z_{in}'' of designed **DCB** triple layer absorber with optimize thickness over the X-band

Table 7.27 Performance parameters of the designed **DCB** triple layer absorber with different thickness of the layers

Total thickness (mm)	**Thickness of individual layers (mm)**			**Maximum absorption with corresponding frequency**		**Bandwidth in (GHz)**	
d	**d1**	**d2**	**d3**	**$RL_{c\ min}$ (dB)**	**f_0 (GHz)**	**-25dB**	**-30dB**
3.4	0.5	0.6	2.3	-39.2	12.0	1.37	0.84
3.5	0.6	0.5	2.4	-22.6	11.9	1.22	0.79
4	0.5	0.6	2.9	-14.1	11.9	0.57	--
4.5	0.5	0.6	3.4	-15.9	11.9	--	--
5	0.6	0.7	3.7	-9.9	12.0	--	--

Figure 7.31(a), (b) and (c) shows the frequency dependent RL_c, real impedance Z_{in}' and imaginary impedance Z_{in}'' results respectively, of the triple layer design **ABC** with optimized thickness. The maximum absorption peak with -25dB and -30dB absorption bandwidth and optimized individual layer thickness is tabulated in table 7.28.

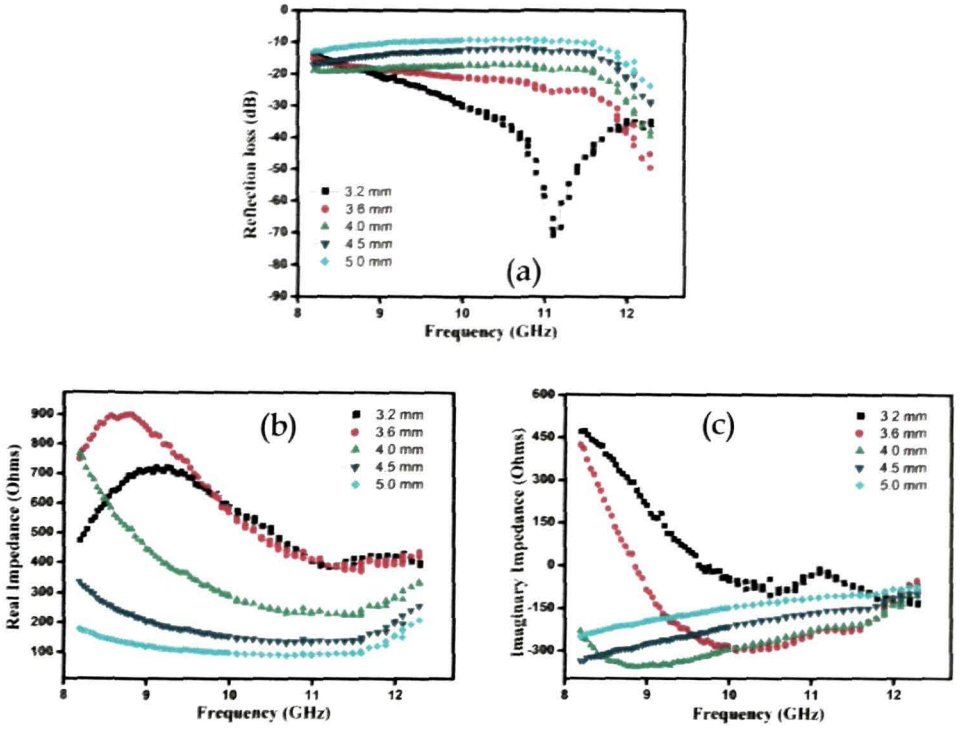

Figure 7.31 Plots of (a) RL_c, (b) Z_{in}' *and* (c) Z_{in}'' of designed **ABC** triple layer absorber with optimize thickness over the X-band

Table 7.28 Performance parameters of the designed **ABC** triple layer absorber with different thickness of the layers

Total thickness (mm)	**Thickness of individual layers (mm)**			**Maximum absorption with corresponding frequency**		**Bandwidth in (GHz)**	
d	**d1**	**d2**	**d3**	**$RL_{c\ min}$ (dB)**	**f_0 (GHz)**	**-25dB**	**-30dB**
3.2	0.5	0.5	2.2	-70.8	11.1	2.74	2.31
3.6	2.6	0.5	0.5	-49.4	12.3	0.74	0.47
4	2.9	0.5	0.5	-39.4	12.3	0.41	0.24
4.5	3.4	0.6	0.5	-29.2	12.3	0.18	--
5	3.9	0.5	0.6	-23.8	12.3	0.19	--

Figure 7.32(a), (b) and (c) shows the frequency dependent RL_c, real impedance Z_{in}' and imaginary impedance Z_{in}'' results respectively, of the triple layer design **ADC** with optimized thickness. The maximum absorption peak with -25dB and -30dB absorption bandwidth and optimized individual layer thickness is tabulated in table 7.29.

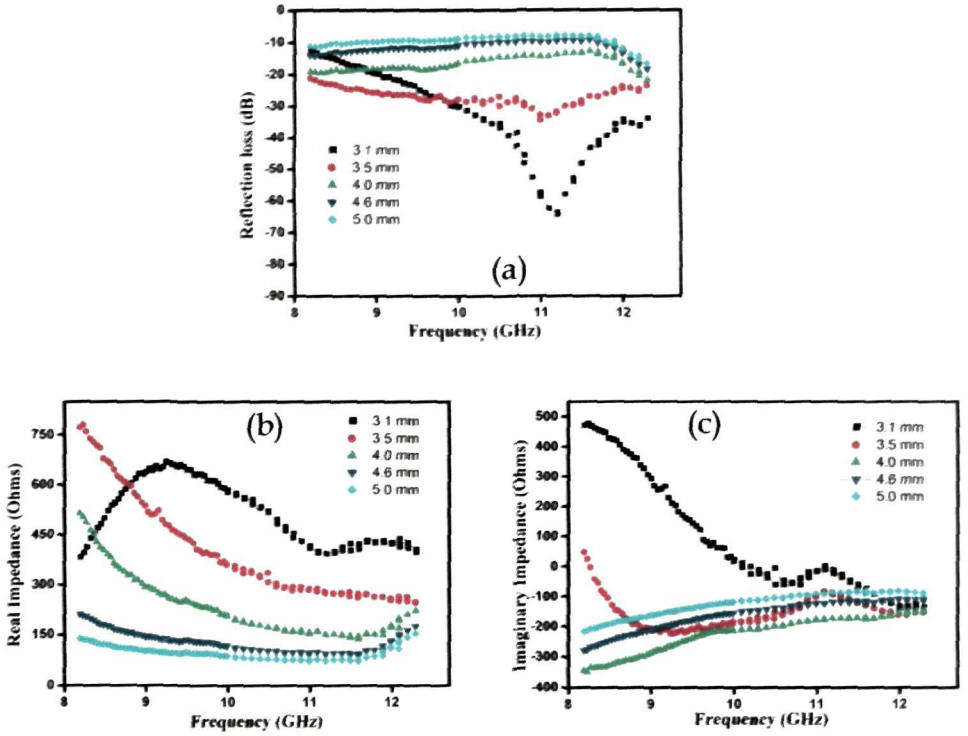

Figure 7.32 Plots of (a) RL_c, (b) Z_{in}' *and* (*c*) Z_{in}'' of designed **ADC** triple layer absorber with optimize thickness over the X-band

Table 7.29 Performance parameters of the designed **ADC** triple layer absorber with different thickness of the layers

Total thickness (mm)	**Thickness of individual layers (mm)**			**Maximum absorption with corresponding frequency**		**Bandwidth in (GHz)**	
d	**d1**	**d2**	**d3**	**$RL_{c\ min}$ (dB)**	**f_0 (GHz)**	**-25dB**	**-30dB**
3.1	0.5	0.6	2.0	-30.9	11.1	2.77	2.32
3.5	0.6	0.5	2.4	-17.0	11.1	2.96	0.43
4	3.0	0.5	0.5	-12.5	12.3	--	--
4.6	3.6	0.5	0.5	-9.4	12.3	--	--
5	3.9	0.5	0.5	-9.3	12.3	--	--

Figure 7.33(a), (b) and (c) shows the frequency dependent RL_c, real impedance Z_{in}' and imaginary impedance Z_{in}'' results respectively, of the triple layer design **BAC** with optimized thickness. The maximum absorption peak with -25dB and -30dB absorption bandwidth and optimized individual layer thickness is tabulated in table 7.30.

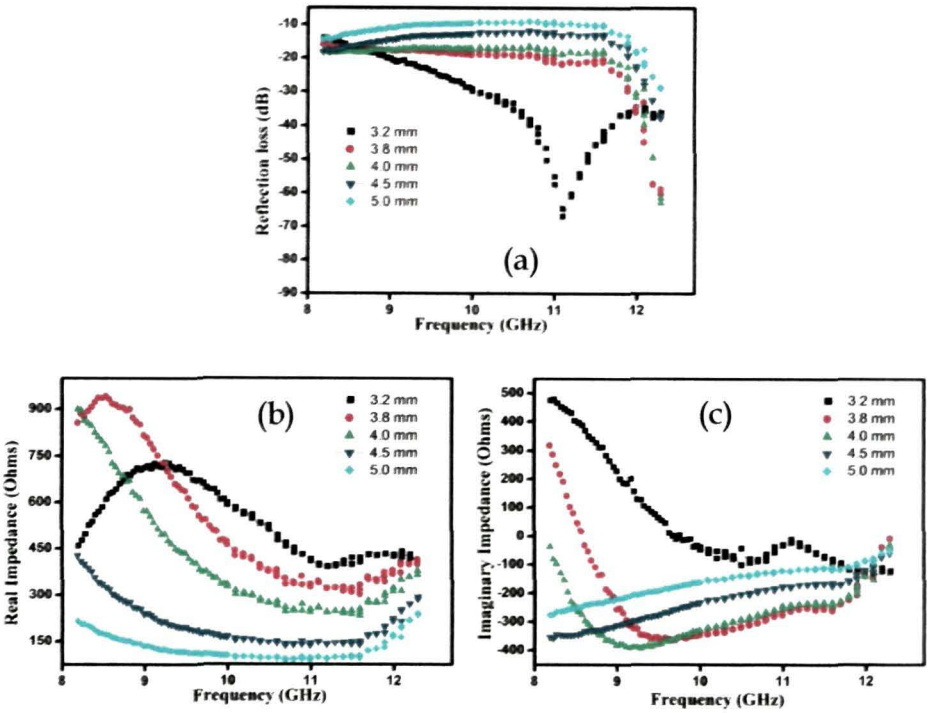

Figure 7.33 Plots of (a) RL_c, (b) Z_{in}' *and* (c) Z_{in}'' of designed **BAC** triple layer absorber with optimize thickness over the X-band

Table 7.30 Performance parameters of the designed **BAC** triple layer absorber with different thickness of the layers

Total thickness (mm)	**Tthickness of individual layers (mm)**			**Maximum absorption with corresponding frequency**		**Bandwidth in (GHz)**	
d	**d1**	**d2**	**d3**	$RL_{c\,min}$ **(dB)**	f_0 **(GHz)**	**-25dB**	**-30dB**
3.2	0.5	0.5	2.2	-42.6	11.1	2.72	2.21
3.8	0.8	2.5	0.5	-45.3	12.3	1.14	0.4
4	0.5	3.0	0.5	-27.3	12.3	0.41	0.29
4.5	0.9	3.1	0.5	-12.9	12.3	0.27	0.18
5	0.6	3.9	0.5	-20.7	12.3	0.22	--

Figure 7.34(a), (b) and (c) shows the frequency dependent RL_c, real impedance Z_{in}' and imaginary impedance Z_{in}'' results respectively, of the triple layer design **BDC** with optimized thickness. The maximum absorption peak with -25dB and -30dB absorption bandwidth and optimized individual layer thickness is tabulated in table 7.31.

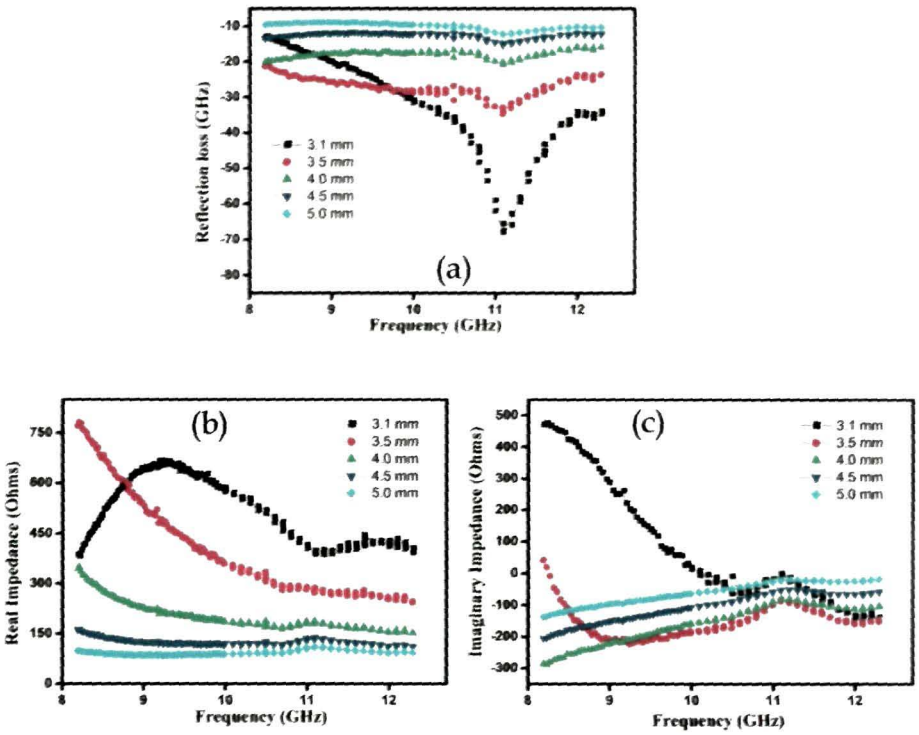

Figure 7.34 Plots of (a) RL_c, (b) Z_{in}' *and* (*c*) Z_{in}'' of designed **BDC** triple layer absorber with optimize thickness over the X-band

Table 7.31 Performance parameters of the designed **BDC** triple layer absorber with different thickness of the layers

Total thickness (mm)	**Thickness of individual layers (mm)**			**Maximum absorption with corresponding frequency**		**Bandwidth in (GHz)**	
d	**d1**	**d2**	**d3**	**$RL_{c\ min}$ (dB)**	**f_0 (GHz)**	**-25dB**	**-30dB**
3.1	0.5	0.6	1.9	-29.5	11.1	2.76	2.39
3.5	0.6	0.5	2.4	-16.8	11.1	2.91	.52
4	0.6	0.5	2.9	-11.8	11.1	--	--
4.5	0.5	0.6	3.4	-12.4	11.1	--	--
5	0.6	0.6	3.8	-7.4	11.1	--	--

Figure 7.35(a), (b) and (c) shows the frequency dependent RL_C, real impedance Z_{in}' and imaginary impedance Z_{in}'' results respectively, of the triple layer design **DAC** with optimized thickness. The maximum absorption peak with -25dB and -30dB absorption bandwidth and optimized individual layer thickness is tabulated in table 7.32.

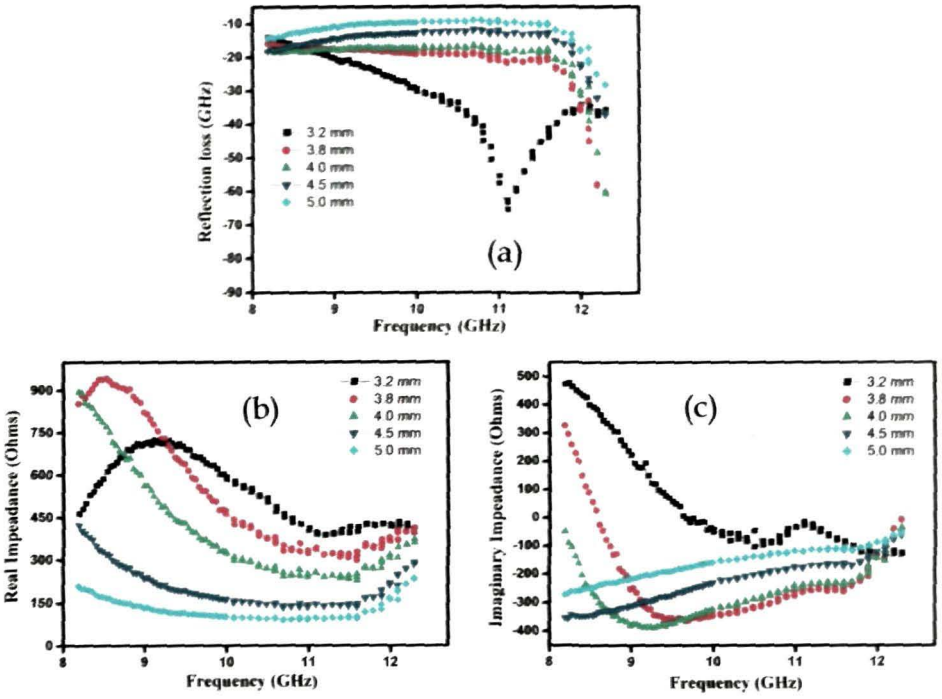

Figure 7.35 Plots of (a) RL_C, (b) Z_{in}' *and* (c) Z_{in}'' of designed **DAC** triple layer absorber with optimize thickness over the X-band

Table 7.32 Performance parameters of the designed **DAC** triple layer absorber with different thickness of the layers

Total thickness (mm)	**thickness of individual layers (mm)**			**Maximum absorption with corresponding frequency**		**Bandwidth in (GHz)**	
d	**d1**	**d2**	**d3**	**$RL_{c\ min}$ (dB)**	**f_0 (GHz)**	**-25dB**	**-30dB**
3.2	0.5	0.5	2.2	-37.8	11.1	2.74	2.25
3.8	0.5	2.8	0.5	-37.6	12.3	0.49	0.4
4	0.6	2.9	0.5	-15.7	12.3	0.41	0.37
4.5	0.5	3.4	0.5	-14.7	12.3	0.26	0.16
5	0.6	3.9	0.6	-13.1	12.3	0.11	--

Figure 7.36(a), (b) and (c) shows the frequency dependent RL_c, real impedance Z_{in}' and imaginary impedance Z_{in}'' results respectively, of the triple layer design **DBC** with optimized thickness. The maximum absorption peak with -25dB and -30dB absorption bandwidth and optimized individual layer thickness is tabulated in table 7.33.

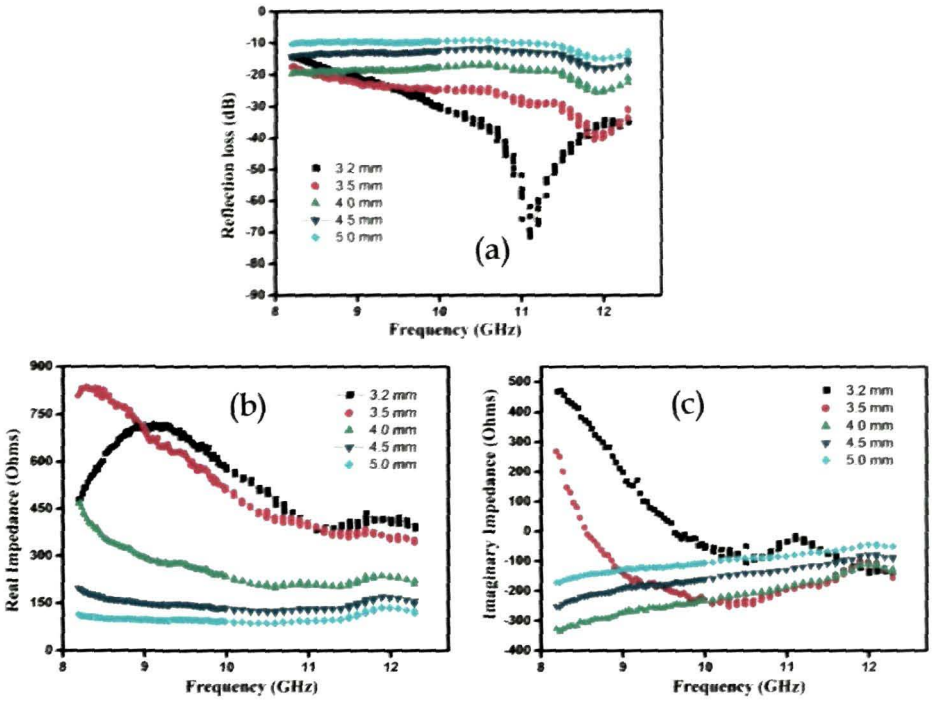

Figure 7.36 Plots of (a) RL_c, (b) Z_{in}' *and* (*c*) Z_{in}'' of designed **DBC** triple layer absorber with optimize thickness over the X-band

Table 7.33 Performance parameters of the designed **DBC** triple layer absorber with different thickness of the layers

Total thickness (mm)	**Thickness of individual layers (mm)**			**Maximum absorption with corresponding frequency**		**Bandwidth in (GHz)**	
d	**d1**	**d2**	**d3**	**$RL_{c\ min}$ (dB)**	**f_0 (GHz)**	**-25dB**	**-30dB**
3.2	0.5	0.5	2.2	-37.8	11.1	2.8	2.35
3.5	0.6	2.3	0.5	-22.3	11.9	1.63	0.73
4	0.5	3.0	0.5	-14.4	11.9	--	--
4.5	0.6	3.4	0.5	-12.8	12	--	--
5	0.6	3.9	0.5	-10.1	12	--	--

Figure 7.37(a), (b) and (c) shows the frequency dependent RL_c, real impedance Z_{in}' and imaginary impedance Z_{in}'' results respectively, of the triple layer design **ABD** with optimized thickness. The maximum absorption peak with -25dB and -30dB absorption bandwidth and optimized individual layer thickness is tabulated in table 7.34.

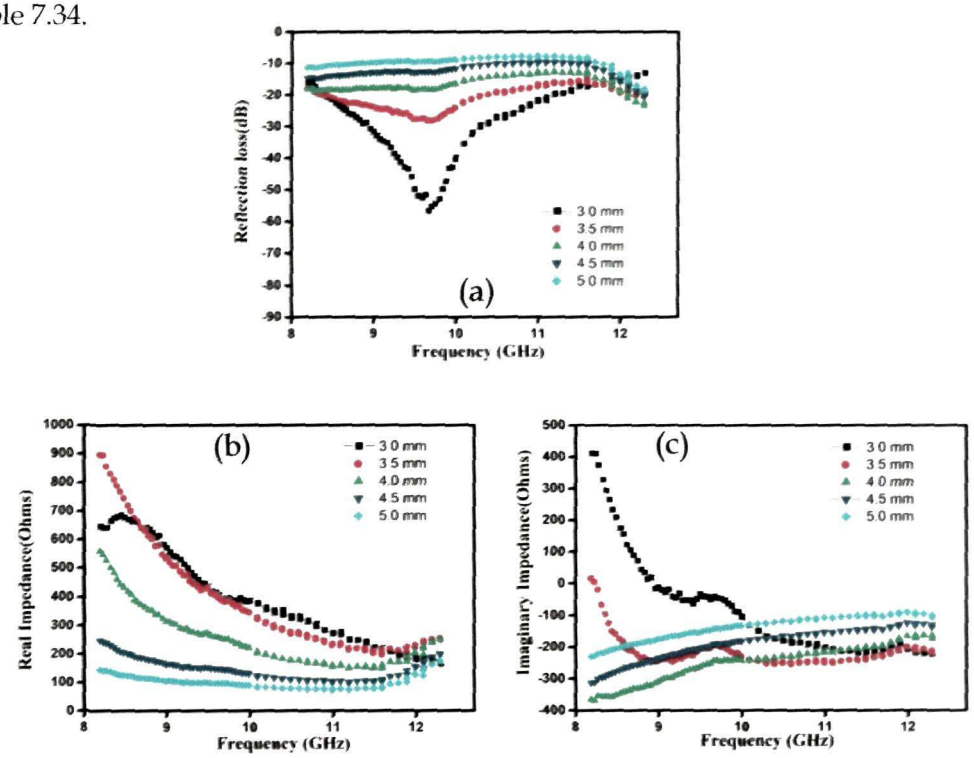

Figure 7.37 Plots of (a) RL_c, (b) Z_{in}' *and* (c) Z_{in}'' of designed **ABD** triple layer absorber with optimize thickness over the X-band

Table 7.34 Performance parameters of the designed **ABD** triple layer absorber with different thickness of the layers

Total thickness (mm)	**Thickness of individual layers (mm)**			**Maximum absorption with corresponding frequency**		**Bandwidth in (GHz)**	
d	**d1**	**d2**	**d3**	**$RL_{c\ min}$ (dB)**	**f_0 (GHz)**	**-25dB**	**-30dB**
3	0.9	0.6	1.6	-29.8	9.7	2.07	1.34
3.5	2.2	0.5	0.8	-18.7	9.7	0.59	--
4	2.9	0.5	0.5	-13.9	12.3	--	--
4.5	3.4	0.6	0.5	-8.3	12.3	--	--
5	3.9	0.6	0.5	-12.1	12.3	--	--

Figure 7.38(a), (b) and (c) shows the frequency dependent RL_c, real impedance Z_{in}' and imaginary impedance Z_{in}'' results respectively, of the triple layer design **ACD** with optimized thickness. The maximum absorption peak with -25dB and -30dB absorption bandwidth and optimized individual layer thickness is tabulated in table 7.35.

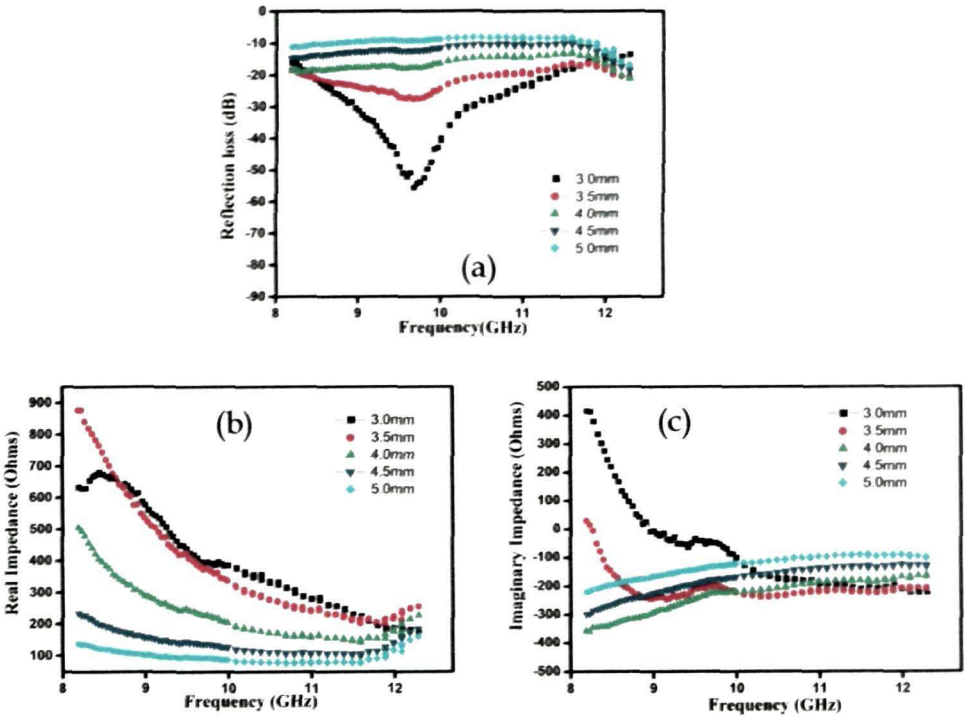

Figure 7.38 Plots of (a) RL_c, (b) Z_{in}' *and* (*c*) Z_{in}'' of designed **ACD** triple layer absorber with optimize thickness over the X-band

Table 7.35 Performance parameters of the designed **ACD** triple layer absorber with different thickness of the layers

Total thickness (mm)	Thickness of individual layers (mm)			Maximum absorption with corresponding frequency		Bandwidth in (GHz)	
d	**d1**	**d2**	**d3**	**$RL_{c\ min}$ (dB)**	**f_0 (GHz)**	**-25dB**	**-30dB**
3	1.0	0.5	1.5	-24.4	9.7	2.06	1.35
3.5	2.3	0.5	0.7	-15.1	9.7	--	--
4	3.0	0.5	0.5	-13.2	12.3	--	--
4.5	3.4	0.5	0.5	-10.1	12.3	--	--
5	3.9	0.5	0.5	-7.7	12.3	--	--

Figure 7.39(a), (b) and (c) shows the frequency dependent RL_c, real impedance Z_{in}' and imaginary impedance Z_{in}'' results respectively, of the triple layer design **BAD** with optimized thickness. The maximum absorption peak with -25dB and -30dB absorption bandwidth and optimized individual layer thickness is tabulated in table 7.36.

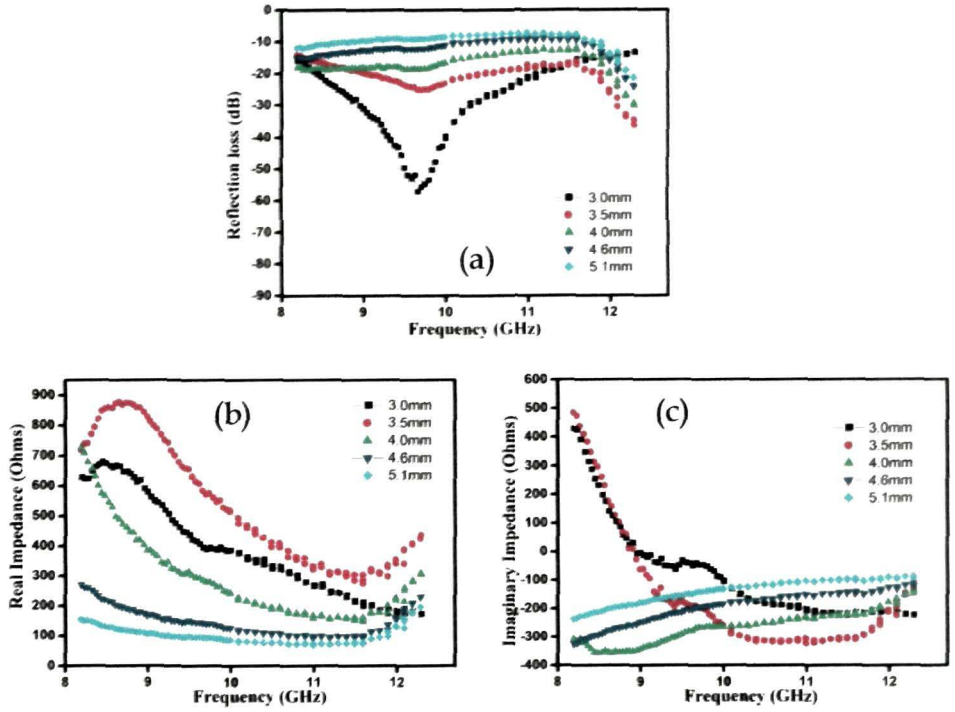

Figure 7.39 Plots of (a) RL_c, (b) Z_{in}' *and* (c) Z_{in}'' of designed **BAD** triple layer absorber with optimize thickness over the X-band

Table 7.36 Performance parameters of the designed **BAD** triple layer absorber with different thickness of the layers

Total thickness (mm)	**Thickness of individual layers (mm)**			**Maximum absorption with corresponding frequency**		**Bandwidth in GHz**	
d	**d1**	**d2**	**d3**	**$RL_{c\ min}$ (dB)**	**f_0 (GHz)**	**-25dB**	**-30dB**
3	0.5	0.8	1.6	-28.9	9.7	2	1.33
3.5	0.9	2.1	0.5	-20.9	12.3	0.33	0.19
4	0.6	2.9	0.5	-18.5	12.3	0.19	--
4.6	0.5	3.5	0.5	-12.4	12.3	0.02	--
5.1	0.6	4.0	0.5	-6.9	12.3	0.02	--

Figure 7.40(a), (b) and (c) shows the frequency dependent RL_c, real impedance Z_{in}' and imaginary impedance Z_{in}'' results respectively, of the triple layer design **BCD** with optimized thickness. The maximum absorption peak with -25dB and -30dB absorption bandwidth and optimized individual layer thickness is tabulated in table 7.37.

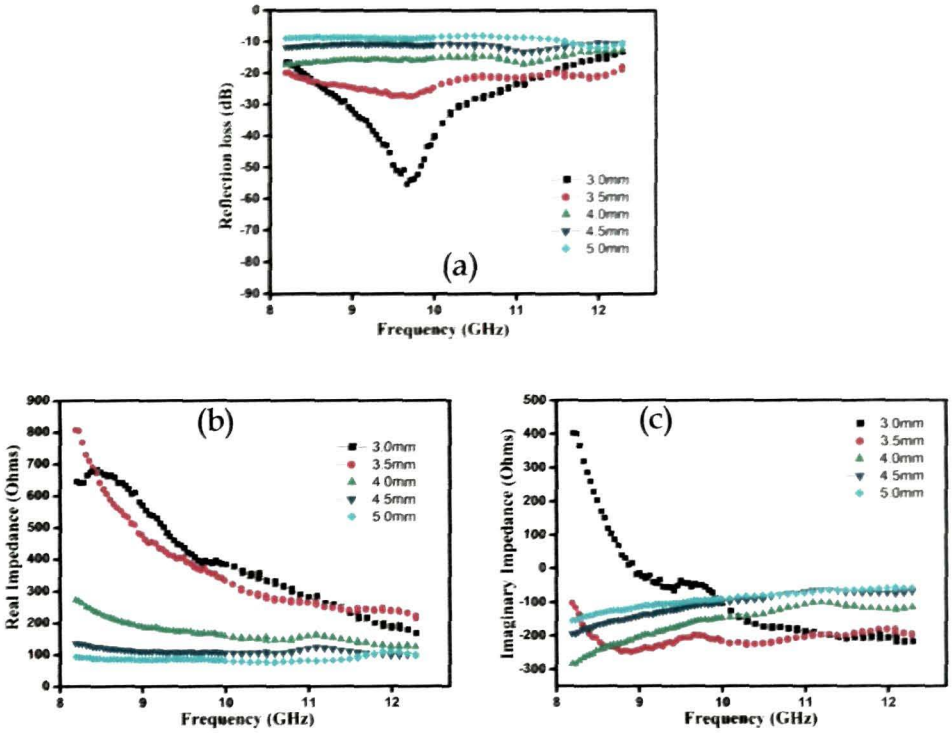

Figure 7.40 Plots of (a) RL_c, (b) Z_{in}' *and* (*c*) Z_{in}'' of designed **BCD** triple layer absorber with optimize thickness over the X-band

Table 7.37 Performance parameters of the designed **BCD** triple layer absorber with different thickness of the layers

Total thickness (mm)	Thickness of individual layers (mm)			Maximum absorption with corresponding frequency		Bandwidth in (GHz)	
d	**d1**	**d2**	**d3**	**$RL_{c\ min}$ (dB)**	**f_0 (GHz)**	**-25dB**	**-30dB**
3	1.0	0.5	1.4	-30.2	9.7	2.14	1.36
3.5	2.5	0.5	0.5	-17.4	9.7	0.62	--
4	0.6	2.9	0.5	-12.5	8.2	--	--
4.5	0.5	3.4	0.5	-9.3	11.1	--	--
5	3.9	0.5	0.5	-7.4	12.0	--	--

Figure 7.41(a), (b) and (c) shows the frequency dependent RL_c, real impedance Z_{in}' and imaginary impedance Z_{in}'' results respectively, of the triple layer design CAD with optimized thickness. The maximum absorption peak with -25dB and -30dB absorption bandwidth and optimized individual layer thickness is tabulated in table 7.38.

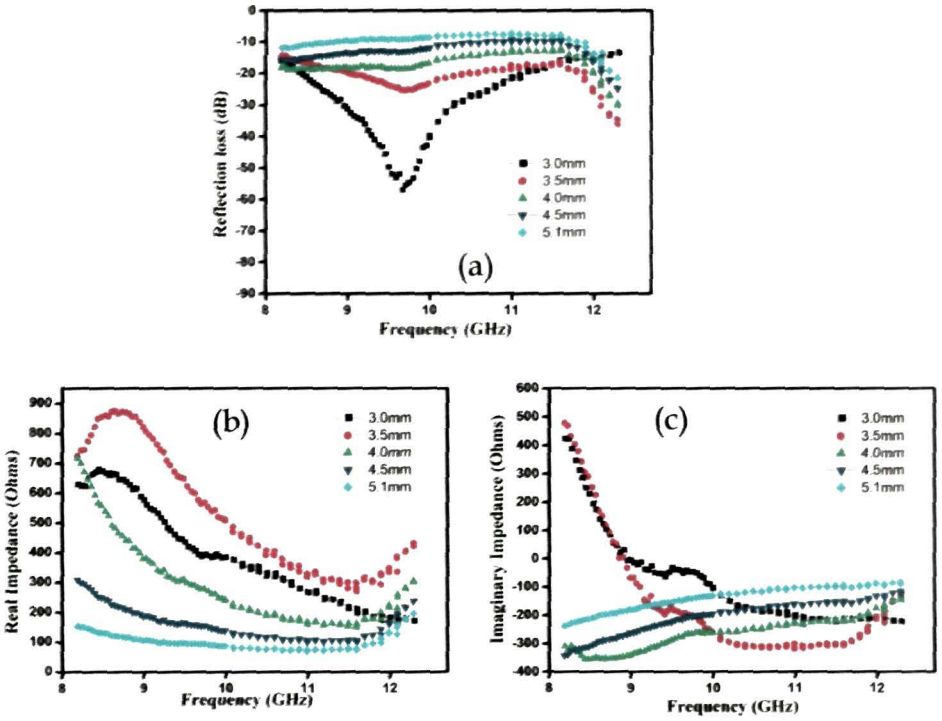

Figure 7.41 Plots of (a) RL_c, (b) Z_{in}' *and* (c) Z_{in}'' of designed **CAD** triple layer absorber with optimize thickness over the X-band

Table 7.38 Performance parameters of the designed **CAD** triple layer absorber with different thickness of the layers

Total thickness (mm)	Thickness of individual layers (mm)			Maximum absorption with corresponding frequency		Bandwidth in (GHz)	
d	**d1**	**d2**	**d3**	**$RL_{c\ min}$ (dB)**	**f_0 (GHz)**	**-25dB**	**-30dB**
3	0.6	0.8	1.6	-26.7	9.7	2.02	1.29
3.5	0.7	2.3	0.5	-14.9	12.3	0.33	0.17
4	0.8	2.7	0.5	-13.2	12.3	0.19	--
4.5	0.8	3.2	0.5	-8.5	12.3	--	--
5.1	0.8	3.8	0.5	-8.1	12.3	--	--

Figure 7.42(a), (b) and (c) shows the frequency dependent RL_c, real impedance Z_{in}' and imaginary impedance Z_{in}'' results respectively, of the triple layer design **CBD** with optimized thickness. The maximum absorption peak with -25dB and -30dB absorption bandwidth and optimized individual layer thickness is tabulated in table 7.39.

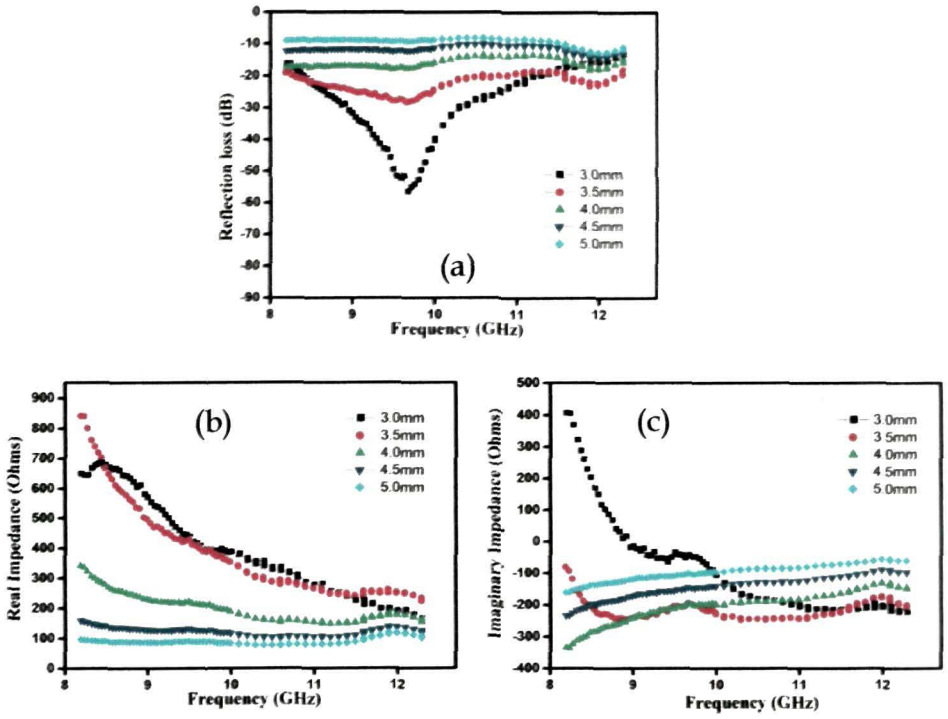

Figure 7.42 Plots of (a) RL_c, (b) Z_{in}' *and* (*c*) Z_{in}'' of designed **CBD** triple layer absorber with optimize thickness over the X-band

Table 7.39 Performance parameters of the designed **CBD** triple layer absorber with different thickness of the layers

Total thickness (mm)	Thickness of individual layers (mm)			Maximum absorption with corresponding frequency		Bandwidth in (GHz)	
d	d1	d2	d3	$RL_{c\ min}$ (dB)	f_0 (GHz)	-25dB	-30dB
3	0.5	1.0	1.5	-25.0	9.7	2.05	1.32
3.5	0.6	2.3	0.6	-18.2	9.7	0.68	--
4	0.5	3.0	0.5	-13.5	12.0	--	--
4.5	1.0	3.0	0.5	-10.9	12.0	--	--
5	0.7	3.8	0.5	-8.2	12.0	--	--

Table 7.40 Different combinations of triple layer design with RL_c<-40dB, -25dB and -30dB bandwidth > 1 GHz

Air-absorber Interface layer	Layer combination with total thickness	Thickness of individual layer (mm)			Bandwidth in (GHz)		Maximum absorption with corresponding frequency	
		d_1	d_2	d_3	-25 dB	-30 dB	$RL_{c\,min}$ (dB)	f_0 (GHz)
A-interface	BCA_3.4	0.54	1.96	0.9	2.21	1.53	-66	12.3
	CBA_3.4	2.19	0.51	0.7	1.92	1.4	-61	12.2
B-interface	ADB_3.1	0.52	2.05	0.53	2.25	1.45	-57	9.7
	ADB_3.5	0.5	0.6	2.4	1.01	0.72	-43	11.9
	CAB_3.4	2.2	0.7	0.5	1.8	1.5	-57	12.3
	CDB_3.1	0.56	2.04	0.5	2.24	1.46	-57	9.7
	CDB_3.5	0.5	0.54	2.46	1.06	0.72	-46	11.92
C-interface	ABC_3.2	0.52	0.52	2.16	2.7	2.28	-70	11.1
	ADC_3.1	0.52	0.61	1.97	2.66	2.28	-63	11.2
	BAC_3.2	0.53	0.51	2.16	2.68	2.22	-66	11.1
	BDC_3.1	0.5	0.64	1.96	2.75	2.34	-67	11.11
	DAC_3.2	0.51	0.52	2.17	2.72	2.26	-65	11..09
	DBC_3.2	0.54	0.51	2.15	2.83	2	-71	11.09
B-interface	ABD_3.0	0.89	0.54	1.57	2.02	1.33	-56.9	9.67
	ACD_3.0	1	0.53	1.47	2.1	1.37	-55.7	9.66
	BAD_3.0	0.53	0.8	1.67	1.99	1.32	-56.99	9.64
	BCD_3.0	1.06	0.5	1.44	2.12	1.38	-55.26	9.66
	CAD_3.0	0.59	0.75	1.66	1.98	1.32	-56	9.67
	CBD_3.0	0.53	0.9	1.57	2.14	1.37	-56.7	9.67

7.3.2. RESULTS AND ANALYSIS OF MEASURED REFLECTION LOSS VALUE OF TRIPLE LAYER MICROWAVE ABSORBER

Similar to double layer absorber, the triple layer microwave absorbers are fabricated by combining the layers of EG-NPR composites of desired wt. % and thickness. The fabrication of triple layer absorber design **BCA_3.4** having thickness d_1=0.54mm, d_2=1.96mm and d_3=0.9mm is synthesized as follows: 5 wt. % composite, 8 wt. % composite and 7 wt. % composite are made seperately by mechanical mixing and thermal treatment method and then combined them using the thermal treatment at 150 °C such that 7 wt. % is next to the metal plate, 8 wt. % is as the middle layer and 5 wt. % as the air-absorber interfacing layer. The dimension of fabricated triple layer sample is 152mm × 152mm × d mm for free space microwave absoption testing. The other design structures **CDB_3.1** and **BDC_3.1** are also fabricated in the similar way with same dimensions of total thickness 3.1mm. The free space microwave absorption measurement is performed similar to single layer and double layer absorption using Agilent E8362C VNA and spot focusing horn lens antenna system described in Chapter VI. The measured RL_m for **BCA_3.4, CDB_3.1** and **BDC_3.1** triple layer absorbers are plotted as function of frequency in figure 7.43.

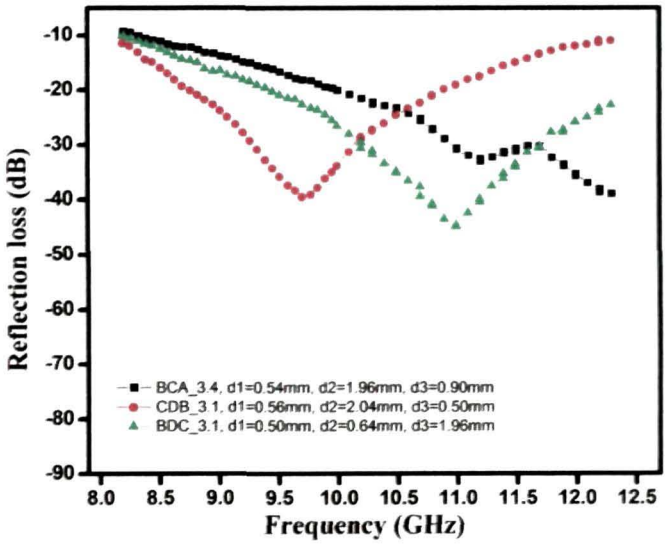

Figure 7.43 Measured reflection loss value of designed triple layer absorbers

The **BCA_3.4, CDB_3.1** and **BDC_3.1** design absorber show -25dB absorption bandwidth of 1.63 GHz (10.67 to 12.3 GHz), 1.37 GHz (9.10 to 10.47 GHz) and

2.16 GHz (9.92 to 12.08GHz), respectively and the -30dB absorption bandwidth for the same layer combinations as 1.33 GHz (frequency band 10.97 to 12.3 GHz), 0.78 GHz (frequency band 9.31to10.15 GHz) and 1.49 GHz (frequency band 10.21 to 11.70 GHz), respectively. The maximum absorption peak or minimum value of RL_m are obtained for **BCA_3.4** is -39dB at 12.23 GHz, for **CDB_3.1** is -39.44 dB at 9.7 GHz and for **BDC_3.1** is -44 dB at 10.99 GHz. The bandwidth and frequency corresponding to the peak minimum return loss value matches quite well for the measured and computed return loss value but the theoretical return loss value is higher than the experimental return loss values for all the combinations.

As mentioned earlier the absorber is modeled as transmission line using some approximations, which may effect the computed values of microwave absorption. The fabrication limitations may reduce the absorption of the layered absorber. The measured return loss value of the triple layer design structure emphasized that absorption frequency band can be tuned by selecting the proper EG-NPR composition with optimum thickness.

Table 7.41 Performance comparison of conductor backed single, double and triple layer microwave absorber.

Performance parameters	Single layer absorber of 8wt. % of thickness 4 mm	Double layer absorber dc_3.2 of thickness 3.2 mm	Triple layer absorber BDC_3.1 of thickness 3.1 mm
Min_RL_m (dB) at GHz	-16dB (10.42 GHz)	-46dB (11.09 GHz)	-44dB (10.99 GHz)
-10dB absorption bandwidth	1.3 GHz	whole X-band (8.2-12.4 GHz)	whole X-band (8.2-12.4 GHz
-25dB absorption bandwidth	--	2.46 GHz	2.16 GHz
-30dB absorption bandwidth	--	1.75 GHz	1.49 GHz

7.4 Discussions and Conclusions

Summarizes the best performance of EG-NPR compositions for single, double and triple layered structure in the X-band range. An enhanced bandwidth is observed for the layered structures almost covering the entire X-band. The thickness of the layered structure is also less than that of a single layered absorber with improved performance and for the triple layer structure the thickness marginally decreases as compared to double layer structure for similar performance.

The EG-NPR layered absorber designed using optimization technique, shows -10dB bandwidth i.e. 90% of incident power beign absorbed over the whole X-band and -25dB bandwidth i.e. 99.7% of the incident power is absorbed for ~ 2GHz range within the X-band. The total thickness of the layered absorber is less than that of single layer. The results shows that EG-NPR composite systems can be used as an efficient absorber over the entire X-band.

References

[1] Pozar, D.M. *Microwave Engineering*, Wiley, India, 2010.

[2] Vuong, X.T. Military X-band very small aperture terminals (VSATs) - to spread or not to spread, in Proceedings, IEEE , Military Communications Conference (MILCOM '96), McLean, VA, 6-10, 1996.

[3] HuangY., Li, N., Ma,Y., Du, F., Li, F., He, X., Lin, X., Gao, H., and Chen, Y. The influence of single-walled carbon nanotube structure on the electromagnetic interference shielding efficiency of its epoxy composites, *Carbon* **45**, 1614-1621, 2007.

[4] Hanna, S. M. Applications of x-band technology in medical accelerators, in Proceedings of the 1999 Particle Accelerator Conference, New York, 1999.

[5] Damini, A., McDonald, M., and Haslam, G.E. X-band wideband experimental airborne radar for SAR, GMTI and maritime surveillance, *IEE Proc.-Radar Sonar Navig.* **150**, 305-312, 2003.

[6] Jung, E. Y., Lee, J. W., Lee, T. K., and Lee, W.K. SIW-based array antennas with sequential feeding for X-band satellite communication, *IEEE Transactions on Antennas and Propagation* **60**, 3632-3639, 2012.

[7] Chu, C.K., Huang, H.K., Liu, H.Z., Lin, C.H., Chang, C.H., Wu, C.L., Chang, C.S., and Wang, Y.H. An X-band high-power and high-PAE PHEMT MMIC power amplifier for pulse and CW operation, *IEEE Microw. Wirel. Compon. Lett.* **18**, 707-709, 2008.

[8] Pande, S., Singh, B. P., Mathur, R. B., Dhami, T. L., Saini, P., and Dhawan, S. K. Improved electromagnetic interference shielding properties of MWCNT-PMMA composites using layered structures, *Nanoscale Res Lett* 4, 327-334, 2009.

[9] Al-Saleh, M. H., and Sundararaj, U. X-band EMI shielding mechanisms and shielding effectiveness of high structure carbon

black/polypropylene composites, *J. Phys. D: Appl. Phys.* **46**, 035304-1-7, 2013.

[10] Asi, M. J., and Dib, N. I. Design of multilayer microwave broadband absorbers using central force optimization, *Progress In Electromagnetics Research B* **26**, 101-113, 2010.

[11] Reinert, J., Psilopoulos, J., Grubert, J. and Jacob, A. F. On the potential of graded-chiral dallenbach absorbers, *Microwave and Optical TechnologyLetters* **30**, 254–257, 2001.

[12] Micheli, D., Pastore, R., Apollo, C., Marchetti, M., Gradoni, G., Primiani, V. M., Moglie, F. Broadband electromagnetic absorbers using carbon nanostructure-based composites, *IEEE Transactions On Microwave Theory And Techniques* **59**, 2633-2646, 2011.

[13] Jiang, L., Cui, J., Shi, L., and Li, X. Pareto optimal design of multilayer microwave absorbers for wide-angle incidence using genetic algorithms, *IET Microw. Antennas Propag.* **3**, 572–579, 2009.

[14] Qin, F., and Brosseau, C. A review and analysis of microwave absorption in polymer composites filled with carbonaceous particles, *Journal of Applied Physics* **111**, 061301-1-24, 2012.

[15] Micheli, D., Apollo, C., Pastore, R., and Marchetti, M. X-Band microwave characterization of carbon-based nanocomposite material, absorption capability comparison and RAS design simulation, *Journal of Composites Science and Technology* **70**, 400–409, 2010.

CHAPTER VIII

PERFORATED DESIGN STRUCTURE OF MICROWAVE ABSORBER

8.1 INTRODUCTION

Structural modification of microwave absorber by embedding frequency selective surface (FSS) in the substrate or circular perforation etc., have been reported to enhance the bandwidth as well as absorption performance [1-5]. The perforation of the dielectric substrate changes the relative permittivity of the substrate [6]. The perforation can be carried out by drilling holes in certain pattern taking into consideration that the distance between the holes should be small in comparison to the operating wavelength and in this way the uniform effective relative permittivity of the whole surface can be ascertained. This effective permittivity depends on the ratio of the perforated hole diameter to the distance between the two consecutive holes. Larger the hole diameter, lower is the effective permittivity. However, it is to be seen that the mechanical strength of the absorber system do not reach the breaking limit. The reflection loss behavior depends on the effective permittivity of the substrate; modification of EG-NPR substrate geometry may change its microwave absorption characteristics.

The chapter describes design and fabrication of a circularly perforated EG-NPR composite microwave absorber with single layered and double layered structure. Rectangular wave-guide method is used for finding S_{11} parameter for the structure.

8.2 Designing of perforated structure

Two types of perforation are carried out on EG-NPR absorber: (i) a through the thickness perforation of single layered structures and (ii) through and partly perforated double layer structure. The reflection loss properties of the perforated substrate backed by a metal plate are carried out. Figure 8.1 shows a circular perforation on a dielectric substrate of relative permittivity,

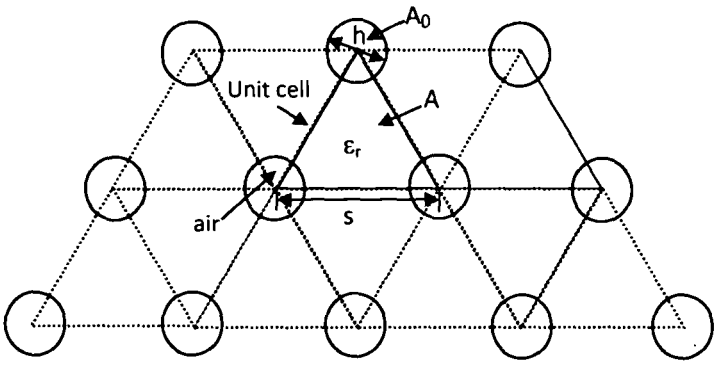

Figure 8.1 Perforated dielectric substrate with triangular lattice

ε_r, with triangular lattice. The maximum value of the ratio of the hole diameter (h) to lattice spacing(s) for the self supporting substrate is reported to be $h/s = 11/12$ and in the present investigation this ratio is maintained with hole diameter 10 times less than the lowest working wavelength [3,6]. The perforation on the dielectric substrate, modifies the relative permittivity of the structure and the change in permittivity termed as effective permittivity ε_{eff} is given as

$$\varepsilon_{eff} = \varepsilon_r(1-\kappa) + \kappa \tag{8.1}$$

Where κ is the filling factor given by $\kappa = \frac{A_0}{2A}$ for triangular lattice. Here A_0 is the area of the circular hole and A is the area of the unit lattice. The filling factor for triangular lattice is obtained as

$$\kappa = \frac{\pi h^2/4}{2\left(\frac{\sqrt{3}}{4}\right)s^2} = \frac{\pi}{2\sqrt{3}}\left(\frac{h}{s}\right)^2 \tag{8.2}$$

Substituting ($\varepsilon_r = \varepsilon_r' - j\varepsilon_r''$) and κ in equation (8.1) we have

$$\varepsilon_{eff} = \varepsilon_{eff}' - j\varepsilon_{eff}'' = \varepsilon_r'(1-\kappa) + \kappa - j\varepsilon_r''(1-\kappa) \tag{8.3}$$

$$\varepsilon_{eff}' = \varepsilon_r'\left(1 - \frac{\pi}{2\sqrt{3}}\left(\frac{h}{s}\right)^2\right) + \frac{\pi}{2\sqrt{3}}\left(\frac{h}{s}\right)^2 \tag{8.4}$$

$$\varepsilon_{eff}'' = \varepsilon_r'' \left(\frac{\pi}{2\sqrt{3}}\left(\frac{h}{s}\right)^2 - 1\right) \quad (8.5)$$

ε_{eff}' and ε_{eff}'' are real and imaginary effective permittivity of the perforated system of triangular lattice. These values are utilized to calculate the reflection loss behavior of the perforated system.

8.2.1 Effective complex permittivity of the through perforated EG-NPR composite structure

The effective complex permittivity, ε_{eff}, of the perforated single layer EG-NPR composites with weight percentages 5, 7, 8 and 10 wt. % are calculated from the measured values ε_r' and ε_r'' discussed in chapter V using

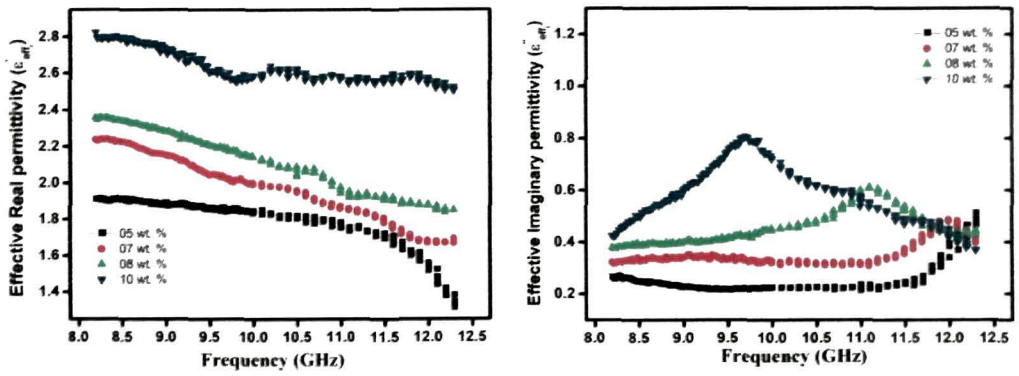

Figure 8.2 Calculated effective permittivity of perforated (5, 7, 8 and 10) wt. % EG-NPR composites (a) Real part and (b) Imaginary part

in equations (8.4) and (8.5). The frequency dependent ε_{eff}' and ε_{eff}'' graphs are shown in figure 8.2 (a) and (b). The calculated ε_{eff}' spectra of the perforated composite shows an increasing trend with increase in EG wt. %, however, the value decreases towards higher X-band frequency. The ε_{eff}' values are sufficiently reduced in comparison to non-perforated EG-NPR composites. One of the impedance matching condition mentioned in Chapter VI is that the real part of permittivity should approach to ~1. From the figure 8.2(a), the 5 wt. % EG-NPR composite is closing to ~ 1 at 12.4 GHz,

excepting a good impedance matching at that frequency. The imaginary ε_{eff}'' spectra of the perforated composites show a similar trend with the non perforated composites but the values are reduce. The reduced values of both the real and imaginary effective permittivity spectra are due to the effect of air present in the perforated region. Using these calculated values, a single layer and double layer perforated microwave absorber is designed.

8.2.2 Perforated Single layer microwave absorber

According to the TLM, the reflection loss, RL_c of the perforated EG-NPR substrate backed by a perfect electric conductor (PEC) as shown in figure 8.3, is given [7] as

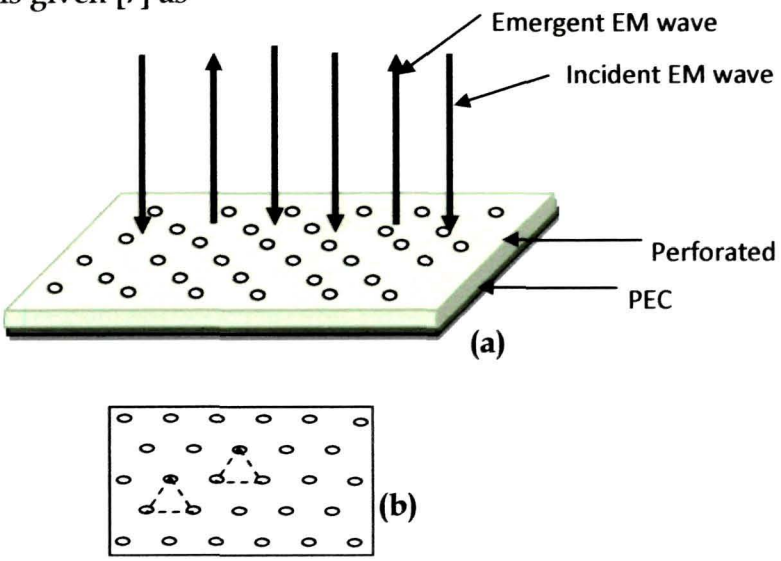

Figure 8.3 (a) Design structure of conductor backed perforated single layer absorber (b) Top view of triangular lattice

$$RL_c = 20\log\left|\frac{\sqrt{1/\varepsilon_{eff}}\tanh(j2\pi f/c)\sqrt{\varepsilon_{eff}}d-1}{\sqrt{1/\varepsilon_{eff}}\tanh(j2\pi f/c)\sqrt{\varepsilon_{eff}}d+1}\right| \quad (8.6)$$

Equation (8.6) shows that RL_c value depends on the effective complex permittivity and thickness of the perforated composite material. For designing a single layer absorber with known complex permittivity, the only variable parameter is the thickness, *d*. A MATLAB program is developed to calculate

the minimum reflection loss value i.e. more negative values in dB by optimizing the thickness parameters within the limit from 1mm to 10 mm over the X-band.

The algorithm of the program is as follows:

Step 1: Read data (ε_{eff}', ε_{eff}'', f) from file.

Step 2: For each thickness from 1 mm to 10 mm at a step size of 0.5 mm, find the minimum value of RL_c among all the thickness and store the data.

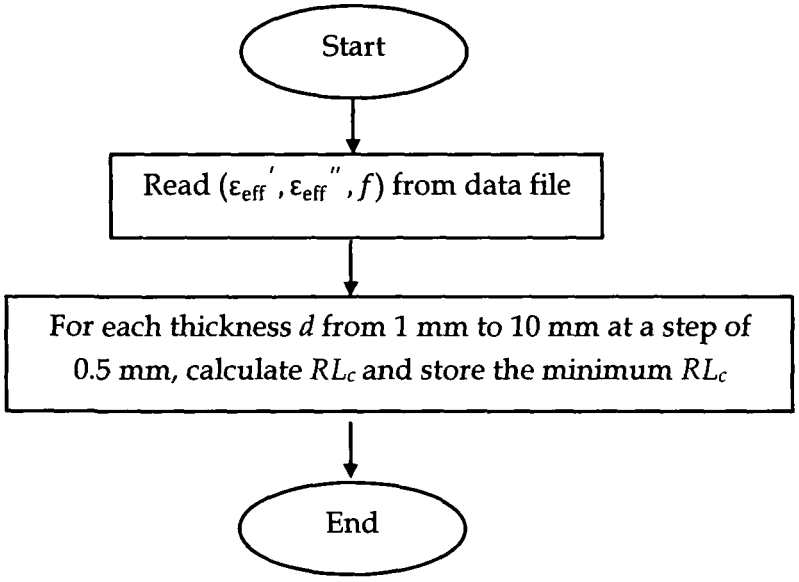

Figure 8.3A Flow chart diagrams for single layer absorber program

Calculated Reflection Loss of through perforated single layer absorber

The calculated RL_c curves for the perforated EG-NPR composites are shown in figure 8.4(a). The RL_c ~-22 dB is observed at 12.4 GHz for 5 wt. % EG composites of thickness 7.5 mm, the RL_c peaks is shifted to lower frequency for higher wt. % EG composition with values RL_c ~-18 dB at 12.2 GHz for 7 wt. % of thickness 6.5 mm, RL_c ~ -19 dB at 11 GHz for 8 wt. % of thickness 6 mm and RL_c~ -21 dB at 9.7 GHz for 10 wt. % of thickness 5.5 mm. The RL_c values are

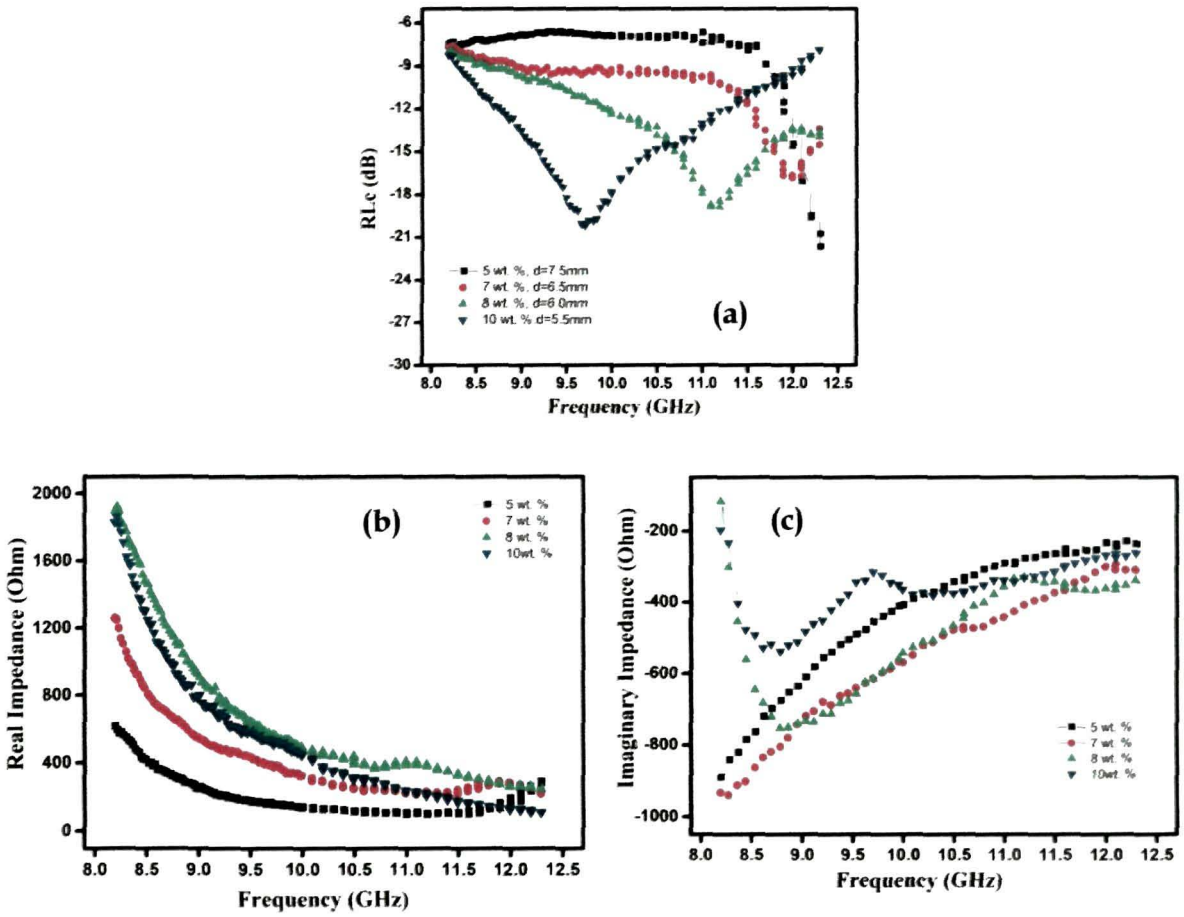

Figure 8.4 (a) calculated Reflection loss, RL_c (b) real impedance and (c) imaginary impedance of perforated single layer microwave

found to be much less in comparison to non-perforated values discussed in chapter VI. The impedance plot of the perforated composites shown in figure 8.4(b) and 8.4(c), can explain the lower values of RL_c. The impedance matching condition requires that the real and imaginary impedance should be simultaneously equals to 377Ω and zero [8]. The frequency dependent impedance spectra should meet these criteria throughout the frequency band and hence the lower values of RL_c. However, the calculated RL_c shows a -10dB absorption bandwidth of ~3 GHz for 8 wt. % and 10 wt. % single layer EG

composites, and since the absorber is perforated, the weight of the absorber system will be reasonably light and could be used in many desired applications.

Reflection Loss measurement of perforated single layered absorber

Based on the calculated RL_C, single layered perforated EG-NPR substrate as shown in figure 8.5(a), is fabricated by making circular holes of diameter, h= 2 mm and lattice spacing, s=2.18 mm, maintaining the ratio h/s = 11/12. The measured RL_m spectra of 5, 7, 8 and 10 wt. % composites are shown in

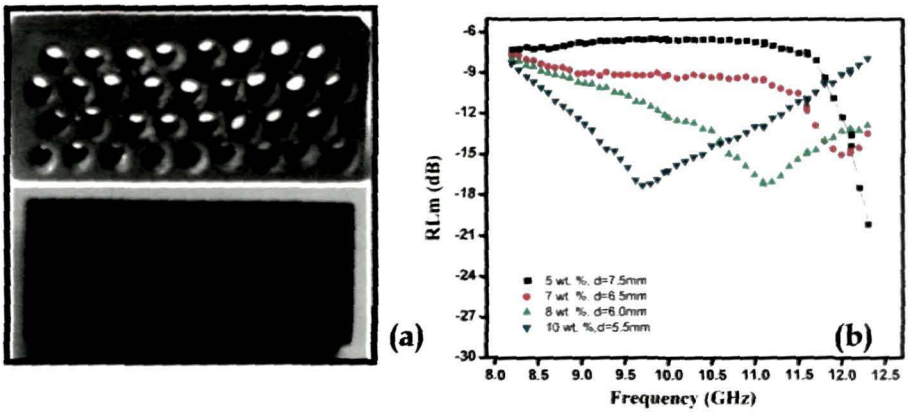

Figure 8.5 (a) Perforated EG-NPR absorber structure and (b) RL_m of perforated EG-NPR composites

figure 8.5 (b). The dimension of the perforated samples is kept 22.86 mm × 10.16 mm × d. The RL_m is measured using rectangular waveguide technique for X-band frequency describes in reference [9].The frequency dependent plots of RL_m shows a similar characteristic as that of calculated RL_C. A maximum reflection loss value of the composites with frequency and -10dB absorption peak is tabulated in table 8.1.

Table 8.1 Performance parameters of perforated single layered absorber

EG-NPR composition	Thickness	Min_RL_m	Frequency	-10dB bandwidth
5 wt. %	7.5 mm	-21dB	12.4 GHz	0.4 GHz
7 wt. %	6.5 mm	-16dB	12.0 GHz	1.0 GHz
8 wt. %	6.0 mm	-18dB	11.0 GHz	3.0 GHz
10 wt. %	5.5 mm	-19dB	9.7 GHz	2.2 GHz

From the table 8.1, it is seen that single layered perforated design of thickness ~6 mm gives a -10dB bandwidth ~3 GHz. Hence, the perforated structure has enhanced the bandwidth.

8.2.3 Partly and through perforated double layered microwave absorber

Reflection loss study of the perforated double layered is studied in two ways: (a) through perforation of the two layers and (b) partly perforated i.e only the 1st layer is perforated.

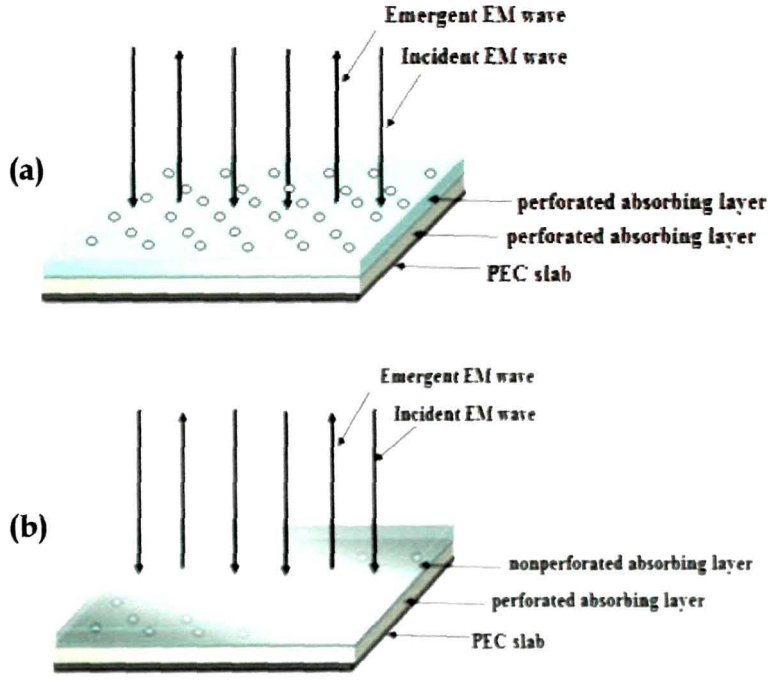

Figure 8.6 Schematic of double layered absorber structure (a) through perforated and (b) partly perforated

The schematic diagram of the through perforated and partially perforated microwave absorber is shown in figure 8.6 (a) and (b) respectively. In this study, the double layered combination **dc_3.2** composed of 10wt. % EG composite as 1st layer and 8wt. % EG composite as 2nd layer, is considered since this structure gives maximum absorption peak and absorption bandwidth out of all the other double layered combination discussed in the previous chapter.

Using the TLM, the reflection loss expression for conductor backed double layered absorber as discussed in chapter II, is given as

$$RL_c = 20\log\left|\frac{\sqrt{1/\varepsilon_{eff}}\left[\frac{\sqrt{1/\varepsilon_{eff}}\tanh\, j(2\pi f/c)\sqrt{\varepsilon_{eff}}\,d_1+\sqrt{1/\varepsilon_{eff}}\tanh\, j(2\pi f/c)\sqrt{\varepsilon_{eff}}\,d_2}{\sqrt{1/\varepsilon_{eff}}+\sqrt{1/\varepsilon_{eff}}\tanh\,(j(2\pi f/c)\sqrt{\varepsilon_{eff}}\,d_1)\tanh\, j(2\pi f/c)\sqrt{\varepsilon_{eff}}\,d_2)}\right]-1}{\sqrt{1/\varepsilon_{eff}}\left[\frac{\sqrt{1/\varepsilon_{eff}}\tanh\, j(2\pi f/c)\sqrt{\varepsilon_{eff}}\,d_1+\sqrt{1/\varepsilon_{eff}}\tanh\, j(2\pi f/c)\sqrt{\varepsilon_{eff}}\,d_2}{\sqrt{1/\varepsilon_{eff}}+\sqrt{1/\varepsilon_{eff}}\tanh\,(j(2\pi f/c)\sqrt{\varepsilon_{eff}}\,d_1)\tanh\, j(2\pi f/c)\sqrt{\varepsilon_{eff}}\,d_2)}\right]+1}\right| \quad (8.7)$$

Using a MATLAB program based on the equation (8.7), the reflection loss value for both the design is calculated.

From figure 8.7 (c), RL_c is not showing a good absorption properties with a maximum value of only -18dB at ~9.7 GHz, however, the partially perforated structure shows a RL_c~-68dB at~11.2 GHz and -25dB bandwidth of ~2.7 GHz. This absorption behavior can be analyzed from the impedance graphs shown in figure 8.7 (d), in which the real and imaginary impedance at 11.2 GHz is approaching to impedance condition of 377Ω and 0Ω, simultaneously. Based on this calculated value a partially perforated double layered combination **dc_3.2** in which the layer **d** is perforated and kept beneath the front layer **c**.

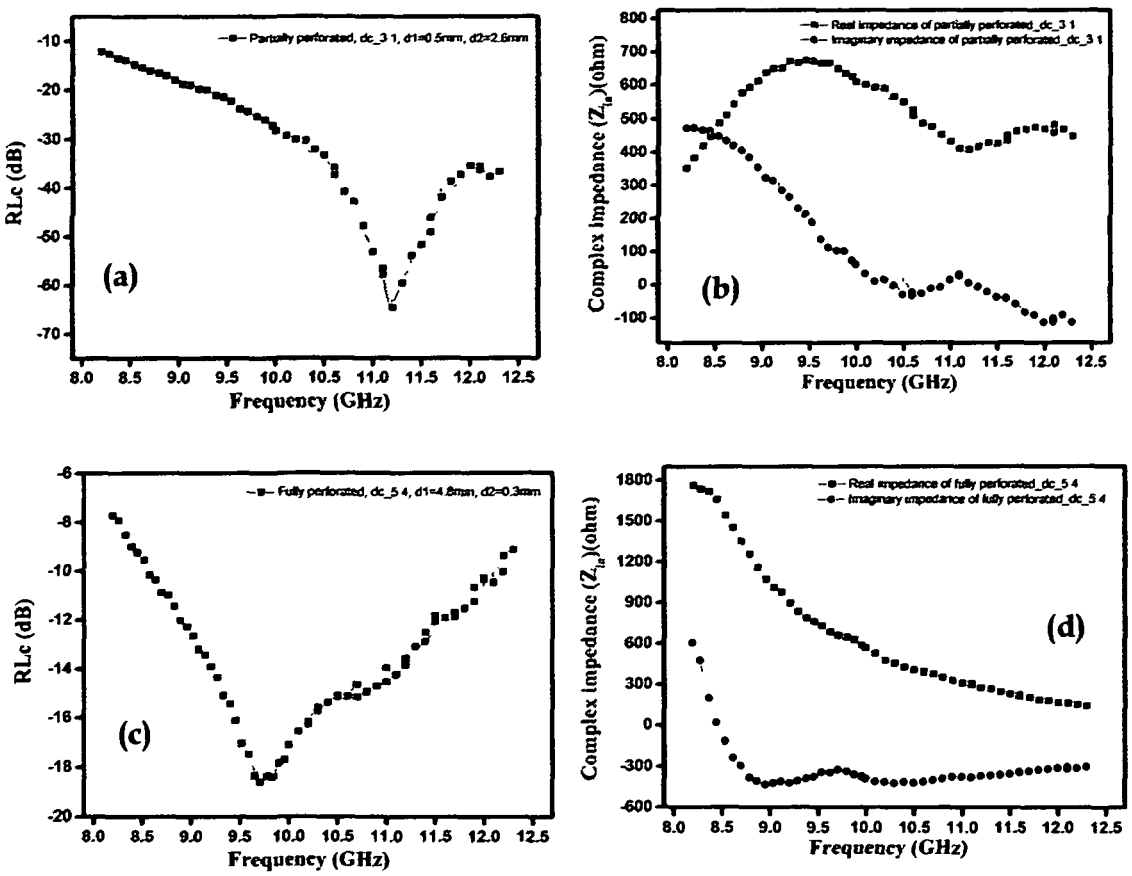

Figure 8.7 Plots of (a) RL_c and (b) complex impedance of partially perforated double layered absorber, (c) RL_c and (d) complex impedance of completely perforated double layered absorber

The dimension of the sample is kept as 22.86 mm x 10.16 mm x 3.2 mm and reflection loss measured is performed using rectangular waveguide method. The measured reflection loss RL_m is plotted as a function of frequency and showing in figure 8.8. The RL_m~-40dB is observed at 11.3 GHz showing a -25dB bandwidth of ~2.4 GHz. The developed partly perforated double layered being light weight and thin is found to be a promising microwave absorber for applications over the X-band.

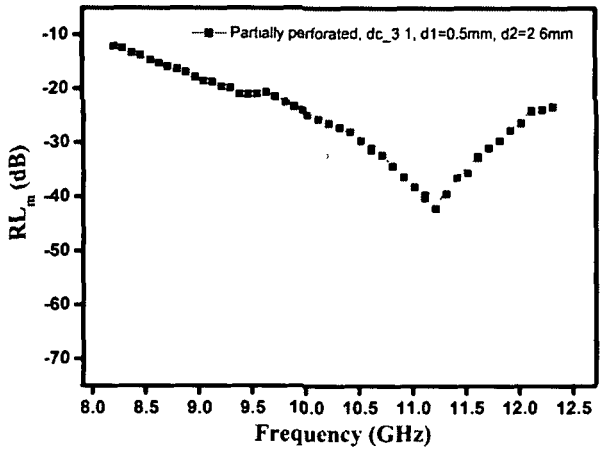

Figure 8.8 RL_m values of partially perforated dc_3.2 microwave absorber

8.3 CONCLUSION

The perforated single layered structure shows an enhancement of bandwidth from ~1GHz for without perforation to about 3GHz. The best performance double layered structure shows comparable results except the weight reduces to by 17.8 %. The weight reduction will make the EG-NPR composites useful to be mounted on many airborne systems. The measurement technique used here is waveguide technique instead free space technique used for non-perforated structure which may give some discrepancy in the performance parameters.

REFERENCES

1. Xie, W., Cheng, H. F., Chu, Z. Y., Zhou, Y. J., Liu, H. T., and Chen, Z. H. Effect of FSS on microwave absorbing properties of hollow-porous carbon fiber composites, *Materials and Design* **30**, 1201–1204, 2009.
2. Luukkonen, O., Costa, F., Simovski, C. R., Monorchio, A., and Tretyakov, S. A. A Thin electromagnetic absorber for wide incidence angles and both polarizations, *IEEE Trans. Antennas and Propag.* **57**, 3119-3125, 2009.
3. Iqbal, M. N., Malek, F., Ronald, S. H., Shafiq, M., Juni, K. M., and Chat, R. A study of the EMC performance of a graded-impedance, microwave, rice-husk absorber, *Progress in Electromagnetics Research* **131**, 19-44, 2012.
4. Fallahi, A., Yahaghi, A., Benedickter, H. R., Abiri, H., Shahabadi, M., and Hafner, C. Thin wideband radar absorbers, *IEEE Trans. Antennas and Propag.* **58**, 4051-4058, 2010.
5. Kern, D. J., and Werner, D. H. A genetic algorithm approach to the design of ultra-thin electromagnetic bandgap absorbers, *Microwave and Optical Technology Letters* **38**, 61-64, 2003.
6. Petosa, A. and Ittipiboon, A. Design and performance of a perforated dielectric Fresnel lens, *IEE Proc. Microw.Antennas Propag.* **150**, 309-314, 2003.
7. Michielssen, E., Sajer, J. M., Ranjithan, S., and Mittra, R. Design of lightweight, broad-band microwave absorbers using genetic algorithms, *IEEE Transactions on Microwave Theory and Techniques* **41**, 1024-1031, 1993.
8. Micheli, D., Apollo, C., Pastore, R., and Marchetti, M. X-Band microwave characterization of carbon-based nanocomposite material, absorption capability comparison and RAS design simulation, *Compos. Sci. Technol.* **70**, 400-409, 2010.

9. Abbas, S.M., Chandra, M., Verma, A., Chatterjee, R. , and Goel, T.C., Complex permittivity and microwave absorption properties of a composite dielectric absorber , *Composites: Part A* 37, 2148–2154, 2006.

CHAPTER IX

ACHIEVEMENTS, LIMITATIONS AND FUTURE DIRECTIONS

The present study is carried out with an objective of developing a broadband microwave absorber in X-band with practical design consideration of light weight, environment inertness, thermally stable and cost effectiveness. A low density expanded graphite (EG) flakes are successfully synthesized from natural graphite flakes and used as reinforcers in novolac phenolic resin (NPR) matrix to develop the dielectric microwave absorber. Formation of EG is confirmed from XRD pattern showing the expansion of the graphite basal planes along c-axis. The thickness of EG sheets ranges from 20nm - 50nm and the homogenous distribution of EG flakes in NPR matrix ensure uniform interaction of microwave with the dielectric composites. FTIR shows presence of hydroxyl and methylene group's in NPR which is responsible for bonding with EG and the interaction is physical in nature. EG-NPR composite system shows low density <1 and has negligible water absorption and thermally stable up to 300 °C with sufficient thermal conductivity and thermal dimensional stability. Complex permittivity of the composites is measured using Nicolson-Ross technique over the X-band. The real permittivity ε_r' increases linearly from 5 to 10 wt. % but further increase in EG wt. % decreases its value. Enhancement of ε_r'', is observed with increase in EG percentage in NPR and both real and imaginary part of complex permittivity shows a decreasing trend with frequency. Dielectric loss tangent ($tan\delta_e$), attenuation constant (α) and microwave conductivity (σ) increase with EG wt. % in the composites.

EG-NPR composite is developed as a conductor backed single layer absorber, using transmission line model, where the thickness of the dielectric absorber substrate is optimized for maximum reflection loss over the X-band. The calculated and measured reflection loss value of 4 mm thickness is found to be adequate matching with RL_c ~ -55dB and RL_m~-43dB at 12.4 GHz for 5 wt. % EG-NPR composite. A -10dB absorption of ~1GHz is observed for 7 to 10 wt. % composites. The EG-NPR composites from 30 wt. % to 50 wt. %

shows high values S_{21}~-40dB over the entire X-band and can be used as shielding material by reflection.

To enhance the absorption bandwidth, a multilayer structure is designed and optimized by the layer compositions and individual layer thickness to find the maximum absorption peak and absorption bandwidth of -25dB and -30dB over the X-band. The double layer design of total thickness 3.2 mm shows -25dB and -30dB bandwidth of 2.46 GHz and 1.75 GHz respectively. The triple layer design shows -25dB and -30dB bandwidth of 2.16 GHz and 1.49 GHz respectively. A perforated design through the EG-NPR composite system reduces the weight without much effecting performance, however single layer structure with perforation shows 2GHz enhancement of bandwidth in X-band range.

The present work shows an ample indication on the potential of EG-NPR composites as microwave absorbing materials for application in the frequency range of 8.2 GHz to 12.4 GHz. The developed microwave absorber has additional advantages of light weight, relatively thin dielectric absorber and cost effective.

The performance of the absorber can be further improved by incorporating magnetic inclusions in addition to EG flakes in the composites. 5 wt. % EG composites shows a minimum RL_m towards the higher X-band, so extension of frequency towards K_u band as well as C-band to study the microwave absorption behaviour of the developed composites could be performed. Furthermore, while designing microwave absorber, the metal plate can be replaced by higher wt. % EG composites due to high reflecting properties of 30 to 50 wt. % composites. The EG-NPR composites developed can be fabricated in the form of tiles and have negligible flexibility. A flexible microwave absorber may be developed by incorporating EG flakes into flexible base matrix like EPDM etc. and check the microwave absorption properties.

APPENDIX

A. The theoretical thickness limit for broadband microwave absorption in the frequency range 8.2 GHz to 12.4 GHz

The minimum thickness limit of a dielectric microwave absorber for broadband absorption in a particular frequency ranges f_1 and f_2, corresponding to wavelength λ_1 and λ_2 is given as

$$\left|\int_0^\infty \ln|R(\lambda)|d\lambda\right| \leq 2\pi^2 \sum_i d_i \qquad \text{(A.1)}$$

Where d_i is the thickness of the i^{th} layer of the absorber, $R(\lambda)$ is the frequency dependent reflectance and $d\lambda = \lambda_1 - \lambda_2$.

Introducing decibel scale of the reflectance i.e RL_c=20log$|R(\lambda)|$ and since $ln|R(\lambda)|$ =2.303log$|R(\lambda)|$, the equation (A.1) is modified to

$$\left|\int_0^\infty 2.303 \frac{RL_c}{40\pi^2} d\lambda\right| \leq \sum_i d_i \qquad \text{(A.2)}$$

For RLc =-30dB absorption over the wavelength ranges λ_1 = 36.58 mm and λ_2 = 24.19 mm, the minimum total thickness limit of the absorber is derived as

$$2.303 \frac{RL_c}{40\pi^2} (\lambda_1 - \lambda_2) \leq d \qquad \text{(A.3)}$$

Substituting the values of RL_c, λ_1 and λ_2, we get

$$\boldsymbol{d > 2.1\ mm.}$$

Thus, to give a RLc=-30dB over the frequency range 8.2 GHz to 12.4 GHz, the thickness of the dielectric microwave absorber could not be less than 2.1 mm.

B. MATLAB program based on Nicolson Ross method for computing complex permittivity

```
clear all;
P=xlsread('C:\Users\k11.xlsb'); % loading k11.xlsb file containing measured S11 values
Q=xlsread('C:\Users\k21.xlsb'); % loading k11.xlsb file containing measured S21 values
    S11=P (1:201, 2);
    S21=Q (1:201, 2);
    V1=S21+S11;
    V2=S21-S11;
    V3=V1 (1: 201,1).*V2(1: 201,1);
    X = (1-V3)./(V1-V2);
    Y = sqrt(X.^2-1);
    R1=X+Y;
    a1=real(R1);
    b1=imag(R1);
    Rf = sqrt((a1).^2+(b1).^2)
    R2=X-Y;
    a2=real(R2);
    b2=imag(R2);
    Rs = sqrt((a2).^2+(b2).^2)
for i=1: 201
    if (Rf(i)>1)K(i)=Rs(i), end;
    if (Rs(i)>1)K(i)=Rf(i); end;
end
R=transpose(K);
T = (V1-R)./(1-V1.*R);
c1= ((1+R)./(1-R)).^2;
f = P(1: 201,3);
w = 2*pi*f(1: 201, 1);
d = 3.7*10^-3;
c = 3*10^8;
M=w.*d;
N=c./M;
c2 = -[N.*log(1./T)].^2;
e = sqrt(c2./c1)
e1=real(e) %real part of complex permittivity
e2=imag(e) %imaginary part of complex permittivity
```

****

C. **A MATLAB program for reflection loss optimization with varying individual layer thickness of multilayer layer absorber system**

The input impedance and reflection loss of a conductor backed multilayer microwave absorber can be calculated using Transmission Line Model. The following program is developed based on the reflection loss expression for triple layer microwave absorber.

```
clear all
load ('C:\Users\hp\Desktop\pf1.txt');  %loading 'pf1.txt' file containing frequency, real and imaginary permittivity of EG-NPR composite
    f=pf1(:,1);              %frequency in X band
    c=3*10^8;                %free space microwave velocity
    c1=c^2;
    e1=pf1(:,2);             %Real permittivity of 1st layer EG-NPR composite
    e2=pf1(:,3);             %Real permittivity of 2nd layer EG-NPR composite
    e3=pf1(:,4);             %Real permittivity of 3rd layer EG-NPR composite
    e11=pf1(:,7);            %Imaginary permittivity of 1st layer EG-NPR composite
    e22=pf1(:,8);            %Imaginary permittivity of 2nd layer EG-NPR composite
    e33=pf1(:,9);            %Imaginary permittivity of 3rd layer EG-NPR composite
    u1=1;                    %Real permeability of 1st layer EG-NPR composite
    u2=1;                    %Real permeability of 2nd layer EG-NPR composite
    u3=1;                    %Real permeability of 3rd layer EG-NPR composite
    u11=0;                   %Imaginary permeability of 1st layer EG-NPR composite
    u22=0;                   %Imaginary permeability of 2nd layer EG-NPR composite
    u33=0;                   %Imaginary permeability of 3rd layer EG-NPR composite
    %d1=1*10^-3;
    %d2=2*10^-3;
    %d3=1*10^-3;
    %thickness=10;
        ArrThickness=[];
        ArrResults=[];
        plot_data=[];
%varying total thickness from 3 mm to 5.4 mm at a step size of 0.5mm, within a selected thickness range say 3 to 3.4 mm, find the individual layer thickness combination which gives
```

minimum value of RL_c, store the data and continue steps for next thickness range say 3.5 to 3.9 mm.

```
for      t=3:.5:5.4
         Results=[];
          RLminLimit=0;

  clear d1minRL d2minRL  d3minRL RL_min f_min  Zr_min Zi_min fBand4minRL
   RLminTillNow Zrealmin  Zimagmin

  for   thickness=t:0.1:(t+0.4)
       %result will have d1 d2 d3 RL f Zr
    for i=1:1000
         while(1)
           d1=rand*thickness;
           d2=rand*(thickness-d1);
           d3=(thickness-(d1+d2));
         if (d1<0.5 | | d2<0.5 | | d3<0.5)
              continue
          else
             break
       end
     end
         d1=d1*10^-3;
         d2=d2*10^-3;
         d3=d3*10^-3;
         a1=u1.*e1+u11.*e11;
         b1=u1.*e11-u11.*e1;
         Aa1=a1./A1;
         Ab1=b1./A1;
         Z1=sqrt(complex(Aa1,Ab1));
         n1=377.*Z1;
         A2=e2.^2+e22.^2;
         a2=u2.*e2+u22.*e22;
         b2=u2.*e22-u22.*e2;
         Aa2=a2./A2;
         Ab2=b2./A2;
```

```
Z2=sqrt(complex(Aa2,Ab2));
n2=377.*Z2;
A3=e3.^2+e33.^2;
a3=u3.*e3+u33.*e33;
b3=u3.*e33-u33.*e3;
Aa3=a3./A3;
Ab3=b3./A3;
Z3=sqrt(complex(Aa3,Ab3));
n3=377.*Z3;
c1=u1.*e1-u11.*e11;
f1=u1.*e11+u11.*e1;
D1=sqrt(complex(c1,(-f1)));
g1=(i*2*pi*f./c).*D1;
c2=u2.*e2-u22.*e22;
f2=u2.*e22+u22.*e2;
D2=sqrt(complex(c2,(-f2)));
g2=(i*2*pi*f./c).*D2;
c3=u3.*e3-u33.*e33;
f3=u3.*e33+u33.*e3;
D3=sqrt(complex(c3,(-f3)));
g3=(i*2*pi*f./c).*D3;
E1=i*tan((2*pi*f.*d1/c).*D1);
E2=i*tan((2*pi*f.*d2/c).*D2)
E3=i*tan((2*pi*f.*d3/c).*D3);
G=n1.*E1;
Gr=real(G);
Gi=imag(G);
H=n2.*E2;
I=n1.*E1.*E2;
A=(n2.*(G+H))./(n2+I);
Ar = real(A);
Ai = imag(A);
B=n3.*E3;
C=A.*E3;
M=A+B;
N=n3+C;
```

```
Z9=M./N;
Zin=n3.*Z9;
Zr=real(Zin);
Zi=imag(Zin);
R1=Zin-377;
R2=Zin+377;
R3=R1./R2;
R4=abs(R3);
RL=20*log(R4)
RL_min=min(RL);
%finding the least RL that we calculated till now.
%once a lesser RL is found, it is kept and earlier
%min RL matrix and f bannd values are replaced.
if      RL_min<RLminLimit
            RLminTillNow=RL,
            fBand4minRL=f;
            d1minRL=d1;
            d2minRL=d2;
            d3minRL=d3;
        f_min=f(find(RL==RL_min,1));
        Zr_min=Zr(find(RL==RL_min,1));
        Zi_min=Zi(find(RL==RL_min,1));
        RLminLimit=RL_min;
        Zrealmin=Zr;
    Zimagmin=Zi;
    end
  end
 end
ArrResults=[ArrResults;                          d1minRL+d2minRL+d3minRL,
d1minRL,d2minRL,d3minRL,RLminLimit,f_min, Zr_min,Zi_min];
str=sprintf('Thickness_%5.2f.mat',t);
toStore=[fBand4minRL, RLminTillNow, Zrealmin,  Zimagmin];
save(str, 'toStore' );
end
```

****

Publications

1. J. P. Gogoi, N. S. Bhattacharyya and K.C. James Raju, "Synthesis and microwave characterization of expanded graphite/novolac phenolic resin composite for microwave absorber applications" *Composites Part B: Engineering, 2011,* doi:10.1016/j.compositesb.2011.01.026.
2. J. P. Gogoi, N. S. Bhattacharyya, "EMI shielding characteristics of expanded graphite/novolac phenolic resin composite for applications in wireless communication", *IEEE proc. ICDeCOM-2011,* BIT Mesra, doi: 10.1109/ICDECOM.2011.5738512
3. J. P. Gogoi and N. S. Bhattacharyya, "Microwave Characterization of Expanded Graphite/Phenolic Resin Composite for Strategic Applications" *Progress In Electromagnetics Symposium-2012 Kaula Lumpur, Malaysia*

Communicated

4. J. P. Gogoi, N. S. Bhattacharyya and S. Bhattacharyya, "Microwave Absorption Studies of Expanded Graphite – Phenolic Resin Composites in X-Band", *communicated to Journal of Physics and Chemistry of Solids, Elsevier*
5. Jyoti P. Gogoi and Nidhi S. Bhattacharyya, "Design and development of double layer microwave absorber based on Expanded Graphite-Novolac Phenolic resin composite for X-band applications". (*ready to be communicated*)
6. Jyoti P. Gogoi and Nidhi S. Bhattacharyya, "Triple layer microwave absorber design using dielectric expanded graphite-novolac phenolic resin composite". (*ready to be communicated*)
7. Jyoti P. Gogoi and Nidhi S. Bhattacharyya, "Perforated dielectric absorber design for bandwidth enhancement for X-band applications". (*ready to be communicated*)
8. Jyoti P. Gogoi and Nidhi S. Bhattacharyya, "Multilayer perforated design microwave absorber based on EG-NPR composite", (*ready to be communicated*)